Light Microscopy Beyond the Diffraction Barrier for Live Cell Studies

Zur Erlangung des akademischen Grades eines

DOKTORS DER NATURWISSENSCHAFTEN

von der Fakultät für Physik des
Karlsruher Instituts für Technologie (KIT)

genehmigte

DISSERTATION

von

Dipl. Phys. Per Niklas Hedde

aus Ulm

April 2013

Tag der mündlichen Prüfung: 17. Mai 2013
Referent: Prof. Dr. Gerd Ulrich Nienhaus
Korreferent: Prof. Dr. Thomas Schimmel

http://www.aph.kit.edu/nienhaus

http://www.cfn.kit.edu

Prüfungskommission:
Prof. Dr. G. U. Nienhaus
Prof. Dr. Th. Schimmel
Prof. Dr. A. Mirlin
Prof. Dr. J. Blümer
Prof. Dr. U. Nierste
Prof. Dr. D. Zeppenfeld

Anschrift:
Per Niklas Hedde

Karlsruher Institut für Technologie (KIT)
Institut für Angewandte Physik
Wolfgang-Gaede-Strasse 1
D-76131 Karlsruhe
AG Nienhaus

hedde@kit.edu
phedde@yahoo.com

Diese Arbeit wurde durch das DFG Center for Functional Nanostructures (CFN) am Karlsruher Institut für Technologie (KIT) und durch das Ministerium für Wissenschaft, Forschung und Kunst Baden-Württemberg finanziell unterstützt.

Contents

1. Introduction **1**
1.1. Fluorescence Microscopy in Biophysics 1
1.2. Thesis Outline 3

2. Far-field Fluorescence Microscopy **5**
2.1. Live Cell Imaging Using Visible Light Microscopy 5
2.2. Fluorescence 6
2.2.1. Light-Matter Interaction 6
2.2.2. Chlorophyll as an Example of a Fluorophore 8
2.2.3. Electronic and Vibronic Coupling 9
2.2.4. Other Energy Dissipation Processes 10
2.2.5. Fluorescent Markers 12
2.3. Resolution Limit in Optical Far-field Microscopy 14
2.3.1. Image Formation - the Lens as a Fourier Transformer 14
2.3.2. Image Resolution 17
2.3.3. The Role of the Objective Lens 18
2.3.4. Resolution Limit in Optical Far-field Microscopy 19
2.4. Microscopy Techniques 22
2.4.1. Widefield Epifluorescence Microscopy 22
2.4.2. Confocal Microscopy 23
2.4.3. Total Internal Reflection Microscopy 24
2.5. Super-resolution Microscopy 26
2.5.1. Localization as Key to Super-resolution 26
2.5.2. Targeted Switching 27
2.5.3. Fluorophore Switching by Stimulated Emission 28
2.5.4. Resolution in Depletion Microscopy 31
2.5.5. Stochastic Switching in Localization Microscopy 33
2.5.6. Resolution in Localization Microscopy 33
2.5.7. Fluorescent Markers for Localization Microscopy 35

3. Studying Dynamics by Fluorescence Microscopy **39**
3.1. Measuring Dynamics 39
3.2. Fluorescence Recovery after Photobleaching 40
3.2.1. The FRAP Principle 40
3.2.2. Modeling Fluorescence Recovery 40
3.2.3. FRAP for Studying Dynamics at Membranes 44

3.3. Fluctuation Spectroscopy . . . 46
3.3.1. Fluorescence Correlation Spectroscopy . . . 46
3.3.2. The Autocorrelation Function . . . 47
3.3.3. Analyzing Fluctuations Generated by Diffusion . . . 47
3.3.4. Brightness Fluctuations in Autocorrelation Analysis . . . 50
3.3.5. Raster Image Correlation Spectroscopy . . . 51
3.3.6. Fluctuations in Laser Scanning Microscopy Images . . . 52
3.3.7. Limitations of Fluctuation Spectroscopy . . . 55

4. Implementation of Advanced Fluorescence Microscopy 57
4.1. Stimulated Emission Depletion Microscopy . . . 57
4.1.1. STED Microscopy with a Broadband Source . . . 57
4.1.2. STED Microscopy with a Ti:Sa Laser . . . 60
4.1.3. Spatial Beam Overlay . . . 62
4.1.4. Timing for Optimal Fluorescence Quenching by STED . . . 64
4.1.5. Polarization . . . 66
4.2. Total Internal Reflection Microscopy . . . 68
4.2.1. Implementation of TIRFM for Live Cell Imaging . . . 68
4.2.2. TIRF/Epi-illumination Microscopy Setup . . . 70

5. Application of STED Microscopy 73
5.1. Application of STED Microscopy . . . 73
5.1.1. Experimental Verification of Fluorescence Quenching by STED . . 73
5.1.2. Experimental Verification of the Resolution Enhancement by STED 74
5.1.3. Application of STED Microscopy to Biological Specimens . . . 78
5.1.4. Summary STED Imaging . . . 84
5.2. Application of STED to Fluctuation Spectroscopy . . . 85
5.2.1. The Idea of STED-FCS . . . 85
5.2.2. Characterization of STED-FCS . . . 86
5.2.3. The Concept of STED-RICS . . . 88
5.2.4. Characterization of STED-RICS . . . 89
5.2.5. STED-RICS Applications . . . 93
5.2.6. Summary and Discussion STED-RICS . . . 97

6. Rapid Actions of the Gluococorticoid Receptor in Mast Cells Studied by TIRFM 101
6.1. Allergic Reactions Due to Signaling in Mast Cells . . . 101
6.1.1. Introduction to the Immune System . . . 101
6.1.2. Allergic Reaction . . . 102
6.1.3. IgE-receptor-mediated Signaling in Mast Cells . . . 103
6.1.4. The Glucocorticoid Receptor Complex . . . 103
6.1.5. Non-genomic Actions of the GR Studied by Spatial Regulation . . 105
6.2. Rapid Actions of the GR Visualized by TIRF Microscopy . . . 107
6.2.1. Rapid Actions of the IgE Receptor . . . 107

6.2.2. Rapid Actions of the GR-GFP . . . 108
6.2.3. Redistribution Dynamics of the GR Studied by FRAP . . . 111
6.2.4. Quantification of the Redistribution Dynamics of the GR . . . 112
6.2.5. Influence of Hormone Administration on the Non-genomic Actions of the GR . . . 113
6.3. Summary and Outlook . . . 115
6.3.1. Model for the Actions of the GR Including GC Administration . . 115
6.3.2. Future Plans Studying the GR . . . 117

7. Organization of Filament Assembly in Live Cells Visualized by PALM 119
7.1. Organization of Perinuclear Actin in Live Tobacco Cells . . . 119
7.1.1. The Role of Actin as Part of the Cytoskeleton . . . 119
7.1.2. Localization of Lifeact-psRFP in BY-2 Cells . . . 119
7.1.3. PALM with Optical Sectioning of Lifeact-psRFP in BY-2 Cells . . 122
7.1.4. Summary and Discussion . . . 125
7.2. Desmin Filament Assembly Visualized by Dual Color PALM . . . 128
7.2.1. The Desmin Protein and ARVC . . . 128
7.2.2. Cells Used to Study the Effects of Desmin Mutations . . . 130
7.2.3. Dual Color PALM . . . 131
7.2.4. Control Experiments . . . 133
7.2.5. Observed Effects of Desmin Mutants . . . 136
7.2.6. Summary . . . 143
7.2.7. Discussion . . . 146

8. Summary - Super-resolution Techniques for Cellular Studies 149
8.1. Technical Considerations and Limitations . . . 149
8.2. Fluorescent Markers and Labeling . . . 150

A. List of Publications 185

B. List of Presentations 187

C. Curriculum Vitae 189

D. Acknowledgement 191

1. Introduction

1.1. Fluorescence Microscopy in Biophysics

Direct visualization of biomolecules, cells, tissues and entire animals is essential for many studies in biology and medicine. Electron microscopy (EM) [1] features molecular resolution and, thus, is a very popular tool for imaging inorganic specimens. However, the application of electron microscopy to biological samples is limited [2]. Cells must be fixed, imaging depth is restricted and real-time imaging of living organisms is hardly feasible. For imaging in medical applications, techniques such as positron-emission tomography (PET) [3], magnetic resonance imaging (MRI) [4, 5] or optical coherence tomography (OCT) [6] are ideally suited. They are minimally invasive and allow for high imaging depths including entire animals. Yet, these methods are limited in resolution (**Fig. 1.1**) and, thus, not employable for studies on the subcellular level. The gap in resolution, imaging depth and bio-compatibility is covered by visible light microscopy. Visible light microscopy is minimally invasive, fast and able to resolve substructures within living cells and tissues and, therefore, has become the most popular tool for such applications. In biology, a major portion of all cellular samples are visualized by far-field fluorescence microscopy. Still, fluorescence microscopy suffers from several limitations. Deep tissue imaging and visualization of entire animals is restricted by absorption and scattering of visible light within the specimen. If high resolution is required, the short working distance of objectives with high numerical aperture (NA) further complicates experiments. Yet, recently developed techniques such as selective plane illumination microscopy (SPIM) [7, 8] are pushing those boundaries. In SPIM, a light sheet is created within the sample perpendicular to the observation axis. The range of such a light sheet can be increased with techniques such as two-photon excitation [9,10] and Bessel beams [11]. Thus, structures of $\gtrsim 1\,\mathrm{mm}$ in diameter can be imaged in 3D with a resolution comparable to the best single-cell imaging techniques such as confocal microscopy. At the other end of the size spectrum, all conventional visible light microscopy techniques are limited in resolution to $\sim 200\,\mathrm{nm}$ by the diffraction barrier. Direct observations on spatial scales beyond this limit have long been performed using EM, near-field techniques such as near-field scanning optical microscopy (NSOM) [12] and non-optical methods such as atomic force microscopy (AFM) [13]. However, in recent years, several ideas of bypassing the diffraction limit were developed independently. Early concepts proposed the application of markers of different colors to allow for a spectral separation of sub-diffractional features. Unfortunately, the absorption and emission spectra of common fluorescent probes are too broad to provide a sufficient number of color channels to yield a substantial improvement in resolution. The first breakthrough in the development of super-resolution, optical far-field fluorescence microscopy, was achieved by application of stimulated emission depletion (STED) [14]. Performing stimulated emission on fluorophores is a non-linear, saturable process. Therefore, by the choice of a suitable depletion pattern, effective, sub-diffractional volumes can be realized while the pattern itself is still diffraction-limited. In fact, all super-resolution concepts implemented so far exploit a non-linear optical property of the fluorophores employed. Among these, localization-based concepts such as photoactivated localization microscopy (PALM) [15] or fluorescence photoactivation localization microscopy (FPALM) [16] and stochastic optical reconstruction microscopy (STORM) [17] are the most popular ones. In localization-based super-resolution microscopy, fluorophores are switched between a dark, non-fluorescent and a bright, fluorescent state. By keeping only a tiny fraction in the active, fluorescence-emitting state at a time, the emitter locations can be determined with sub-diffractional precision. Current super-resolution nanoscopy allows for an increase in spatial resolution by more than one order of magnitude, i.e., $< 20\,\text{nm}$. By application of STED to fluorescent nitrogen vacancies in diamond, resolutions of a few nanometers have been realized [18]. However, up to now, achieving the best possible resolution is a trade-off between other important imaging parameters such as acquisition speed, 3D capability and multicolor compatibility. Also, high-end fluorescent probes are sometimes difficult to use in live-cell environments. Therefore, the aim of current research is to develop methods and equipment to provide molecular resolution that can reliably and universally be applied to biological specimens.

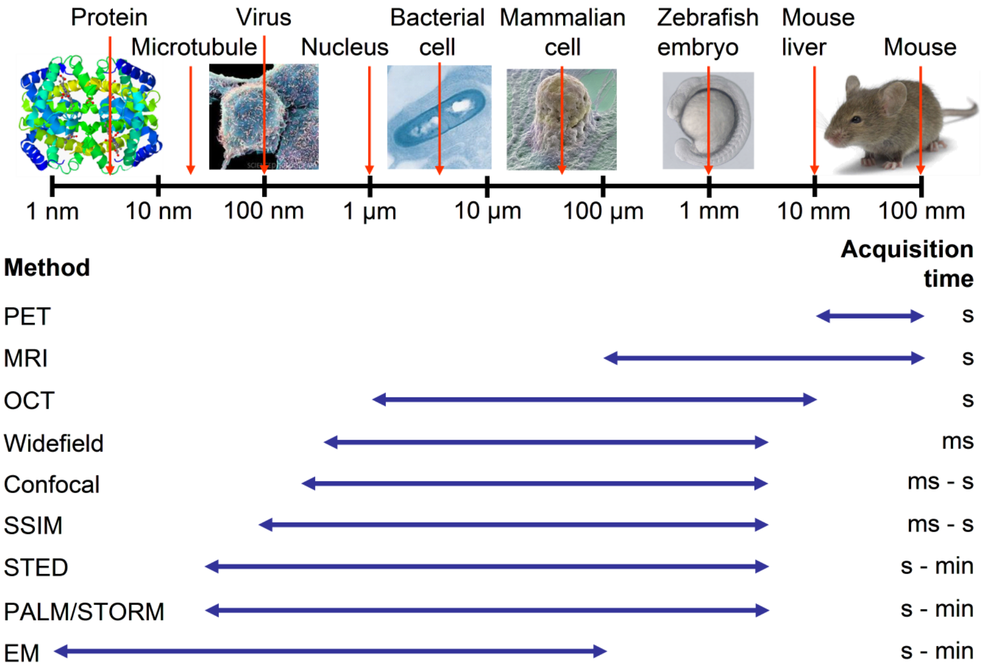

Figure 1.1.: Overview of popular imaging techniques in biology and medicine, including the applicable length scales and temporal resolutions; adopted from Fernández-Suárez et al. [19]. Pictures of structures/organisms taken from references [20–25] (left to right).

1.2. Thesis Outline

In the context of this thesis, several fluorescence microscopy techniques providing a resolution beyond the diffraction barrier were implemented, refined and applied to answer specific biological questions. Chapter 2 contains a brief introduction to the basics of far-field fluorescence microscopy including the phenomenon of fluorescence, image formation and a description of the microscopy techniques relevant within the context of this work. In the last section of chapter 2, the super-resolution microscopy techniques implemented and applied in this thesis are presented. Chapter 3 explains how dynamics can be studied by relaxation and fluctuation methods in fluorescence microscopy. In chapter 4, the microscopy setups that were implemented are described, including the beam alignment procedure for the STED setup. In the following chapters, it is shown how these machineries and methods were applied to various biological problems. In the first section of chapter 5, the improvement in spatial resolution by STED is demonstrated by means of various reference samples and biological specimens. In the second section of chapter 5, the application of STED to fluctuation spectroscopy is presented because, in this thesis, STED microscopy has been combined with raster image correlation spectroscopy (RICS) [26] as a new method to resolve dynamics in living cells. Chapter 6 is focused on the rapid action of the glucocorticoid receptor in immune cells as an important aspect of allergic disease introduced in the first section. Section two of chapter 6 is about the application of total internal reflection microscopy (TIRFM) [27] including fluorescence recovery after photobleaching (FRAP) [28], to study the spatial distribution and redistribution dynamics of the glucocorticoid receptor at the plasma membrane of mast cells, as response to allergen activation and homone treatment. This section is followed by a summary including a proposal for further studies. Furthermore, the organisation of intracellular filament assembly was visualized by means of PALM as presented in chapter 7. The structural integrity of cells is maintained by the cytoskeleton, composed and connected to other cellular structures by various filamentous assemblies of proteins including actin and desmin, respectively. As presented in the first section of chapter 7, the organization of perinuclear actin in plant cells was studied in 3D by a combination of super-resolution PALM with z-stacking. Specific labeling of perinuclear actin was achieved by steric hindrance of a tetrameric fluorescene marker, not binding to other sub-populations of actin. The other protein under study was desmin (chapter 7, section two). Desmin forms intermediate filaments important for the function of cardiac, skeletal and smooth muscle cells. Mutations in the gene encoding for the desmin protein can lead to a disruption of filament assembly and the formation of abnormal desmin aggregates, resulting in skeletal and cardiac myopathies. Therefore, the effects of several desmin mutations on filament assembly was analyzed using dual color PALM. These data contribute to the understanding of the structures and molecular assembly of desmin in living cells. After demonstration of the versatility and practicality of far-field fluorescence microscopy beyond the diffraction limit to answer essential questions in biology and medicine, this thesis concludes with a discussion as to further enhance and apply the current techniques to continuing studies (chapter 8).

2. Far-field Fluorescence Microscopy

2.1. Live Cell Imaging Using Visible Light Microscopy

In all microscopy techniques, the structures of interest, e.g., cells within an organism or tissue sample or substructures inside a single cell, have to be discriminated against background. For example, some parts of a specimen such as cell walls in plant cells show a high natural absorption of visible light and can thus be studied by the application of simple brightfield microscopy. In brightfield microscopy, the sample is illuminated by visible light and the transmitted portion is imaged onto a widefield detector such as a camera or the human eye. Image contrast is determined by the absorbance of dense areas within the sample. Unfortunately, most cells and tissues show only poor contrast due to low light absorption. In dark field microscopy, directly transmitted light is excluded and only scattered light will enter the detector, significantly reducing the background. However, the signal is usually very low for this method. Other optical properties of the sample can be exploited to generate contrast, such as birefringence as in polarized light microscopy or refractive index as in phase contrast microscopy (Fritz Zernike, 1942) [29]. Differential interference contrast (DIC) imaging patented by Georges Nomarski in 1952 is a refined implementation of phase contrast microscopy. In DIC imaging, a beam of polarized light is guided through a Wollaston prism, splitting the beam into two fractions with perpendicular polarization. Those two beams are then focused such that they propagate through the sample in close proximity, i.e., at a distance similar to the optical resolution of the microscope. Index variations of the sample will result in relative phase shifts between the two beams. The beams are subsequently refocused by the objective lens before passing a second Wollaston prism yielding a single, recombined beam. An analyzer blocks all light with the initial state of polarization, i.e., portions of the two beams of perpendicular polarization that have traveled the same optical distance. Yet, at locations where the two adjacent beams of perpendicular polarization propagate through regions of different refractive index, such as cell membrane and outside medium, the recombined beam will possess states of polarization different from the initial state after interference at the second Wollaston prism. Thus, these portions will pass the analyzer and contribute to the image.

Still, for many structures of interest, the contrast obtained by such methods is far too low. Consequently, staining of the sample is required, artificially increasing, e.g., the absorption. Fluorescent molecules can also be used as markers to tag the target structures. Fluorescence microscopy has become the most popular microscopy method in biology, mainly for two reasons. First, structures of interest can be labeled in a highly specific manner. This can be achieved by coupling the fluorescent markers to target structures using antibodies. Alternatively, fluorescent proteins can be expressed by the cell itself. In this approach, the cells are transfected with a short DNA sequence coding for a suitable fusion protein. Either the sequence encoding the fluorescent protein is fused to the sequence of the protein of interest, or, to the sequence of a protein known to bind to the structure of interest. The second reason is that fluorescence is spectrally red-shifted and time-delayed. Thereby, scattered excitation light can be efficiently suppressed in detection leading to excellent image contrast.

2.2. Fluorescence

2.2.1. Light-Matter Interaction

Whenever electrons are confined in space, e.g., as part of a molecule, a quantum system with discrete energy levels is created. By absorption of a photon, this system can evolve from the electronic ground state to an excited state. The energy difference can be reemitted as a photon, usually red-shifted in wavelength compared to the excitation photon. This red shift arises from partial conversion of the energy into phonons within the absorbing molecule and relaxation of the surrounding solvent. Another characteristic of fluorescence light is the time delay with respect to the absorption process. In the simplest case, the fluorescence response can be described by an exponential decay with a single, characteristic lifetime, similar to the description of radioactive decay in nuclear physics. The fluorescence lifetime can be influenced by the surrounding molecules. This dependence is of great importance for advanced microscopy techniques such as fluorescence lifetime imaging (FLIM) [30] or Foerster resonance energy transfer (FRET) [31]. For visible light microscopy, large delocalized electron systems with a high absorption and a high quantum yield are preferred. They should also spectrally differ from strongly fluorescent moieties naturally contained within the biological specimen under study, such as the amino acid tryptophan or chloroplasts in plant cells. Let us start with a simple system with two states, i and j, of different energies, E_i and $E_j > E_i$, with population numbers, n_i and n_j, (**Fig. 2.1**). Absorption of an incident photon causes a transfer of a molecule from state i to state j. The probability of that process is described by the Einstein coefficient B_{ij}. Since the process is reversible, a photon can also induce emission of a second photon of the same energy and momentum from a molecule already

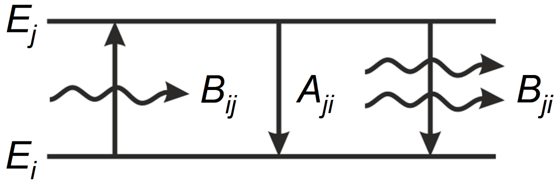

Figure 2.1.: Two state system of different energies, E_i, E_j, and, probabilities for absorption, B_{ij}, spontaneous emission, A_{ji}, and stimulated emission, B_{ji}, of a photon.

in state j. This transition from the excited state, j, to the ground state, i, is termed induced emission and is described by the coefficient B_{ji}, with $B_{ji} = B_{ij}$, since it is the inverse of absorption. Yet, in addition to the field of a second photon, quantum vacuum fluctuations can also induce a relaxation from the excited state to the ground state, consequently termed spontaneous emission, A_{ji}. Thus, the ratio of the number of molecules residing in the ground state, n_i, to the number of molecules in the excited state, n_j, is given by

$$\frac{n_i}{n_j} = \frac{I(\nu)B_{ji} + A_{ji}}{I(\nu)B_{ij}}, \tag{2.1}$$

with the radiation density of a black body,

$$I(\nu) = \frac{8\pi\nu^2}{c^3} \cdot \frac{1}{\exp(h\nu/k_BT) - 1} \cdot h\nu, \tag{2.2}$$

including the density of states (first term; with photon frequency, ν, and speed of light, c), bose-statistics (second term; with Planck constant, h, Boltzmann constant, k_B, and temperature, T) and the energy of the photon (last term). In thermal equilibrium, the states are distributed according to Boltzmann's law,

$$\frac{n_j}{n_i} = \exp\left(-\frac{(E_j - E_i)}{k_BT}\right). \tag{2.3}$$

As a consequence, the relation between spontaneous and induced emission is given by

$$A_{ji} = \frac{8\pi h\nu^3}{c^3}B_{ji}. \tag{2.4}$$

Thus, the probability for spontaneous emission strongly depends on the frequency of the photons, i.e., the energy difference of the states, $\Delta E = E_j - E_i$. For visible light ($\sim 500\,\mathrm{nm}$) and moderate excitation intensities, induced emission can be neglected and, therefore, the rate of spontaneous emission is given by

$$\frac{\mathrm{d}n_j(t)}{\mathrm{d}t} = -A_{ji}n_j(t). \tag{2.5}$$

Integration of equation 2.5 yields,

$$n_j(t) = n_j(0) \cdot \exp(-A_{ji}t) = n_j(0) \cdot \exp(-t/\tau_R), \tag{2.6}$$

with the radiative lifetime of state n_j given by $\tau_R = 1/A_{ji}$. Absorption, on the other hand, is related to the dipole strength, D_{ij}, of the electronic system,

$$B_{ij} = \frac{4\pi^2}{3\hbar^2}D_{ij}, \tag{2.7}$$

assuming that the energy of the incident photons is similar to the energy difference of the states, ΔE, and that the angular momentum is conserved. The dipole strength is linked to the extinction coefficient, ϵ_{ij}, via

$$D_{ij} = 9.81 \cdot 10^{-3} \int \frac{\epsilon_{ij}}{\nu}\mathrm{d}\nu. \tag{2.8}$$

Because spontaneous emission is proportional to absorption, $A_{ji} \propto B_{ij}$, the extinction coefficient is inversely related to the excited state lifetime. Therefore, strongly absorbing molecules also display short excited state lifetimes; typical values of τ_R observed for fluorescent molecules are in the range of $10^{-6} - 10^{-9}\,\mathrm{s}$.

2.2.2. Chlorophyll as an Example of a Fluorophore

Molecules with multiple conjugated double bonds are often fluorescent because the electrons involved in those bonds can move effectively freely along the atom chain. A prominent example of a fluorescent biomolecule is chlorophyll, responsible for photosynthesis in plants. Chlorophyll absorbs light in the blue and the red range of the visible spectrum. A central magnesium atom is surrounded by a planar arrangement of twelve carbon and four nitrogen atoms (**Fig. 2.2**). The electron system can be considered as a circular path for the electrons involved in the conjugated double bonds. The resulting one-dimensional electron gas with spatial coordinate x consists of a total of 18 electrons, considering that two are immobilized by the central Mg^{2+}. The stationary Schrödinger equation is given by

$$\hat{H}\psi = (\hat{T} + \hat{V})\psi(x) = E\psi(x). \tag{2.9}$$

The contribution of the potential operator, $\hat{V}$, to the Hamiltonian, $\hat{H}$, can be neglected; the kinetic energy operator, $\hat{T}$, of a single electron of mass m_e is determined by the angular momentum operator, $\hat{L}$, and the moment of inertia, I,

$$\hat{T} = \frac{\hat{L}^2}{2I} = \frac{r^2\hat{p}^2}{2m_e r^2} = \frac{\hat{p}^2}{2m_e}. \tag{2.10}$$

Insertion of equation 2.10 in 2.9 and application of the momentum operator, $\hat{p} = -i\hbar\nabla$, results in

$$-\frac{\hbar^2}{2m_e}\frac{\partial^2}{\partial x^2}\psi(x) = E\psi(x). \tag{2.11}$$

The solution of this equation with respect to the periodic boundary condition, $\psi(x) = \psi(x + nL)$, is given by

$$\psi(x) = N \cdot \exp\left(\frac{2\pi i k x}{L}\right), \tag{2.12}$$

with the quantum number, $k = \{0, \pm 1, \pm 2, ...\}$, the length of the conjugated electron system, $L \sim 2.2\,\mathrm{nm}$, and a normalizing factor, N. Consequently, the distribution of the energy states is determined by

$$E_m = \frac{2\pi^2\hbar^2}{m_e L^2}k^2. \tag{2.13}$$

Filling up the available states with a total of 18 electrons to account for the Pauli exclusion principle results in an occupation of the states $k = 0 - 4$. Thus, $E_{4,5}$ is the transition with the lowest energy gap for absorption of a photon, yielding an absorption wavelength,

$$\lambda_{\text{chlorophyll}} = \frac{m_e c L^2}{9\pi\hbar} = 440\,\mathrm{nm}. \tag{2.14}$$

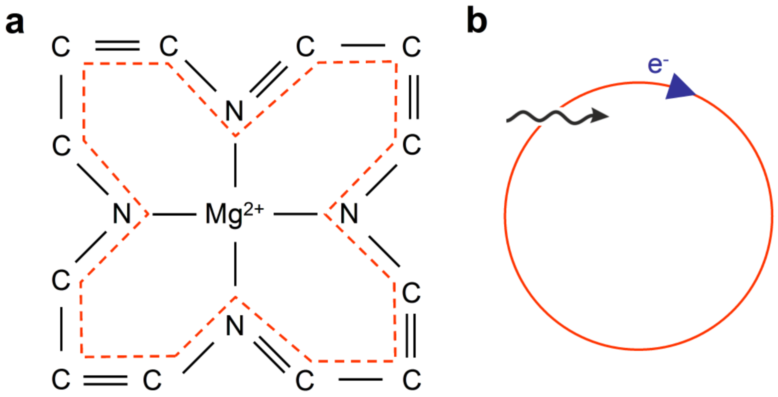

Figure 2.2.: Light interaction of chlorophyll. (**a**) Structure of chlorophyll near the central magnesium atom. (**b**) Electrons can move along the conjugated bonds approximated by a circle.

This blue absorption band called Soret band [32] is the most prominent peak in the visible light absorption spectrum of chlorophyll.

2.2.3. Electronic and Vibronic Coupling

Apart from electronic transitions, there are other modes of molecular excitation, i.e., vibration, rotation and translation. Since the nuclei have a much greater mass (factor 10^3) compared to the electrons, they remain stationary ($\tau_{vib} \sim 100\,\mathrm{fs}$) during absorption of a photon ($\sim 1\,\mathrm{fs}$). Yet, in general, the interatomic distances in the first excited singlet state, S_1, are different from the distances in the ground state, S_0. Due to the huge mass difference, it can often be assumed that the electrons instantaneously follow the nuclear movements, allowing for a separation of the overall wave function into its electronic and nuclear components (Born-Oppenheimer approximation),

$$\psi(\vec{r},\vec{R}) = \varphi(\vec{r},\vec{R}) \cdot \phi(\vec{R}), \tag{2.15}$$

with the wave function of the electrons, $\varphi(\vec{r},\vec{R})$, and the wave function of the nuclei, $\phi(\vec{R})$. The positions of the electrons and nuclei are denoted by $\vec{r}$ and $\vec{R}$, respectively. The dipole strength, D_{ij}, is defined as the square of the absolute value of the matrix element,

$$\begin{aligned} < \psi_j|e\vec{r}|\psi_i > &= -e\iint \varphi_j^*(\vec{r})\phi_j^*(\vec{R})\vec{r}\varphi_i(\vec{r})\phi_i(\vec{R})\mathrm{d}^3\vec{r}\mathrm{d}^3\vec{R} && (2.16)\\ &= -e\int \varphi_j^*(\vec{r})\vec{r}\varphi_i(\vec{r})\mathrm{d}^3\vec{r}\int \phi_j^*(\vec{R})\phi_i(\vec{R})\mathrm{d}^3\vec{R}. && (2.17)\end{aligned}$$

The second integral represents the overlap of the wave functions of the nuclei and is known as the Franck-Condon factor [33,34]. Often, the interatomic distances are larger in the excited state (**Fig. 2.3a**). Also, for higher vibrational modes, the probability of residence is increased toward the edges of the potential well. Thus, upon excitation of the electronic system of a molecule, transitions to an excited vibrational state of S_1 are often more probable than transitions to the vibrational ground state of S_1, resulting in an absorption spectrum as sketched in **Fig. 2.3b**. For the same reason, relaxations to vibrationally excited states of S_0 are more likely to occur than transitions to the vibrational ground state of S_0. Therefore, the emission spectrum usually represents the mirror image of the absorption spectrum (**Fig. 2.3c**). However, local vibrational modes of high energy would result in a spectrum of several narrow, clearly separated peaks, depicted as spikes. Yet, in a complex, polyatomic fluorophore there are also many global vibrational modes of low energy. In addition to solvent effects, these low energy modes result in a blurred structure of the absorption/emission spectrum. For many common fluorescence markers the $S_{0,0} - S_{1,0}$ transition is still dominant but strongly broadened due to a variety of low energy vibronics.

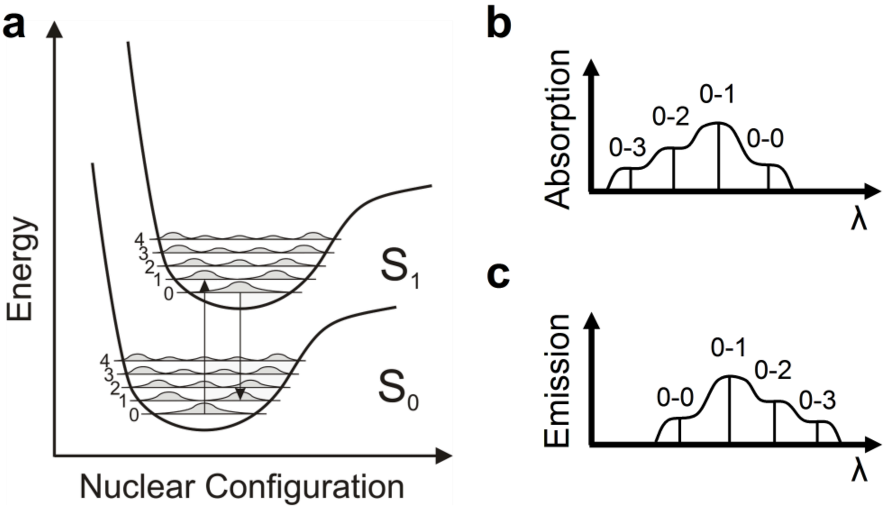

Figure 2.3.: Franck-Condon principle. (**a**) Due to different molecular geometries in the electronic ground state, S_0, and excited state, S_1, the overlap of the wave functions of the vibrational ground state of S_0 is stronger for higher vibronic modes of S_1 and vice versa. Illustration of the respective (**b**) absorption and (**c**) emission spectra.

2.2.4. Other Energy Dissipation Processes

In addition to induced and spontaneous emission of a photon, other processes can be involved in energy dissipation, usually summarized in a Jablonski diagram [35] (**Fig. 2.4**). First of all, after absorption of a photon in the ground state, S_0, a higher vibronic mode of the excited state, S_1, may be populated due to the Franck-Condon principle. A quick relaxation ($\sim 10^{-12}$ s) to the vibronic ground state occurs due to the coupling to other local and global vibrations of the molecule. This loss of energy causes a red shift of the

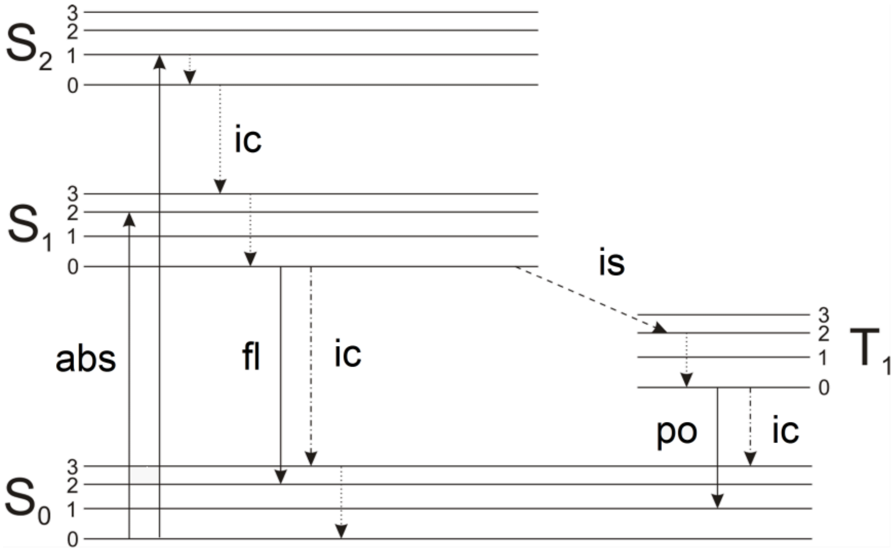

Figure 2.4.: Jablonski diagram depicting possible conversions between the electronic ground state, S_0, excited states, S_1 and S_2, and triplet state, T_1. The transitions include photon absorption, abs, emission of a fluorescence photon, fl, internal conversion, ic, intersystem crossing, is, and phosphorescence, po.

fluorescence photons, referred to as the static Stokes shift. By means of vibrational relaxation, a fluorophore can also return to the electronic ground state in a process termed internal conversion. In an electric dipole transition, the spin is conserved. Thus, if the ground state is a singlet state, only other singlet states are accessible by electric dipole transitions. However, in S_1, magnetic interactions, although very weak, can induce a spin flip resulting in the population of a triplet state, T_1, termed intersystem crossing. Because the transition back to the ground state requires another spin flip, the triplet state has a long lifetime ($\sim 10^{-2} - 10^{2}\,\mathrm{s}$). Furthermore, fluorophores can be excited to higher electronic states, S_2. Molecules in higher electronic states typically relax to S_1 via internal conversion and not via fluorescence emission (Kasha's rule [36]).

The environment of a fluorophore can significantly influence the spectral properties of the system. After excitation, reorientation of solvent molecules in favor of the different molecular geometry of the S_1 state leads to a loss of energy. Subsequently, after fluorescence emission, energy is consumed by reorientation of solvent molecules to readjust to the molecular geometry of the S_0 state. Both relaxations cause an additional red shift of the fluorescence light. The process is referred to as dynamic Stokes shift. In quenching or external conversion, the energy is removed from the excited state by collision with solvent molecules. Dipole-dipole interactions with other chromophores can lead to a tranfer of the energy to a different molecule. This process, termed FRET [31], can be exploited to, e.g., resolve intramolecular distances. All these alternative pathways compete with the emission of a fluorescence photon. Thus, the fluorescence quantum yield, Φ_F, is defined as the fraction of absorbed photons that are reemitted as fluorescence photons,

$$\Phi_F = \frac{k_R}{k_R + k_{ic} + k_{is} + k_q + ...}, \tag{2.18}$$

with the rate coefficients of the fluorescence decay, k_R, internal conversion, k_{ic}, intersystem crossing, k_{is}, and quenching, k_q. The depopulation of the excited state, $n_1(t)$, is given by the differential equation

$$-\frac{\mathrm{d}n_1(t)}{\mathrm{d}t} = (k_R + k_{ic} + k_{is} + k_q) \cdot n_1(t) = \frac{1}{\tau_F} \cdot n_1(t), \tag{2.19}$$

with the solution

$$n_1(t) = n_1(0) \cdot \exp(-t/\tau_F). \tag{2.20}$$

The experimentally observed fluorescence lifetime, τ_F, is the result of all processes by which the system can return from the excited state to the ground state. Consequently, the quantum yield can be expressed as the ratio of the observed lifetime to the lifetime of the radiative decay, τ_R, introduced in equation 2.6,

$$\Phi_F = \frac{\tau_F}{\tau_R}. \tag{2.21}$$

2.2.5. Fluorescent Markers

An important aspect in fluorescence microscopy and other techniques that rely on the reemission of fluorescence photons are the employed fluorescence markers. Fluorescent markers should have a strong absorption and weak non-radiative deexcitation, i.e., a quantum yield close to one. Furthermore, high photoresistance is important, especially for extensive imaging over long periods and high resolution microscopy. In addition, fluorescent markers need to be of small size (a few nanometer) to prevent alteration of the structure to be observed and, in general, to keep sample perturbation at a minimum. A popular class of markers in cell biology and medicine are small organic dyes (**Fig. 2.5a**). Since the discovery of fluorescein in 1871 by Adolf von Baeyer, advances in chemical synthesis have led to the development of a colorful ensemble of dyes with spectra ranging from ultra violet (UV) to infrared (IR). Many of these dyes combine a strong absorption, a high quantum yield and a high photostability. Such high-end dyes also form the basis of super-resolution microscopy by means of STED [38]. In addition, there have been advances in the development of photochromic probes, including rhodamines and photoswitchable cyanines. Their ability to be optically switched between a dark, non-fluorescent and a bright, fluorescent state is exploited in super-resolution STORM imaging [17]. Yet, application of such non-biological probes requires considerable effort in targeting proteins and other biomolecules. In so-called immunofluorescence assays, antibodies are employed to couple fluorescent dyes to specific biomolecules for visualization within cells or tissues. However, many organic dyes and antibodies are not membrane permeable. Thus, in immunofluorescence assays, the cells are usually fixed,

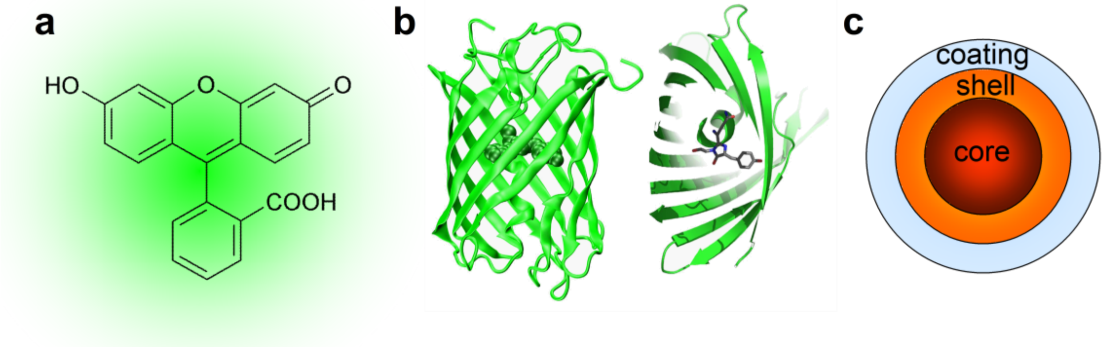

Figure 2.5.: (**a**) Chemical structure of fluorescein. (**b**) Cartoon depiction of a monomeric, GFP-like protein, view of the chromophore inside, adopted from [37]. (**c**) Composition of a core-shell semiconductor quantum dot.

followed by membrane permeabilization and subsequent labeling. To study dynamics, multiple batches of cells have to be fixed at different time points. Furthermore, immunostaining is often compromised by a low labeling efficiency. Also, the large size of antibodies ($\sim 10 - 20\,\mathrm{nm}$) adds uncertainty to the position and/or extension of their target structure, which is especially problematic in super-resolution microscopy.

Another class of markers are fluorescent proteins (FPs). Biomolecules are labeled by fusing the DNA sequence encoding the protein of interest to the sequence coding for the FP. This fusion protein is then expressed by the cell or organism of interest. Because the fluorophore forms spontaneously, FPs can be utilized as genetically encoded fluorescence markers in essentially all living cells and organisms. No further invasive labeling steps are required, which is a great advantage over immunofluorescence assays with organic dyes. Also, since the entire labeled structure is a single fusion protein, FP staining is extremely specific and efficient. The first FP discovered was green fluorescent protein (GFP) of the jellyfish *Aequorea victoria* (*av*GFP) characterized by Osamu Shimomura in 1962 [39,40] (**Fig. 2.5b**). After cloning the gene of *av*GFP by Prasher and co-workers in 1992 [41], *av*GFP could be recombinantly expressed in *Escherichia coli* and *Caenorhabditis elegans* by Martin Chalfie and collaborators [42]. These achievements were recognized by the 2008 Nobel Prize in Chemistry. Orange and red FPs, highly demanded due to the reduced scattering and cellular autofluorescence in the red spectral range as well as the possibility for multicolor experiments, were identified in the late 1990s and early 2000s [43–45]. More recently, photoactivatable fluorescent proteins (paFPs) have emerged as powerful new tools for cellular imaging [19, 46–48]. Similar to photochromic dyes, these paFPs can either be switched reversibly between a fluorescent and a non-fluorescent state (photoswitching), or they can change their fluorescence emission intensity or color irreversibly (photoconversion). Photoactivatable FPs have markedly enhanced super-resolution microscopy including methods such as (F)PALM [15, 16] and reversible saturable optical fluorescence transitions (RESOLFT) [49]. Unfortunately, the brightness and photostability of FPs do not match the performance of non-genetically encoded probes. A bright monomeric FP in the far-red spectral range including high photostability has yet remained elusive.

A third class of fluorescence markers are artificial nanoclusters, including semiconductor quantum dots (QDs) (**Fig. 2.5c**) [50], nanodiamonds [51] and metal nanoclusters [52]. Their brightness and photostability can exceed even the performance of organic dyes. For example, no sign of photobleaching was found for fluorescent nanodiamonds even after several hours of continuous excitation [53]. Thus, nanodiamonds are ideally suited for 3D super-resolution imaging using STED; they allow for repeated imaging of the same region of interest without compromising signal or spatial resolution [54]. However, specific tagging of biomolecules by nanoclusters is even more difficult than with organic dyes. Also, these nanoparticles can be cytotoxic. For example, cytotoxic effects observed for CdTe QDs are a consequence of the release of Cd^{2+} ions as well as the intracellular distribution of these nanoparticles and the associated nanoscale effects [55]. Thus, until now, their application in live cell imaging has been restricted to a few special cases. For example, the blinking of quantum dots, a limiting factor for their application in single particle tracking, has been exploited in a super-resolution microscopy variant termed superresolution optical fluctuation imaging (SOFI) [56].

2.3. Resolution Limit in Optical Far-field Microscopy

2.3.1. Image Formation - the Lens as a Fourier Transformer

In the theory of image formation, Fourier optics is a helpful tool [57, 58]. Thus, in this subsection, we define the Fourier transform of a function in position space, $u(x)$, with position variable, x, to frequency space with frequency variable, ν, as

$$\mathcal{FT}(u(x)) = \int_{-\infty}^{\infty} u(x)\exp(-2\pi i x\nu)\mathrm{d}x = U(\nu). \tag{2.22}$$

Subsequently, the inverse Fourier transform is defined as

$$\mathcal{FT}^{-1}(U(\nu)) = \int_{-\infty}^{\infty} U(\nu)\exp(2\pi i\nu x)\mathrm{d}\nu = u(x). \tag{2.23}$$

Image formation by a lens can be described by simple, geometric or ray optics (**Fig. 2.6a**). When using a single lens of focal length f to image an object, $g(x, y)$, placed at a distance a in front of that lens, an image of the object, $h(x', y')$, is formed at the distance b behind the lens, determined by the lens equation,

$$\frac{1}{f} = \frac{1}{a} + \frac{1}{b}. \tag{2.24}$$

The image formation process can be described by two sucessive Fourier transforms,

$$g(x, y) \xrightarrow{\mathcal{FT}} G(\nu, \mu) \xrightarrow{\mathcal{FT}} h(x', y'). \tag{2.25}$$

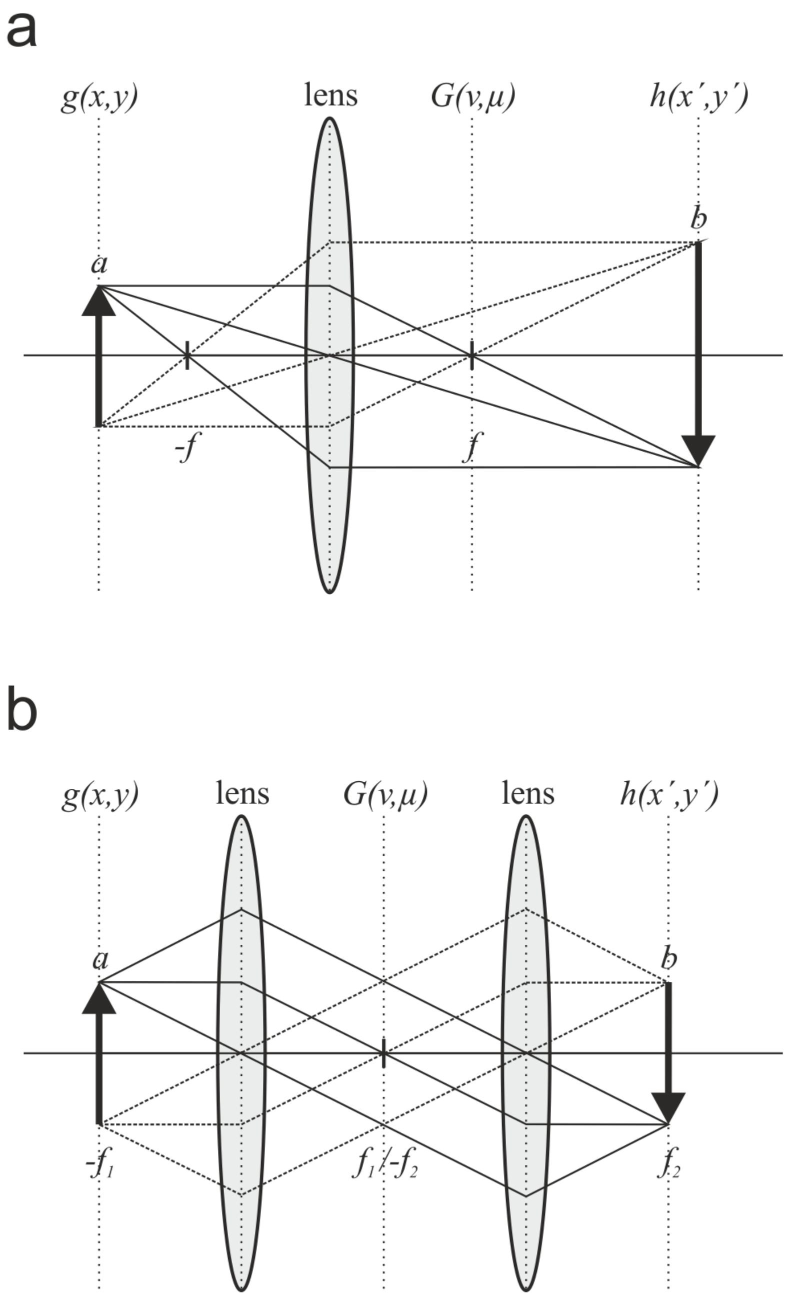
a
g(x,y)
lens
G(ν,μ)
h(x′,y′)
a
b
-f
f
b
g(x,y)
lens
G(ν,μ)
lens
h(x′,y′)
a
b
-f₁
f₁/-f₂
f₂

Figure 2.6.: Lenses as Fourier transformers. Image formation using (**a**) a single lens and (**b**) two lenses placed at a distance of the sum of their focal lengths.

The first Fourier transform, i.e., the frequency space image, $G(\nu, \mu)$, can be observed in the back focal plane of the lens. The second Fourier transform of the object, $h(x', y')$, is formed at the distance b behind the lens. Alternatively, a system of two lenses can be used for imaging, one lens for each transform, placed at a distance corresponding to the sum of their focal lengths, f_1 and f_2 (**Fig. 2.6b**). Since lenses can only perform forward transforms, the image appears upside down on the screen in both cases. Due to the identity, $\mathcal{FT}(\mathcal{FT}(u(x, y))) = -u(x, y)$, the image is identical to the object. However, in reality, a lens is not a perfect imaging system but suffers from aberrations. Let us consider the limited aperture of a lens. This constraint can be modeled by introducing a filter function, $\tau(\nu, \mu)$, into the Fourier plane. Thus, image formation is given by

$$g(x, y) \xrightarrow{\mathcal{FT}} G(\nu, \mu) \xrightarrow{\tau(\nu,\mu)} H(\nu, \mu) \xrightarrow{\mathcal{FT}} h(x', y'). \tag{2.26}$$

The simplest object would be a point source,

$$g(x, y) = \vec{E}_0 \delta(x - x_0)\delta(y - y_0), \tag{2.27}$$

with the amplitude of the electric field, $\vec{E}_0$, and delta functions, $\delta(x - x_0), \delta(y - y_0)$, modeling a point-source at position x_0, y_0. Thus, the first Fourier transform yields

$$\begin{aligned} G(\nu, \mu) &= A \iint\limits_{-\infty}^{\infty} \vec{E}_0 \delta(x - x_0)\delta(y - y_0) \exp(-2\pi i(\nu x + \mu y)) \mathrm{d}x \mathrm{d}y & (2.28) \\ &= A\vec{E}_0 \exp(-2\pi i(\nu x + \mu y)), & (2.29) \end{aligned}$$

where A is a phase factor with $|A| = 1$ and does not have to be considered, since we are only interested in the intensity distribution, $I = |E|^2$. As a filter function, we choose an annular aperture,

$$\tau(\rho) = \begin{cases} 1, & \rho \leq \rho_0 \\ 0, & \rho > \rho_0 \end{cases}, \tag{2.30}$$

where $\rho = \sqrt{\nu^2 + \mu^2}$. Since $\tau(\rho)$ is a radially symmetric function, it is useful to switch to polar coordinates for the second Fourier transform. With $r' = \sqrt{x'^2 + y'^2}$, $x' = r' \cos \vartheta$, $y' = r' \sin \vartheta$, $\rho = \sqrt{\nu^2 + \mu^2}$, $\nu = \rho \cos \varphi$ and $\mu = \rho \sin \varphi$, we get

$$\begin{aligned} h(r') &= A' \int\limits_0^{2\pi} \int\limits_0^{\infty} \vec{E}_0 \tau(\rho, \varphi) \exp(-2\pi i \rho r(\cos \vartheta \cos \varphi + \sin \vartheta \sin \varphi)) \rho \mathrm{d}\rho \mathrm{d}\varphi & (2.31) \\ &= A' \int\limits_0^{2\pi} \int\limits_0^{\infty} \vec{E}_0 \tau(\rho, \varphi) \exp(-2\pi i \rho r \cos(\vartheta - \varphi)) \rho \mathrm{d}\rho \mathrm{d}\varphi. & (2.32) \end{aligned}$$

With the zero order Bessel function of the first kind,

$$J_0(a) = \frac{1}{2\pi} \int\limits_0^{2\pi} \exp(-ia \cos(\vartheta - \varphi)) \mathrm{d}\varphi, \tag{2.33}$$

we obtain

$$h(r') = 2\pi A' \int_0^\infty \vec{E_0}\tau(\rho,\varphi)J_0(2\pi\rho r)\rho \mathrm{d}\rho. \tag{2.34}$$

Insertion of the annular filter function, τ, yields

$$h(r') = 2\pi A' \int_0^{\rho_0} \vec{E_0}J_0(2\pi\rho r)\rho \mathrm{d}\rho. \tag{2.35}$$

Using the identity,

$$\int_0^a \xi J_0(\xi)\mathrm{d}\xi = aJ_1(a), \tag{2.36}$$

with the first order Bessel function, J_1, we finally obtain

$$h(r') = A' \cdot \frac{J_1(2\pi\rho_0(r'+r_0))}{2\pi\rho_0(r'+r_0)}, \tag{2.37}$$

as the image of a point source produced by a lens of finite diameter. In the literature, this result is often denoted as limiting factor for the resolution in far-field microscopy. However, this is only partially true. The so-called diffraction barrier is a consequence of a much more general concept in physics, the uncertainty relation. The uncertainty relation applies to any kind of measurement and states that position and momentum of a particle are not independent from each other. The application of this principle in optical far-field microscopy is presented in subsection 2.3.4.

2.3.2. Image Resolution

Image resolution is determined by the ability to distinguish two structures from each other by means of intensity contrast. Therefore, we need a criterion for the minimal contrast required for such a discrimination [59]. A very popular one is the Rayleigh criterion [60]. Here, it is assumed that two objects can be distinguished if the central maximum of the diffraction pattern of one object coincides with the first minimum of the diffraction pattern of the other object. According to equation 2.37, the intensity of the diffraction pattern of a point source on the optical axis is proportional to

$$I(r) \propto \left(\frac{J_1(2\pi\rho_0 r)}{2\pi\rho_0 r}\right)^2. \tag{2.38}$$

For a thin lens of diameter d, $\rho_0 = d/2 \approx \sin\alpha/2\lambda$. The first root of $J_1(x)$ can be found at $x \approx 3.83$ and, thus,

$$r_{\min} = 3.83\frac{1}{2\pi\rho_0} = 1.22\frac{\lambda}{\sin\alpha}. \tag{2.39}$$

The superposition of the intensities from two incoherent point sources at this minimal resolvable distance is shown in **Fig. 2.7a**; a clear contrast is visible. For coherent sources emitting in phase, the amplitudes have to be summed up before computing the square. In the resulting intensity distribution, there is no contrast visible at all (**Fig. 2.7b**). Luckily, for fluorescene microscopy, we can assume that fluorophores are incoherent sources. The Sparrow criterion is another possibility to define the resolvable distance between two structures. It is based on the fact that the human eye is very sensitive to changes in intensity. Hence, two objects count as resolved if their superimposed intensity distribution exhibits a minimum along their connecting line,

$$\left(\frac{\mathrm{d}^2 I}{\mathrm{d}r^2}\right)_{r=r_{\mathrm{min}}/2} = 0. \tag{2.40}$$

Application of this condition to the Bessel function results in

$$r_{\mathrm{min}} = 0.95\frac{\lambda}{\sin\alpha}, \tag{2.41}$$

for two incoherent point sources and

$$r_{\mathrm{min}} = 1.46\frac{\lambda}{\sin\alpha}, \tag{2.42}$$

for two coherent point souces, respectively (**Fig. 2.7c,d**). Thus, the Sparrow criterion performs equally well for both, incoherent and coherent sources. However, in a real experiment, the intensity distributions are overlaid by noise impeding the identification of a minimum along the connecting line as defined by Sparrow. Consequently, the Rayleigh criterion is more popular in fluorescence microscopy.

2.3.3. The Role of the Objective Lens

Often, the resolution limit in light microscopy is attributed to the limited aperture of the objective lens. However, this is only partially true. As stated by Ernst Abbe in 1873, the minimal resolvable distance, d_{min}, in far-field microscopy is given by

$$d_{\mathrm{min}} = \frac{\lambda_0}{2n\sin\alpha}, \tag{2.43}$$

where λ_0 denotes the vacuum wavelength of the light employed, n the refractive index of the medium surrounding the sample and α the half angle of the objective aperture. Yet, the angle can only be increased to a maximum of 90°, and, therefore, even with an infinite aperture of the objective lens, the resolution remains finite. A higher resolution, by means of the objective lens, can only be realized using a sample immersion medium with a high refractive index. The gain in resolution results from shifting the light employed, λ_0, to shorter wavelengths, λ', within the medium,

$$\lambda' = \frac{\lambda_0}{n}. \tag{2.44}$$

In photolithography, the use of high index fluids is a common practice to produce smaller structures [61]. For biological specimens, this technique cannot easily be applied since they often require water ($n = 1.33$) as an immersion medium.

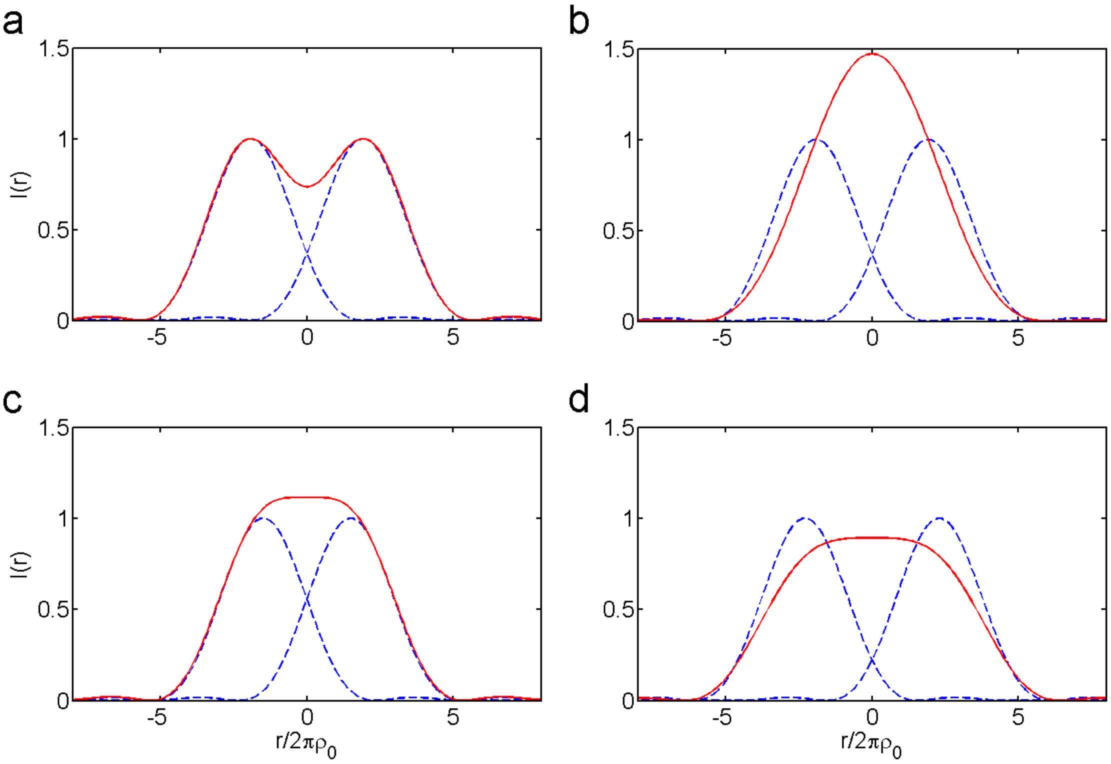

Figure 2.7.: Intensity distributions as the sum (solid lines) of two point sources (dashed lines) at various distances determined by different resolution criteria. (**a**) Rayleigh criterion, incoherent light. (**b**) Rayleigh criterion, coherent light. (**c**) Sparrow criterion, incoherent light. (**d**) Sparrow criterion, coherent light.

2.3.4. Resolution Limit in Optical Far-field Microscopy

As an electromagnetic wave, light fulfils the wave equation,

$$\nabla^2\psi + k_0^2\psi = 0. \tag{2.45}$$

Therefore, at a distance far from the source, the electric field, $E(\vec{r},t)$, at position $\vec{r}$ and time t can be discribed as

$$\vec{E}(\vec{r},t) = \vec{E}_0 e^{-i(\vec{k}\vec{r}-\omega t)}, \tag{2.46}$$

with the field amplitude, $\vec{E}_0$, the wave vector perpendicular to the direction of propagation, $\vec{k}$, and the frequency of the electromagnetic wave, ω. Let us imagine a point-like source homogeneously emitting in all directions. The purpose of a microscope is to collect as much of the emitted light as possible and to refocus it to create an image on a suitable detector. Thus, one could think of a reflecting ellipsoid as the most perfect objective lens, by placing the source in one focal spot and the detector in the other (**Fig. 2.8**). A general principle in physics is the uncertainty relation as found by Werner

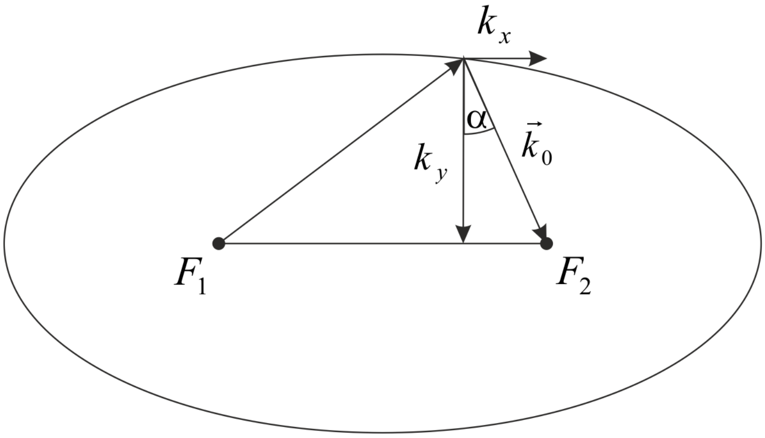

Figure 2.8.: Reflecting ellipsoid as a perfect imaging system. Every photon of momentum $\vec{k}$ originating from focal point, F_1, ends up in the other focal point, F_2.

Heisenberg in 1927 [62]. Its essence is that two conjugate variables of a particle cannot be measured with infinite precision at the same time. For the uncertainty in position, δx, and in momentum, δp, of a particle,

$$\delta x \delta p_x \geq \hbar \;\text{ or }\; \delta x \delta k_x \geq 2\pi. \tag{2.47}$$

In x direction, the wave vector, k_x, can assume values of

$$-|\vec{k}_0|\sin\alpha \leq k_x \leq +|\vec{k}_0|\sin\alpha, \tag{2.48}$$

where $|\vec{k}_0| = 2\pi/\lambda_0$ according to the de Broglie relation [63]; λ_0 is the wavelength of the photon detected. Since the (co)sine function can only assume values between -1 and 1, the range of values for k_x is,

$$\delta k_x = 2|\vec{k}_0| = \frac{4\pi}{\lambda_0}. \tag{2.49}$$

Plugging this into the uncertainty relation yields

$$\delta x = \frac{\lambda_0}{2}. \tag{2.50}$$

Thus, the resolution is fundamentally limited. For the Fourier approach in subsection 2.3.1, this means that the bounds of integration are restricted to $|\vec{k}_{\text{max}}| = 2\pi/\lambda_0$, higher values cannot be transmitted in the far field. All frequencies allowed lie on the so-called Ewald sphere (**Fig. 2.9**). For an ellipsoid as imaging system, there is no difference between lateral and axial resolution because the light is collected from all directions (4π). However, for a single objective lens, fluorescence is detected from half of the spatial angle only (2π). With the half angle of the objective aperture, $\alpha \leq \pi/2$, the wave vector in lateral direction is

$$\frac{\delta k_r}{2} = \frac{2\pi}{\lambda_0} \cdot \sin\alpha. \tag{2.51}$$

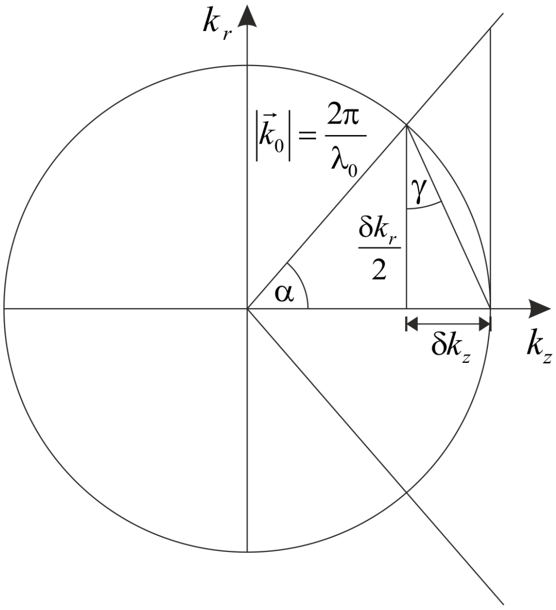

Figure 2.9.: Lateral and axial resolution determined by the Ewald sphere. Frequencies above $2\pi/\lambda$ are not accessible. Also, for a single objective lens, the collection angle is limited to $\alpha \leq \pi/2$.

According to equation 2.47, we obtain for the lateral uncertainty,

$$\delta r = \frac{\lambda_0}{2\sin\alpha}, \tag{2.52}$$

which is the famous Abbe equation. In axial direction, the wave vector is determined by

$$\delta k_z = \frac{\delta k_r}{2} \cdot \tan\gamma = \frac{2\pi}{\lambda_0} \sin\alpha \cdot \frac{\sin\frac{\alpha}{2}}{\cos\frac{\alpha}{2}} = \frac{4\pi}{\lambda_0} \sin^2\frac{\alpha}{2}. \tag{2.53}$$

Application of the uncertainty relation yields

$$\delta z = \frac{\lambda_0}{2\sin^2\left(\frac{\alpha}{2}\right)}, \tag{2.54}$$

for the axial resolution. Often, the relation between δk_r and δk_z is approximated by

$$\left(\frac{\delta k_r}{2}\right)^2 = \delta k_z(|\vec{k}_0| - \delta k_z) \approx \delta k_z |\vec{k}_0|, \tag{2.55}$$

resulting in

$$\delta z = \frac{\lambda_0}{\sin^2\alpha}. \tag{2.56}$$

These are the results for a single photon. If we have N photons, however, and can assure they are emitted from the same spot, the uncertainties must include a factor of $1/\sqrt{N}$.

For example, the lateral uncertainty becomes,

$$\delta r = \frac{\lambda_0}{2 \sin \alpha \sqrt{N}}. \tag{2.57}$$

This is an interesting result, as it tells us that, by isolating the source from other emitters nearby, the resolution is governed by a marker property.

Here, the resolution limit is presented as a consequence of the uncertainty relation. In the original work of Heisenberg entitled 'the gamma microscope' [64], the uncertainty relation is motivated by Abbe's resolution limit, proving the ubiquitous application of quantum mechanics. Nowadays, the universal validity of the uncertainty principle has been proven in a multitude of different experiments and, therefore, Abbe's equation can be considered as a result of this principle.

2.4. Microscopy Techniques

2.4.1. Widefield Epifluorescence Microscopy

In widefield microscopy, fluorescence light is collected from a large area by an objective lens and imaged onto a detector array such as a charge coupled device (CCD) camera or the human eye. Usually, the field of view is illuminated via the same objective lens as the one used for detection, termed epi-illumination. The magnification of the object, M, is given by the focal width of the objective lens, f_{Obj}, the tube lens, f_{Tbl}, and their respective distance, T,

$$M = \frac{T - f_{\mathrm{Tbl}}}{f_{\mathrm{Obj}} f_{\mathrm{Tbl}}}. \tag{2.58}$$

Yet, this factor determines sampling only, the resolution of a widefield microscope is limited by the wavelength of the fluorescence light, λ, and the NA of the objective lens (see subsection 2.3.3). According to subsection 2.3.4,

$$d_{\mathrm{lat}} = \frac{\lambda}{2n \sin \alpha} \tag{2.59}$$

for the resolution in the lateral and

$$d_{\mathrm{axl}} = \frac{\lambda}{2n \sin^2\left(\frac{\alpha}{2}\right)} \tag{2.60}$$

for the resolution in the axial direction. However, in this configuration, the entire sample is illuminated in the axial direction. The objective lens cannot discriminate between fluorescence light from different planes, which will result in high background depending on sample thickness. This obfuscation of the signal from the focal plane compromises contrast amongst sample structures, especially in the axial direction.

2.4.2. Confocal Microscopy

In confocal microscopy, a point-like light source is imaged into the sample via an objective lens and, thus, only a single spot is illuminated in the object plane. According to equation 2.37, the electric field in this spot, $\vec{E}(\vec{r})$, is given by

$$\vec{E}(\vec{r}) = \vec{E}_0 \cdot \frac{2J_1(\vec{k}_0\vec{r}n\sin\alpha)}{\vec{k}_0\vec{r}n\sin\alpha} = \vec{E}_0 \cdot a(\vec{r}), \tag{2.61}$$

termed excitation point spread function (PSF) of the microscope. Light emanating from this focal spot is collected, usually by means of the same objective lens. Signal photons are separated from the excitation light via a beamsplitter and imaged onto a point detector located in the same focal plane as the source, i.e., confocal to the source (**Fig. 2.10**). Thus, the amplitude of the electric field in the image plane is given by the product of the excitation and detection PSF,

$$\vec{E}_{\text{det}}(\vec{r}) = \vec{E}_0 \cdot a_{\text{exc}}(\vec{r}) \cdot a_{\text{det}}(\vec{r'} - \vec{r}). \tag{2.62}$$

Often, a circular aperture, a so-called pinhole, is placed into the image plane at position $\vec{r'} = 0$, eliminating light emanating from sources outside the focal plane. Consequently, the resulting amplitude registered by the detector is given by

$$\vec{E}_{\text{det}}(\vec{r}) = \vec{E}_0 \cdot a_{\text{exc}}(\vec{r}) \cdot a_{\text{det}}(\vec{r}) = \vec{E}_0 \cdot a^2(\vec{r}). \tag{2.63}$$

The signal of a confocal microscope is described by the product of the excitation and

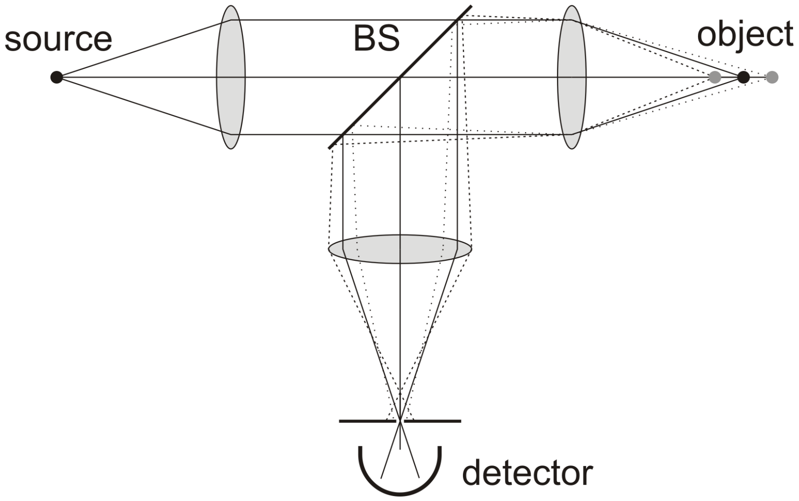

Figure 2.10.: Confocal Microscopy. A point-like source is imaged into the sample by a lens system. Sample photons are collected by the objective lens and separated from excitation light by a beamsplitter (BS) before being focused onto an aperture in front of the detector. By this aperture, out-of-focus light is blocked, resulting in an excellent optical sectioning capability.

detection PSFs. An image is acquired by scanning the focal spot across the sample. The signal intensity at the detector is given by

$$I_{\mathrm{det}}(\vec{r}) = I_0 \cdot a^4(\vec{r}). \tag{2.64}$$

Since, in fluorescence microscopy, we can assume to work with incoherent emitters, the Rayleigh criterion can be applied to calculate the resolution of a confocal microscope. Yet, due to the unchanged position of the minima, there is no improvement in resolution compared to widefield microscopy. However, application of the Sparrow criterion results in a slight lateral resolution improvement,

$$d_{\mathrm{min}} = 0.32 \cdot \frac{\lambda}{n \sin \alpha}, \tag{2.65}$$

since the second derivative of $J_1^2(x)$ features a root at $x \approx 1.08$. More importantly, the pinhole allows for axial sectioning of the sample. Since the fluorescence light is not directly focused onto the detector but onto a pinhole first, light emanating from out-of-focus planes is efficiently blocked.

2.4.3. Total Internal Reflection Microscopy

TIRFM is usually implemented as a widefield technique [27]. In TIRFM, the sample is immersed in a medium of lower refractive index (e.g., water, $n_2 = 1.33$) than the medium used to inject the excitation light (e.g., glass, $n_1 = 1.52$). If propagating at an angle greater than the critical angle, α_{crit},

$$\sin \alpha_{\mathrm{crit}} = \frac{n_2}{n_1}, \tag{2.66}$$

the excitation light will be totally reflected at the interface, z_0. Yet, due to the continuity conditions,

$$\begin{aligned} \vec{E}_{\mathrm{water}}(z_0) &= \vec{E}_{\mathrm{glass}}(z_0), \text{ and} && (2.67) \\ \frac{\partial}{\partial z}\vec{E}_{\mathrm{water}}(z_0) &= \frac{\partial}{\partial z}\vec{E}_{\mathrm{glass}}(z_0), && (2.68) \end{aligned}$$

the electric field, $\vec{E}$, cannot instantaneously decay to zero. Before reaching the critical angle, the transmitted electic field, $\vec{E}_t(\vec{r}, t)$, at position $\vec{r}$ and time t can be described by [65]

$$\vec{E}_t(\vec{r}, t) = \vec{E}_0 \exp(i(\vec{k_t}\vec{r} - \omega t)). \tag{2.69}$$

Choosing the coordinate system in a way that incident, reflected and transmitted waves lie within the xz-plane (**Fig. 2.11**), the individual components of the wave vector, $\vec{k_t}$, can be written as

$$\begin{aligned} k_{t,x} &= |\vec{k_t}| \sin \beta, && (2.70) \\ k_{t,y} &= 0, \text{ and} && (2.71) \\ k_{t,z} &= |\vec{k_t}| \cos \beta. && (2.72) \end{aligned}$$

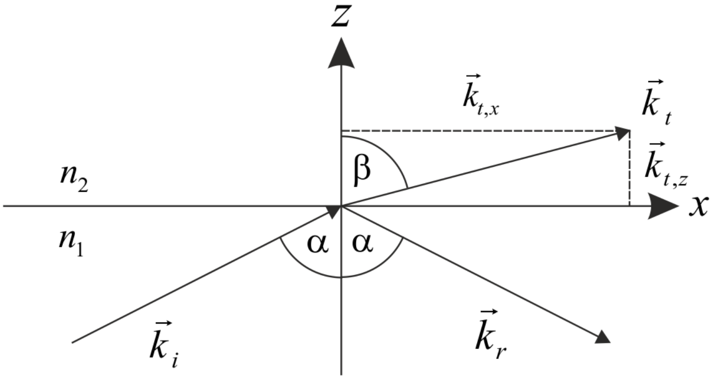

Figure 2.11.: Incident light of wave vector $\vec{k_i}$ is transmitted, $\vec{k_t}$, and reflected, $\vec{k_r}$, at an interface of two media of different refractive index, $n_1 > n_2$.

Using Snell's law, $n_1 \sin\alpha = n_2 \sin\beta$, we obtain

$$k_{t,x} = |\vec{k_t}|\frac{n_1}{n_2}\sin\alpha, \tag{2.73}$$

$$k_{t,y} = 0, \text{ and} \tag{2.74}$$

$$k_{t,z} = \pm|\vec{k_t}|\sqrt{1-\frac{n_1^2}{n_2^2}\sin^2\alpha}. \tag{2.75}$$

For angles $\alpha \geq \alpha_{\text{crit}}$, the expression under the square root becomes negative,

$$k_{t,z} = \pm i|\vec{k_t}|\sqrt{\frac{n_1^2}{n_2^2}\sin^2\alpha - 1} = \pm i\frac{\delta}{2}. \tag{2.76}$$

Thus, the electric field,

$$\vec{E}_t(\vec{r},t) = \vec{E}_0 e^{-\frac{\delta}{2}z} e^{i(|\vec{k_t}|x\frac{n_1}{n_2}\sin\alpha - \omega t)}, \tag{2.77}$$

describes a wave that travels parallel to the surface and decays exponentially perpendicular to the surface. The intensity of this evanescent field is given by

$$I(z) = I_0 \exp(-\delta z). \tag{2.78}$$

With the definition of the critical angle, the de Broglie relation, $k_2 = 2\pi/\lambda_2$, and the vacuum wavelength, $\lambda_0 = n_2\lambda_2$, the excitation depth, δ, can be written as

$$\delta = \frac{4\pi n_2\sqrt{\sin^2\alpha - \sin^2\alpha_{\text{crit}}}}{\lambda_0}. \tag{2.79}$$

With common experimental parameters, δ is in the range of $50-150$ nm and, thus, only fluorophores within this depth are excited. In contrast to standard widefield microscopy, no fluorescence from out-of-focus planes is created. Therefore, this technique provides excellent image contrast but is limited to the imaging of structures close to the index step such as cell membranes.

2.5. Super-resolution Microscopy

2.5.1. Localization as Key to Super-resolution

Long before super-resolution techniques such as STED and PALM were invented, it was known that single, point-like emitters can be localized with great precision, much better than the image resolution itself (compare subsection 2.3.4). So why has it taken until the 1990s that STED and the mid 2000s that PALM have first been demonstrated? The localization of fluorophores is only feasible for spatially well separated molecules. As soon as the density of markers increases beyond the optical resolution, localization becomes impossible. However, as already noted by Harry Nyquist [66] in 1928, the sampling frequency has to be at least twice as high as the frequency of the signal to be measured, or, as formulated by Claude E. Shannon in 1949, the maximum bandwidth available is limited to less than half of the transmission frequency [67]. In the case of fluorescence microscopy, the marker density along a single dimension has to be at least twice as high (2^1) as the desired spatial resolution. Consequently, for a three-dimensional structure, the required number of labels within a single, optically resolved volume element must be at least 2^3 times higher; thus, the PSFs of the individual emitters overlap. Therefore, besides marker localization, a second ingredient is essential for super-resolution microscopy. To ensure spatial separation, only subsets of markers may emit fluorescence at a particular point in time. The sampling criterion is met by a sequential repetition of a separation step followed by marker localization. During localization of a subset of markers, all surrounding markers need to be shut off, ideally by an optical mechanism. This demand for an effective off-switching mechanism poses several challenges for STED as well as PALM. In STED microscopy, fluorophores are switched off by stimulated emission. The cross section for this process is usually very low, so high power densities are required which are only feasible in a confocal setup, where all light is focused into a single spot. The principle of confocal microscopy was already patented in 1957 by Marvin Minsky. Yet, it took twenty more years and several technical innovations to be able to apply 3D laser scanning to biological specimens labeled with fluorescent markers, as in 1978 by Christoph and Thomas Cremer [68]. It became a standard technique only by the end of the 1980s. Furthermore, besides suitable instrumentation including powerful laser sources, high-end fluorophores enduring hundreds to thousands of excitation-depletion cycles required for STED microscopy were only recently developed. In regard to instrumentation, PALM is not as demanding as STED, as it can be performed on any fluorescence microscope with high-sensitivity widefield detection. However, in PALM, markers are stochastically activated from a non-fluorescent state. Thus, the markers used must provide a suitable, preferably optical switching mechanism. Although photochromism had already been discovered at the end of the 19th century, these compounds could only recently be applied as fluorescence markers to label biological specimens. For example, in 2002, the first photoactivatable variant of a FP was generated by mutagenesis of the original GFP [69]. Furthermore, in PALM, the super-resolution image requires intense post-processing of the data, involving computational power widely available only on present-day computers.

2.5.2. Targeted Switching

In STED microscopy, the markers surrounding the point of interest are prevented from contributing to the detected signal by inducing stimulated emission. A STED microscope is based on a confocal design. Thus, markers are localized by positioning the focal spot within the sample. Using a piezo stage, for example, the localization precision can easily be on the sub-nanometer scale. Yet, despite this great mechanical precision, the extension of the focal spot is still limited by diffraction, as discussed in subsection 2.3.4. Thus, the signal of all markers within this excited spot overlap, blurring the final image. Therefore, stimulated emission is induced for those markers that are not within the center of the focal spot. This is achieved by overlaying the excitation beam with a second, spectrally red-shifted beam with zero intensity in the center but high intensity towards the outskirts. As a result, fluorophores not in close vicinity to the center of the excitation spot are deexcited by stimulated emission before they can spontaneously emit fluorescence photons (**Fig. 2.12**). Hence, the effective PSF is confined to a sub-diffractional volume. Still, the signals of all marker molecules are needed; an image is reconstructed by scanning across the sample with an adequately small step size.

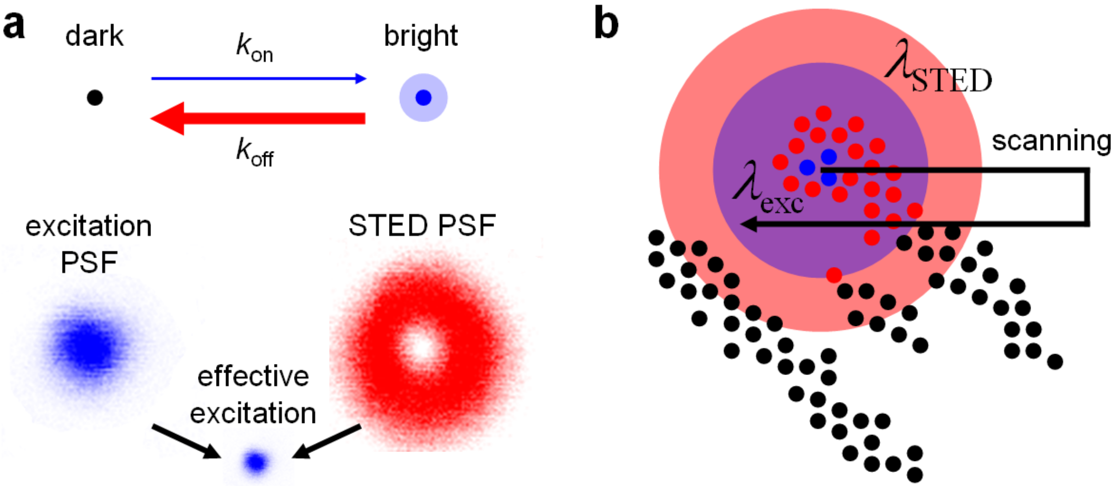

Figure 2.12.: STED principle. (**a**) After excitation (k_{on}), the bright fluorescent state of a marker can be depleted by stimulated emission (k_{off}). Hence, by overlaying the excitation PSF with a second, spectrally red-shifted beam with zero intensity in the center, STED yields a smaller effective PSF. (**b**) By scanning both beams across the sample with a sufficiently small step size, a super-resolution image is obtained.

2.5.3. Fluorophore Switching by Stimulated Emission

In a STED microscope, the fluorophores within the excitation volume undergo transitions between the ground state, S_0, and the excited state, S_1,

$$S_0 \underset{k_{\mathrm{fl}},k_{\mathrm{STED}}}{\overset{k_{\mathrm{exc}}}{\rightleftharpoons}} S_1, \tag{2.80}$$

assuming the transition from the excited state back to the ground state is dominated by emission of a fluorescence photon, either by spontaneous emission, k_{fl}, or stimulated emission, k_{STED}. The fluorophores can be excited and deexcited either by pulsed or continuous wave (CW) lasers. In pulsed STED, a short, δ-like excitation pulse, $I_{\mathrm{exc}}(t)$, at time t_0 induces a transition of the fluorophores from S_0 to S_1 [38]. The excitation is immediately followed by a STED pulse,

$$I_{\mathrm{STED}}(t) = \begin{cases} I_0, & t_0 \leq t \leq t_0 + \tau_{\mathrm{STED}} \\ 0, & \text{else} \end{cases}, \tag{2.81}$$

of duration τ_{STED}, to depopulate the excited state (**Fig. 2.13a**). Thus, only a tiny fraction of markers can spontaneously emit fluorescence. In CW-STED, a constant depletion intensity, $I(t) = I_0$, is applied. Thus, at the same average depletion power as in pulsed STED, the power density is much lower resulting in a slower depopulation of S_1. In this depletion mode, excitation can either be pulsed (**Fig. 2.13b**) [70] or continuous (no periodic time structure) [71]. With pulsed excitation, the fluorescence emission can be time-gated (τ_G, dotted line) to help to cut down the average power requirement of CW-STED for a depletion equal to pulsed STED (dash-dotted line). In contrast, continuous excitation is a stochastic process and, thus, the intensity of the depletion beam must be very high to ensure depletion before spontaneous emission at any time. A quantitative discussion of the fluorescence quenching by pulsed STED as well as CW-STED can be found in reference [72]. In pulsed STED, the excitation pulse is immediately followed by the STED pulse ($t = 0$). Therefore, the time dependence of the population number of the excited state, $N_1(t)$, is given by

$$\frac{\mathrm{d}N_1(t)}{\mathrm{d}t} = -(k_{\mathrm{fl}} + k_{\mathrm{STED}})N_1(t). \tag{2.82}$$

The solution of this first-order differential equation is

$$N_1(t) = N_1(0)\exp(-t(k_{\mathrm{fl}} + k_{\mathrm{STED}})). \tag{2.83}$$

The number of fluorophores remaining in the excited state after a STED pulse of duration τ is given by

$$N_1(t+\tau) = N_1(0)\exp(-(tk_{\mathrm{fl}} + \tau k_{\mathrm{fl}} + tk_{\mathrm{STED}} + \tau k_{\mathrm{STED}})). \tag{2.84}$$

The STED pulse is applied within a very short period compared to the lifetime of the excited state, $\tau \ll 1/k_{\mathrm{fl}}$, this term can thus be neglected. Also, at times $t > \tau$, no more stimulated emission is performed, $k_{\mathrm{STED}}(t > \tau) = 0$, resulting in

$$N_1(t+\tau) = N_1(0)\exp(-(tk_{\mathrm{fl}} + \tau k_{\mathrm{STED}})). \tag{2.85}$$

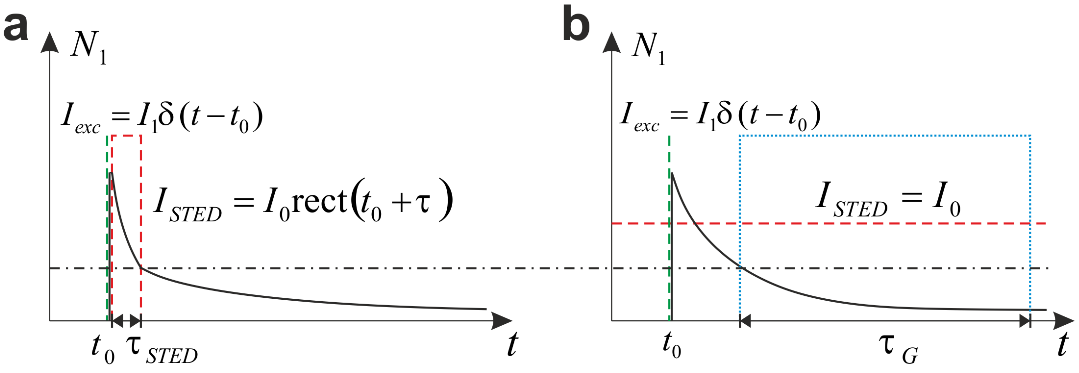

Figure 2.13.: STED modes. (**a**) In pulsed STED, a short, δ-like excitation pulse $I_{\text{exc}}(t)$ at time t_0 is immediately followed by a STED pulse $I_{\text{STED}}(t)$ of length τ_{STED} during which the excited state, S_1, is depopulated (solid line). (**b**) In CW-STED with pulsed excitation, a constant depletion intensity, I_0, is applied. Thus, at the same average depletion power as in pulsed STED, the power density is lower resulting in a slower depopulation of S_1 (solid line). However, the fluorescence emission can be time-gated (τ_G, dotted line) to help to reduce pre-depletion fluorescence to the same level as with pulsed depletion (dashed-dotted line).

Experimentally, the number of fluorophores remaining in the excited state can be evaluated by collecting the fluorescence photons, F_{STED}. Therefore, we integrate over time $t = 0 \to \infty$,

$$F_{\text{STED}} = N_1(0)\int_{t=0}^{\infty} \exp(-(tk_{\text{fl}} + \tau k_{\text{STED}}))\mathrm{d}t \tag{2.86}$$

$$= N_1(0)\frac{1}{k_{\text{fl}}}\exp(-\tau k_{\text{STED}}). \tag{2.87}$$

The STED efficiency, η, can be calculated by relating F_{STED} to the fluorescence in the absence of depletion, $F_{\text{confocal}} = N_1(0)/k_{\text{fl}}$,

$$\eta = \frac{F_{\text{STED}}}{F_{\text{confocal}}} = \exp(-\tau k_{\text{STED}}). \tag{2.88}$$

Besides the duration of the depletion pulse, the probability of stimulated emission depends on the effective cross section, σ_{STED}, and the intensity of the STED pulse inducing the emission, I_{STED}. Thus, we obtain

$$\eta = \exp(-\tau\sigma_{\text{STED}}I_{\text{STED}}). \tag{2.89}$$

Experimentally, the effective cross section for stimulated emission is difficult to access. Therefore, we replace it with the saturation intensity, I_{sat}, representing the STED intensity at which half of the population of the excited state is quenched to the ground state,

$$I_{\mathrm{sat}} = \frac{\ln 2}{\tau \sigma_{\mathrm{STED}}}. \tag{2.90}$$

Thus, the STED efficiency becomes,

$$\eta = \exp\left(-\frac{I_{\mathrm{STED}}}{I_{\mathrm{sat}}} \ln 2\right). \tag{2.91}$$

As a result, it can be seen that stimulated emission is a suitable off-switching mechanism. More importantly, spontaneous emission of fluorescence photons can be suppressed by a non-invasive, optical far-field method, a crucial finding towards the implementation of far-field optical microscopy beyond the diffraction limit. For resolution enhancement, the shape of the depletion pattern has to be considered, too, as will be discussed in subsection 2.5.4.

Yet, at this point, the laser intensity required for a significant resolution increase can already be estimated. Stimulated emission is in direct competition with spontaneous emission. The fluorescence lifetime, $\tau_{\mathrm{fl}} = 1/k_{\mathrm{fl}}$, of common dyes is in the range of a few nanoseconds. For a significant increase in spatial resolution, the rate of stimulated emission should be at least as high as the rate of spontaneous emission. Thus, we can start with

$$k_{\mathrm{STED}} = k_{\mathrm{fl}} = 10^9\,\mathrm{s}^{-1}. \tag{2.92}$$

The intensity necessary to induce sufficient stimulated emission is

$$I_{\mathrm{STED},\lambda} = \frac{E_\lambda\, k_{\mathrm{STED}}}{\sigma_{\mathrm{STED}}} = \frac{h\, c\, k_{\mathrm{STED}}}{\lambda\, \sigma_{\mathrm{STED}}}, \tag{2.93}$$

with the energy of a depletion photon, $E_\lambda = hc/\lambda$. For common dyes, the effective cross section for stimulated emission is $\sim 10^{-16}\,\mathrm{cm}^2$ [73]. Assuming a depletion wavelength of 750 nm for a red fluorescent dye,

$$I_{\mathrm{STED,750nm}} = \frac{6.6 \cdot 10^{-34}\,\mathrm{J}\cdot\mathrm{s} \cdot 3 \cdot 10^{8}\,\mathrm{m}\cdot\mathrm{s}^{-1} \cdot 10^{9}\,\mathrm{s}^{-1}}{0.75 \cdot 10^{-6}\,\mathrm{m} \cdot 10^{-16}\,\mathrm{cm}^2} \sim 2.6\,\mathrm{MW/cm}^2. \tag{2.94}$$

This is a quite high power density. In a widefield microscope, power densities are in the $\mathrm{kW/cm}^2$ range using common laser sources. Thus, STED microscopy is only feasible in a confocal setup. However, other transitions with much lower saturation intensities than stimulated emission can be used to deplete the active state of the fluorescent markers around the center of the excitation beam. Such transitions include triplet state population [74, 75] and *cis-trans* isomerization of photoswitchable fluorophores [49, 76, 77]. All targeted, depletion-based super-resolution techniques have been summarized by the term RESOLFT microscopy [49].

2.5.4. Resolution in Depletion Microscopy

In a STED microscope, a phase mask is inserted into the depletion beam path to modify the shape of the resulting focal spot in the sample plane. For resolution enhancement, the depletion pattern must feature at least one intensity zero along the direction of interest. In this work, two different phase masks were utilized, one for resolution improvement in the xy-direction, the other one for improvement in the z-direction (**Fig. 2.14a,d**). The first design (VPP1a, RPC Photonics, Rochester, USA) adds a helical phase retardation of $0 - 2\pi$ to the depletion beam. If the light passing the phase mask has a circular polarization with the same sense of rotation as the mask, a circular, ring-shaped pattern is created in the xy-plane after focusing by an objective lens (**Fig. 2.14b**). However, with this phase mask, the intensity distribution in z-direction is unaffected. Therefore, a second design was used when a resolution improvement along the z-axis was required [78]. In that design, the light passing the inner circle is phase-shifted by π relative to the light passing the outer part. The resulting pattern after focusing exhibits two strong lobes in axial direction with zero intensity in the center (**Fig. 2.14e**). Similar to the helical phase mask, a ring-shaped pattern is created in the xy-plane. Yet, the intensity of the ring structure is weak compared to the lobes in axial direction. Thus, an isotropic resolution enhancement requires combination of both depletion patterns. For quantification of the

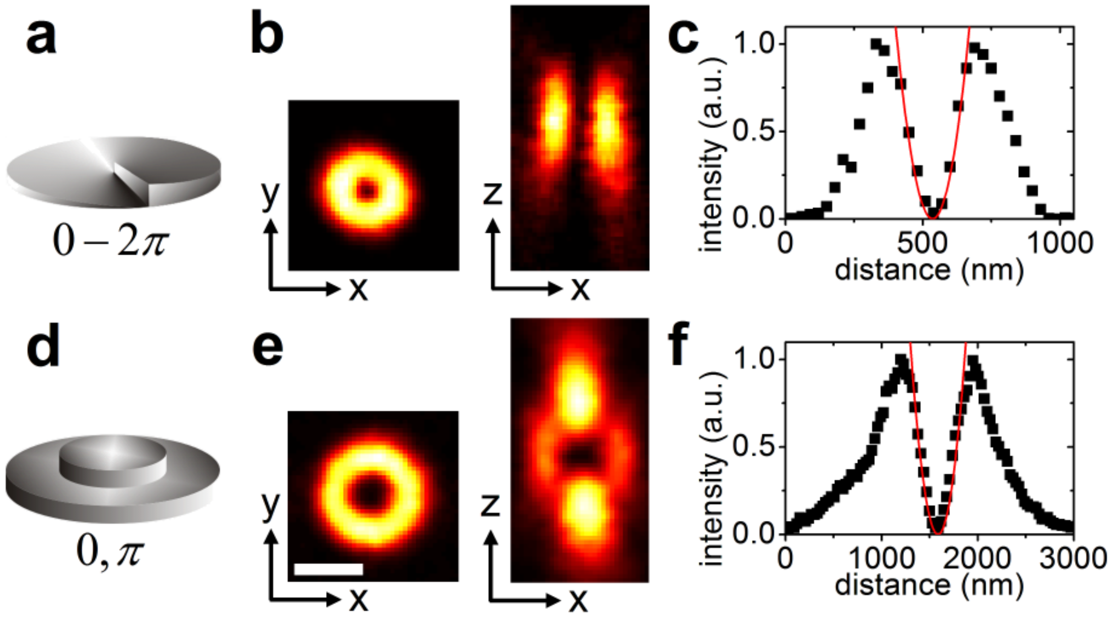

Figure 2.14.: (**a,d**) Helical and circular phase mask. (**b,e**) xy- and xz-images of the resulting PSFs after focusing obtained by measuring reflection off 80 nm gold beads (GC-80, BBI, Dundee, UK). (**c,f**) Cross sections along the x- and z-axis of the depletion patterns (squares), respectively, with the central zeros approximated by parabolas (red lines). Scale bar, 300 nm.

resulting resolution enhancement, the shape of both depletion patterns around their central zero (**Fig. 2.14c,f**) can be approximated by a parabola, $y = a^2 r^2$ [72]. By defining $4I_{\mathrm{STED,max}}$ as the maximum intensity present within the depletion pattern, we obtain

$$I_{\mathrm{STED}} = 4I_{\mathrm{STED,max}} a^2 r^2. \tag{2.95}$$

The Airy pattern of the focused excitation beam can be well approximated by a Gaussian distribution of full width at half maximum (FWHM), d_{conf},

$$F_{\mathrm{conf}}(r) = F_0 \cdot \exp\left(-\frac{4\ln(2) r^2}{d_{\mathrm{conf}}^2}\right). \tag{2.96}$$

To compute the detected fluorescence, the excitation pattern has to be weighted with the STED efficiency, η, (equation 2.91), resulting in

$$F_{\mathrm{STED}}(r) = F_0 \cdot \exp\left(-\frac{4\ln(2) r^2}{d_{\mathrm{conf}}^2}\right) \cdot \exp\left(-\frac{4\ln(2) I_{\mathrm{STED,max}} a^2 r^2}{I_{\mathrm{sat}}}\right). \tag{2.97}$$

The resulting PSF is a Gaussian distribution of FWHM, d_{STED},

$$d_{\mathrm{STED}} = \frac{d_{\mathrm{conf}}}{\sqrt{1 + d_{\mathrm{conf}}^2 a^2 \frac{I_{\mathrm{STED}}}{I_{\mathrm{sat}}}}}. \tag{2.98}$$

As a consequence, even though the pattern of the STED beam itself does not display a finer structure than the excitation beam because it is limited by diffraction as well, an effective feature below the optical resolution is created. This saturation effect is visualized in **Fig. 2.15**. Here, the image intensity represents the power density of the STED-PSF, and, the maximum of the color map represents the saturation intensity, I_{STED}, of the dye. Thus, it can be seen that only a sub-diffractional population around the central zero escapes depletion by stimulated emission; its spatial extension decreases with increasing STED intensity.

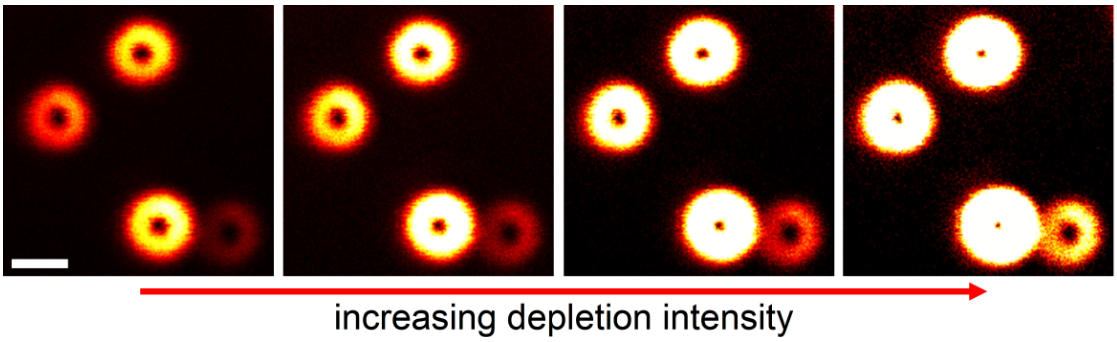

Figure 2.15.: Depletion pattern at increasing depletion intensity and constant saturation intensity. A sub-diffraction sized pattern emerges. Scale bar, 300 nm.

2.5.5. Stochastic Switching in Localization Microscopy

In recent years, a variety of localization-based super-resolution methods have been developed independently. Among these are PALM [15] or FPALM [16] and STORM [17]. In localization-based concepts, fluorescent markers are optically switched between a bright and a dark state and imaged with a camera-based, widefield-type microscope. The activation of the individual markers to the bright fluorescent state occurs sparsely and stochastically distributed over a large area, thereby avoiding spatial overlap of the signals of the molecules within one single image (**Fig. 2.16**). The positions of the markers within the image can subsequently be determined by software [79]. Depending on the number of photons collected per emitter, their locations can be measured with a much higher precision (equation 2.57) than the width of their PSFs, i.e., the optical resolution of the microscope (equation 2.59). To meet the sampling criterion, other subsets of markers are switched to their bright states and imaged after bleaching and/or off-switching of the prevenient subset of markers. This procedure is repeated until the entire marker population is captured. In a final step, the positions of all molecules are combined in a super-resolution image. The resolution of such a fluorophore density map is no longer determined by the optical resolution of the microscope, but by the localization precision of the individual markers.

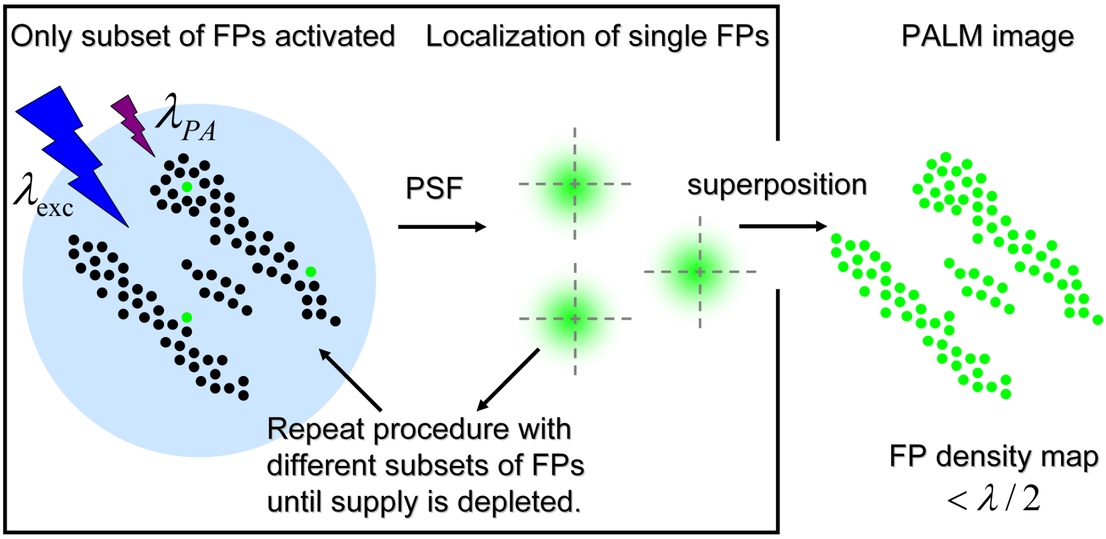
Only subset of FPs activated
Localization of single FPs
PALM image
λ_{PA}
λ_{exc}
PSF
superposition
Repeat procedure with different subsets of FPs until supply is depleted.
FP density map
$< \lambda / 2$

Figure 2.16.: PALM principle as explained in the text.

2.5.6. Resolution in Localization Microscopy

As long as the labeling density is high enough to fulfil the sampling criterion (subsection 2.5.1), the resolution of a localization-microscopy image depends on the localization precision of the individual markers. As noted in subsection 2.3.4, the uncertainty of the position, Δx, of a single, point-like emitter decreases with increasing number of photons,

N, detected. With the NA of the objective lens, $n \sin\alpha$, equation 2.57 becomes

$$\Delta x = \frac{\lambda}{2n\sin\alpha} \cdot \frac{1}{\sqrt{N}} = s \cdot \frac{1}{\sqrt{N}}. \tag{2.99}$$

The following derivation of the overall localization error is based on a publication by Thompson et al. [80]. According to equation 2.99, the variance of the uncertainty in position is given by

$$(\Delta x)^2 = \frac{s^2}{N}. \tag{2.100}$$

This would be true for a perfect detector in the absence of background noise. However, a camera detection area is subdivided into individual pixels. Therefore, we have to introduce pixelation noise, arising from the fact that we do not know where the photon arrives within a single pixel of size a, adding to the uncertainty,

$$(\Delta x)^2 = \frac{s^2}{N} + \frac{a^2}{12N}, \tag{2.101}$$

where $a^2/12$ is the variance of a rectangular (top-hat) distribution of size a. The uncertainty is further increased by background photons originating from random positions or counting events produced by the detector itself. Assuming that least-squares fitting is applied to determine the marker locations, we can start with the criterion that the sum of the squared errors,

$$\chi^2(x) = \sum_i \frac{(y_i - N_i(x))^2}{\sigma_i^2}, \tag{2.102}$$

is minimized, with the events, y_i, detected in each pixel, i, the expected number of counts, $N_i(x)$, from a particle located at x, and the expected uncertainty in counts, σ_i^2. The uncertainty in counts can be separated into photon-counting and background noise, b,

$$\sigma_i^2 = N_i(x) + b^2. \tag{2.103}$$

Application of the condition for the minimum, $\mathrm{d}\chi^2(x)/\mathrm{d}x = 0$, results in an equation for the measured position x. In a first order approximation, the mean square error can be expressed as

$$(\Delta x)^2 = \frac{1}{\sum_i \left(\frac{\mathrm{d}N_i(x)}{\mathrm{d}x}\frac{1}{\sigma_i}\right)^2}. \tag{2.104}$$

Replacing the sum with an integral and taking only background noise into account results in

$$(\Delta x_{\mathrm{bkg}})^2 = \frac{4\sqrt{\pi} s^3 b^2}{a N^2}, \tag{2.105}$$

for a single dimension. Usually, the position of a molecule is determined within a two-dimensional image. Here, the background induced variance becomes

$$(\Delta x_{\mathrm{bkg}})^2 = \frac{8\pi s^4 b^2}{a^2 N^2}. \tag{2.106}$$

Thus, the overall variance in the position of a single source detected by a camera is given by

$$(\Delta x)^2 = \frac{s^2}{N} + \frac{a^2}{12N} + \frac{8\pi s^4 b^2}{a^2 N^2}. \tag{2.107}$$

Notably, the pixelation noise decreases, whereas the background noise increases with smaller pixel size. The transition between the two regimes occurs at

$$\frac{a^2}{12N} = \frac{8\pi s^4 b^2}{a^2 N^2}. \tag{2.108}$$

Consequently, the best ratio of pixel size to spot size, a/s, can be found for,

$$\left(\frac{a}{s}\right)^4 = \frac{96\pi b^2}{N}, \tag{2.109}$$

and, thus, depends on the number of photons emitted by the fluorophore. The optimal ratio is important for microscope construction. As fluorescent dyes generally have a higher photon yield than fluorescent proteins, the pixel size in STORM imaging ($70-100\,\mathrm{nm}$ [81, 82]) is usually chosen a bit smaller than in PALM imaging ($100-130\,\mathrm{nm}$ [15, 16]).

2.5.7. Fluorescent Markers for Localization Microscopy

In localization microscopy, paFPs and synthetic dyes are the most frequently employed markers. Up to now, synthetic dyes are brighter and more photostable than FPs, allowing for a higher localization precision. As an example, for the photoswitchable fluorophore pair Cy3-Cy5, ~ 6000 photons per switching cycle of a single pair were reported [83, 84]. For tdEosFP, one of the brightest paFPs for PALM imaging, only ~ 2600 photons were detected per molecule [85]. Furthermore, popular monomeric FPs often only yield a few hundred detected photons before they bleach [86]. However, even with only a few hundred photons per fluorophore, a ten-fold resolution enhancement is feasible, and, unlike synthetic dyes, FPs are ideally suited for *in vivo* experiments because they can be expressed by the cell itself [87, 88]. In contrast, synthetic dyes usually require high concentrations of reductants inducing photoswitching, as well as additional labeling procedures that often limit their application to fixed specimens [83, 89]. Noteworthy, in addition to FPs and synthetic dyes, nanocrystals have been employed in localization microscopy, too. They show great promise due to their high brightness and photostability. Nevertheless, we have employed paFPs in our *in vivo* localization microscopy studies because of their excellent biocompatibility.

paFPs can be subdivided into different classes according to their response to light irradiation. The photoreaction can either by irreversible, termed photoconversion or reversible, termed photoswitching. Photoconversion results from changes in the covalent bonds of the chromophore or amino acids close by. These modifications either cause a conversion from a non-fluorescent to a fluorescent state, or, a change of the emission color of the fluorescent state. Photoswitching results from a *cis-trans* isomerization of the chromophore accompanied by conformational rearrangements of amino acids in its vicinity. The photoswitching mode is defined by the switching direction during excitation. If irradiation of the excitation wavelength populates the non-fluorescent state, the protein is called a negative photoswitcher. If irradiation of the excitation wavelength populates the fluorescent state, the protein is called a positive photoswitcher. In **Fig. 2.17**, photoconversion and photoswitching is illustrated on the basis of IrisFP, a paFP that combines the two photoactivation modes [86,90]. IrisFP is reversibly switchable in the green, and, after violet light-induced photoconversion, becomes a red reversibly switchable marker.

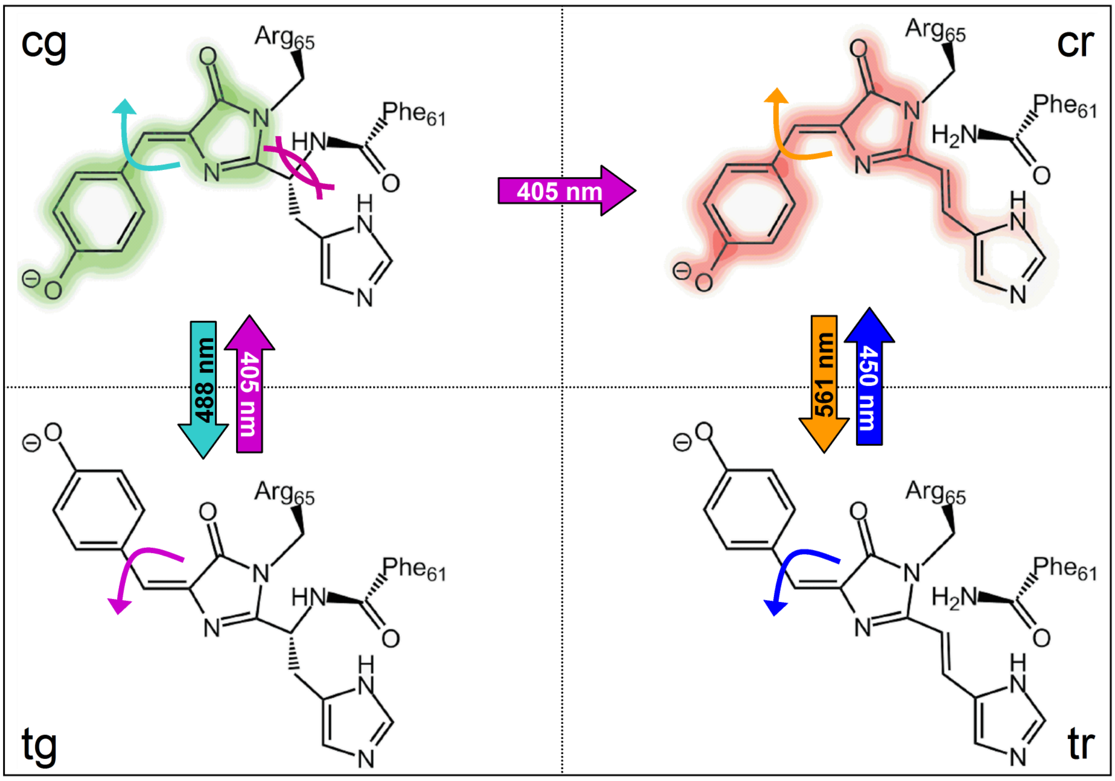

Figure 2.17.: Photoactivation modes of IrisFP. In the *cis* conformation of the green chromphore (cg), fluorescence can be excited with 488-nm light. The excitation wavelength isomerizes the chromophore to the non-fluorescent *trans* conformation (tg). This process can be reversed by 405-nm light. Extensive irradiation with the same wavelength induces a backbone cleavage in the green chromophore, thereby adding covalent bonds to the conjugated π-electron system. Fluorescence of the red *cis* chromphore (cr) can be excited by 561-nm light. Again, the excitation wavelength induces switching to the non-fluorescent *trans* conformation (tr), which can be reversed by 450-nm light. Scheme adopted from reference [91].

The first photoconvertible fluorescent protein, PA-GFP, was generated by mutagenesis of the original GFP [69]. Illumination with $\sim$ 400-nm light induces a decarboxylation of glutamic acid (Glu) at position 212 of the amino acid sequence causing a reorientation of the hydrogen bonding network surrounding the chromophore. Thereby, fluorescence emission of PA-GFP is increased $\sim$ 100 fold. PA-GFP was followed by the photoactivatable monomeric red fluorescent protein PA-mRFP1-1, which exhibits a $\sim$ 70 fold increase in red fluorescence after irradiation with violet light [92]. Despite the application of PA-GFP in FPALM imaging to determine the diffusion coefficient of haemagglutinin in live fibroblasts [87], the use of both proteins in super-resolution imaging is limited by their low contrast ratio between bright and dark states. In general, the contrast of photoconvertible fluorescent proteins shifting their emission color is much better. Very common is a shift of the fluorescence from green (GFP-like) to red (RFP-like), as exhibited by the natural Kaede [93], the engineered KikGR [94] and EosFP [95,96], which was engineered into a monomeric form for imaging of cellular proteins [97]. In these paFPs, the protein backbone between histidine (His) at position 62 and phenylalanine (Phe) at position 61 is cleaved by absorption of a $\sim$ 400-nm photon. Thus, a double bond is established between the C_α and C_β of the His62 side chain extending the π-electron system [96,98]. The cyan-to-green convertible marker PS-CFP2 could be used for dual-color super-resolution PALM imaging [85].

Reversible photoswitching between a fluorescent and a non-fluorescent state was already observed in a single molecule study of avGFP, at that time described as blinking [99]. The first reversible switcher reported as such was FP595 [100], followed by Dronpa [101]. Usually, photoisomerization involves a protonation/deprotonation of the chromophore, a change in its planarity and its interaction with surrounding amino acids [102, 103]. Often, photoswitchable FPs exhibit a lower contrast ratio between bright and dark states than photoconvertible FPs. But, due to the sampling criterion, an increase in the optical resolution by a factor of n requires a n^3 higher density of labels for a three-dimensional sample. Consequently, the contrast ratio is crucial to be able to identify an individual fluorophore within hundreds to thousands of other emitters. An overview of a selection of paFPs used in localization microscopy is shown in **Tab. 2.1**.

Table 2.1.: Selection of paFPs used in localization microscopy.

Fluorescent protein	Pre/post color	Excitation/ emission (nm)	Activation light	Contrast ratio	Photons per burst
Dark-to-bright photoconvertible FPs					
PA-GFP [69]	dark/green	504/517	violet	100	300
PA-mRFP1-1 [92]	dark/red	578/605	violet	70	ND
Photoconvertible FPs shifting their emission color					
PS-CFP2 [104]	cyan/green	490/511	violet	1,500	260
Kaede [93]	green/red	572/582	violet	2,000	400
mKikGR [94]	green/red	580/591	violet	400	970
mEos2 [95]	green/red	573/584	violet	>2,000	500
Photoswitchable FPs					
FP595 [100]	dark/red	590/600	green	30	ND
Dronpa [101]	dark/green	503/517	violet	<1,000	120
Padron [105]	green/dark	503/522	blue	ND	ND

ND – not determined. Table adopted from Fernández-Suárez et al. [19], numbers from reference [106].

3. Studying Dynamics by Fluorescence Microscopy

3.1. Measuring Dynamics

Starting with a simple two-state model, with states A and B and the rate coefficients, k_1 and k_{-1}, for transitions between A and B,

$$A \underset{k_{-1}}{\overset{k_1}{\rightleftharpoons}} B, \tag{3.1}$$

the question is how to measure the dynamics of such a system. In equilibrium, the system is characterized by the equilibrium coefficient, K,

$$K = \frac{[B]}{[A]} = \frac{k_1}{k_{-1}}. \tag{3.2}$$

Although the ratio of the rate coefficients is given by the ratio of the concentrations, the individual values have yet to be determined. Hence, a perturbation such as a pressure change can be introduced to the system favoring the population of, e.g., state B (**Fig. 3.1**). By measuring the relaxation toward equilibrium, the apparent rate coeffi-

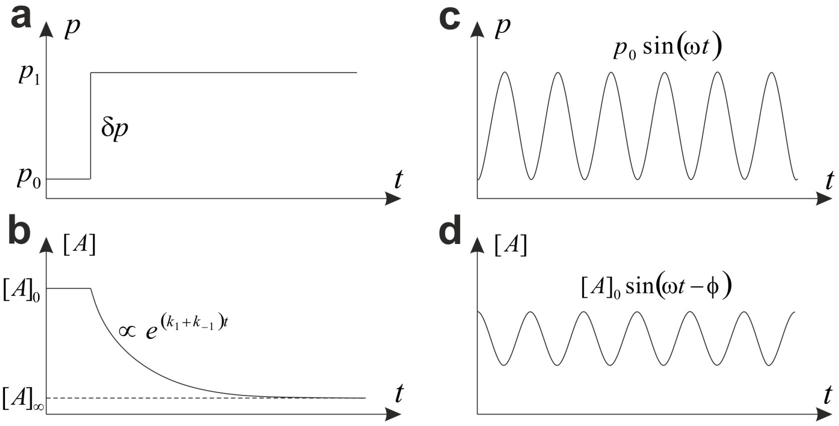

Figure 3.1.: Relaxation Methods. (**a**) An experimental parameter such as pressure, p, is suddenly changed by δp. (**b**) Subsequently, the relaxation toward equilibrium is monitored. (**c**) Alternatively, a periodic pressure modulation is applied. (**d**) Here, the relaxation time is determined by the amplitude, $[A]_0$, and the phase shift, ϕ, of the response.

cient, $\lambda = k_1 + k_{-1}$, is obtained. With the known value for the equilibrium coefficient, K, k_1 and k_{-1} can be computed individually. A perturbation might either be a single, fast change of an experimental parameter, following the relaxation in the time domain or, alternatively, a periodic modulation, measuring the amplitude, $[A]_0$, and the phase shift, ϕ, of the response. However, a perturbation has to be faster than the intrinsic dynamics of the system under study and is sometimes difficult to apply. For example, changes in temperature or pH often require a considerable amount of time. Here, fluctuation methods can help. If the energy barrier, ΔE, between states A and B is not too high compared to the thermal energy, $E_T = k_B T$, available at temperature T, interconversions take place in equilibrium as well. Yet, when studying a large, macroscopic system, these microscopic fluctuations average out and, thus, cannot be measured. In order to overcome this averaging problem, the population included in a fluctuation measurement has to be limited to a microscopic system of a few particles only. Under these circumstances, the fluctuations can be evaluated using an autocorrelation analysis.

3.2. Fluorescence Recovery after Photobleaching

3.2.1. The FRAP Principle

FRAP belongs to the family of relaxation methods. The perturbation introduced by FRAP is photobleaching of fluorescent markers by brief but strong laser illumination within a limited region of interest (**Fig. 3.2**). In a dynamic system, non-fluorescent, bleached markers can move out of the bleached region whereas fluorescent markers from the surrounding area can move in. Thus, fluorescence within the bleached spot recovers. The course of the recovery depends on the underlying processes such as diffusion, active transport and/or binding. By appropriate modeling of the recovery curve, the corresponding rate coefficients can be obtained.

3.2.2. Modeling Fluorescence Recovery

The following discussion is based on a publication by Axelrod et al. [28]. Let us consider translation dynamics within in a lipid bilayer. Simple, lateral diffusion is described by the differential equation

$$\frac{\partial C(\vec{r},t)}{\partial t} = D\nabla^2 C(\vec{r},t), \tag{3.3}$$

with the fluorophore concentration, $C(\vec{r},t)$, at position $\vec{r}$ and time t, and the diffusion coefficient, D. Irreversible photobleaching is induced by a laser with an intensity distribution, $I_\mathrm{b}(\vec{r})$, at a rate $\sigma I_\mathrm{b}(\vec{r})$, where σ is the effective cross section for bleaching. For further calculations we assume a Gaussian bleaching profile,

$$I_\mathrm{b}(r) = \frac{2I_0}{\pi\omega^2}\exp\left(-\frac{2r^2}{\omega^2}\right), \tag{3.4}$$

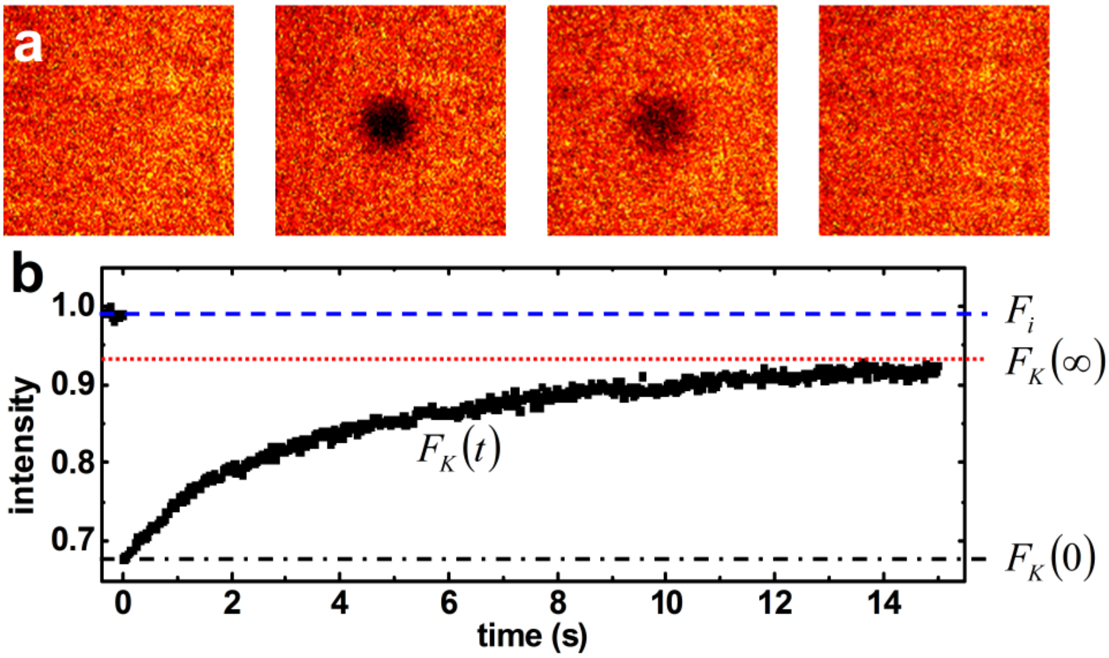

Figure 3.2.: FRAP principle. (**a**) A fluorescently labeled lipid bilayer (first image) is quickly bleached at a small spot (second image), followed by fluorescence recovery due to lipid diffusion (third and fourth image). (**b**) By time-resolved monitoring of the fluorescence intensity at the bleached spot, $F_K(t)$, the dynamics of the system can be probed. Indicated are the initial fluorescence, F_i (dashed line), the fluorescence after bleaching, $F_K(0)$ (dashed-dotted line), and, the fluorescence after recovery, $F_K(\infty)$ (dotted line).

with the radius at $1/e^2$ height, ω, and the total laser intensity, I_0. Thus, the concentration of unbleached fluorophores is given by the differential equation,

$$\frac{\mathrm{d}C(\vec{r},t)}{\mathrm{d}t} = -\sigma I_\mathrm{b}(\vec{r})C(\vec{r},t), \tag{3.5}$$

assuming that bleaching occurs within a time interval, Δt_b, short compared to fluorophore transport into and out of the bleached spot. The solution at time $t = 0$ after bleaching, i.e., at the beginning of the recovery is

$$C(\vec{r},0) = C_0 \exp(-\sigma \Delta t_b I_\mathrm{b}(\vec{r})) = C_0 \exp(-K(\vec{r})), \tag{3.6}$$

with the initial fluorophore concentration, $C_0 = C(\infty, t)$. Defining the solution of equation 3.3 with respect to this initial fluorophore concentration as $C_K(\vec{r},t)$, the fluorescence recovery, $F_K(t)$, at times $t > 0$ is given by

$$F_K(t) = \gamma \iint I_\mathrm{r}(\vec{r})C_K(\vec{r},t)\mathrm{d}^2 r, \tag{3.7}$$

with the laser intensity at the area monitored during recovery, $I_{\mathrm{r}}(\vec{r})$, and, the product of fluorophore quantum yield and detection efficiency, γ. The fluorescence shortly after bleaching, $F_K(0)$, does not depend on the type of recovery but is a function of the (Gaussian) bleaching profile,

$$F_K(0) = F_{\mathrm{i}} \frac{1 - e^{-K(\vec{r})}}{K(\vec{r})}. \tag{3.8}$$

Thus, the depth of bleaching, $K(\vec{r})$, can be determined directly from the initial fluorescence before bleaching, F_{i}, and the fluorescence at $t = 0$ after bleaching. The fluorescence recovery, $F_K(t)$, can be calculated as a series expansion,

$$F_K(t) = F_{\mathrm{i}} \sum_{n=0}^{\infty} \frac{(-K(\vec{r}))^n}{n!} \left[1 + n\left(1 + \frac{8Dt}{\omega^2}\right)\right]^{-1}, \tag{3.9}$$

For small $K(\vec{r})$, i.e., at low bleaching depth, the fluorescence recovery can be approximated by

$$F_K(t) = \frac{F_K(0) + \frac{4Dt}{\beta\omega^2} F_K(\infty)}{1 + \frac{4Dt}{\beta\omega^2}}, \tag{3.10}$$

with $\beta = 1$ and the fluorescence after recovery, $F_K(\infty)$. For a high bleaching depth, the parameter $\beta > 1$ can be retrieved from a linearization procedure described by Yguerabide et al. [107]. When dealing with pure diffusion within an area large compared to the size of the bleached spot, we can assume a full recovery such that $F_K(\infty) = F_{\mathrm{i}}$. However, if there is a static fraction of fluorophores, the fluorescence will not fully recover but only to a value $F_K(\infty) < F_{\mathrm{i}}$. This population is referred to as the immobile fraction,

$$P_{\mathrm{im}} = \frac{F_{\mathrm{i}} - F_K(\infty)}{F_{\mathrm{i}} - F_K(0)}, \tag{3.11}$$

so the mobile fraction is

$$P_{\mathrm{mob}} = 1 - P_{\mathrm{im}} = \frac{F_K(\infty) - F_K(0)}{F_{\mathrm{i}} - F_K(0)}. \tag{3.12}$$

If the reservoir of intact fluorophores is small, not all bleached molecules can be replaced, and the fluorescence will also not recover to its initial value. Luckily, both cases are easy to distinguish. Outside the bleached spot, a difference between the initial fluorescence and the fluorescence after recovery indicates a limited reservoir. After recovery, a difference between the fluorescence at and outside the bleached spot denotes the presence of an immobile fraction.

Another dynamic process that can be probed by FRAP is binding. A simple example is an accumulation of static molecules, S, to which fluorescent markers, F, can attach from the outside forming a complex, X, as described by

$$S + F \underset{k_{\mathrm{off}}}{\overset{k_{\mathrm{on}}}{\rightleftharpoons}} X, \tag{3.13}$$

with k_{on} and k_{off} representing the rate coefficients for attachment and detachment, respectively. In equilibrium ($t \to \infty$),

$$\frac{[X]}{[S][F]} = \frac{k_{\mathrm{on}}}{k_{\mathrm{off}}} = K, \tag{3.14}$$

with the equilibrium coefficient, K. The temporal evolution of the system can be described by the differential equation

$$\frac{\mathrm{d}[X(t)]}{\mathrm{d}t} = [S(t)][F(t)]k_{\mathrm{on}} - [X(t)]k_{\mathrm{off}}. \tag{3.15}$$

The rate coefficients are to be determined by the FRAP method. Strong laser illumination bleaches the molecule-marker complexes, X, within the illuminated region. However, the bleached fluorophores are still attached and, thus, for the fluorescence to recover, they have to detach before an intact marker can bind. Therefore, recovery is a two-step process,

$$X_{\mathrm{dark}} + F_{\mathrm{bright}} \underset{k_{\mathrm{on}}}{\overset{k_{\mathrm{off}}}{\rightleftharpoons}} S + F_{\mathrm{dark}} + F_{\mathrm{bright}} \underset{k_{\mathrm{off}}}{\overset{k_{\mathrm{on}}}{\rightleftharpoons}} X_{\mathrm{bright}} + F_{\mathrm{dark}}, \tag{3.16}$$

assuming that the reaction is not affected by bleaching. The corresponding system of differential equations is,

$$\begin{aligned}
\frac{\mathrm{d}[X_{\mathrm{dark}}(t)]}{\mathrm{d}t} &= [S][F_{\mathrm{dark}}]k_{\mathrm{on}} - [X_{\mathrm{dark}}]k_{\mathrm{off}}, && (3.17)\\
\frac{\mathrm{d}[S(t)]}{\mathrm{d}t} &= [X_{\mathrm{dark}}]k_{\mathrm{off}} - [S][F_{\mathrm{dark}}]k_{\mathrm{on}} + [X_{\mathrm{bright}}]k_{\mathrm{off}} - [S][F_{\mathrm{bright}}]k_{\mathrm{on}}, && (3.18)\\
\frac{\mathrm{d}[X_{\mathrm{bright}}(t)]}{\mathrm{d}t} &= [S][F_{\mathrm{bright}}]k_{\mathrm{on}} - [X_{\mathrm{bright}}]k_{\mathrm{off}}. && (3.19)
\end{aligned}$$

In general, this is a complicated situation. The reaction depends on the local marker concentration, which in turn depends on diffusion. If the diffusion time is similar to the lifetime of the molecule-marker complex ($\tau_{\mathrm{D}} \sim \tau_{\mathrm{off}} = 1/k_{\mathrm{off}}$), these two processes overlap and are impossible to disentangle from the recovery curve (**Fig. 3.3b**). However, if marker diffusion is much faster than the lifetime of the molecule-marker complex ($\tau_{\mathrm{D}} \gg \tau_{\mathrm{off}}$), the response can be separated into two steps (**Fig. 3.3a**). At short times, fluorescence recovery is dominated by replacement of the unbound, non-fluorescent markers by new fluorophores in the observation volume by diffusion, as described above. At later times, fluorescence recovery is a result of detachment of dark markers followed by rebinding of intact markers. For the rebinding step, we can assume that $[F_{\mathrm{bright}}] \gg [F_{\mathrm{dark}}]$. This means that, after detachment of a dark marker, rebinding of a bright marker is much more likely, which can be expressed by the boundary condition $[X_{\mathrm{dark}}(\infty)] = 0$. Therefore, the differential equation for the dark molecule-marker complex reduces to

$$\frac{\mathrm{d}[X_{\mathrm{dark}}(t)]}{\mathrm{d}t} = -[X_{\mathrm{dark}}(t)]k_{\mathrm{off}}. \tag{3.20}$$

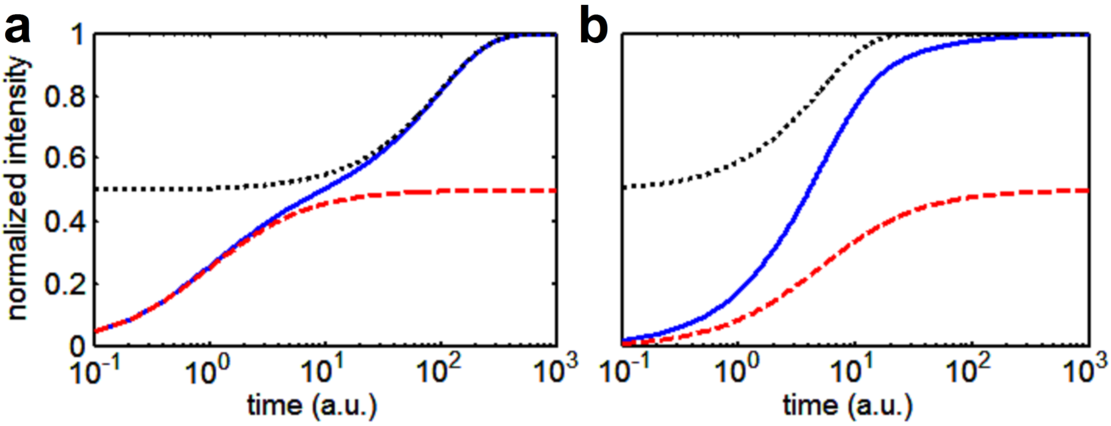

Figure 3.3.: FRAP due to diffusion and binding. (**a**) Fast diffusion (dashed line) followed by slow binding (dotted line) results in a two-step recovery curve (solid line) allowing for identification of each process. (**b**) Diffusion (dashed line) and binding (dotted line) occurring on the same time scale cannot be discriminated any more in the total recovery curve (solid line).

By applying the initial condition, $\frac{\mathrm{d}[X_{\mathrm{dark}}(0)]}{\mathrm{d}t} = \Delta[X_{\mathrm{dark}}(0)]$,

$$\frac{\mathrm{d}[X_{\mathrm{dark}}(t)]}{\mathrm{d}t} = \Delta[X_{\mathrm{dark}}(0)]e^{-k_{\mathrm{off}}t}. \tag{3.21}$$

Also, FRAP measurements are usually performed at high marker concentrations to obtain a good signal-to-noise ratio. Thus, we adjust the conditions such that there are far less free molecules than molecule-marker complexes $[S] \ll [X]$. Consequently, the temporal evolution of the bright molecule-marker complex concentration becomes

$$\frac{\mathrm{d}[X_{\mathrm{bright}}(t)]}{\mathrm{d}t} = [X(\infty)] - [X_{\mathrm{dark}}(t)] = [X(\infty)] - \Delta[X_{\mathrm{dark}}(0)]e^{-k_{\mathrm{off}}t}. \tag{3.22}$$

Therefore, the total fluorescence recovery is given by fast, free diffusion followed by rebinding and can be expressed as

$$F_{K,R}(t) = \frac{F_K(0) + \frac{t}{\beta\tau_D}F_K(\infty)}{1 + \frac{t}{\beta\tau_D}} + F_R(\infty) - (F_R(\infty) - F_R(0))e^{-\frac{t}{\tau_{\mathrm{off}}}}, \tag{3.23}$$

with the fluorescence from freely diffusing markers, F_K, and, the fluorescence from bound markers, F_R.

3.2.3. FRAP for Studying Dynamics at Membranes

As an example, fluorescence recovery was probed in a fluorescently labeled lipid bilayer as a model of the cell membrane. The lipids forming the layer can freely diffuse in the lateral direction, whereas their positions are fixed in the axial direction. The data of a

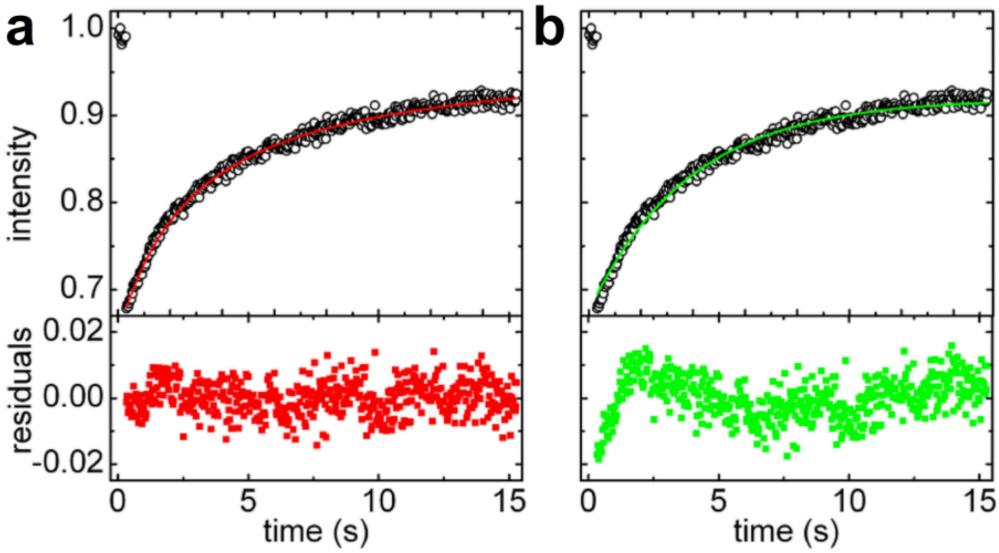

Figure 3.4.: FRAP at lipid bilayer fitted by a (**a**) free diffusion and (**b**) binding model.

representative FRAP experiment are displayed in **Fig. 3.4**. In **Fig. 3.4a**, the data set has been fitted with equation 3.10 modeling free diffusion,

$$F_K(t) = \frac{F_K(0) + \frac{4Dt}{\omega^2}F_K(\infty)}{1 + \frac{4Dt}{\omega^2}}.$$

In **Fig. 3.4b**, the same data set has been fitted with an equation representing a simple binding model (equation 3.23 without diffusion term),

$$F_R(t) = F_R(\infty) - (F_R(\infty) - F_R(0))e^{-\frac{t}{\tau_{\text{off}}}},$$

As expected, the residuals show that the fluorescence recovery in a lipid bilayer is better represented by the free diffusion model.

Materials and Methods

Lipid bilayer preparation: Planar lipid bilayers were prepared by dissolving 1,2-dioleoyl-sn-glycero-phosphocholine (DOPC) (Avanti Polar Lipids, Alabaster, USA) and cholesterol (Sigma-Aldrich, St. Louis, USA) in chloroform at a ratio of 4:1. Atto647N-dipalmitoylphosphatidylethanolamine (DPPE) (Atto-Tec, Siegen, Germany) was added in the amount of 0.01 mol% to the stock solution (5 mg/ml). 10 µl of the lipid solution was evaporated for 1 h under vacuum and afterwards rehydrated with 10 mM 4-(2-hydroxyethyl)-1-piperazineethanesulfonic acid (HEPES) buffer (pH 7.4) containing 150 mM NaCl. The vortexed suspension was sonicated at 60°C for 1 h, and 100 µl were placed in a chamber slide to form the bilayer. Lipid bilayers were prepared by René Dörlich.

FRAP experiment: FRAP measurements were performed on a spinning disk confocal microscope (Andor Revolution XD, BFI Optilas, Gröbenzell, Germany). A circular spot (diameter 3.5 µm) within the lipid bilayer was bleached using 640-nm light. The fluorescence recovery was measured with a temporal resolution of 86 ms. Spinning disk microscopy was performed by René Dörlich.

3.3. Fluctuation Spectroscopy

3.3.1. Fluorescence Correlation Spectroscopy

Often, fluorescent markers are used to label the molecules of interest, e.g., proteins. Dynamic processes of interest include protein folding, diffusion and binding to other proteins. These properties can be quantified by fluorescence correlation spectroscopy (FCS). In FCS, the fluorescence intensity of a small ensemble of labeled molecules is continuously monitored over time. As an example, free diffusion of proteins in an aqueous solution shall be measured. Therefore, a confocal fluorescence microscopy setup is most suitable, where the spatial confinement is given by the NA of the objective lens and the size of the pinhole (see subsection 2.4.2), resulting in an observation volume of $\sim 1\,\text{fl}$. This volume is placed into a highly dilute (nanomolar) solution of the molecules under study (**Fig. 3.5**). Hence, on average, only a few particles reside within this volume. Due to Brownian motion their number and, thus, the fluorescence intensity originating from the confocal volume fluctuates. These fluctuations are evaluated by autocorrelation analysis. Using a suitable model, the average particle number, $< N >$, as well as the average residence time, τ_D, inside the observation volume can be obtained from the autocorrelation, $G(\tau)$. In this way, the diffusion coefficent, D, and the hydrodynamic radius, R_H, can be computed. In the following, it is shown how such a diffusion process is analyzed by using FCS.

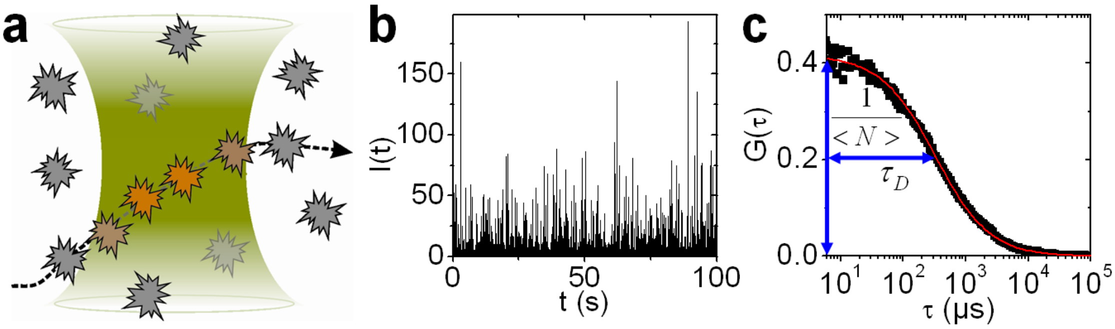

Figure 3.5.: FCS Principle. (**a**) In a solution, fluorescent particles move through the confocal volume due to Brownian motion. (**b**) Particles moving in and out of the observation volume cause fluctuations in the intensity time trace. (**c**) Autocorrelation analysis of the fluorescence time trace (squares), fitted with an equation modeling 3D diffusion (red line), yields the average number of particles, $< N >$, and average transit time, τ_D.

3.3.2. The Autocorrelation Function

Let us look at a small ensemble of particles rendered fluorescent by attachment of a dye to monitor underlying processes such as diffusion. Thus, we can define the autocorrelation function,

$$h(\tau) =< (F(t) \cdot F(t+\tau) >_t, \tag{3.24}$$

as the average product of the fluorescence intensity $F(t)$ at time t and the fluorescence intensity $F(t+\tau)$ at a later time $t+\tau$. Normalized by the square of the average signal, $< F(t) >_t^2$, we obtain

$$H(\tau) = \frac{< (F(t) \cdot F(t+\tau) >_t}{< F(t) >_t^2}. \tag{3.25}$$

Often, instead of the absolute amplitude of the signal, $F(t)$, the deviation from the average amplitude, $\delta F(t) = F(t) - < F(t) >_t$, is used, which defines the fluctuation autocorrelation function,

$$\begin{aligned} G(\tau) &= \frac{< \delta F(t) \cdot \delta F(t+\tau) >_t}{< F(t) >_t^2} && (3.26) \\ &= \frac{< F(t) \cdot F(t+\tau) >_t}{< F(t) >_t^2} - 1. && (3.27) \end{aligned}$$

The fluorescence is proportional to the number of molecules, $N(t)$, inside the observation volume, $F(t) \propto N(t)$. Also, since we are looking at single, independent particles, Poisson statistics applies,

$$\frac{< \delta F(t)^2 >_t}{< F(t) >_t^2} = \frac{< \delta N(t)^2 >_t}{< N(t) >_t^2} = \frac{1}{< N(t) >_t}. \tag{3.28}$$

Therefore, the fluctuation autocorrelation function yields the average number of particles, $< N(t) >_t$, inside the observation volume as τ approaches zero,

$$G(0) = \frac{< \delta F(t) \delta F(t) >_t}{< F(t) >_t^2} = \frac{1}{< N(t) >_t}. \tag{3.29}$$

3.3.3. Analyzing Fluctuations Generated by Diffusion

The following deduction follows a textbook chapter by Schwille et al. [108]. FCS theory and application was first published by Magde et al. in 1974 [109, 110]. Let us consider a solution of fluorescent particles which can freely diffuse in all three dimensions. The confocal volume is placed within this solution and the fluorescence monitored with a single photon counting device. Particles passing that volume are excited and the resulting fluorescence intensity, $F(t)$, is given by

$$F(t) = \kappa \sigma q \int W(\vec{r}) C(\vec{r}, t) \mathrm{d}V, \tag{3.30}$$

with the quantum yield, κ, and the absorption cross section, σ, of the fluorescent markers, the detection efficiency, q, the shape of the observation volume, $W(\vec{r})$, and, finally, the particle concentration, $C(\vec{r},t)$, containing the information about the diffusion process. In confocal microscopy, the shape of the observation volume is usually approximated by a three-dimensional Gaussian,

$$W(\vec{r}) = I_0 \exp\left(-2\frac{x^2+y^2}{r_0^2}\right)\exp\left(-2\frac{z^2}{z_0^2}\right), \tag{3.31}$$

where r_0 and z_0 represent the $1/e^2$ radii of the Gaussian volume in lateral and axial direction, respectively. Free, three-dimensional particle diffusion can be described by equation 3.3,

$$\frac{\partial}{\partial t}C(\vec{r},t) = D\nabla^2 C(\vec{r},t).$$

The solution of this equation is given by

$$C(\vec{r},t) = \frac{1}{(4\pi Dt)^{3/2}}\exp\left(-\frac{|\vec{r}|^2}{4Dt}\right). \tag{3.32}$$

The deviation from the average particle concentration, $\delta C(\vec{r},t)$, within the effective volume, V_{eff}, of the focal spot leads to deviations from the average fluorescence signal,

$$\delta F(t) = \eta \int W(\vec{r})\delta C(\vec{r},t)\mathrm{d}V, \tag{3.33}$$

with $\eta = \kappa\sigma q$, assuming that marker quantum yield, absorption cross section and detection efficiency are constant parameters. Thus, the autocorrelation,

$$G(\tau) = \frac{< \delta F(t)\delta F(t+\tau) >_t}{< F(t) >_t^2}, \tag{3.34}$$

of the fluorescence fluctuation can be calculated by insertion of equation 3.30 and 3.33 into equation 3.34, yielding

$$G(\tau) = \frac{\iint W(\vec{r})W(\vec{r'}) < \delta C(\vec{r},t)\delta C(\vec{r'},t+\tau) >_t \mathrm{d}V\mathrm{d}V'}{\left(\int W(\vec{r}) < C(\vec{r},t) >_t \mathrm{d}V\right)^2}. \tag{3.35}$$

Assuming a constant diffusion coefficient, the autocorrelation does not depend on the time of observation, so we choose, $t = 0$. With equation 3.32 and $< C(\vec{r},t) >_t = < C >$, we obtain for the number density autocorrelation term,

$$< \delta C(\vec{r},0)\delta C(\vec{r'},\tau) > = \frac{< C >}{(4\pi D\tau)^{3/2}}\exp\left(-\frac{|\vec{r}-\vec{r'}|^2}{4D\tau}\right). \tag{3.36}$$

For the autocorrelation of the fluorescence fluctuation, we obtain

$$G(\tau) = \frac{\frac{<C>}{(4\pi D\tau)^{3/2}}\iint W(\vec{r})W(\vec{r'})\exp\left(-\frac{|\vec{r}-\vec{r'}|^2}{4D\tau}\right)\mathrm{d}V\mathrm{d}V'}{\left(< C > \int W(\vec{r})\mathrm{d}V\right)^2}. \tag{3.37}$$

With the size of the effective observation volume, defined as

$$V_{\text{eff}} = \frac{\left(\int W(\vec{r})\text{d}V\right)^2}{\int W^2(\vec{r})\text{d}V} = \pi^{3/2} \cdot r_0^2 \cdot z_0, \tag{3.38}$$

containing the average number of particles, $< N >= V_{\text{eff}} \cdot < C >$, the fluctuation autocorrelation function of freely diffusing molecules results,

$$G_{3D}(\tau) = \frac{1}{< N >} \left[1 + \frac{4D\tau}{r_0^2}\right]^{-1} \left[1 + \frac{4D\tau}{r_0^2}\left(\frac{r_0}{z_0}\right)^2\right]^{-1/2}. \tag{3.39}$$

The geometric parameters r_0 and z_0 are usually measured by using a reference sample. Experimental data obtained by correlating the fluorescence time trace from a solution of FePt particles labeled with DY 636 are shown in **Fig. 3.5c**. Fluorescence was excited at a wavelength of 640 nm and an average intensity of 25 µW using a 80 MHz pulsed laser diode. Two important parameters can be extracted from the data. First, the average number of fluorescent particles observable in the confocal volume, $< N >$, corresponds to the inverse of $G(\tau)$ as τ approaches zero (equation 3.29). Second, the underlying dynamics are revealed from the decay of the autocorrelation amplitude towards longer correlation times. For free diffusion, the average transit time of the particles through the confocal volume is related to the diffusion coefficient by

$$\tau_D = \frac{r_0^2}{4D}. \tag{3.40}$$

The line in **Fig. 3.5c** represents a fit of equation 3.39 to the experimental data yielding $< N >= 2.4$ and $\tau_D = 330\,\mu\text{s}$ for the FePt particles in phosphate buffered saline (PBS). For two-dimensional diffusion, e.g., particles within a lipid bilayer, a similar result is obtained for the autocorrelation function. If the layer extends in the same plane as the focal plane, the extension of the observation area is isotropic for both dimensions. Thus, the correlation function reduces to

$$G_{2D}(\tau) = \frac{1}{< N >} \left[1 + \frac{4D\tau}{r_0^2}\right]^{-1}. \tag{3.41}$$

With the geometric parameters r_0 and z_0, the average particle concentration, $< C >$, can be determined from the amplitude of the autocorrelation curve, $G(0)$,

$$< C >= \frac{1}{V_{\text{eff}} \cdot G(0)}. \tag{3.42}$$

Using the diffusion coefficient, other properties of the particles such as their hydrodynamic radius can be calculated,

$$R_H = \frac{k_B T}{6\pi\eta D}, \tag{3.43}$$

with the viscosity of the particle solution, η, at temperature T. This relation is known as the Stokes-Einstein relation, which arises from the Einstein-Smoluchowski relation [111, 112] assuming diffusion of spherical particles through a liquid of low Reynolds number. Thus, e.g., tiny changes in the hydrodynamic radius of nanoparticles by protein adsorption to the particle surface have been measured by FCS [113].

3.3.4. Brightness Fluctuations in Autocorrelation Analysis

In the previous subsection, fluctuations in fluorescence intensity were assumed to only result from particle motility. However, depending on the marker, there are photophysical and other processes that influence marker fluorescence and, thus, cause additional signal fluctuations. Consequently, these effects have to be considered in the analysis of the resulting autocorrelation function. In the following, the population of a triplet state and a reaction term representing conformational changes of the particles will be discussed.

Triplet State

In the excited state, a spin flip can occur due to interaction with surrounding molecules. Thus, the marker is transiently trapped in a dark, non-fluorescent state. Usually, the relaxation time of the triplet state is much shorter than the diffusion transit time through the observation volume [114]. Thus, triplet state population results in a correlation at short lag times in addition to the correlation at longer lag times due to particle translation, and the total autocorrelation function decays in two temporally distinct steps,

$$G_{\text{total}}(\tau) = G_{\text{trip}}(\tau) \cdot G_{\text{diff}}(\tau), \tag{3.44}$$

where $G_{\text{diff}}(\tau)$ is the diffusional and $G_{\text{trip}}(\tau)$ the triplet term. Triplet blinking can be described by a reversible transition between a bright, fluorescent state, F, and a dark, non-fluorescent state, T,

$$F \underset{k_F}{\overset{k_T}{\rightleftharpoons}} T, \tag{3.45}$$

characterized by the corresponding on- and off-rate coefficients, k_F and k_T. The resulting normalized autocorrelation function of the system can be described by a simple exponential decay [115],

$$G_{\text{trip}}(\tau) = 1 + \frac{T}{1-T} \cdot \exp\left(-\frac{\tau}{\tau_T}\right), \tag{3.46}$$

with the average fraction of molecules in the triplet state, $T = k_T/(k_T + k_F)$, and the apparent relaxation time, $\tau_T = 1/(k_T + k_F)$.

Kinetic Term

Conformational changes of the molecule-marker system or changes of the surrounding environment can affect the quantum yield of the fluorophore. These transient states of lower photon emission also affect the trend of the autocorrelation function. Quick changes in brightness can be modeled the same way as triplet blinking, resulting in a modification of the total autocorrelation function,

$$G_{\text{total}}(\tau) = G_{\text{kin}}(\tau) \cdot G_{\text{diff}}(\tau), \tag{3.47}$$

with the normalized kinetic term,

$$G_{\mathrm{kin}}(\tau) = 1 + \frac{K}{1-K} \cdot \exp\left(-\frac{\tau}{\tau_K}\right), \tag{3.48}$$

with the apparent relaxation time, $\tau_K = 1/(k_K + k_F)$. Yet, if the low brightness state is not entirely dark, two different quantum yields, η_K and η_F, have to be included in the weighted amplitude [108],

$$K = \frac{k_K k_F (\eta_K - \eta_F)^2}{(k_K + k_F)(k_K \eta_K^2 + k_F \eta_F^2)}. \tag{3.49}$$

Often, this fraction is small ($K \ll 1$) and, thus, the kinetic term can be simplified,

$$G_{\mathrm{kin}}(\tau) = 1 + K \cdot \exp\left(-\frac{\tau}{\tau_K}\right). \tag{3.50}$$

3.3.5. Raster Image Correlation Spectroscopy

In a static FCS experiment, the position of the confocal volume is constant with respect to the sample. Thus, dynamics are measured at a single spot only. Another way of performing correlation spectroscopy is RICS [26]. In this approach, a wide area is imaged repeatedly by moving the observation volume across the sample (**Fig. 3.6**). Thus, each image contains a time structure determined by the pixel and line dwell times. Subsequently, by correlating the images pixel by pixel and line by line, a two-dimensional correlation function can be obtained. The pixel-to-pixel correlation covers the short lag times (µs), whereas the longer lag times (ms) are resolved by the line-to-line correlation. Correlations of even longer lag times (s) can be analyzed by recording multiple images

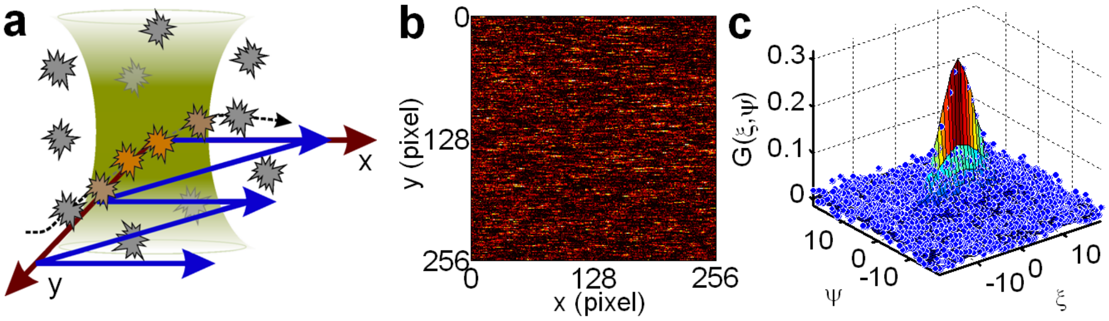

Figure 3.6.: RICS Principle. (**a**) Fluorescent particles move through the confocal volume due to Brownian motion, while the volume is scanned across the sample (indicated by arrows). (**b**) Confocal laser scanning image of a solution of FePt particles labeled with DY 636. (**c**) Two-dimensional autocorrelation, $G(\xi, \psi)$, resulting from pixel-to-pixel, ξ, and line-to-line, ψ, correlation (dots) fitted with an equation modeling 3D diffusion (surface).

of the same region, followed by a frame-to-frame correlation. However, this is often not necessary. Still, multiple frames are usually acquired in a RICS measurement, yielding more data for an improved signal-to-noise ratio of the resulting correlation. Furthermore, an immobile fraction can be substracted. In this approach the average pixel intensity is substracted from each frame, followed by addition of the global average intensity. Thereby, bright, immobile features can be excluded from correlation analysis. Another advantage of RICS is the multiplexing capability when applied to heterogeneous samples. Here, different regions of interest can be analyzed in a single set of images. Also, in static FCS, bleaching can be a problem. If particle diffusion is slow, the fluorescent markers will have bleached before they could have passed through the observation volume, resulting in a distortion of the correlation function. By scanning across the sample, the effective residence time of the particles within the confocal volume is reduced and, thus, a prolonged light exposure that causes bleaching of the fluorophores is prevented.

3.3.6. Fluctuations in Laser Scanning Microscopy Images

Let us consider free, three-dimensional diffusion of particles within a homogenous, isotropic medium. Hence, the particle concentration, $C(\vec{r},t)$, is proportional to the probability of finding molecules, driven by Brownian motion, at position $\vec{r}$ and at time t starting at the origin, $\vec{r}=0$ and $t=0$ (equation 3.32). This equation can be split into a temporal term and a spatial, Gaussian term [116]. In static FCS, the concentration is sampled at a constant position $\vec{r}=\vec{r_0}$ (see subsection 3.3.3). For an image acquired with a laser scanning microscope, $F(x,y)$, the time structure of the image is determined by the respective pixel size, δ_r, and pixel and line dwell times, τ_p and τ_l. By correlating each pixel with the following one, the autocorrelation at lag time $\tau=\tau_p$ can be computed (**Fig. 3.7**). By increasing the respective shift between two pixels, ξ, the autocorrelation at longer times, $\tau=\xi\tau_p$, can be computed. The same procedure can be applied to pixels within different lines of the image, with the respective line shift, ψ, resulting in lag times $\tau=\psi\tau_l$. Of course, pixel and line shift can be combined; in this way, a two-dimensional autocorrelation function is obtained. Replacing t with x,y and τ with ξ,ψ in equation 3.34 yields

$$G_{\text{RICS}}(\xi,\psi)=\frac{<\delta F(x,y)\delta F(x+\xi,y+\psi)>_{x,y}}{<F(x,y)>^2_{x,y}}. \tag{3.51}$$

When imaging with a laser scanning microscope, the sample is probed at different spatial locations, $\vec{r}=\vec{r}(t)$. The scanning motion appears as an active particle transport. Application of FCS to uniform particle translation combined with free diffusion through a Gaussian observation volume has first been discussed by Magde et al. in 1978 [117]. The particle concentration is described by the transport-diffusion equation,

$$\frac{\partial}{\partial t}C(\vec{r},t)=D\cdot\nabla^2 C(\vec{r},t)-\vec{v}\cdot\nabla C(\vec{r},t), \tag{3.52}$$

with the scan velocity, $\vec{v}$. The solution of this equation is given by

$$C(\vec{r},t)=\frac{1}{(4\pi Dt)^{3/2}}\exp\left(-\frac{|\vec{r}-\vec{v}t|^2}{4Dt}\right). \tag{3.53}$$

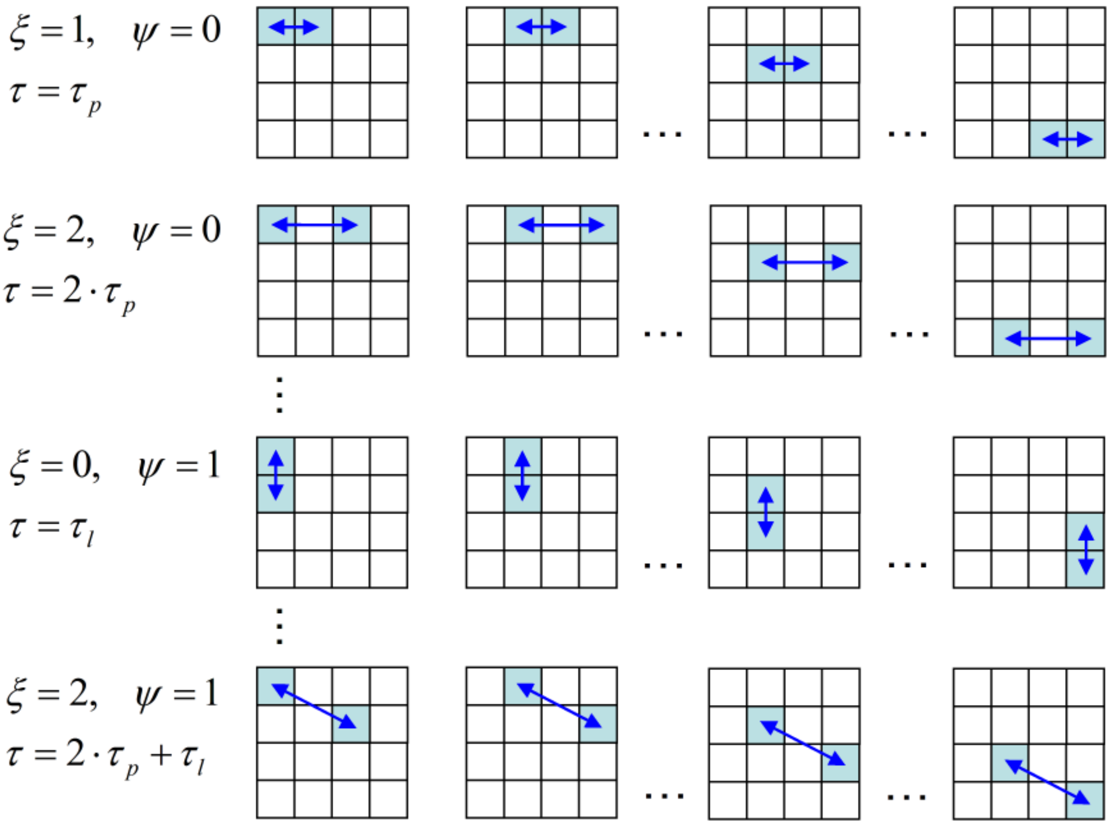
$\xi = 1, \quad \psi = 0$
$\tau = \tau_p$
$\xi = 2, \quad \psi = 0$
$\tau = 2 \cdot \tau_p$
$\xi = 0, \quad \psi = 1$
$\tau = \tau_l$
$\xi = 2, \quad \psi = 1$
$\tau = 2 \cdot \tau_p + \tau_l$
...

Figure 3.7.: Raster image correlation. All pixels within a raster-scanned image are correlated (left to right) using different pixel shifts, ξ, (first and second row), line shifts, ψ, (third row) and both (last row). Thus, a two-dimensional autocorrelation function is obtained.

If the sample is scanned in the lateral direction only, $\vec{v} = (v_x, v_y)$, the autocorrelation of the fluorescence time trace is

$$G_{\text{diff,scan}}(\tau) = G(\tau) \cdot S(\tau), \tag{3.54}$$

with the diffusional part, $G(\tau)$, given by equation 3.39 and the term for the movement of the observation volume,

$$S(\tau) = \exp\left[-\left(\frac{\tau}{\tau_F}\right)^2 \frac{1}{1 + 4D\tau/r_0^2}\right]. \tag{3.55}$$

The time for the laser focus of radius r_0 to move across a particle, $\tau_F = 2r_0/\vec{v}$, is determined by the scan velocity, $\vec{v} = (\delta_r/\tau_p, \delta_r/\tau_l)$. Consequently, with $\tau = \xi\tau_p + \psi\tau_l$, the raster image correlation function for particles freely diffusing in a three-dimensional volume becomes

$$G_{\text{RICS}}(\xi, \psi) = G(\xi, \psi) \cdot S(\xi, \psi), \tag{3.56}$$

with the diffusional part,

$$G(\xi, \psi) = \frac{1}{< N >}\left[1 + \frac{(\tau_p\xi + \tau_l\psi)4D}{r_0^2}\right]^{-1}\left[1 + \frac{(\tau_p\xi + \tau_l\psi)4D}{r_0^2}\left(\frac{r_0}{z_0}\right)^2\right]^{-1/2}, \tag{3.57}$$

and the scanning part of the correlation [26],

$$S(\xi, \psi) = \exp\left[-\frac{\left(\frac{2\xi\delta_r}{r_0}\right)^2 + \left(\frac{2\psi\delta_r}{r_0}\right)^2}{2\left(1 + \frac{(\tau_p\xi + \tau_l\psi)4D}{r_0^2}\right)}\right]. \tag{3.58}$$

Due to the raster scan pattern, the correlation appears on two different time scales. The pixel-to-pixel correlation covers short lag times, usually in the microsecond range, whereas longer lag times are resolved by the line-to-line correlation, usually in the millisecond range. This means that the scanning parameters of the measurement have to be adjusted to fit with the expected diffusion times, ensuring that $\tau_p < \tau_D$. If the approximate diffusion constant is not known, test measurements using different pixel dwell times are required. Experimental data obtained by correlating images acquired in a solution of FePt particles labeled with DY 636 are shown in **Fig. 3.6c**. Fluorescence was excited at a wavelength of 640 nm and an average intensity of 25 µW using a 80 MHz pulsed laser diode. Images were raster-scanned with a pixel dwell time of 10 µs and a pixel size of 40 nm. The surface in **Fig. 3.6c** represents a fit of equation 3.56 to the experimental data, yielding $< N >= 2.1$ and $\tau_D = 380\,\mu s$ for the FePt particles in PBS. These values are in good agreement with the ones obtained by static FCS ($< N >= 2.3$ and $\tau_D = 330\,\mu s$, see subsection 3.3.3).

3.3.7. Limitations of Fluctuation Spectroscopy

Despite its finesse, there are several limitations in the application of fluctuation spectroscopy. First of all, measurement of the diffusion coefficient by means of fluorescence correlation spectroscopy requires precise knowledge of the observation volume geometry. However, the effective confocal volume depends on the excitation power, spectral properties of the marker, refractive index of the sample and pinhole size, to name but a few parameters. Thus, a reference measurement using a similar sample with known diffusion coefficient is required. This problem is adressed by two-focus FCS [118]. In this method, fluorescence is recorded from two overlapping foci with a fixed mutual displacement. By controlling this distance, an internal reference is introduced to the measurement. Another issue in FCS are aggregates. Complexes of several particles sticking together will produce an intensity burst when moving through the confocal volume, disturbing the correlation analysis. As long as there are only a few aggregates present in the sample, this obstacle can be overcome by software-based correlation. Due to the vast amount of storage available on present-day computers, the fluorescence time trace can be saved at the full temporal resolution. Thus, large intensity peaks caused by aggregates can be identified in the time trace and excluded from subsequent correlation analysis. When using correlation spectroscopy in living cells and tissues, further problems such as bright immobile features and bleaching can restrict the application. In that case, scanning methods such as RICS are preferred over static FCS. By moving the focus, immobile features can be identified and removed from the data. Furthermore, bleaching of slowly moving particles is prevented by the scanning motion. For heterogeneous samples such as cells, the multiplexing capability of RICS is a great advantage, too. In a single set of images, different regions of interest can be analyzed. However, this subdivision of image data is compromised by the limited spatial resolution of optical far-field microscopy because regions of interest cannot be as small as desired. Also, due to the extension of the confocal volume, details such as molecules being transiently trapped on spatial scales smaller than the optical resolution cannot be discerned from freely moving molecules with standard FCS and RICS. Finally, with a diffraction-limited observation volume of $\sim 1\,\mathrm{fl}$, the application of correlation spectroscopy is restricted to nanomolar fluorophore concentrations. However, these limitations can be adressed by application of STED, as described in chapter 5.

4. Implementation of Advanced Fluorescence Microscopy

4.1. Stimulated Emission Depletion Microscopy

4.1.1. STED Microscopy with a Broadband Source

In this work, two different, pulsed STED configurations were implemented. The first configuration (**Fig. 4.1**, schematic and **Fig. 4.2**, photograph) is based on a supercontinuum source (SC450-HE, Fianium, Southampton, UK) with a usable output spectrum of $500 - 800\,\mathrm{nm}$. The pulse repetition rate is $2\,\mathrm{MHz}$ with a pulse duration of $\sim 90\,\mathrm{ps}$. Because of the broad output spectrum, this laser can supply both, the excitation and depletion light. The output of linear polarization of random orientation is first split by a polarizing beamsplitter cube (PBS) yielding two beams of linearly polarized light perpendicular to each other. The transmitted part is filtered by an acousto optic tunable filter (AOTF) (AOTFnC-400.650, AA Opto Electronic, Orsay Cedex, France) with a bandwidth of 2 nm and spatially cleaned by 2 m of polarization maintaining single-mode fiber (SMF) (PMC-530, Schäfter und Kirchhoff, Hamburg, Germany) before used for excitation. The reflected light is filtered by a custom built, prism-based monochromator. After spectral expansion by a prism, the beam is collimated by a lens, followed by a variable slit to select a suitable depletion band of 20 nm bandwidth. An inverse arrangement of an identical prism and lens rejoin the spectral components before the light is coupled into 2 m of polarization maintaining SMF (PMC-630, Schäfter und Kirchhoff). To ensure simultaneous arrival of the excitation and depletion pulses at the sample, the delay between excitation and STED pulses can be adjusted by moving the excitation coupler. For phase modulation of the depletion beam, either a helical phase plate (PP) (VPP1a, RPC Photonics) or a custom made circular PP [78] can be used (see subsection 2.5.4). The excitation and depletion beams are spatially overlayed at a 730 nm or 640 nm shortpass (SP) dichroic mirror (z730sprdc/z640sprdc, Chroma, Bellows Falls, USA), depending on the spectral properties of the employed fluorophores. A quarter-wave plate phase-shifts the initially linearly polarized beams to obtain circularly polarized light. Circular polarization is required for the correct formation of the depletion pattern and avoids photoselection of the dye molecules by the orientation of their excitation dipoles. Subsequently, the light passes a galvanometric scanning system (Yanus IV, Till Photonics, Gräfelfing, Germany). The scanning plane is relayed via a telescope, composed of a scan lens and a tube lens, to the oil immersion objective (HCX PL APO CS 100x/1.46, Leica, Wetzlar, Germany) which focuses the combined beams into the sample. The distance of the objective lens with respect to the sample is ad-

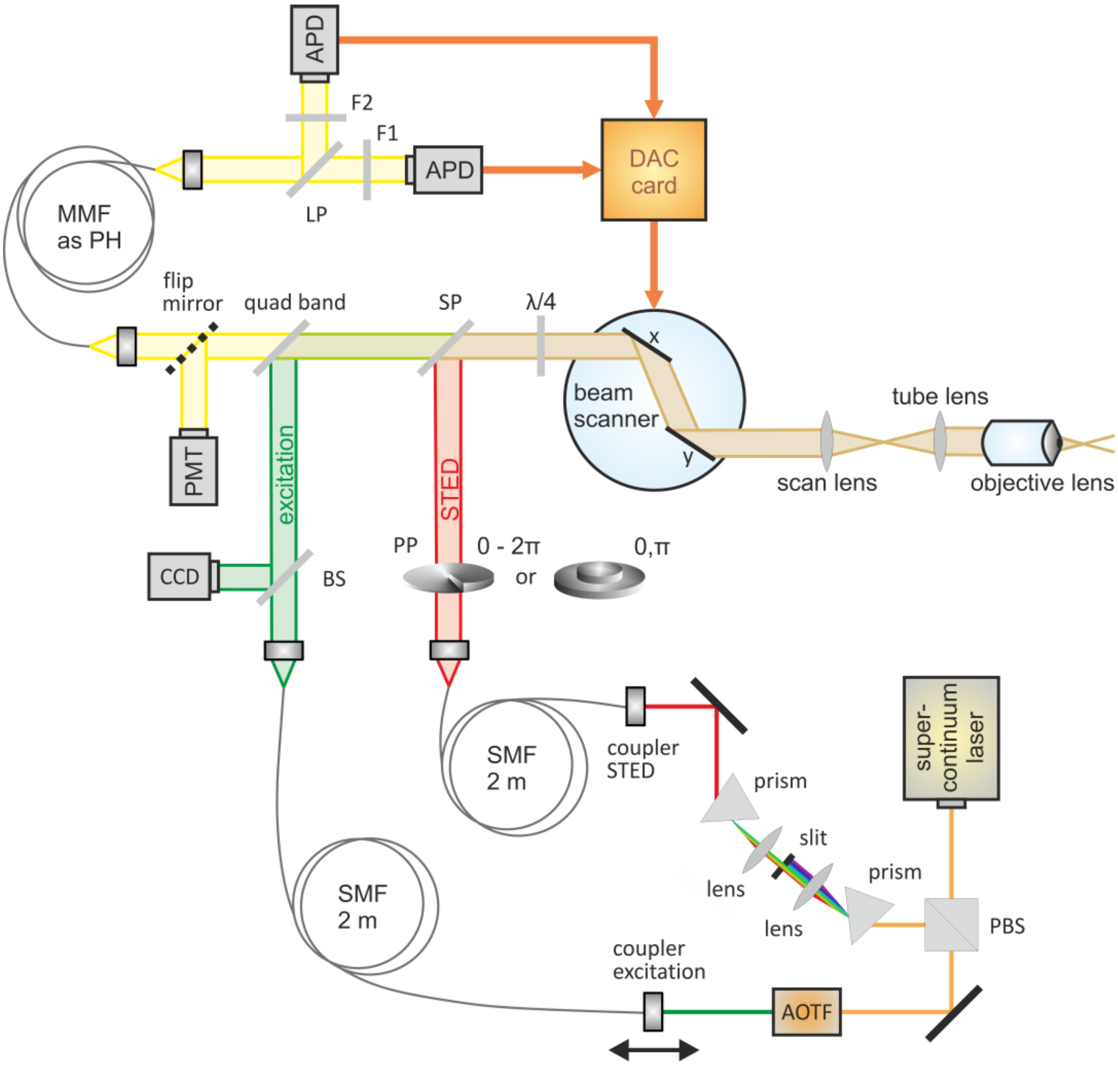
APD
F2
F1
APD
DAC card
MMF as PH
LP
flip mirror
quad band
SP
λ/4
x
beam scanner
y
tube lens
scan lens
objective lens
PMT
excitation
STED
CCD
BS
PP
0 - 2π
or
0,π
SMF 2 m
coupler STED
prism
super-continuum laser
slit
lens
prism
lens
PBS
SMF 2 m
coupler excitation
AOTF

Figure 4.1.: STED microscopy setup with a broadband source as described in the text.

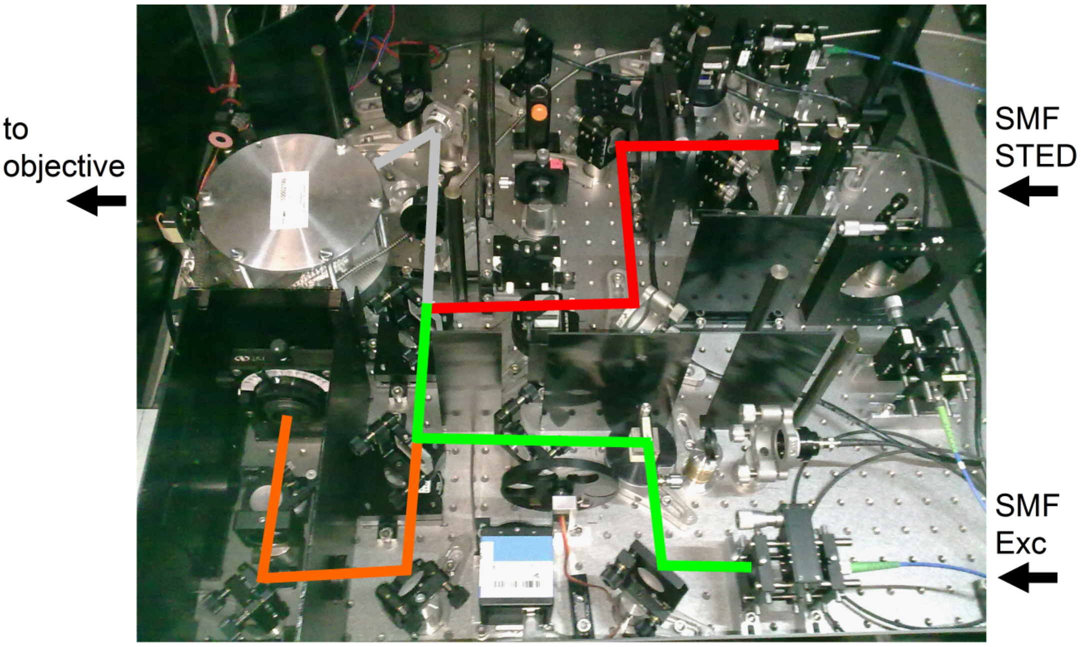

Figure 4.2.: Photograph of the main part of the STED microscopy setup based on a broadband source. Indicated are the paths of excitation (green), STED (red), combined beams (gray) and fluoresence light (orange).

justed by a translation stage (M-122, Physik Instrumente, Karlsruhe, Germany). The reflection of the excitation beam at the coverslips of the samples, extracted by a beam-splitter (BS), is used to monitor the z-position of the focal spot with a CCD camera (DMK 21, Imaging Source, Bremen, Germany). Fluorescence light is separated by a quad band dichroic mirror (zt405/488/561/640rpc, Chroma) and focused onto a multi mode fiber (MMF) (M31L02, Thorlabs, München, Germany) which serves as a confocal pinhole (PH) such that the core diameter corresponds to one Airy unit. After passing the MMF, the fluorescence is split by a longpass (LP) dichroic mirror and two bandpass filters, F1 and F2, for the transmitted and reflected light, respectively, chosen according to the emission spectra of the employed fluorophores. Single photons are counted in two detection channels by avalanche photodiodes (APDs) (τ-SPAD-50, PicoQuant, Berlin, Germany) and registered by a time-correlated single photon counting (TCSPC) system (Simple-Tau 152 TCSPC, Becker & Hickl, Berlin, Germany). Alternatively, a flip mirror can be used to reroute the detection to a photomultiplier (PMT) (PMC-100, Becker & Hickl). This configuration is used for the alignment of the setup, where apodisation of the detected light by the pinhole is undesirable. For imaging, the laser focus is laterally scanned across the sample by the galvanometric scanning system and axially by moving the objective lens with a piezo stage (P-720, Physik Instrumente). Scan signals are generated by a digital-to-analog converter (DAC) card (PCI-6259, National Instruments, München, Germany) controlled by the software Imspector (Max-Planck-Innovation, München, Germany).

One advantage of using a broadband source for STED microscopy is the flexibility in the choice of excitation and depletion wavelengths. Also, with a single source, the time delay between excitation and depletion pulses is determined by the difference of the optical path lengths, only. No additional, sensitive electronics that might cause timing jitter are required. At a repetition rate of 2 MHz, the average light exposure is low compared to high repetition rate or CW systems. Therefore, phototoxic effects to biological samples can be kept to a minimum. However, at a low repetition rate, the number of excitation/emission cycles within a given time interval is also low and, thus, image acquisition speed is limited. Therefore, a second pulsed STED configuration with a higher repetition rate was implemented, as presented in the following subsection.

4.1.2. STED Microscopy with a Ti:Sa Laser

At higher pulse repetition rates, more excitation/emission cycles can be accommodated within the same time interval, resulting in a higher average fluorescence signal. Thus, in raster-scanning, the signal accumulation time for a single image pixel can be reduced, allowing for faster imaging. Therefore, in a second configuration, a STED microscopy setup with laser sources of 80 MHz repetition rates was constructed (**Fig. 4.3**, schematic and **Fig. 4.4**, photograph). Excitation light is generated by a 640-nm pulsed diode laser (LDH-P-C-640B, PicoQuant) featuring pulses of $\sim$ 100 ps length, spectrally cleaned by a 640/14 nm bandpass filter (HC 640/14, Semrock, Rochester, USA) and spatially cleaned by 2 m of polarization maintaining SMF (PMC-630, Schäfter und Kirchhoff). Depletion light is provided by a mode-locked Ti:Sa laser (Mai Tai HP, Spectra-Physics, Darmstadt, Germany) of variable wavelength ($690 - 1040$ nm). A half-wave plate is used to change the orientation of the linearly polarized light. A Glan-laser prism only allows p-polarized light to pass. Thus, the intensity can be adjusted by rotation of the half-wave plate. The pulses of the Ti:Sa laser have a length of $\sim$ 100 fs and are subsequently stretched by 60 cm of SF6 glass followed by 100 m of polarization maintaining SMF (PMJ-A3HPC, OZ Optics, Ottawa, Canada) to $\sim$ 300 ps [119]. On the one hand, this measure ensures a complete coverage of the duration of the exciation pulses suppressing pre-STED fluorescence emission. On the other hand, longer pulse lengths avoid multi-photon processes leading to excitation of the fluorophores by depletion photons. The laser pulses of the Ti:Sa laser are monitored by an internal photodiode and the output is used to trigger the diode laser after signal amplification by custom-built electronics. To ensure simultaneous arrival of the excitation and depletion pulses at the sample, the time delay can be adjusted by choosing the proper cable length and trigger threshold of the diode laser. After passing the SMF, the depletion beam is split by a polarizing beamsplitter cube (PBS); the splitting ratio can be set by the orientation of a half-wave plate. The transmitted beam is phase modulated by a helical PP (VPP1a, RPC Photonics) while the reflected beam passes through a custom made circular PP [78] (see subsection 2.5.4). Both depletion beams are recombined at a second PBS. Samples are raster-scanned, and fluorescence is detected as described in the previous subsection for the setup based on the broadband source.

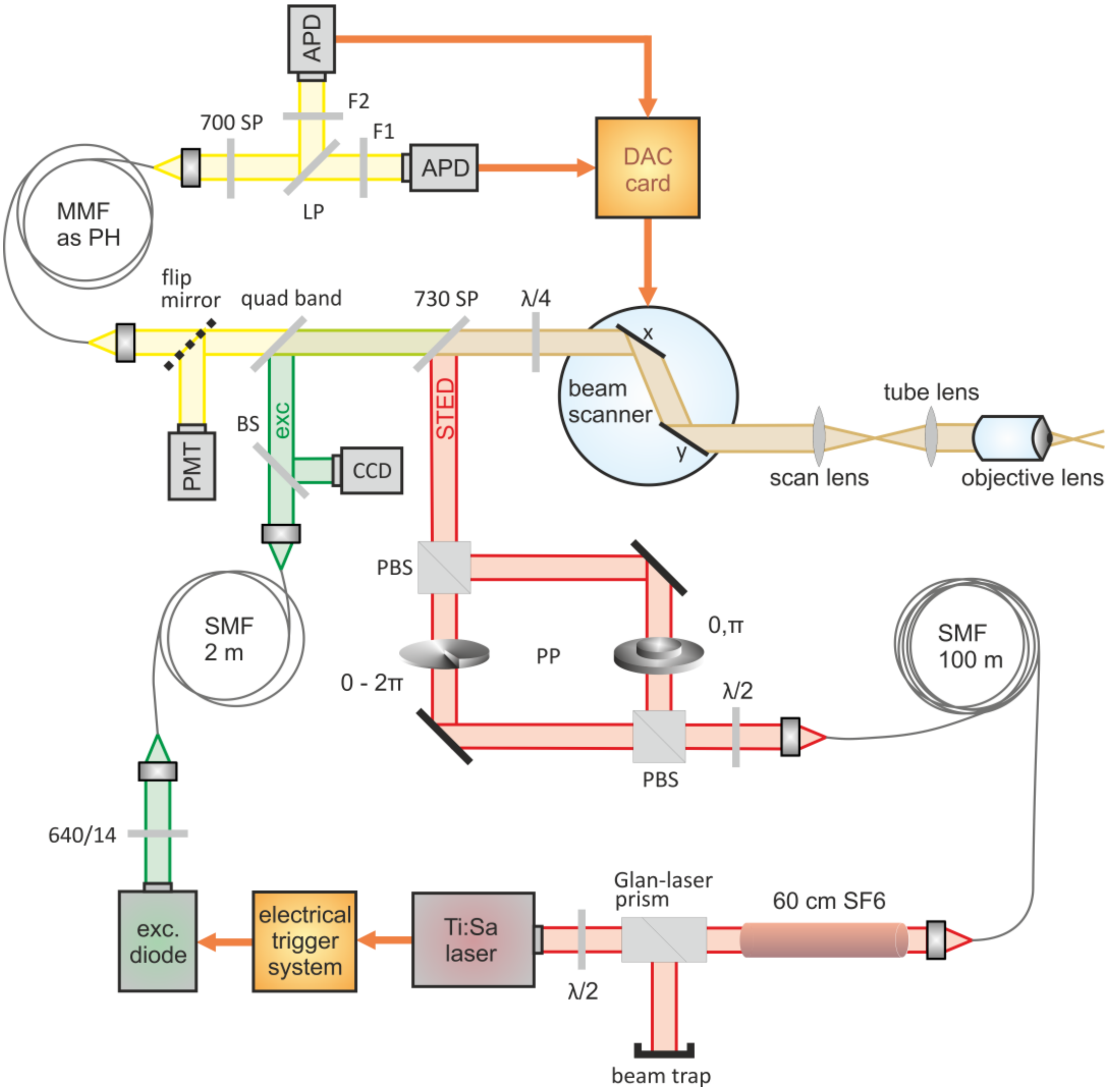
APD
F2
700 SP
F1
APD
DAC card
MMF as PH
LP
flip mirror
quad band
730 SP
λ/4
x
beam scanner
tube lens
y
BS
exc
STED
CCD
PMT
scan lens
objective lens
PBS
0,π
SMF 2 m
PP
SMF 100 m
0 - 2π
λ/2
PBS
640/14
Glan-laser prism
60 cm SF6
exc. diode
electrical trigger system
Ti:Sa laser
λ/2
beam trap

Figure 4.3.: STED microscopy setup with a Ti:Sa and a diode laser as described in the text.

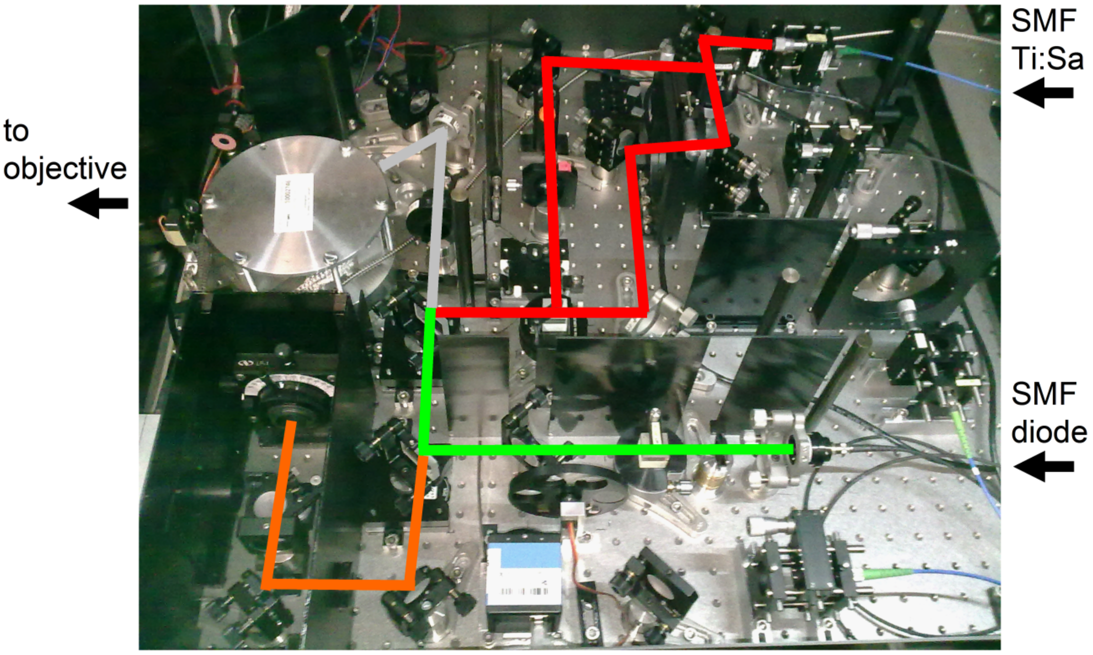

Figure 4.4.: Photograph of the main part of the STED microscopy setup based on a Ti:Sa and a diode laser. Indicated are the paths of excitation (green), STED (red), combined beams (gray) and fluoresence light (orange).

4.1.3. Spatial Beam Overlay

A great challenge in STED microscopy is to stably overlay the excitation and the depletion beam. The tolerance is within the range of a few tens of nanometers for the spatial domain and within a few tens of picoseconds for the temporal domain. In general, for building a STED microscope, stable optical mounts close to the optic table are extremely important. Also, the room in which the microscope is operated should be kept at a constant temperature to avoid thermal drifts in the optic and electric system. Furthermore, all cables associated with timing should be mounted in fixed positions. These precautions are mandatory to obtain reliable results.

In conventional confocal microscopy, the overlay of multiple excitation wavelengths is required for multicolor imaging. An adequate procedure is to feed all wavelengths through a common optical fiber to ensure an intrinsic spatial overlay. However, in STED microscopy, the depletion beam has to be phase-modulated to provide zero intensity in the center after focusing. There have been efforts in designing an optical element that will modulate the depletion wavelength only and, thus, allow the use of a common fiber for excitation and depletion light [120, 121]. In this approach, however, the choice of excitation and depletion wavelengths is limited, as is the use of various depletion patterns for, e.g., 3D-STED. Therefore, in the setup constructed in this work, the light from two separate fiber outputs was combined at a SP dichroic mirror. Before being passed into the objective lens, the beams could be directed onto two position sensing photodiodes (PSDs) (PDP90A, Thorlabs) via a removable mirror (RM) (**Fig. 4.5**). A 50/50 beamsplitter (BS) separated both position sensors by an optical path length of ~ 60 cm. According to the manufacturer, the photodiodes provide a resolution of < 0.7 µm. This was a good start but not sufficient. Therefore, excitation and depletion beam were more precisely aligned by imaging the reflections of small gold particles within a transparent medium [119, 122]. Thus, the mirror RM was removed and, after passing the depletion SP and excitation LP dichroic mirrors, the reflected signal was detected on a PMT while scanning across the sample. The top image of **Fig. 4.5b** displays the overlay of excitation beam (green) and depletion beam signal (red) after alignment with the position sensing devices. A displacement of 54 nm was measured after determination of the center of mass, which is even better than expected from the resolution specified for the position sensing diodes. Fine adjustments to the position of the depletion beam resulted in an overlay according to the central image of **Fig. 4.5b**. A negligible displacement of 17 nm was found by quantitative evaluation. After precise beam overlay, the PP modulating the depletion beam was inserted into the setup. The position of the phase plate was adjusted for maximum symmetry of the resulting doughnut-shaped PSF. A this point, it should be noted that, depending on the depletion wavelength, the insertion of the phase plate again introduced a small beam displacement, which required a slight repositioning of the depletion beam.

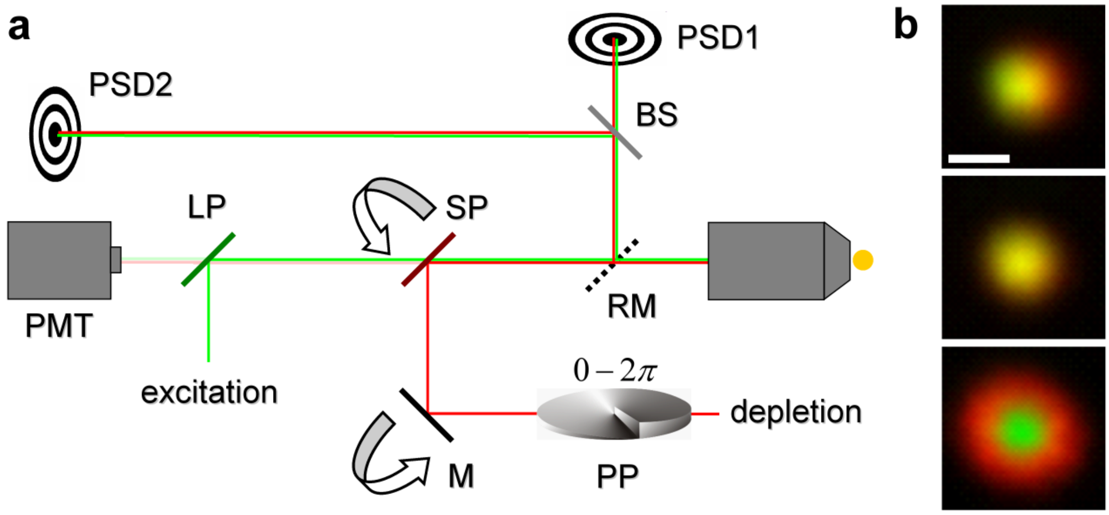

Figure 4.5.: Spatial beam alignment. (**a**) The depletion beam was overlaid with the excitation beam at a SP dichroic mirror. The beams were coarsely aligned using two PSDs. (**b**) The overlay was finely adjusted by measuring the reflections off 80 nm gold beads. Excitation and STED PSF after overlay with the PSDs (top), after measuring the reflection off 80 nm gold beads (middle) and, finally, after insertion of the helical PP (bottom). Scale bar, 300 nm.

Interestingly, this way of aligning a STED microscope already makes use of an imaging procedure capable of providing sub-diffraction resolution. Again, localization is the key. In this case there are only two sources, namely, excitation and depletion beam. Their center of mass is determined individually by spectral separation. Unfortunately, this approach of spectral separation is not applicable to biological samples featuring tens to hundreds of emitters within a single, diffraction limited spot, as this would require the same number of detection channels.

Materials and Methods

Surface covered with 80 nm gold beads: A droplet ($\sim$ 20 µl) of gold beads solution (80 nm diameter, GC80, BBI) was placed on top of a coverslip (No. 1, Menzel, Braunschweig, Germany). After all water had evaporated, a droplet of immersion oil (Immersol 518 F, Zeiss, Jena, Germany) was placed at the same spot and capped with another coverslip of smaller size. Subsequently, the gap between the two coverslips was sealed with two-component silicone (Wirosil, MW Dental, Büdingen, Germany). The use of immersion oil ensured a constant refractive index within the sample in order to avoid reflections other than off the gold beads.

Reflection measurement: Reflections off gold beads were measured with the same setup as described in subsection 4.1.2. The Ti:Sa laser was set to a wavelength of 760 nm. The excitation and depletion focus were imaged separately by alternate switching of the diode and the Ti:Sa laser. To avoid an overload of the photomultiplier, several neutral density filters were used to attenuate both the excitation and, especially, the high intensity depletion beam.

4.1.4. Timing for Optimal Fluorescence Quenching by STED

For optimal fluorescence quenching by stimulated emission, the depletion photons should arrive at the sample immediately after excitation. Thus, spontaneous emission of fluorescence photons is suppressed around the central zero of the doughnut shaped depletion PSF, which is the principle of STED microscopy. As a consequence, the use of CW excitation and depletion requires a very high intensity of the depletion beam to ensure early depletion (see subsection 2.5.3). In CW-STED, pulsed excitation followed by time gating of the fluorescence response (g-STED) has helped to significantly reduce the intensity required for efficient depletion [70]. The advantage of CW-STED lies within the simplification of the setup, since no synchronization between excitation and depletion laser is required. Also, CW lasers are less expensive, more compact and easier to maintain than high power pulsed sources. However, even in g-STED, a lot of depletion light is wasted, so a high average power density is required. Photodamage and undesired effects such as optical trapping can be a problem when working with biological specimens. In contrast, by concentrating the depletion photons to a short burst immediately following the excitation pulse, stimulated emission is most efficient. Thus, the use of both pulsed excitation as well as pulsed depletion is principally superior in terms of the depletion efficiency-to-intensity ratio. **Fig. 4.6a,c** shows single Atto550 molecules imaged in confocal mode. Application of 38 mW of CW-STED at 642 nm yielded a moderate resolution enhancement, the average FWHM of the molecules was ∼ 90 nm (**Fig. 4.6b**). In contrast, by using pulsed STED at 2 MHz (see subsection 4.1.1) with only 3.6 mW of average intensity, a mean FWHM of ∼ 50 nm was feasible (**Fig. 4.6d**). As the resolution in STED microscopy scales with the square root of the depletion intensity (equation 2.98), the same resolution would have required > 120 mW of CW-STED. Yet, at 2 MHz repetition rate, image acquisition was slow, usually with a pixel dwell time of 100 − 500 µs. The correlation spectrocopy technique described in subsection 3.3.6, however, requires pixel dwell times of 8 − 20 µs. Therefore, a second configuration running at a repetition rate of 80 MHz was constructed as described in subsection 4.1.2.

For evaluation of the respective arrival times, fluorescence was excited in a solution of a STED-compatible dye (Atto655) at a depth of 5 µm within the sample with an average excitation intensity of 30 µW. By measuring the average count rate at the detector with STED, F_{STED}, and without STED, F_{confocal}, the depletion efficiency, η, can be calculated via

$$\eta = 1 - \frac{F_{\mathrm{STED}}}{F_{\mathrm{confocal}}}. \tag{4.1}$$

The resulting STED efficiencies at different delay times between excitation and depletion

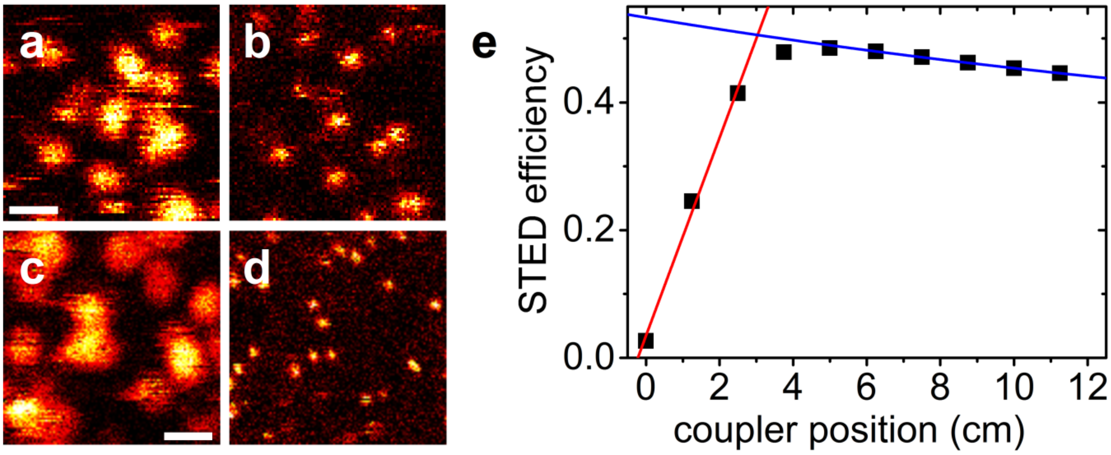

Figure 4.6.: Temporal beam alignment. (**a,b**) Confocal and CW-STED image of single Atto550 dyes at 38 mW of average depletion intensity. (**c,d**) Confocal and pulsed STED image of single Atto550 molecules at 3.6 mW of average depletion intensity. (**e**) STED efficiency for different delay times between excitation and depletion pulses (1 cm $\widehat{=}$ 30 ps). The red line represents a linear fit through the first three data points, whereas the blue line represents a fit of an exponential decay to the last five data points. Scale bars, 500 nm.

pulses are shown in **Fig. 4.6e**. If the depletion pulse arrives earlier than the excitation pulse, all fluorophores are still in the ground state and, thus, there is no depletion effect. This explains the steep decline in STED efficiency towards early times. Mathematically, this trend can be described by the multiplication of the depletion and excitation pulses, both approximated by rectangle functions, yielding a linear increase. A linear fit (red curve) within this regime (first three data points) yielded a pulse length of $\sim$ 90 ps, a result that matches the specification stated by the laser manufacturer (Fianium), verifying the assumptions taken. If the depletion pulse arrives later than the excitation pulse, fluorophores in the excited state can already spontaneously emit fluorescence. As spontaneous emission follows an exponential decay, this trend is also represented in the decline in STED efficiency towards later times. On the basis of an exponential fit (blue curve) to the data within this regime (last five data points), the lifetime of the fluorophores was estimated yielding $\sim$ 0.8 ns, which is at least the same order of magnitude as the 1.8 ns stated by the dye manufacturer (Atto-Tec). Another fact to consider is that a change of wavelength for the excitation and/or the depletion beam, e.g., when working with a different dye, requires different timing. Since the propagation time of the photons is influenced by dispersion within the optical elements involved, a shift of the efficiency curve was observed. The greatest influence on timing was caused by the wavelength dependent dispersion within the single mode fiber of 2 m length used for this experiment. When working with the Ti:Sa laser, this behavior became more pronounced due to the 100 m of fiber length required for pulse stretching. Additionally, the response of the photodiode used for triggering of the diode laser is wavelength dependent. Therefore, every change of the depletion wavelength required a readjustment of the timing.

Materials and Methods

Dye solution: For quantitative evaluation of the STED efficiency, a dye solution was prepared. Atto655 with a free COOH group (AD 655-21, Atto-Tec) was dissolved in dimethyl sulfoxide (DMSO) yielding a stock solution of 2.4 mM. This solution was diluted using purified water (Milli-Q, Millipore, Billerica, USA) to a concentration of $\sim$ 50 nM. As sample holder, a hole was drilled into a block of teflon and sealed with a coverslip (No. 1, Menzel) using two-component epoxy adhesive (Epoxyd, Weicon, Münster, Germany). The resulting volume was filled with $\sim$ 200 µl of dye solution and sealed with another coverslip.

STED setup: The STED setup as described in subsection 4.1.1 was used for this measurement. Fluorescence was filtered by a 676/37 nm bandpass filter (HC 676/37, Semrock).

4.1.5. Polarization

Last but not least, the state of polarization is important for the formation of the depletion pattern. Excitation as well as depletion light are initially linearly polarized. While the PP designed for resolution enhancement in z-direction (see subsection 2.5.4) works with any kind of polarization, light of circular polarization is crucial for the helical PP (VPP1a, RPC Photonics) used for STED in the xy-direction [123]. In **Fig. 4.7a**, the depletion pattern for linear (middle) and circular polarization (bottom) is shown, respectively. The most important aspect of the depletion pattern, the central zero, is lost for linear polarization. As an additional benefit of using circularly polarized light, photoselection of the dye molecules due to different orientations of their excitation dipoles is avoided. To obtain circular polarization, the combined excitation and depletion beams passed through a quarter-wave plate before entering the objective lens. For optimal positioning of the quarter-wave plate, fluorescence correlation spectroscopy was performed on a lipid bilayer labeled with a STED-compatible dye (Atto647N). Based on a constant average marker concentration within the bilayer, the amplitude from the correlation measurement is proportional to the inverse of the extension of the confocal volume (see subsection 3.3.3). By maximizing the correlation amplitude, the optimal position of the quarter-wave plate was obtained (**Fig. 4.7b**).

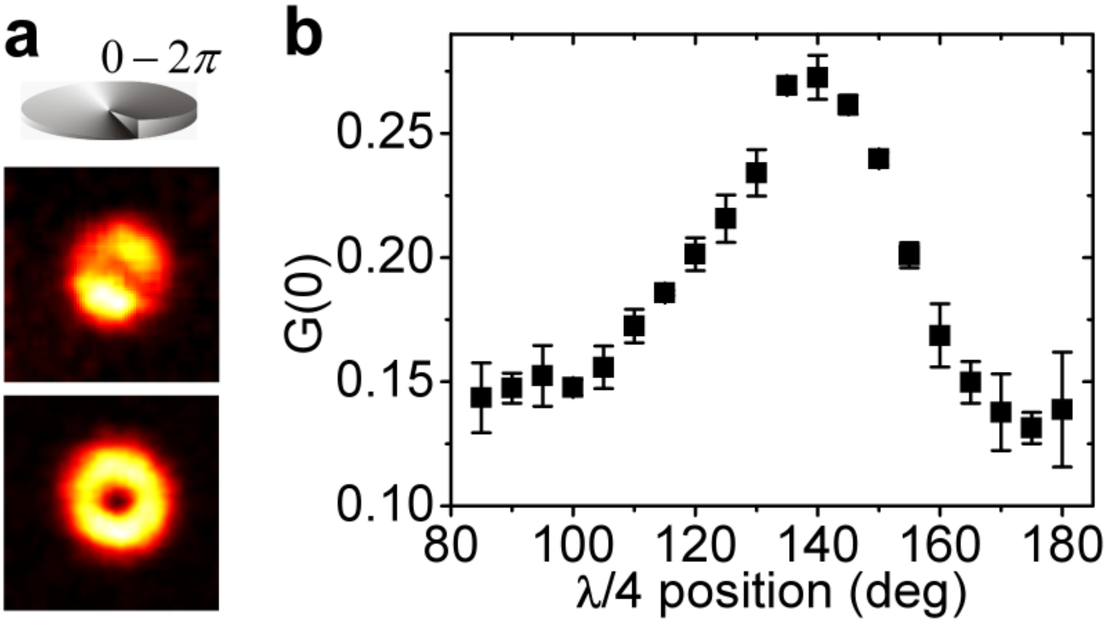

Figure 4.7.: STED polarization dependence. (**a**) For the helical PP (top), irradiation with linearly polarized light resulted in a depletion pattern without a clear central zero (middle). For correct orientation of the quarter-wave plate, yielding light of circular polarization, the central zero was well defined (bottom). (**b**) Amplitudes of a FCS experiment in a lipid bilayer. Optimal orientation of the quarter-wave plate resulted in the smallest possible observation volume, i.e., in a maximum of the correlation amplitude.

Materials and Methods

Lipid bilayer preparation: Planar lipid bilayers were prepared according to subsection 3.2.3.

STED setup: The STED microscope described in subsection 4.1.1, with the helical PP and a depletion wavelength of 780/20 nm, was used for these measurements. The fluorescence emission was filtered by a 676/37 nm bandpass filter (HC 676/37, Semrock), recorded with a TCSPC system (Simple-Tau 152, Becker & Hickl) and autocorrelated with the company's software.

4.2. Total Internal Reflection Microscopy

4.2.1. Implementation of TIRFM for Live Cell Imaging

In general, there are two basic geometries used for total internal reflection (TIRF) microscopy. In prism-based TIRFM, excitation is decoupled from detection (**Fig. 4.8a**). One side of the sample is covered by a prism, usually made of quarz glass. Due to the shape of the prism, incident excitation light strikes the interface of prism and the aqueous solution, immersing the specimen at angles larger than the critical angle (see subsection 2.4.3). Thus, an evanescent field is created at the interface, and excitation of the sample fluorophores is limited to the depth of that field. The other side of the sample is covered by a standard coverslip, followed by the objective lens used for fluorescence detection.

In objective-type TIRFM, the specimen is excited and fluorescence is detected via the same objective lens (**Fig. 4.8b**). As in standard widefield epifluorescence microscopy, the excitation light is focused into the back focal plane of the objective lens, such that the entire field of view is homogeneously illuminated. By displacing the incident beam from the optical axis, the excitation beam leaves the objective at an angle. At some point, the critical angle is reached, causing total reflection at the interface of coverslip and aqueous solution of the sample. However, this geometry requires the use of special objective lenses with a very high NA. With the definition of the critical angle, $\alpha_{\text{crit}} = \sin^{-1}(n_1/n_2)$, (equation 2.66), the refractive index of the sample, n_1, the refractive index of the imaging medium (objective immersion fluid), $n_2 > n_1$, and the NA of the objective lens, $n_2 \sin\alpha$, we obtain

$$NA_{\text{crit}} = n_1. \tag{4.2}$$

Assuming a specimen immersed in water, a NA of at least 1.33 is required. Additionally, the back aperture of the objective lens must be large enough to allow for a sufficient displacement of the excitation beam to reach the critical angle.

In contrast, a prism-based microscopy setup can be equipped with any objective lens because the objective is used for detection only. Also, in prism-based TIRFM, the angle

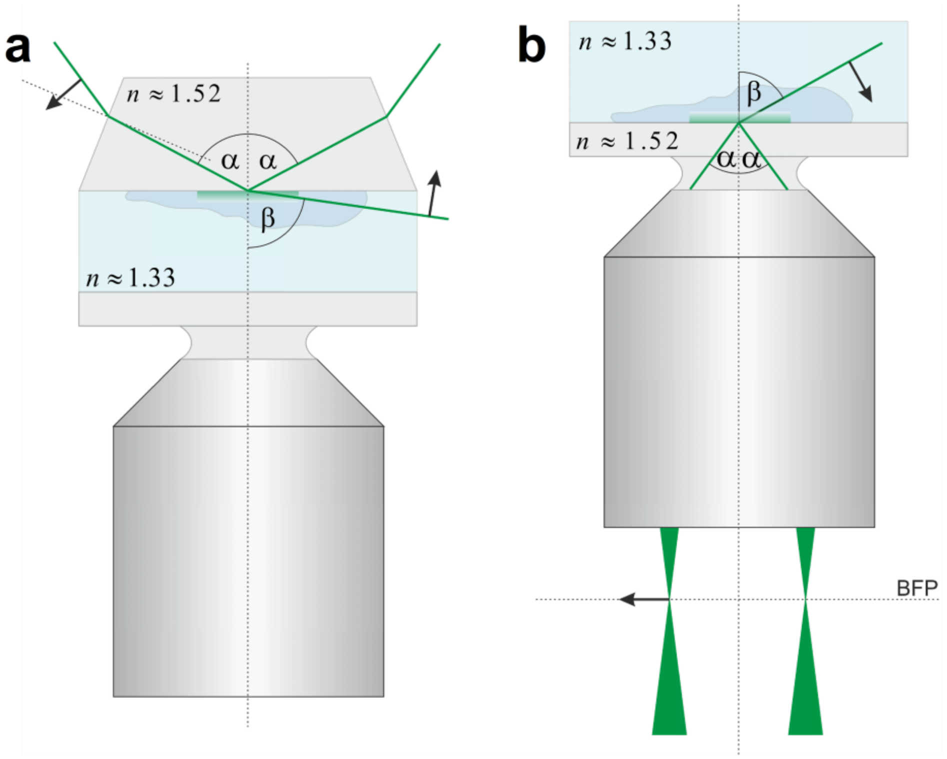

Figure 4.8.: TIRFM implementations. (**a**) Prism-based TIRF microscopy. (**b**) Objective-type TIRF microscopy.

of incidence is not limited by an aperture, in principle providing the lowest possible excitation depth, i.e., the best possible background suppression. Finally, since excitation and detection paths are decoupled, there is no need for any beam separation by means of an optical element and, thus, fluorescence photon throughput is maximized. However, if a high lateral resolution and photon yield are necessary, only high-NA objectives are suitable for detection. Such objective lenses have a small working distance (100 − 200 µm), limiting the total thickness of the sample in prism-based TIRF microscopy. In live cell imaging, limited sample space is a severe problem. While cell thickness is usually in the range of only a few tens of microns, they require a reservoir of cell culture medium in order to sustain their metabolism. Also, sample handling is more difficult in prism-based TIRFM. After each sample change, slight variations in the position of the prism require an adjustment of the excitation beam. Furthermore, the illumination mode via excitation through an objective lens, i.e., TIRF or epifluorescence, can be quickly changed by a variation of the excitation beam displacement from the optical axis. Being able to promptly switch the excitation mode is very helpful for studies of cellular structures at different depths, e.g., the plasma membrane and the nucleus. These simple practical issues favor the application of objective-type TIRFM for live cell imaging.

4.2.2. TIRF/Epi-illumination Microscopy Setup

For TIRF and epi-illumination widefield microscopy, a custom-built setup was constructed (**Fig. 4.9**). It is based on a modified inverted microscope (Axio Observer.Z1, Zeiss) equipped with an oil immersion TIRF objective (Plan-Apochromat 63×/1.46 Oil, Zeiss). Four laser lines including 640 nm (OXX-LBX, Laser 2000, Wessling, Germany), 561 nm (GCL-150-561, CrystaLaser, Reno, USA), 473 nm (LSR473-200-T00, Laserlight, Berlin, Germany) and 405 nm (CLASII 405-50, Blue Sky, Milpitas, USA) are combined via dichroic mirrors (R405, R473, R561, AHF, Tübingen, Germany) and coupled into 2 m of SMF (QPMJ-A3A, OZ Optics) to create a clean, spatially uniform beam profile. During the experiment, laser intensities are controlled via an AOTF (AOTFnC-400.650, AA Opto Electronic). After passing the fiber and subsequent collimation, the laser beam is magnified (3.75×) by a telescope. This measure ensures an even illumination of the entire field of view ($55 \times 55\,\mu m^2$) covered by the electron multiplying charge coupled device (EMCCD) camera (Ixon DV897ECS-BV, Andor, Belfast, UK) provided with 512×512 pixels and a minimum exposure time of 30 ms. The scan lens focuses the parallel beam into the back focal plane of the objective lens, providing an epi-illumination of the sample. By tilting a mirror placed within the image of the back focal plane created by the scan lens, the beam can be displaced from the optical axis to change the excitation to TIRF mode. At the same time, a portion of light is reflected by a polarizing beamsplitter cube (PBS) and passes through the FRAP lens forming a telescope with the scan lens via a second PBS. Upon opening the FRAP shutter and closing the illumination shutter, the objective is illuminated by a parallel beam resulting in excitation of a spot confined to a diameter of 1 µm in the lateral direction. This spot can be utilized in FRAP experiments (chapter 6). Fluorescence is collected via the same objective lens. After passing a quad band dichroic mirror (z 405/473/561/640, AHF), fluorescence light is imaged onto a slit via the tube lens. The image is then relayed by another lens through a 555 nm LP dichroic mirror (Chroma), to split the fluorescence into two color channels. After subsequent filtering via a 525/50 nm bandpass (green channel) and a 610/75 nm bandpass (red channel), respectively, light from both channels is focused side-by-side on the EMCCD camera chip. The set of relay lenses is also used for image magnification (2×) in order to provide a pixel size of 107 nm suitable for PALM imaging. Alternatively, a flip mirror can be used to direct the fluorescence onto a second, faster EMCCD camera (Ixon EM+ DU-860, Andor) provided with 128×128 pixels covering a field of view of $14 \times 14\,\mu m^2$ and a minimum exposure time of 2 ms. In that optical path, the image formed by the tube lens is magnified (2×) by a single lens. Before detection, fluorescence is filtered by exchangable bandpass filters chosen according to the emission spectra of the employed fluorophores. An incubator (XL-5 DARK, Pecon, Erbach, Germany) covering the objective lens as well as the sample is used for measurements at 37℃. AOTF and shutter signals are generated by a DAC card (USB-6229, National Instruments) controlled by homemade software developed in Labview (National Instruments) [124]. Images are acquired by the software provided by the camera manufacturer (Andor).

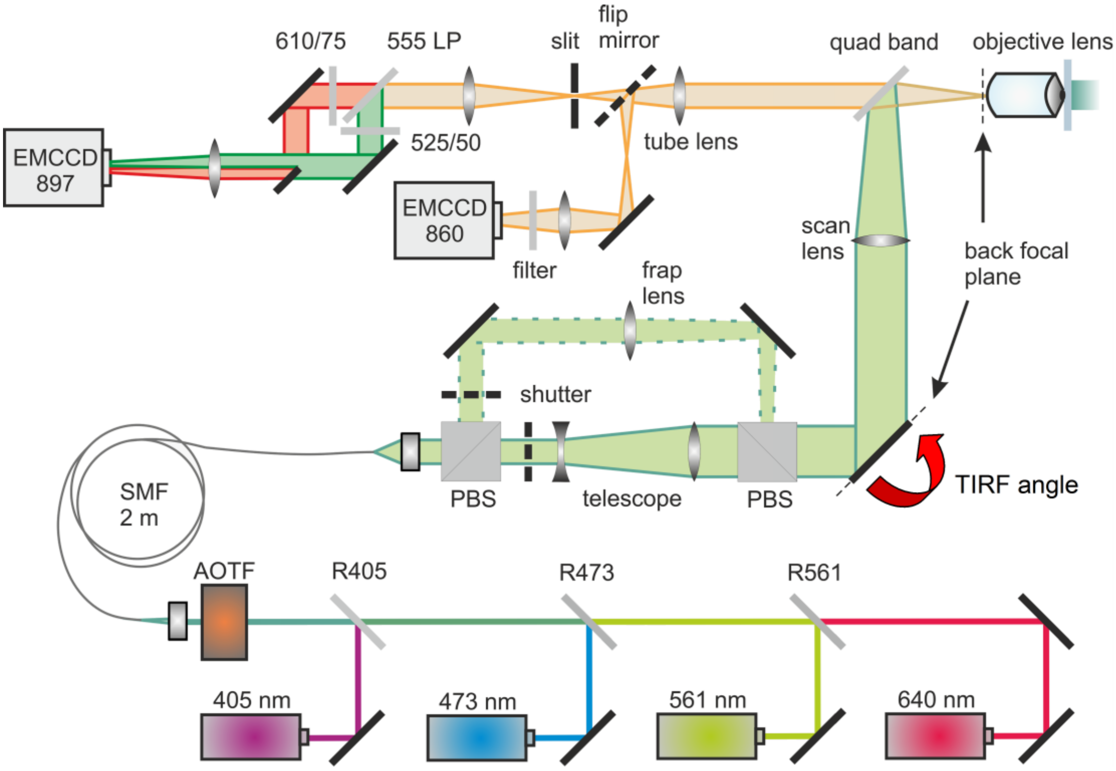
610/75
555 LP
slit
flip mirror
quad band
objective lens
EMCCD 897
525/50
tube lens
EMCCD 860
filter
scan lens
back focal plane
frap lens
shutter
SMF 2 m
PBS
telescope
PBS
TIRF angle
AOTF
R405
R473
R561
405 nm
473 nm
561 nm
640 nm

Figure 4.9.: Custom-built objective-type TIRF/epi-illumination microscopy setup as described in the text.

5. Application of STED Microscopy

5.1. Application of STED Microscopy

5.1.1. Experimental Verification of Fluorescence Quenching by STED

The saturation intensity for STED depends on the fluorescence lifetime and the stimulated emission cross section of the dye at the STED wavelength employed (equation 2.90). In order to generate stimulated emission, the STED wavelength has to be within the range of the emission spectrum of the fluorescent marker. At the same time, excitation by means of the depletion light must be prevented under any circumstance. Thus, the dye should not at all be excitable at the depletion wavelength. Therefore, dyes with a large Stokes shift are preferred in STED microscopy. In a STED measurement, the residual fluorescence after depletion is probed. For this purpose, a filter is placed in front of the detector to block reflected excitation light. Yet, backscattered depletion photons would also distort the measurement. Thus, the wavelength of the STED beam must be outside the detection window, limiting its application towards longer wavelengths within the emission spectrum. As a consequence, dyes with a large vibronic shoulder are preferred (**Fig. 5.1a**). Furthermore, the dyes must be quenched to the ground

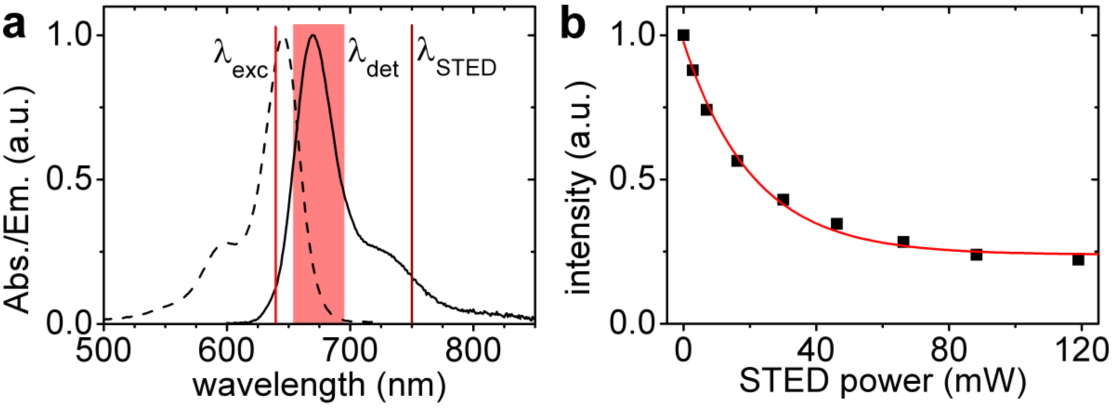

Figure 5.1.: Fluorescence quenching of Atto647N. (**a**) Absorption and emission spectra of Atto647N (data provided by Atto-Tec) with respective excitation wavelength, λ_{exc}, detection window, λ_{det}, and depletion wavelength, λ_{STED}. (**b**) Normalized fluorescence intensity excited in an Atto647N solution at various STED intensities (squares), fitted with equation 2.91 plus an offset to account for background (line).

state by means of stimulated emission before they can spontaneously emit fluorescence photons. The shorter the lifetime of the excited state, the more likely pre-depletion emission can occur, and, in order to compensate for that, a higher depletion intensity is required. Therefore, dyes with a long lifetime are more suitable for STED microscopy. Also, during raster-scanning, each fluorophore is excited and depleted many times before contributing to the image by spontaneous emission of fluorescence photons in the center of the focal spot. Consequently, STED-dyes should be very resistant to photobleaching. The dye Atto647N meets all these criteria and is thus widely applied in STED microscopy [71, 125–127]. For evaluation of the fluorescence quenching by stimulated emission, we focused 5 µm deep into a solution of Atto647N, exciting fluorescence at an average intensity of 30 µW using 640-nm light. Hence, the average photon count was recorded for 30 s using various intensities of the depletion beam (**Fig. 5.1b**). Subsequently, we fitted the data with equation 2.91 which resulted in a saturation intensity of $I_{\mathrm{sat,780nm}} = 15\,\mathrm{mW}$ for Atto647N at a depletion wavelength of 780 nm. Based on a focal area of $0.25\,\mu\mathrm{m}^2$ for the depletion beam, obtained from a reflection measurement on gold beads (subsection 2.5.4), this saturation intensity translates into a power density of $6\,\mathrm{MW/cm}^2$, confirming the value estimated in subsection 2.5.3.

Materials and Methods

Dye solution: For quantitative evaluation of the STED efficiency, a solution of Atto647N with a free COOH group (AD 647N-21, Atto-Tec) was prepared as described in subsection 4.1.4.

STED setup: The high repetition rate STED setup as described in subsection 4.1.2 was used for this measurement. Emission light was filtered by a 676/37 nm bandpass filter (HC 676/37, Semrock).

5.1.2. Experimental Verification of the Resolution Enhancement by STED

In order to determine the resolution enhancement by means of STED, point sources can be imaged. A structure can be considered as a point-like emitter if it is smaller, ideally at least one order of magnitude smaller, than the minimum distance resolvable by the imaging system. If that condition holds, the width of the emitters within the acquired images is determined by the optical resolution. Fluorescent beads are a popular choice for benchmarking [119, 128, 129]. They are bright, photostable and do not show any blinking because the signal originates from multiple fluorophores within a single bead. **Fig. 5.2a** shows fluorescence images of 20 nm dark red beads as an overlay of confocal and STED images acquired by pulsed excitation at 640 nm with an average intensity of 0.5 µW and depletion at 750/20 nm with an average intensity of 3.6 mW, both at a repetition rate of 2 MHz. The sample was raster-scanned with a pixel size of 20 nm and a pixel dwell time of 200 µs. The resolution enhancement due to STED is obvious from the magnified areas shown in **Fig. 5.2b-e**. For a single bead, an exemplary evaluation of the cross section resulted in a FWHM of 258 nm for the confocal and 48 nm for the

STED image, respectively (**Fig. 5.2f**). Yet, the width measured is a convolution of the PSF of the microscope and the intrinsic size of the beads, here 20 nm in diameter. This extension of the underlying structure could have been removed from the resulting data by deconvolution. However, the exact diameter of each individual bead can vary, leading to errors. Instead, another surface covered with single Atto647N molecules was prepared for a more precise analysis of the resolution. Bleaching and blinking was compensated by imaging an area large enough to ensure a high number of valid signals. The resulting confocal and STED images are shown as an overlay and as individual subsets in **Fig. 5.2g-k**. An exemplary evaluation of the cross section of a single dye molecule resulted in a FWHM of 298 nm for the confocal and 45 nm for the STED image, respectively (**Fig. 5.2l**). For better statistics, the FWHM of a total of 375 molecules were analyzed by fitting the signal of the individual emitters with a 2D Gaussian. This procedure resulted in an average FWHM of (49 ± 10) nm for the STED image, while the extension in confocal mode was ~ 250 nm. Thus, a five-fold improvement of the lateral resolution was obtained by STED. For a quantitative evaluation of the resolution

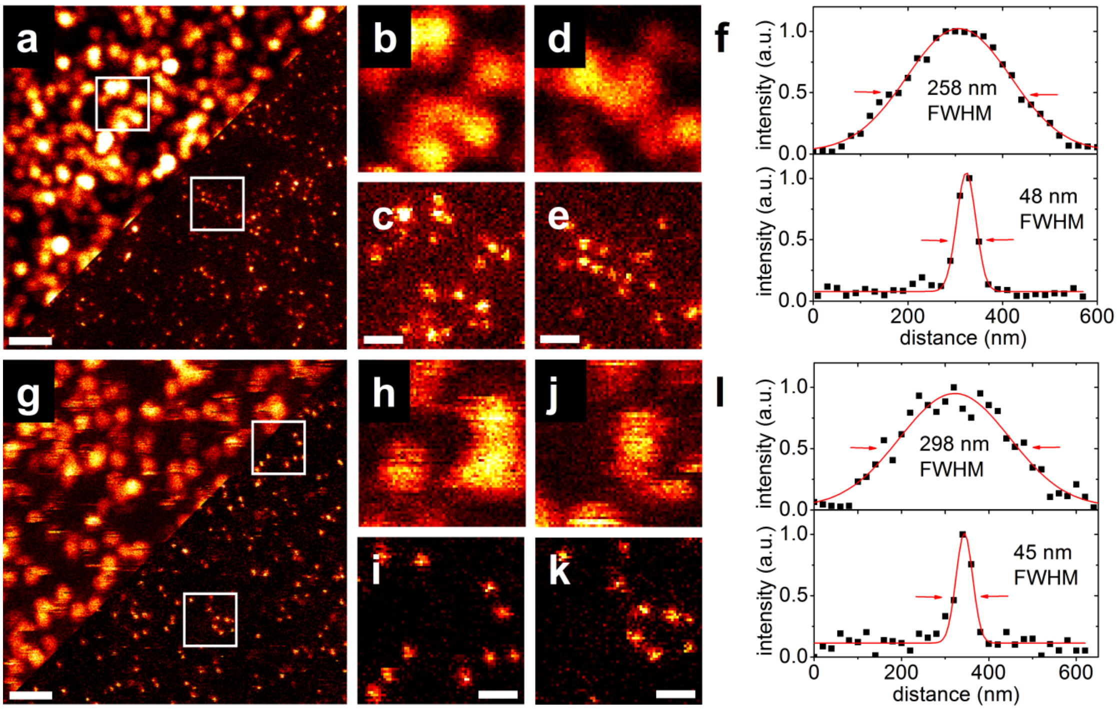

Figure 5.2.: (**a,g**) Fluorescence images of 20 nm beads and single Atto647N molecules in a confocal (upper-left) and STED (lower-right) overlay. (**b,d** and **h,j**) Confocal and (**c,e** and **i,k**) STED images of the regions marked by the white frames. (**f,l**) Cross sections of a single bead/dye taken from the confocal (top) and STED images (bottom), respectively. Scale bars, 1 µm (panels a,g) and 300 nm (panels c,e,i,k).

scaling of STED microscopy, single dye molecules were imaged using pulsed excitation at 640 nm with an average intensity of 1.3 µW and a depletion wavelength of 780 nm at various intensities, both at a repetition rate of 80 MHz. Four examplary images of single dye molecules are shown in **Fig. 5.3a** at depletion intensities of 0 mW, 32 mW, 100 mW and 203 mW, respectively. The spatial resolution was quantified by fitting a 2D Gaussian to 20 individual molecules (**Fig. 5.3b**). In confocal mode, the signals of the individual molecules exhibited a FWHM of (239 ± 15) nm, whereas, at 203 mW of STED intensity, the FWHM reduced to (69 ± 18) nm. The trend is well reflected by the square root law describing the resolution in STED microscopy (equation 2.98) which was fitted to the data, verifying the assumptions taken. A depletion wavelength of 780 nm was chosen because it produced the best results for STED application to the fluctuation methods described in section 3.3.

Instead of measuring the width of the signals originating from individual, point-like emitters, objects with substructures causing dips in the fluorescence intensity can also be used to demonstrate the capability of STED microscopy. Therefore, unilamellar vesicles of various sizes were prepared. Since only the membrane was labeled, no fluorescence was to be expected from the inside, which should result in a dip in the course of the cross section. In the confocal image, the vesicles were too small to be identified as hollow objects (**Fig. 5.4a**). However, application of STED yielded the resolution improvement required to distinguish vesicles from solid spheres (**Fig. 5.4b**). By taking the cross

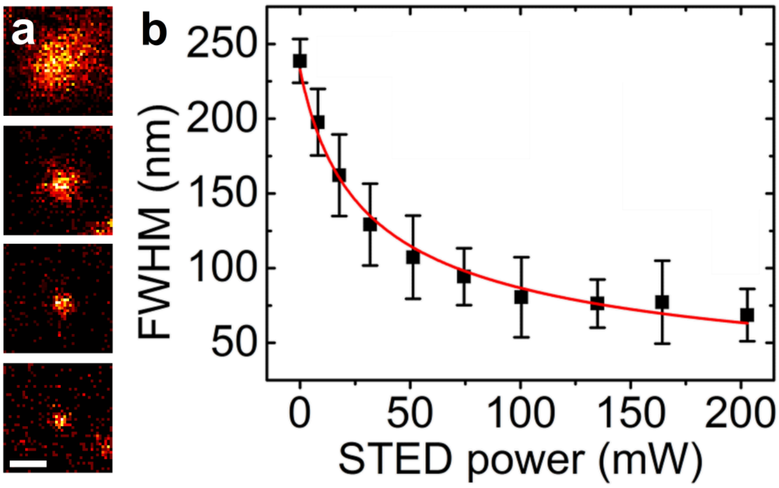

Figure 5.3.: (**a**) Fluorescence images of single Atto647N dyes at STED intensities of 0 mW, 32 mW, 100 mW and 203 mW (top to bottom), using a depletion wavelength of 780 nm. (**b**) Quantitative analysis of the FWHM of single Atto647N dyes at various STED intensities (squares). For each depletion intensity, 20 molecules were fitted with a 2D Gaussian. The resulting data points were fitted with equation 2.98 (red line). Data were acquired and analyzed in collaboration with Rosmarie Blomley. Scale bar, 200 nm.

section from the STED image followed by subsequent fitting of a Gaussian function to each peak, a wall-to-wall distance of 470 nm was obtained for that particular vesicle (**Fig. 5.4c**).

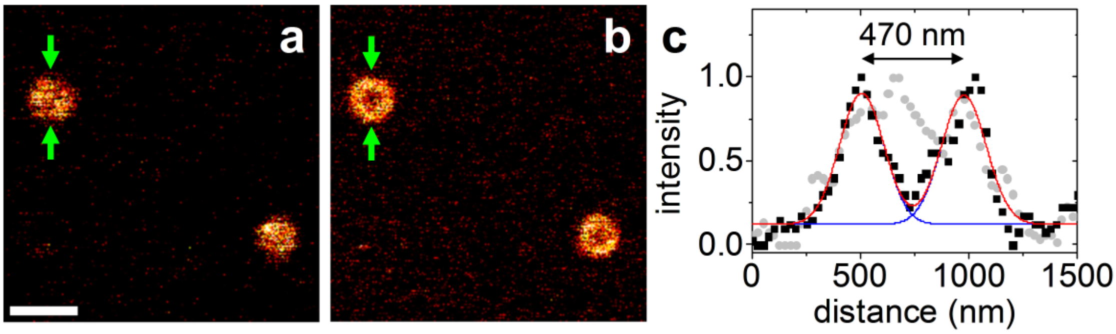

Figure 5.4.: Fluorescence images of unilamellar vesicles labeled with Atto647N-DPPE, (**a**) confocal image and (**b**) STED image, respectively. (**c**) Cross sections along the direction indicated by green arrows in the confocal (gray circles) and STED (black squares) images, respectively; blue lines, Gaussian fit of each peak resulting in a peak-to-peak distance of 470 nm; red line, sum of both Gaussians. Scale bar, 1 µm.

Materials and Methods

Surface covered with 20 nm beads: A solution of deep red fluorescent beads of 20 nm diameter (F-8783, Invitrogen, Grand Island, USA) was diluted to a concentration of ~ 100 nM using purified water (Milli-Q, Millipore). A droplet (~ 20 µl) of solution was placed on top of a coverslip (No. 1, Menzel). After evaporation of the liqid, the spot was covered with PMMA.

Surface covered with Atto647N dyes: Atto647N featuring a free NHS group (AD 647N-21, Atto-Tec) was dissolved in DMSO yielding a stock solution of 2.4 mM. This solution was diluted to a concentration of ~ 100 nM using purified water (Milli-Q, Millipore). A droplet (~ 20 µl) of solution was placed on top of a coverslip (No. 1, Menzel). After evaporation of the liqid, the spot was covered with immersion oil (Immersol 518 F, Zeiss). A second coverslip of smaller size was placed on top and sealed with two-component epoxy adhesive (Epoxyd, Weicon).

Unilamellar vesicles labeled with Atto647N: Giant unilamellar vesicles (GUVs) were prepared by dissolving DOPC (Avanti Polar Lipids) and cholesterol (Sigma-Aldrich) in chloroform at a ratio of 4:1. Atto647N-DPPE (Atto-Tec) was added in the amount of 0.01 mol% to the stock solution (1 mg/ml). For GUV formation, a homemade teflon chamber was used housing two platinum wires. On those wires, 6 µl of lipid solution was spread, followed by a 2 h evaporation step under vacuum to allow for solvent dissipation. The teflon chamber was filled with 350 µl of sucrose solution (300 mM) and heated to

60℃. A sinusoidal voltage of 2 V at a frequency of 10 Hz was applied to the platinum wires for 1.5 h, followed by 15 min at a freqency of 2 Hz. An observation chamber was incubated with a blocking solution of 2 mg/ml bovine serum albumin (BSA) for 30 min. After rinsing the observation chamber with water, 350 µl of glucose solution (300 mM) were added before transfer of the GUV suspension from the teflon chamber. GUVs were prepared by René Dörlich.

STED setup: The microscope hardware complies with the description in section 4.1, the helical PP was used for these measurements. Emission light was filtered by a 676/37 nm bandpass filter (HC 676/37, Semrock).

5.1.3. Application of STED Microscopy to Biological Specimens

Several subcellular structures were fluorescently labeled in fixed as well as in live cells and imaged by standard confocal as well as STED microscopy. Often, subcellular structures cannot be fully resolved by standard diffraction-limited visible light microscopy whereas STED microscopy provides a more detailed insight into their composition and function.

Cell Membrane

The cell membrane itself as well as many embedded proteins with an extracellular domain such as receptors, glycoproteins or transport channels can be fluorescently labeled from the outside. Thus, these structures are perfectly suited for live-cell STED microscopy, since STED works best with state-of-the-art synthetic dyes that are often not membrane permeable [130]. **Fig. 5.5a** displays the fluorescence image of a live *Xenopus* tissue culture (XTC) cell adhering to the coverslip surface with the plasma membrane labeled by Atto647N-DPPE. Fluorescence was excited with laser pulses of 640 nm wavelength

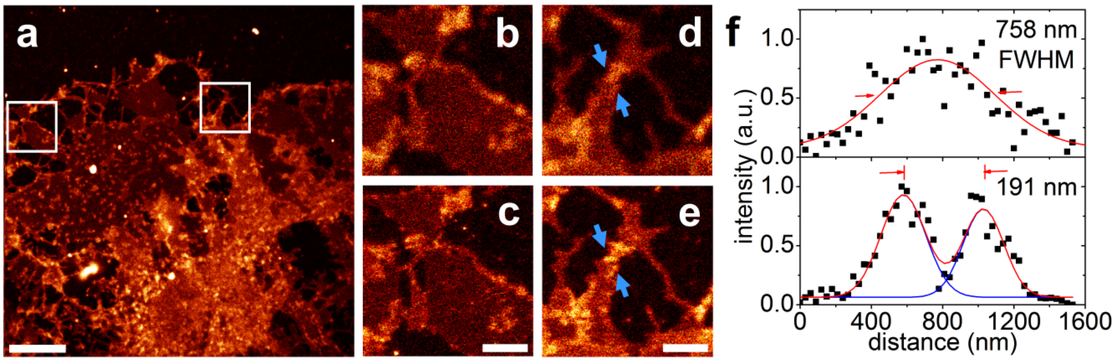

Figure 5.5.: (**a**) Fluorescence image of the plasma membrane of a live XTC cell labeled with Atto647N-DPPE. (**b,d**) Confocal and (**c,e**) STED images of the regions marked by the white frames. (**f**) Cross sections along the feature indicated by arrows in confocal (top) and STED mode (bottom). Scale bars, 10 µm (panel a) and 2 µm (panels c,e).

and an average intensity of 3 µW, whereas fluorescence was depleted at 780 nm and 160 mW of average intensity, both at a repetition rate of 80 MHz. At this high rate, the pixel dwell time of the raster scan could be reduced to 10 µs to minimize image blurring due to cell movement. The regions of interest marked by the white boxes are shown in **Fig. 5.5b-e** as acquired in standard confocal mode and by application of STED. A fit of the cross section indicated by arrows with a Gaussian resulted in an FWHM of 758 nm in confocal mode. However, in STED mode, a substructure exhibiting two peaks was revealed. Analysis by fitting two Gaussians resulted in a mutual distance of 191 nm (**Fig. 5.5f**).

FcϵRI Complex

In another experiment, the membrane-bound, high affinity FcϵRI receptor was labeled by Atto647N-IgE in live RBL-2H3 mast cells. This receptor plays an important role in triggering of immune reactions as described in detail in subsection 6.1.3. After cell adhesion, clustering of the FcϵRI receptor complex in sub-micron sized patches was detected by confocal fluorescence microscopy (**Fig. 5.6a**). Again, after zooming into regions of interest indicated by the white boxes, application of STED revealed a much more detailed substructure than standard confocal imaging (**Fig. 5.6b-e**). Quantitative analysis of the cross section as indicated by arrows resulted in an unclear structure for the confocal image, whereas the STED image revealed three clusters with mutual distances of 259 nm and 292 nm (**Fig. 5.6f**). Fluorescence was excited with laser pulses of 640 nm wavelength and an average intensity of 3 µW, whereas fluorescence was depleted at 780 nm and 100 mW of average intensity, both at a repetition rate of 80 MHz. Images were raster-scanned at 10 µs dwell time per pixel.

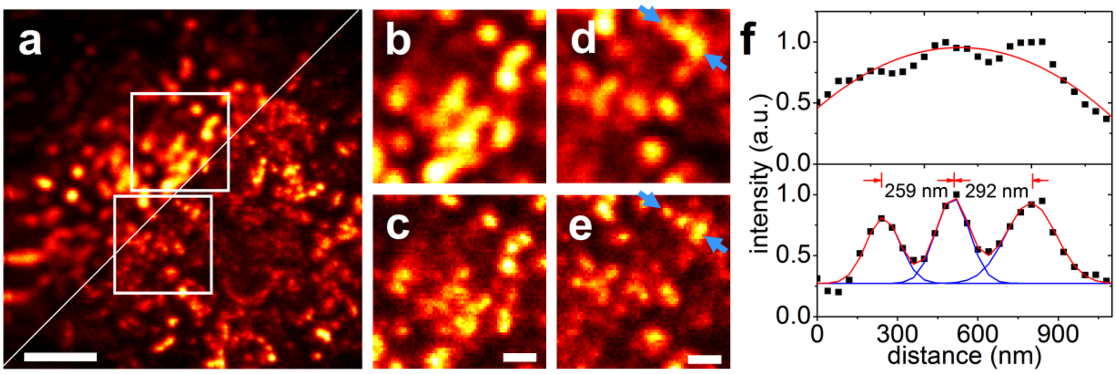

Figure 5.6.: (**a**) Fluorescence image of the FcϵRI complex in the plasma membrane of a live RBL-2H3 mast cell labeled with Atto647N-IgE. (**b,d**) Confocal and (**c,e**) STED images of the regions marked by the white frames. (**f**) Cross sections along the feature indicated by arrows in confocal (top) and STED mode (bottom). Scale bars, 2 µm (panel a) and 500 nm (panels c,e).

Microtubules

The cytoskeleton, composed of actin filaments and microtubules, is a fine network in the cytoplasm that is responsible for the structural integrity of a cell. Furthermore, cytoskeletal filaments are essential for many dynamic processes such as intracellular transport, cell adhesion and cell division. Microtubules are hollow cylindrical structures composed of bundled protofilaments present in all eukaryotes. A single protofilament is formed by a repeating arrangement of α- and β-tubulin heterodimers. Originating from microtubule organizing centers, microtubules are used as highways for organelle transport; the cargo is moved toward the plus-ends of microtubules by kinesins [131] and toward the minus-ends by dyneins [132]. During cell division, microtubules form the mitotic spindle that determines the plane of cell cleavage followed by segregation of the chromosomes to the opposite poles of the spindle. Microtubules are an ideal benchmark for nanoscopy. Other methods such as electron microscopy revealed their well defined diameter of 25 nm [133]. **Fig. 5.7a** displays the fluorescence image of a fixed HeLa cell with the microtubules labeled by Alexa594-β-tubulin. Due to the optical sectioning capability, confocal imaging of a subregion showed single microtubules at a high signal-to-noise ratio, yet image resolution was limited by diffraction (**Fig. 5.7b**). By application of STED, this limitation was overcome, resulting in a more detailed

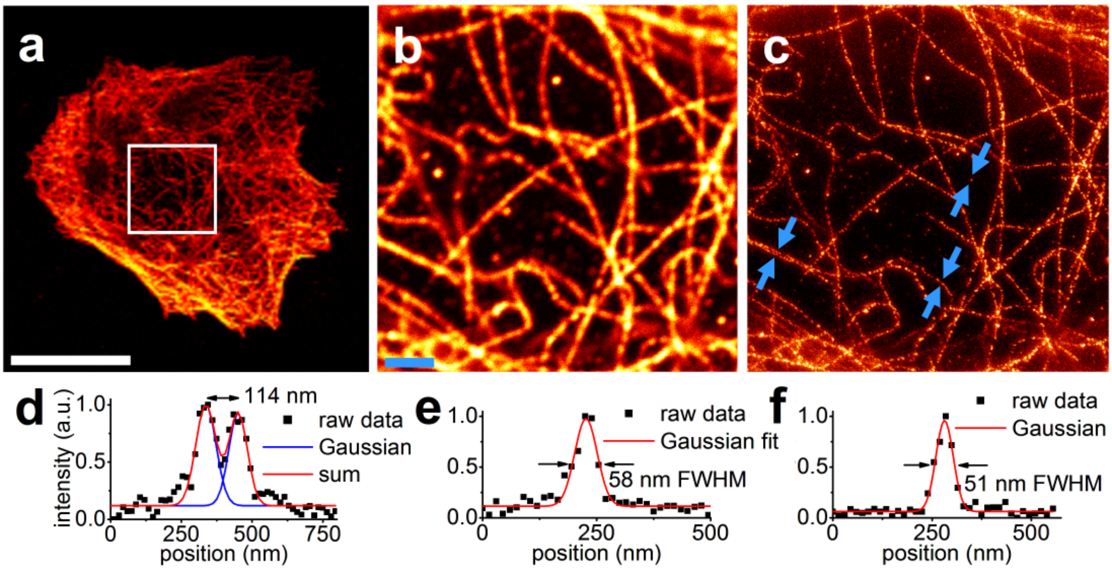

Figure 5.7.: (**a**) Fluorescence images of microtubules in a fixed HeLa cell labeled with Alexa594-β-tubulin. (**b**) Confocal and (**c**) STED images after zooming into the region of interest marked by the white frame. Indicated by arrows are three cross sections; their intensity distributions are shown below. Gaussian fitting resulted in a distance of (**d**) 114 nm and width of (**e**) 58 nm and (**f**) 51 nm for the analyzed structures. Scale bars, 20 µm (panel a) and 2 µm (panel b).

insight into microtubule arrangement (**Fig. 5.7c**). What appeared as a single strand in standard confocal mode actually resolved into two individual microtubules in the STED image. A fit of two Gaussians revealed a mutual distance of 114 nm (**Fig. 5.7d**). An evaluation of the FWHM of single strands resulted in 58 nm (**e**) and 51 nm (**f**) for the STED image, whereas the widths in the confocal image were 277 nm and 283 nm. This corresponds to a more than five-fold improvement in image resolution. The resolution of the STED image was even better than 50 nm, considering the intrinsic 25-nm width of the tubule structures. Fluorescence was excited using 560-nm light at an average intensity of 1.8 µW, whereas fluorescence was depleted within a band of 670/20 nm with 2.5 mW of average intensity. The pulse repetition rate was set to 2 MHz; images were raster-scanned at 200 µs pixel dwell time.

Actin

Actin is found in almost all eukaryotic cells. While being a highly conserved protein, actin has to perform many different tasks. Arranged into filaments, the actin network is responsible for, e.g., cell motility and forms the contractile apparatus of muscle. A more detailed introduction to the role of the actin protein is presented in subsection 7.1.1. For a single actin bundle, a diameter of 35 nm has been reported, however, several of such bundles can arrange into thicker structures [134]. In this experiment, actin was labeled by Atto647N-phalloidin staining fixed HeLa cells (**Fig. 5.7a**). The helical PP was replaced by a circular PP causing a relative phase shift of π in the central region of the depletion beam. The resulting depletion pattern displays a central zero flanked by two strong lobes in axial direction (see subsection 2.5.4). Therefore, a resolution enhancement in

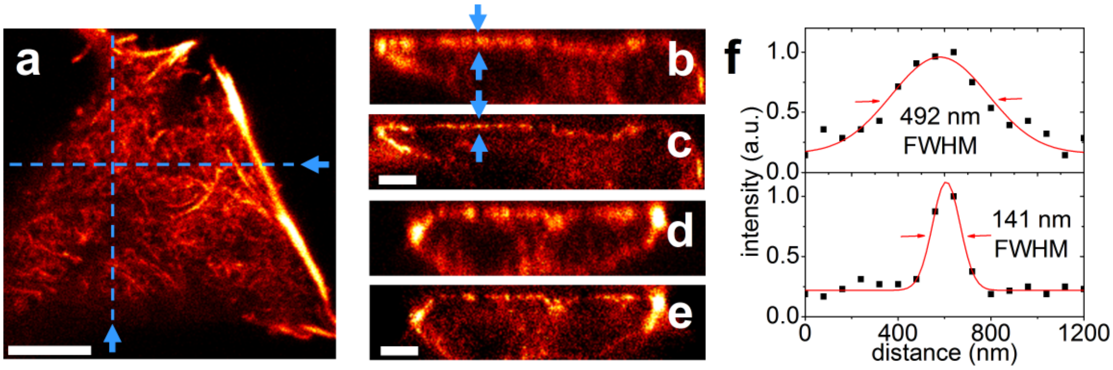

Figure 5.8.: (**a**) Fluorescence image of actin in a fixed HeLa cell labeled with Atto647N-phalloidin. (**b,d**) Confocal and (**c,e**) STED images of single *xz*- and *yz*-planes indicated by dashed lines (panel a). (**f**) Intensity distributions across the feature indicated by arrows. Gaussian fitting resulted in a FWHM of 492 nm for the confocal (top) and a width of 141 nm for the STED image (bottom). Scale bars, 5 µm (panel a) and 2 µm (panels c,e).

axial direction was to be expected. Subsequently, a 3D-stack with a voxel size of 80 nm was recorded for an entire cell, a single xy-plane is shown in **Fig. 5.7a**. From this stack, single xz- and yz-planes were extracted (**Fig. 5.7b-e**). A comparison of confocal and STED images confirmed the resolution enhancement in axial direction by emission depletion. A quantitative evaluation of the cross section marked by arrows resulted in a FWHM of 492 nm for the confocal image, whereas the FWHM of the actin filament was only 141 nm in the STED image, corresponding to a 3.5-fold increase in z-resolution. Fluorescence was excited using 640-nm light at an average intensity of 0.5 µW, whereas fluorescence was depleted within a band of 740/20 nm with 2.2 mW of average intensity. The pulse repetition rate was set to 2 Mhz, images were raster-scanned at 200 µs dwell time per pixel.

Focal Adhesions

Another interesting research area in cell biology addresses focal adhesions. These cell-matrix adhesions are large macromolecular assemblies responsible for cell anchorage onto surfaces. Through focal adhesions, which contain over one hundred different proteins, the cytoskeleton of the cells connects to the extracellular matrix. In this assembly, integrins, which consist of one α- and one β-unit, mediate the contact between focal adhesions and proteins of the extracellular matrix, such as fibronectin. In the intracellular domain, e.g., integrin binds to actin filaments [135] via the adapter protein α-actinin [136]. In this work, β1-integrin was labeled by the antibody 8C8 rendered fluorescent by attachment of Atto647N. **Fig. 5.9a** shows a fluorescence image of a live XTC cell after attachment to the coverslip. Focal adhesions of various sizes and shapes are visible. In **Fig. 5.9b-e**,

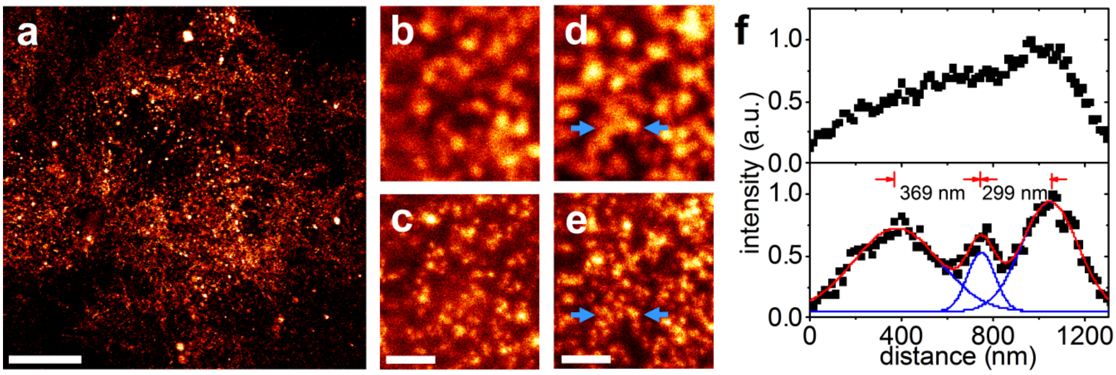

Figure 5.9.: (**a**) Fluorescence image of β1-integrin labeled by Atto647N-8C8 in a live XTC cell. (**b,d**) Confocal and (**c,e**) STED images after zooming into a small region of interest. (**f**) Cross section along the feature indicated by arrows for the confocal (top) and STED image (bottom). Scale bars, 20 µm (panel a) and 1 µm (panels c,e).

regions of interest are shown in confocal and in STED mode, respectively, demonstrating the sub-diffraction resolution achieved by STED. A quantitative evaluation of the fluorescence signal along the direction indicated by arrows revealed three features for the STED image, whereas this structure was blurred in the confocal image. Fluorescence was excited with laser pulses of a wavelength of 640 nm and an average intensity of 1.6 µW, whereas fluorescence was depleted at 780 nm and 100 mW of average intensity, both at a repetition rate of 80 MHz. Images were raster-scanned at 20 µs dwell time per pixel.

Materials and Methods

STED setup: The microscope hardware matched the description given in section 4.1. For 3D image acquisition of actin by Atto647N-phalloidin staining in fixed HeLa cells, the helical phase plate was replaced by the circular phase plate. Fluorescence was filtered by a 676/37 nm bandpass filter (HC 676/37, Semrock) for Atto647N and by a 600/37 nm bandpass filter (HC 600/37, Semrock) for Alexa594.

Protein labeling: Atto647N-DPPE lipids were mixed with BSA to avoid micelle formation in aqueous solution [137]. Briefly, 100 nM of Atto647N-DPPE (Atto-Tec) stock solution ($CHCl_3$) was dried under vacuum followed by addition of ethanol (20 µl) to dissolve the dried lipids. For complex formation, 1 ml of defatted BSA solution (100 µM defatted BSA in HEPES-buffered Dulbecco's modified Eagle's medium (HDMEM)) was added and vigorously vortexed. Addition of 9 ml HDMEM yielded a final concentration of 10 µM BSA. The monoclonal antibodies β1-integrin 8C8 (Hybridoma Bank, Iowa City, USA) and anti-DNP IgE (Sigma-Aldrich) were incubated with Atto647N-NHS (Atto-Tec) for 2 h at 24℃ according to the labeling instructions provided by the manufacturer. Then, the solutions were purified by gel filtration using Sephadex G-25 columns (Sigma-Aldrich).

Cell labeling: For studying the cell membrane, XTC cells attached to chamber slides were incubated on ice for 30 min with Atto647N-DPPE-BSA. For studying focal adhesions, XTC cells cultured in Dulbecco's modified Eagle's medium (DMEM) containing 30% H_2O and 10% fetal bovine serum at 24℃ and 7% CO_2 were first solubilized in complete medium using 10% chicken serum and 2 mM EDTA. For labeling of β1-integrin, $\sim 10^4$ cells were incubated with Atto647N-8C8 (15 µM) for 40 min at 4℃ under constant motion. After that, the cell solution was transferred into chamber slides coated with fibronectin. XTC integrins were labeled by Claudia Winter. For studying dynamics of the FcϵRI complex, RBL-2H3 mast cells cultured in DMEM supplemented with 15% fetal bovine serum at 37℃, 5% CO_2 and 95% humidity were incubated with Atto647N-IgE (15 µM) for 90 min at 37℃, 5% CO_2 and 95% humidity. The cells were then harvested, washed twice with calcium free phosphate buffered saline (137 mM NaCl, 2.7 mM KCl, 6.4 mM Na_2HPO_4, 1.5 mM KH_2PO_4) and resuspended in Tyrode's buffer (137 mM NaCl, 2.7 mM KCl, 1 mM $MgCl_2$, 1.8 mM $CaCl_2$, 0.2 mM Na_2HPO_4, 12 mM $NaHCO_3$, 5.5 mM D-glucose) with 0.1% bovine albumin serum. Then the cell solution was transferred into chamber slides. Mast cells were labeled by Emmanuel Oppong. For imaging of microtubules, HeLa cells cultured at physiological conditions were fixed using 4% PFA (Sigma-Aldrich) in PBS, followed by permeabilization of the cell membrane with a solution of PBS containing 2% BSA and 0.1% Triton X-100 for 30 min. For labeling of tubulin, the cells were first incubated with 1:1000 of polyclonal rabbit anti-β-tubulin (Thermo Scientific, Langenselbold, Germany), followed by incubation with 1:300 of Alexa594 mouse anti-rabbit IgG (Invitrogen), both at 4°C for 12 h. Microtubules in HeLa cells were labeled by Naghmeh Azadfar. For imaging of actin, HeLa cells cultured at physiological conditions were fixed using 4% PFA (Sigma-Aldrich) in PBS, followed by permeabilization of the cell membrane with a solution of PBS containing 0.1% Triton X-100 for 15 min. For labeling of actin, the cells were incubated with 1 µM of Atto647N-phalloidin (Sigma-Aldrich) at 24°C for 70 min. Actin in HeLa cells was labeled by Rosmarie Blomley.

5.1.4. Summary STED Imaging

As part of this work, a STED microscope was implemented and characterized. Fluorescent beads as well as single dye molecules were imaged with a spatial resolution of $40-60$ nm. Consequently, several fluorescently labeled biological specimens were probed by STED microscopy. In HeLa cells, the arrangement of microtubules was visualized in great detail at a lateral resolution more than five times as high as the resolution in standard confocal mode. With a different depletion pattern, 3D stacks of actin were acquired at 3.5 times the standard confocal resolution in the axial direction. For those fixed specimens, the limited temporal resolution of the image acquisition process (several minutes) due to a pulsed laser configuration with a repetition rate of only 2 MHz was not an obstruction.

To study dynamic samples, a second laser configuration with a pulse repetition rate of 80 MHz was implemented. At that repetition rate, the image acquisition time could be reduced to a few seconds. Thus, in living cells, lipids in the plasma membrane, focal adhesions and membrane-bound receptors were imaged by STED microscopy. Within small, micron-sized regions of interest the temporal resolution could be increased to a few frames per second. Yet, processes even faster than that are accessible by STED microscopy. In the next section it is shown how the time structure of a raster-scanned image can be used to uncover dynamics on the microsecond timescale, such as particle translation due to diffusion.

5.2. Application of STED to Fluctuation Spectroscopy

5.2.1. The Idea of STED-FCS

Particle translation dynamics such as free diffusion of fluorescently labeled particles in a lipid bilayer can be probed by FCS (see subsection 3.3.3). Yet, the fluctuations in fluorescence intensity caused by particle movement can only be measured at low average occupation numbers of the molecules inside the observation volume. Otherwise the fluorescence variability caused by particle dynamics is small compared to noise-related fluctuations, e.g., photon shot noise and detector noise. In standard confocal microscopy, the size of the observation volume is governed by diffraction, resulting in a size of $\sim 0.1\,\mathrm{fl}$. Spatial confinement to $\sim 200\,\mathrm{nm}$ in the xy-direction is a result of focusing light by means of a high NA objective lens, whereas the limitation to $\sim 500\,\mathrm{nm}$ in the z-direction is a consequence of either introducing a limiting aperture (pinhole), or of exciting fluorescence using a multi-photon process. Thus, the usable concentration is limited to the pico- to nanomolar range. However, if, e.g., a low affinity binding process is under study, high ligand concentrations are required. Or, in living specimens, the concentrations cannot be controlled at all. In STED microscopy, the effective size of the observation volume can be regulated by the intensity of the STED beam to probe a smaller fraction of molecules (**Fig. 5.10**). At higher concentrations, a decrease of the observation volume can keep the average number of monitored molecules at a level that still produces meaningful correlation amplitudes. Thus, by the application of STED, the usable concentration range of FCS is extended. As an additional benefit, sample inhomogeneities at small, subdiffractional spatial scales, such as the formation of lipid rafts and transient lipid-protein interactions, can be detected by STED-FCS [128, 137]. In a standard confocal measurement, fluctuations due to such interactions are hidden from the observer because of the limited spatial resolution.

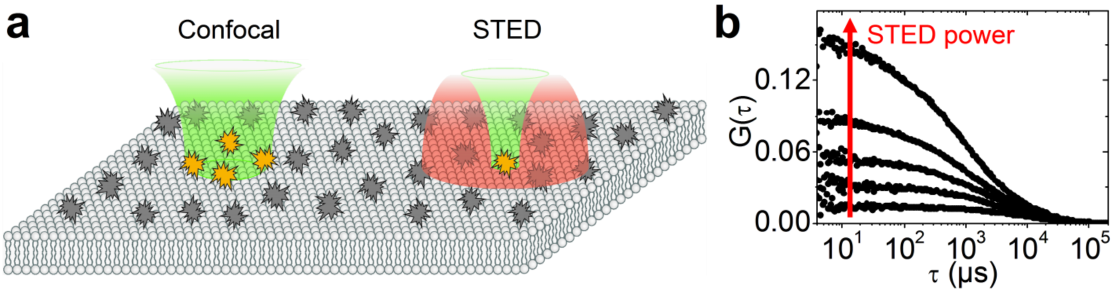

Figure 5.10.: STED-FCS Principle. (**a**) In a lipid bilayer, the fluorescence of freely diffusing molecules passing through a static confocal volume is continuously monitored over time (left). By application of STED, the size of the observation volume can be reduced (right). (**b**) As a result, the correlation amplitude increases with increasing STED intensity (indicated by arrow).

5.2.2. Characterization of STED-FCS

For quantitative evaluation of the reduction of the effective observation volume by means of STED, a lipid bilayer marked by Atto647N-DPPE was prepared. A confocal image of such a bilayer is shown in **Fig. 5.11a**. Fluorescence intensity time traces were recorded at the indicated spot using depletion intensities of $0-200\,\mathrm{mW}$, followed by autocorrelation of the data. The resulting correlation curves were fitted by an equation modeling free, two-dimensional diffusion (**Fig. 5.11b**). At a fixed concentration, the average number of particles residing within the observation volume is directly proportional to the size of the observation volume (equation 3.42). On the other hand, in STED microscopy, the width, σ_{STED}, of the effective focal spot is determined by the square root law (equation 2.98). As a result, the average number of particles representing the inverse of the autocorrelation amplitude, $G(0)$, should scale with the applied STED intensity, I_{STED}, according to,

$$< N > \propto \sigma^2_{\mathrm{STED}} = \frac{\sigma^2_{\mathrm{conf}}}{1+\sigma^2_{\mathrm{conf}} a^2 \frac{I_{\mathrm{STED}}}{I_{\mathrm{sat}}}}. \tag{5.1}$$

This dependence was confirmed by a fit of equation 5.1 to the experimental data as presented in **Fig. 5.11c**.

It is noteworthy that this linear dependence of the autocorrelation amplitude, $G(0)$, on the STED power was only found at larger STED wavelengths. At STED wavelengths closer to the emission maximum of Atto647N, saturation occurred, as depicted in **Fig. 5.12**. Presumably, this effect was due to excitation rather than depletion by STED photons.

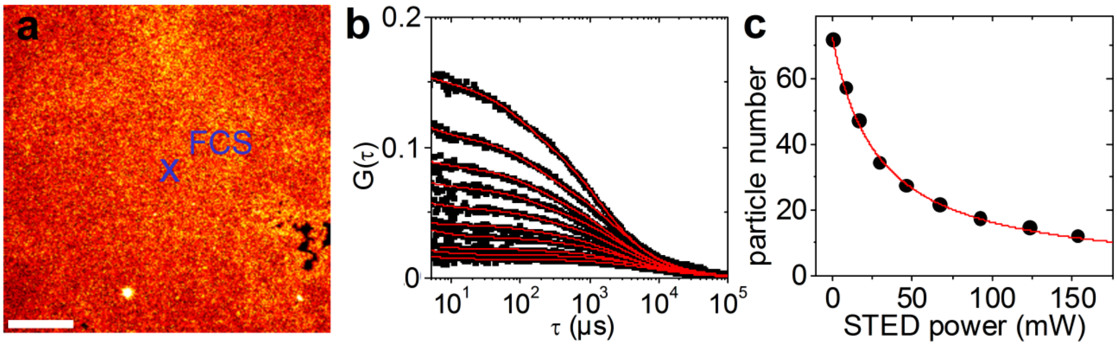

Figure 5.11.: STED-FCS in a lipid bilayer. (**a**) Fluorescence image of a lipid bilayer labeled with Atto647N-DPPE. The location of the subsequent FCS measurements is marked by a cross. Scale bar, 10 µm. (**b**) Autocorrelation data (squares) and fits with a two-dimensional diffusion model (red lines). (**c**) Average particle numbers that resulted from the fits at different STED intensities (dots) fitted by equation 5.1 (red line).

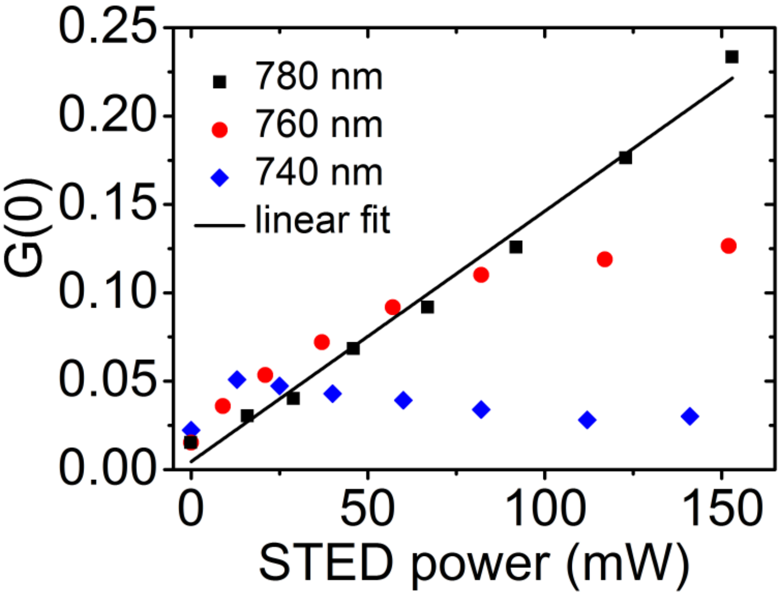

Figure 5.12.: Autocorrelation amplitudes of STED-FCS measurements in a lipid bilayer labeled with Atto647N-DPPE at different STED wavelengths and intensities.

Materials and Methods

Lipid bilayer preparation: Planar lipid bilayers were prepared according to subsection 3.2.3.

STED setup: The STED microscope described in subsection 4.1.2, with the helical PP and a depletion wavelength of 780 nm, was used for these measurements. The fluorescence emission was filtered by a 676/37 nm bandpass filter (HC 676/37, Semrock), recorded with a TCSPC system (Simple-Tau 152, Becker & Hickl) and autocorrelated with the company's software.

FCS data analysis: The FCS data were fitted according to a model that took into account diffusional dynamics, triplet state population and a kinetic term representing changes in the fluorescence brightness. Thus, the model function was

$$G(\tau) = \frac{1}{< N >} \cdot G_D(\tau) \cdot G_T(\tau) \cdot G_K(\tau), \tag{5.2}$$

with translational diffusion term, $G_D(\tau)$, (equation 3.41), triplet term, $G_T(\tau)$, (equation 3.46), kinetic term, $G_K(\tau)$, (equation 3.50) and the average number of particles, $< N >$, inside the observation volume. In the analysis, the characteristic time for triple state population, τ_T, was fixed at 5 µs, and the time for changes in brightness, τ_K, was limited to a range of $50 - 150$ µs [137].

5.2.3. The Concept of STED-RICS

In general, static FCS measurements work very well with structures displaying homogeneous dynamics over a wide area, so the point of observation is not relevant. However, when it comes to simultaneous monitoring of multiple regions of interest as required for samples with heterogeneous dynamics, static FCS is difficult to apply. Under these circumstances, as is often the case with living cells and tissues, RICS is a more suitable approach. In RICS, a wide area is imaged by repeated scanning across the sample followed by a correlation analysis of relevant subregions within the acquired images (see subsection 3.3.5). By this multiplexing approach, for example, translational dynamics of protein complexes in cell adhesions was studied [138] and diffusion restrictions on adenosine triphosphate (ATP) in rat cardiomyocytes were quantified [139]. Furthermore, as for other scanning FCS methods [140, 141], such as line scanning FCS [142] or circle scanning FCS [143], bright immobile objects can be isolated and removed in RICS data analysis [144]. In static FCS, such objects distort the autocorrelation analysis and falsify the results. Unfortunately, the spatial resolution of a mobility map obtained by RICS is again limited by the optical resolution during image acquisition. However, by the application of STED to RICS, dynamics can be studied within smaller regions of interest due to the improved spatial resolution (**Fig. 5.13a**). Also, STED-RICS exhibits the same benefits as STED-FCS. At high particle concentrations a decrease of the effective size of the observation volume yields more meaningful correlation amplitudes (**Fig. 5.13b**). Likewise, a higher spatial resolution enables the detection of sample inhomogeneities at smaller spatial scales. Hence, the combination of STED and RICS yields a powerful tool for studying cellular dynamics.

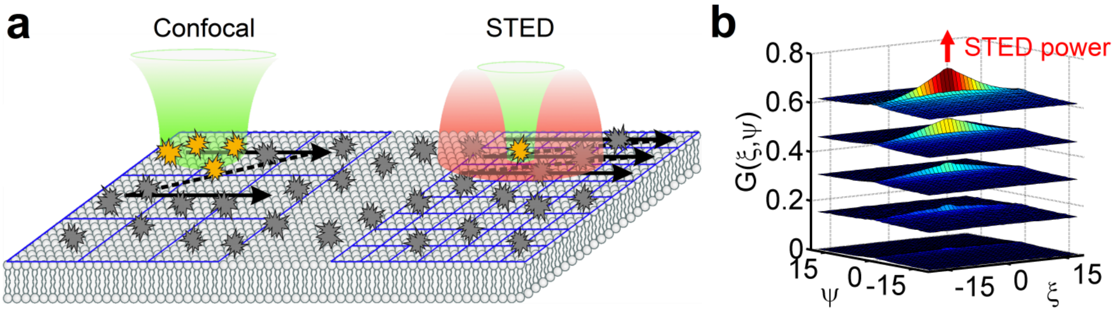

Figure 5.13.: STED-RICS Principle. (**a**) Fluorescence images of, e.g., the plasma membrane of a cell are acquired by scanning the confocal volume across the sample (left). By application of STED the size of the observation volume and, thus, the pixel size can be reduced (right). (**b**) As in STED-FCS, the correlation amplitude increases with increasing STED intensity (red arrow).

5.2.4. Characterization of STED-RICS

To evaluate the performance of STED-RICS, a lipid bilayer labeled with Atto647N-DPPE was prepared as a model for diffusion within cell membranes. In this homogeneous bilayer, a region of $2 \times 8\,\mu m^2$ (256×1024 pixels, $8\,\mu s$ pixel dwell time) was imaged repeatedly (20 frames) at various STED intensities. Due to the high marker concentration within the sample, the confocal volume is densely populated. As a result, in confocal mode, the fluorescence fluctuations due to particle translation are small compared to the fluctuations by photon shot noise (**Fig. 5.14a**, upper-left). At a STED wavelength of 780 nm and a focal power of ~ 200 mW, the effective size of the observation volume is significantly decreased (see subsection 5.1.2). Thus, due to the lower average number of molecules within the smaller volume, the movement of single markers in and out of the observation volume strongly affects the fluorescence signal. These fluctuations

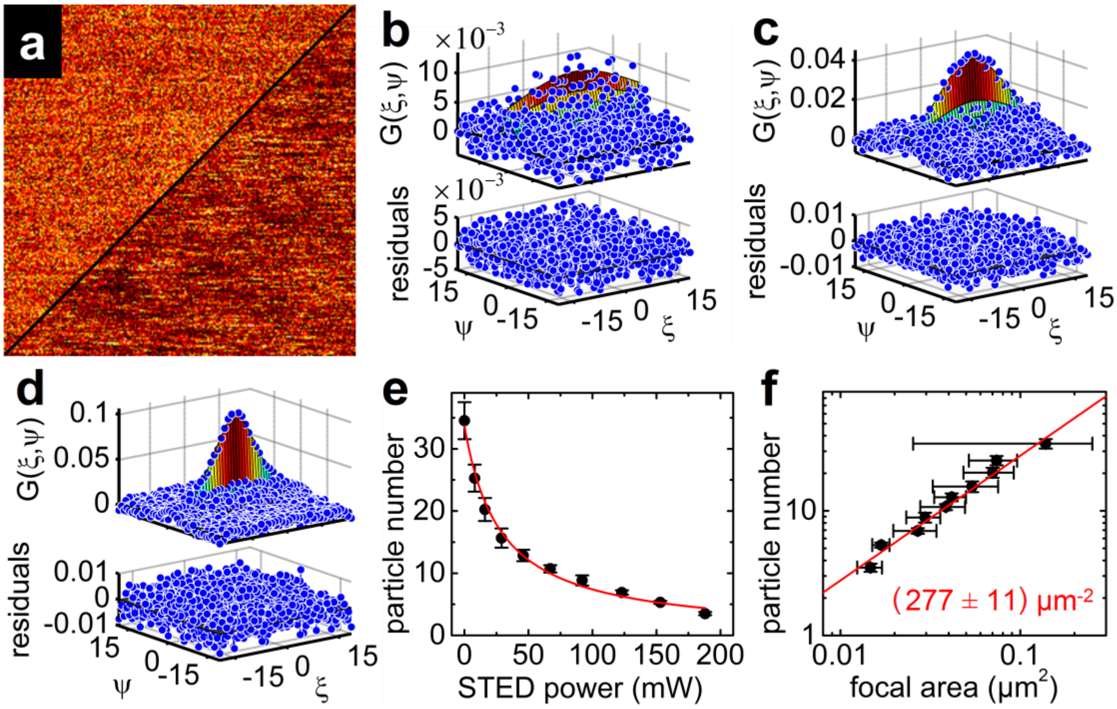

Figure 5.14.: STED-RICS in a lipid bilayer. (**a**) Confocal laser scanning image of Atto647N-DPPE in confocal (upper-left) and STED mode (lower-right). (**b-d**) Exemplary data sets of image correlations (dots) and subsequent fitting of a function modeling free diffusion on a surface at 0 mW, 67 mW and 188 mW of STED power, respectively. (**e**) Average number of particles obtained from STED-RICS analysis as a function of the STED power (dots) fitted by equation 2.98 (red line). (**e**) Average number of particles as a function of the focal area, both obtained from STED-RICS analysis. The particle concentration was determined by a linear fit (red line).

of the marker population appear as stripes in the image, emerging from an accidental agreement of the motion direction of one or more markers with the scanning direction, temporarily increasing the local marker concentration (**Fig. 5.14a**, lower-right). Image stacks of the same region were recorded in confocal mode and at nine different STED intensities at 24°C. Eight sub-regions (128×128 pixels) were extracted from each image set and autocorrelated, followed by fitting of a function modeling free diffusion (**Fig. 5.14b-d**). For the analysis, a reference value for the diffusion coefficient of the labeled lipids, $D = (2.9 \pm 0.4)\,\mu\text{m}^2/\text{s}$, was determined by FRAP, which is in good agreement with the literature value, $D = (3.5 \pm 0.3)\,\mu\text{m}^2/\text{s}$, obtained for a similar sample [145]. In **Fig. 5.14e**, the average particle numbers that resulted from the fits are plotted as a function of the applied STED power. As for STED-FCS, the experimental data were validated by a fit of equation 5.1. In **Fig. 5.14f**, the same average particle numbers are plotted as a function of the focal areas obtained from the analysis. By a fit of equation 3.42, the average particle concentration was determined, $< C >= 277\,\mu\text{m}^{-2}$. At high marker concentrations, application of STED can significantly increase the precision of a RICS experiment, as indicated by the reduced standard deviation at higher STED intensities.

At the same time, RICS measurements can directly profit from an increase in spatial resolution. In confocal RICS, particle movement within structures smaller than $\sim \lambda/2$ cannot be mapped. Application of STED to RICS can provide access to dynamics inside such structures. This is also true for static STED-FCS which, however, does not provide multiplexing. And, since the resolution of the diffusion map from a RICS measurement scales with the image resolution, the multiplexing capability of STED-RICS is even greater than of confocal RICS. To prove this point, another lipid bilayer was prepared that had local defects. The corresponding confocal and STED images are shown in **Fig. 5.15a,c**. Small defects were washed out in confocal mode due to insufficient spatial resolution. RICS relies on the assumption that there is no variation of particle mobility within the region of interest to be analyzed, here marked by a blue box (64×64 pixel, $2 \times 2\,\mu\text{m}^2$). In confocal mode, the defects, which contained no molecules at all, were represented as dim patches of low marker concentration. Additionally, insufficient sampling led to poor statistics for the intact area. Therefore, after image correlation, these local variations appeared as false long-range correlations (**Fig. 5.15b**), rendering further data analysis quite complicated. However, in STED mode, the defects were correctly imaged as tiny, empty regions. Also, due to the increased image resolution, the image intensity fluctations due to lateral diffusion were much higher giving rise to significantly improved statistics for the populated regions. Thus, false long-range correlations hardly showed up in the correlation functions (**Fig. 5.15d**).

An important aspect of both standard RICS and STED-RICS measurements is the use of appropriate pixel sizes. The pixel size has an influence on two image acquisition parameters, the image resolution and the scanning speed. If the raster is too coarse, the optical resolution available is not utilized and small subregions cannot be analyzed. To be able to temporarily resolve the particle motion, the pixel dwell time, τ_p, must be

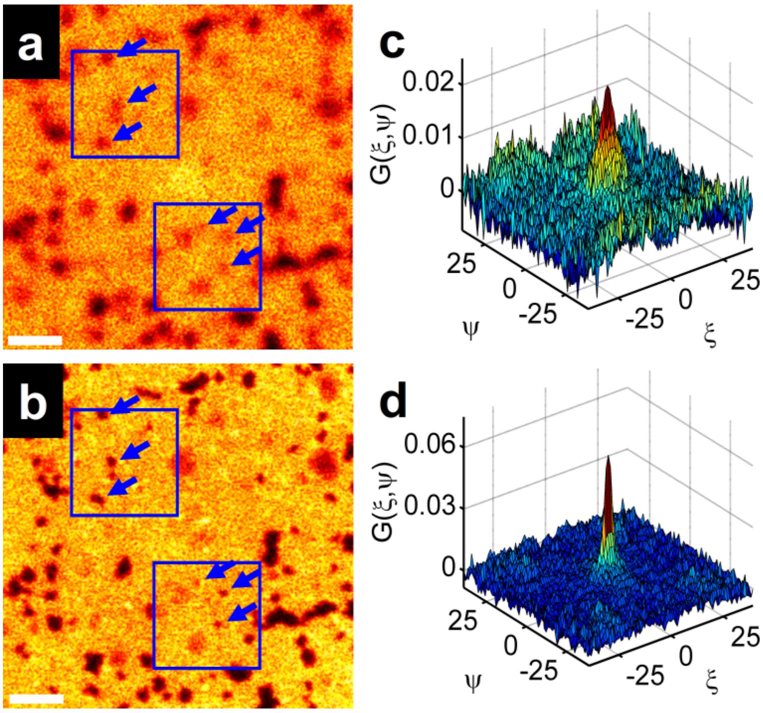

Figure 5.15.: Lipid bilayer with local defects. Compared to (**a**) standard confocal imaging, the resolution enhancement by (**b**) 60 mW of STED power can be seen from the projections of the image stacks recorded. For correlation analysis, subregions of 64 × 64 pixels were selected (blue boxes). Image details can be differentiated more clearly in STED mode, whereas they are blurred in standard confocal mode (indicated by blue arrows). Thus, false, long-range correlations showed up in (**c**) confocal mode, whereas these were mostly suppressed in (**d**) STED mode. Scale bars, 1 µm.

smaller than the diffusion time, $\tau_p < \tau_D$. In laser scanning microscopy, the pixel size, δ_r, is related to the scanning velocity of the focus, v_s, and the pixel dwell time via $\delta_r = v_s \tau_p$. On the other hand, the particle displacement, Δ_r, due to, e.g., two-dimensional diffusion with diffusion coefficient, D, is determined by

$$\Delta_r = \sqrt{4D\tau_D}. \tag{5.3}$$

Thus, to be able to spatially resolve the underlying process, the pixel size should be chosen such that

$$\delta_r < \sqrt{4D\tau_D}. \tag{5.4}$$

As an example, the pixel-to-pixel correlation of STED-RICS measurements in a lipid bilayer labeled with Atto647N-DPPE using 200 mW of STED intensity and various pixel sizes is shown in **Fig. 5.16**. The correlation amplitude increased with decreasing pixel size and saturated at 10 nm.

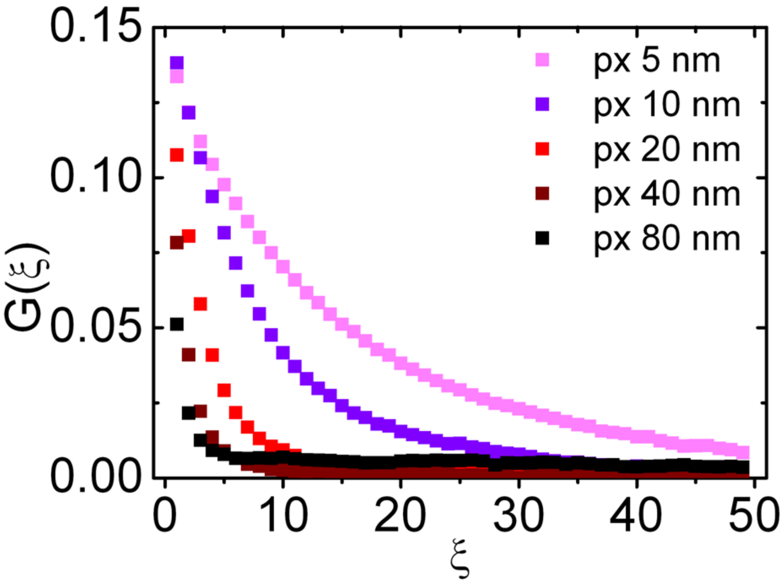

Figure 5.16.: Pixel-to-pixel correlation of STED-RICS measurements on a lipid bilayer labeled with Atto647N-DPPE, using 200 mW of STED intensity and various pixel sizes.

Since the diffusion coefficient of the lipid bilayer was known, it was used as a reference for further live-cell experiments. For that purpose, the inverse of the focal area, which was determined by STED-RICS analysis (see **Fig. 5.14f**), was plotted as a function of the STED power and modeled by a linear fit (**Fig. 5.17**).

Materials and Methods

Lipid bilayer preparation: Planar lipid bilayers were prepared according to subsection 3.2.3.

STED setup: The STED microscope described in subsection 4.1.2 was used, with the helical PP and a depletion wavelength of 780 nm. Fluorescence was filtered by a 676/37 nm bandpass filter (HC 676/37, Semrock).

RICS data analysis: After substraction of an immobile fraction according to Rossow et al. [146], the images were correlated by homemade software written in Matlab (MathWorks, Ismaning, Germany). The RICS data were fitted with a model that took into account lateral diffusion, $G_D(\xi,\psi)$, (equation 3.41), a kinetic term representing changes in the fluorescence brightness, $G_K(\xi,\psi)$, (equation 3.50), and the scanning motion of the observation volume, $S(\xi,\psi)$, (equation 3.58). Thus, the model function was

$$G(\xi,\psi) = \frac{1}{<N>} \cdot G_D(\xi,\psi) \cdot G_K(\xi,\psi) \cdot S(\xi,\psi). \tag{5.5}$$

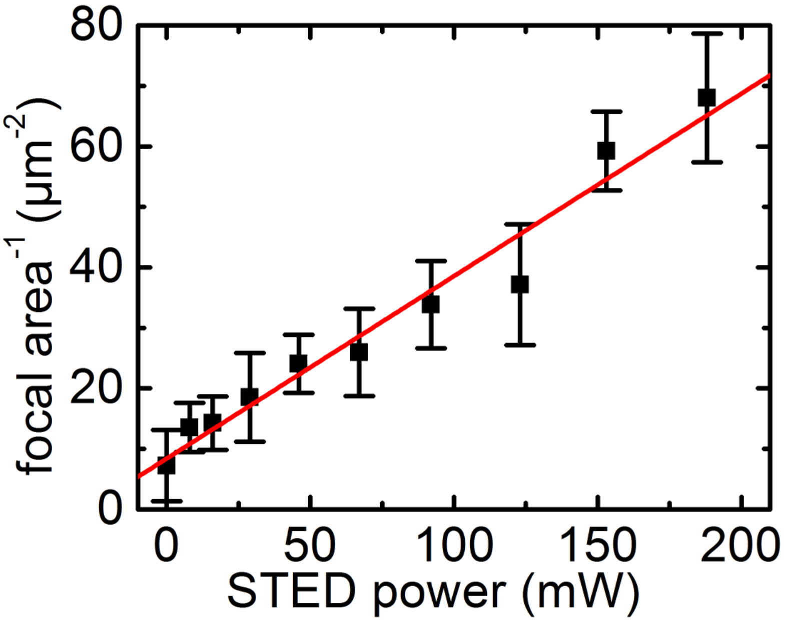

Figure 5.17.: Inverse of the focal area as a function of the STED power determined by STED-RICS in a lipid bilayer of $D = (2.9 \pm 0.4)\,\mu\text{m}^2/\text{s}$ (dots) modeled by a linear fit (red line).

In contrast to STED-FCS, it was not necessary to include a triplet term in STED-RICS analysis, since the characteristic time for triplet state population, $\tau_T \sim 5\,\mu\text{s}$, was not covered by the temporal resolution of the measurement due to pixel dwell times of $\tau_p \geq 8\,\mu\text{s}$.

5.2.5. STED-RICS Applications

In a perfectly homogeneous environment such as an ideal lipid bilayer, the multiplexing capability of (STED-)RICS is not of any particular advantage. However, when studying living cells and tissues, which display a pronounced heterogeneity, the situation is completely different. For static (STED-)FCS, the observation volume has to be placed precisely into the region of interest. If this region is small, cell movement can easily lead to misplacement of the observation volume. This problem might even remain undetected, since there is no image information available during the FCS measurement and, thus, meaningless data may be recorded. Furthermore, many processes in cell biology are limited to a certain time frame. Static FCS data at multiple areas can only be acquired in a serial manner and, consequently, the temporal resolution required for the observation might not be sufficient. In contrast, multiple regions of interest can be selected from a single RICS measurement. Furthermore, an overview of the sample status is always available from the individual image frames acquired during the measurement. Therefore, cell movement can be tracked and questionable regions excluded from the analysis. Additionally, fluorescence from static emitters can be removed by subtracting an immobile fraction in RICS analysis. To demonstrate how the application of STED can considerably improve the data quality of RICS, we measured translational diffusion in different live cell samples.

Plasma Membrane of XTC Cells

In a first experiment, we labeled the lipid membrane of XTC cells using Atto647N-DPPE (**Fig. 5.18a**). Membrane dynamics was analyzed using STED-RICS as well as conventional RICS within a total area of $18 \times 20\,\mu\mathrm{m}^2$ by scanning seven regions of 256×2048 pixels at 24℃. A cut-out of such a region is shown on the right-hand side of **Fig. 5.18a** in STED (left) and confocal (right) mode. Here, it can be seen that structures in the STED image are visible in much more detail. As an example, correlation data were analyzed within a region of $640 \times 640\,\mathrm{nm}^2$ marked by a white box. The corresponding results are shown in **Fig. 5.18d** for STED-RICS and standard RICS, respectively. The analysis of the STED-RICS data resulted in a diffusion coefficient of $(1.7 \pm 0.5)\,\mu\mathrm{m}^2/\mathrm{s}$ for DPPE in the plasma membrane of XTC cells, similar to the value of the lipid bilayer as described in subsection 5.2.4 at the same temperature (**Fig. 5.19**). The image correlation obtained by confocal RICS was difficult to evaluate because of a low amplitude resulting from the high marker concentration and a low signal-to-noise ration due to the small size of the region of interest with respect to the optical resolution.

Focal Adhesions of XTC Cells

In another experiment, the translation dynamics within focal adhesions of XTC cells was studied by imaging β1-integrin marked with the monoclonal antibody 8C8 labeled with Atto647N (**Fig. 5.18b**). After cell adhesion, RICS data were recorded in areas of $4 \times 16\,\mu\mathrm{m}^2$ (256×1024 pixels) at 24℃. A cut-out of a STED (left) and a confocal (right) RICS measurement is shown on the right-hand side of **Fig. 5.18b**. While super-resolution pulse-chase experiments could already resolve the assembly and disassembly of single focal adhesions in detail by looking at paxillin [86], STED-RICS analysis inside individual, established focal contacts of sub-micron size revealed slow dynamics for β1-integrin with $D = (0.10 \pm 0.06)\,\mu\mathrm{m}^2/\mathrm{s}$ at 24℃, as indicated by a strong line-to-line correlation (**Fig. 5.18e**, left). In contrast, the correlation of confocal RICS data was of too poor quality to be further evaluated.

IgE Receptor at the Plasma Membrane of Mast Cells

Another important application of (STED-)RICS is the study of receptor-ligand interactions at the cell membrane. Therefore, we added monoclonal anti-DNP IgE-Atto647N to live RBL-2H3 mast cells binding to the IgE receptor FcϵRI located at the plasma membrane. It can be seen that the bound complex was not homogeneously distributed over the cell membrane, but concentrated in patches of high local concentration (**Fig. 5.18c**). Again, a significant correlation amplitude was obtained only by application of STED (**Fig. 5.18f**). STED-RICS data analysis of such sub-micron sized areas revealed a diffusion coefficient of $(0.6 \pm 0.3)\,\mu\mathrm{m}^2/\mathrm{s}$ at 37℃. Due to the high label concentration and

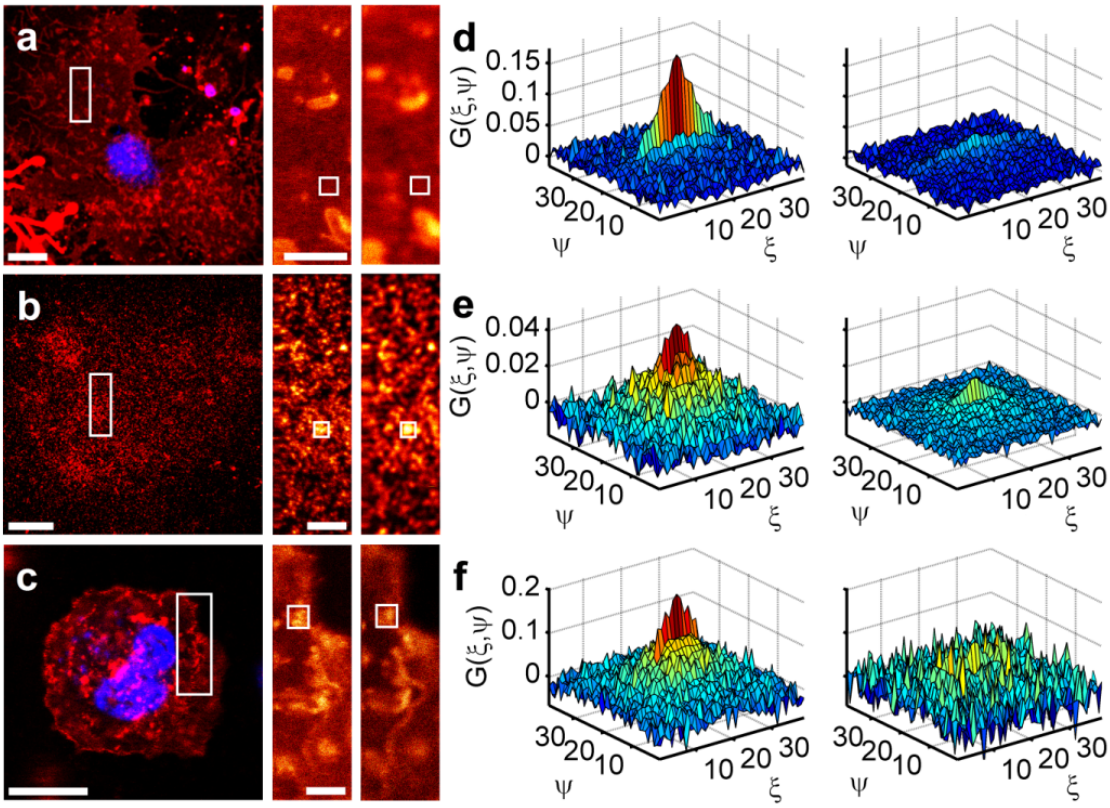

Figure 5.18.: STED-RICS in living cells. (**a-c**) Fluorescence images of DPPE in XTC cells, 8C8 in XTC cells and IgE in RBL-2H3 mast cells, all labeled with Atto647N (red channel). For samples (a,c), the cell nucleus was stained by Hoechst 33258. Blue fluorescence of Hoechst was excited at 780 nm by means of a two-photon process. On the right hand side of each image, the region marked by the white box is expanded and shown as STED (left) and confocal (right) images. (**d-f**) Results of raster image correlation within the corresponding regions marked by the white frames for the STED (left) and confocal (right) images. Scale bars, 10 µm (panels a-c, left) and 2 µm (panels a-c, right).

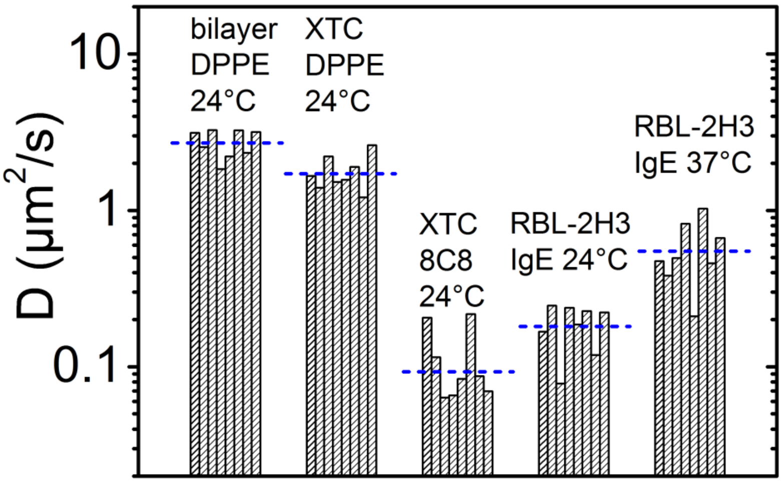

Figure 5.19.: Overview of the diffusion coefficients obtained by STED-RICS for different samples and temperatures. The individual measurements are represented as narrow colums, the average is marked by dotted lines.

sub-micron sized regions of interest, the image correlations resulting from the confocal data sets showed poor signal-to-noise and were thus not suitable for further analysis by fitting of a model equation.

Data for RICS analysis were acquired with different pixel sizes, dwell times and STED intensities, adapted to the different dynamics of the samples under study (**Tab. 5.1**). For example, for the fast diffusion of DPPE in XTC cells, a pixel size of 10 nm and a dwell time of 10 µs were used. In the case of the much slower dynamics of 8C8 antibodies binding to β1-integrin on XTC cells, the pixel size was increased to 16 nm and the dwell time was reduced to 20 µs.

Table 5.1.: Overview of the imaging parameters used in the STED-RICS measurements for different samples.

Sample	τ_p (µs)	δ_r (nm)	I_{STED} (mW)	T (°C)
Bilayer DPPE	8	8	188	24
XTC DPPE	10	10	203	24
XTC 8C8	20	16	100	24
RBL-2H3 IgE	10	16	203	24/37

Extensive Mapping of Large Regions of Interest

In RICS, line-to-line correlation analysis becomes impossible if the dynamic process under study is so fast that the correlation has decayed from one line to the next. Therefore, to maintain a short line-to-line delay time, the maximum number of pixels in a single line is limited. However, the maximum number of lines in a single frame is not limited as long as the dynamics does not change within the total acquisition time. As a consequence, it is advantageous to image narrow strips instead of quadratic regions. Data acquisition can be extended in the horizontal direction by dividing a large region of interest into several image strips that are sequentially acquired. In **Fig. 5.20**, diffusion of Atto647N-DPPE in the membrane of an XTC cell was extensively mapped by recording seven regions of 256 × 2048 pixels each (10 nm pixel size) in STED and confocal mode, resulting in a total observation area of $18 \times 20\,\mu\text{m}^2$. Exemplary subregions were analyzed by image correlation shown on the left and the right of the images. Again, the difference in signal-to-noise between correlation of the STED and confocal data was clearly visible.

Materials and Methods

Protein labeling: Proteins were labeled as described in subsection 5.1.3.

Cell preparation: Cells were prepared as described in subsection 5.1.3. The nucleus was stained by incubating the cells with Hoechst 33258 (Sigma-Aldrich) for 30 min.

STED setup: The STED microscope described in subsection 4.1.2 was used, cells were imaged according to subsection 5.2.4.

RICS data analysis: RICS data were analyzed as described in subsection 5.2.4.

5.2.6. Summary and Discussion STED-RICS

One of the main advantages of super-resolution microscopy by STED is its imaging speed. Recently, video-rate STED has been demonstrated for micron-sized regions of interest, mapping the vesicle mobility within the highly confined space of synaptic boutons [127]. In this work, similar pixel dwell times ($< 10\,\mu\text{s}$) were used to apply STED to RICS. RICS is an elegant and powerful tool for studying dynamics in living cells and tissues. By application of STED microscopy, the versatility of RICS can be significantly increased. Due to the improvement in spatial resolution, cellular dynamics can be quantified within tiny moieties. Also, as for STED-FCS, the applicable concentration range can be extended, more suitable for the concentrations usually encountered in biological specimens. Thus, we were able to quantify membrane, focal adhesion and receptor dynamics in sub-micron sized regions at high signal-to-noise in living cells. This super-resolution technique will be of great help for uncovering cellular dynamics in much greater detail, especially in combination with recently developed labeling techniques such as SNAP-tag [147] and CLIP-tag systems [148] that allow for an intracellular application of STED-compatible dyes in living cells.

The limitation of RICS in comparison to static FCS is the rather confined timescale available for the observation of dynamics. On the one hand, the lower limit is determined

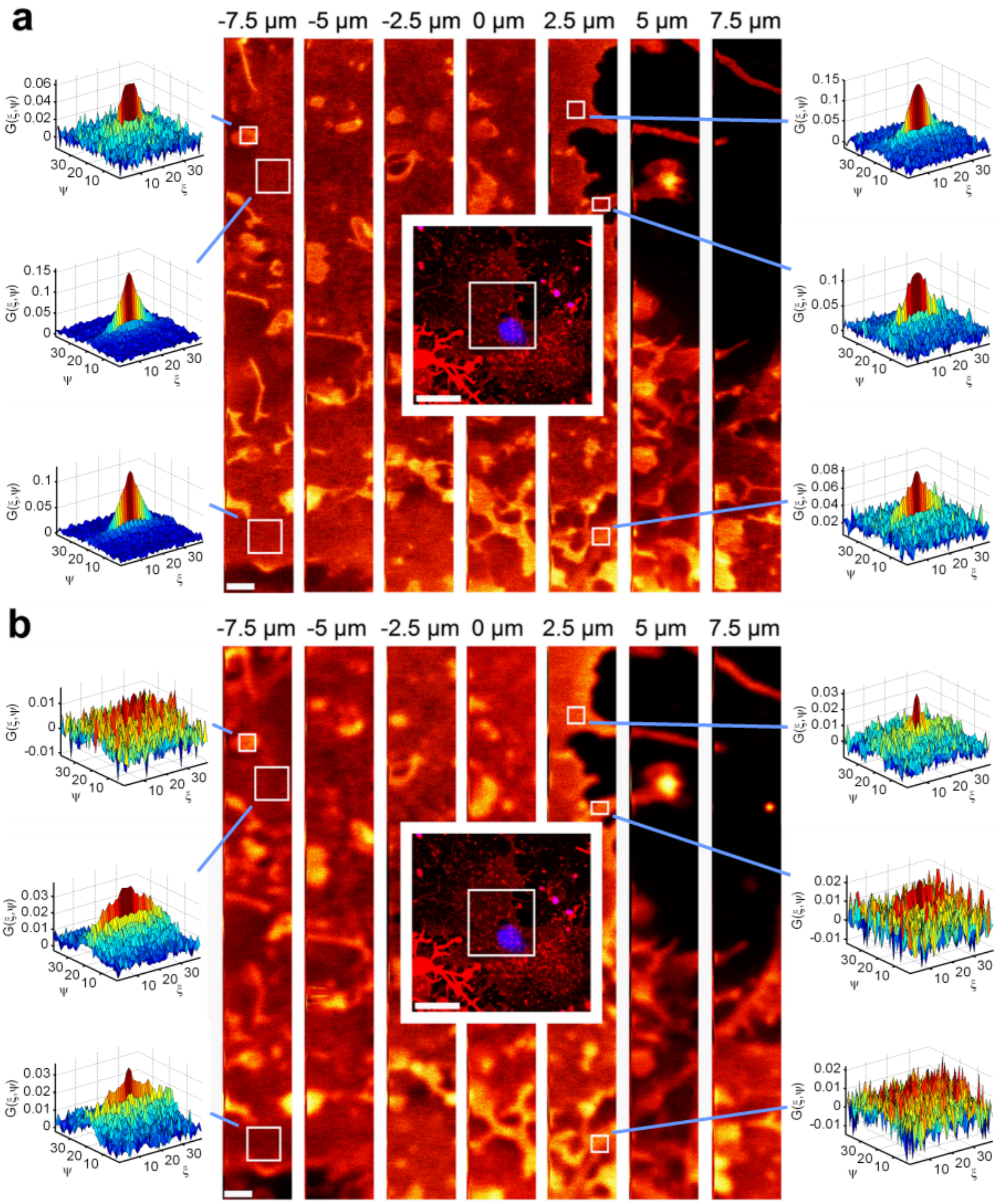

Figure 5.20.: The diffusion of Atto647N-DPPE in the membrane of an XTC cell was extensively mapped by recording multiple regions in (**a**) STED and (**b**) confocal mode. An overview of the entire cell is shown in the centers of the middle panels as insets. RICS correlation functions are shown on the left and on the right hand sides of the images for subregions indicated by white rectangles in the middle panels. Scale bars, 20 µm (central insets) and 1 µm.

by the minimum pixel dwell time, which is typically in the range of a few microseconds in a confocal laser scanning setup. Consequently, faster processes on the nanosecond timescale such as rotational dynamics and antibunching effects [149] cannot be probed by RICS. On the other hand, the scanning motion superimposed on particle translation causes an additional exponential decay of the autocorrelation function. Thus, a correlation due to particle dynamics on timescales much slower than the pixel and line dwell times is strongly suppressed. The limited timescale impedes the application of more advanced fitting models such as multi-component systems or anomalous diffusion. For example, STED-FCS data of Atto647N-DPPE in the plasma membrane of XTC cells prepared according to the same protocol as used in this work could not be fitted well with a simple, single-component diffusion model [150]. Instead, the data were better represented if a two-component model was assumed, which resulted in a diffusion coefficient of $D = 0.8\,\mu\text{m}^2/\text{s}$ for the fast component. The lowest value for such a sample found by STED-RICS with the data analyzed by a single-component diffusion model was $D = 1.2\,\mu\text{m}^2/\text{s}$. However, with STED-FCS, the sample was probed at a single, specific region. For better statistics, the specimen needs to be probed at many different spots. Yet, this is difficult with static FCS due to the lack of multiplexing. Furthermore, in STED-RICS analysis, an immobile fraction was identified and removed from the data which was not possible for STED-FCS. Such a static or very slowly moving subpopulation could shift the resulting diffusion coefficient towards lower values. This potential influence on the data is supported by measurements in a lipid bilayer. Here, static FCS data were only well represented with an anomalous diffusion model. A fit with such a model resulted in a time-dependent diffusion coefficient of $D = 1.5\,\mu\text{m}^2/\text{s}^\alpha$ with $\alpha = 0.7$ indicating hindered diffusion [150]. For such a sample, higher diffusion coefficients were measured by FRAP, i.e., $D = (2.9 \pm 0.4)\,\mu\text{m}^2/\text{s}$, the reference value used for STED-RICS data evaluation. Like RICS, FRAP also distinguishes between a mobile and an immobile fraction in the analysis, and the fluorescence recovery was well represented with a standard, single-component diffusion model (**Fig. 3.4a** in subsection 3.2.3). Furthermore, for a bilayer composed of the same lipids but labeled with rhodamine-DHPE (structurally identical to DPPE) instead of Atto647N-DPPE, a similar diffusion coefficient of $D = (3.5 \pm 0.3)\,\mu\text{m}^2/\text{s}$ was reported by Ries et al. [145], from line-scanning two-foci FCS.

Still, for many specimens, normal single-component diffusion might not suffice as a model. The correlation range of a RICS measurement could be extended towards longer lag times by a second measurement with different imaging parameters. Thus, several measurements with scan parameters optimized for different timescales followed by a global fitting procedure could accommodate for more sophisticated models to study a system including a wider range of dynamics.

6. Rapid Actions of the Gluococorticoid Receptor in Mast Cells Studied by TIRFM

6.1. Allergic Reactions Due to Signaling in Mast Cells

6.1.1. Introduction to the Immune System

The immune system of the human body involves complex interactions of cells, tissues and organs taking place on several spatial scales. Usually, the immune system is triggered by small molecules, i.e., on the nanoscale. Intracellular signaling is followed by cells interacting with other cells and tissues on the microscale resulting in systemic changes, i.e., changes on the macroscale of the entire body. The purpose of the immune system is to keep potentially harmful invaders from attacking and permanently damaging the structure and function of our body. Among these attackers are tiny organisms such as bacteria, parasites and fungi as well as viruses, a more primitive construct lacking its own metabolism. However, the human body also houses foreign organisms that are essential for the function of our metabolism, including food digestion in the bowel by *E. coli* bacteria. Therefore, the first step of an immune response is friend or foe recognition. The body's own cells, or friendly cells, carry specific molecules on their plasma membrane identifying them as 'self'. Cells or organisms not carrying these markers or decorated with different molecules are recognized as 'foreign', and the immune system quickly launches an attack on them. Any particle provoking such an immune response is called an antigen.

The organs of the immune system are called lymphoid organs; they are distributed all over the body. They include thymus, spleen, several lymph nodes/vessels and are home to white blood cells called lymphocytes. The stem cells in the bone marrow are the sources of lymphocytes just as for all other blood cells. Among lymphocytes are T cells, maturing in the thymus before migrating to other tissues, B cells and plasma cells, which are activated B cells producing antibodies. Lymphocytes can move within the entire body patrolling for foreign antigens using either the blood vessel system or the system of lymphatic vessels. The surface of T cells is decorated with specialized receptors that recognize fragments of antigens on the membrane of other infected or cancerous cells. Helper T cells communicate with other immune cells; they stimulate the production of antibodies in B cells, attract phagocytes to digest microbes and activate different T cells. Killer T cells contain potent chemicals to attack cells carrying foreign molecules on their surfaces. B cells produce and secrete antibodies into the bloodstream that bind foreign antigens. Each B cell produces one specific type of antibody. Only upon recognition of the matching antigen, the B cell is activated, giving rise to the production of other B cells producing the same antibody, then referred to as a plasma cell. Whereas phagocytes are large cells that can ingest entire microbes, granulocytes destroy foreign microorganisms by the release of granules filled with potent chemicals. In the same way, mast cells attack harmful cells or microbes nearby. Yet, mast cells are not blood cells but located in tissues and organs such as lung, skin, tongue, and nose.

Normally, the immune system will only attack foreign and potentially harmful intruders. However, in rare cases, the immune system misinterprets own antigens and launches an attack against the body's own cells and tissues. Such a behavior is called an autoimmune disease. Also, the immune system can respond to harmless foreign substances such as pollen from certain plants. Such substances are named allergens, and the inappropriate response of the immune system is called allergy. While the vigorous immune response eliminating all kinds of threats ensures survival, misguided reaction can result in severe illness and even death. Therefore, understanding signaling events triggering an immune response is of great importance in biology and medicine. Based on this knowledge, the effectiveness of the immune system against particles and microbes causing diseases can be enhanced, whereas misguided attacks can be eased or inhibited.

6.1.2. Allergic Reaction

Allergic reactions are a response of the immune system to harmless material. Common allergens include pollen, mold, substances contained in certain foods, or house dust mites. These allergies are related to the immunoglobulin E (IgE)-antibody. Normally, IgE is involved in the battle against parasitic infections. All antibodies are specific, e.g., a particular IgE antibody might recognize rapeseed pollen, another one might act against common dandelion. Upon first contact of the allergy-prone person with, e.g., dandelion, the pollen is inhaled and arrives at the mucous membrane and the lung. Thus, the allergens contained in the pollen get into the bloodstream. In the blood vessels, an allergen is recognized by a B cell (**Fig. 6.1a**). As a consequence, the B cell is activated, and large amounts of anti-dandelion IgE antibodies are produced in plasma cells. These antibodies attach themselves onto mast cells, ready to attack (**Fig. 6.1b**). The next time the person inhales dandelion pollen followed by the uptake of the dandelion antigen into the bloodstream, the particles are recognized by the mast cells carrying the anti-dandelion IgE antibodies. Upon contact, the mast cell seeks to destroy the intruder by releasing its chemicals (**Fig. 6.1c**). This release of chemicals results in an irritation of the surrounding cells and tissues and elicits systemic responses on the macroscale such as sneezing, watery eyes and itching. In severe cases, the reactions can also include swelling of the throat causing shortness of breath or even sudden cardiac arrest.

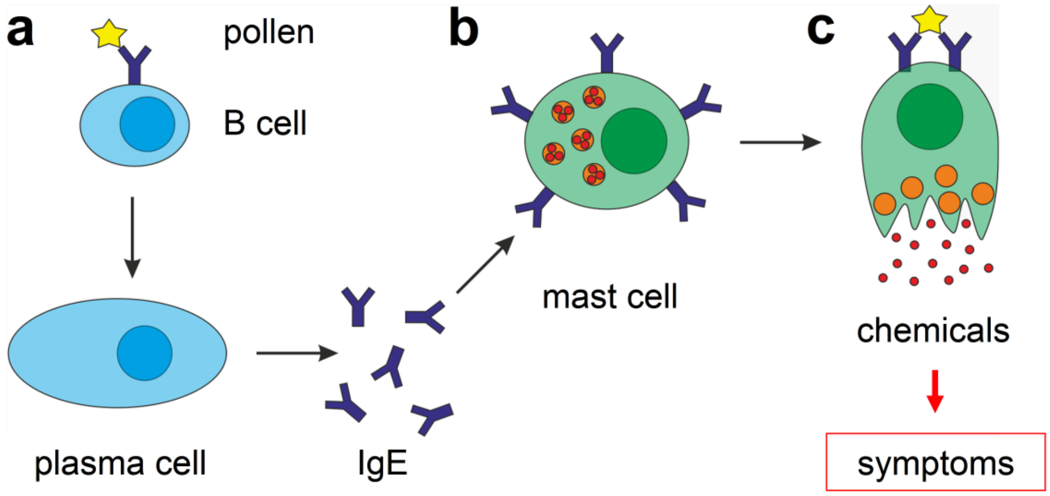

Figure 6.1.: Simple scheme of an allergic reaction as explained in the text. Adopted from reference [151].

6.1.3. IgE-receptor-mediated Signaling in Mast Cells

As mast cells often contribute to the symptoms of allergy, they are the model system in the following study. Mast cells carry the IgE receptor FcϵRI. The natural job of IgE is to protect against parasitic infections; yet, it is frequently responsible for allergic symptoms. After particle uptake due to, e.g., inhalation, the allergens act as multivalent ligands cross-linking several IgE-FcϵRI located in the plasma membrane of mast cells (**Fig. 6.2**). Clustering of IgE receptors results in a transmembrane signal. In this signaling cascade, tyrosine kinase Lyn first phosphorylates the immune tyrosine activation motifs of the FcϵRI-β and -γ subunits. Subsequently, tyrosine kinase Syk is recruited to phosphorylated FcϵRI-γ and activated by Lyn. Other downstream signaling molecules are then activated by phosphorylation of Syk. On the one hand, linker for activation of T cells (LAT) is recruited to FcϵRI. On the other hand, phospholipase Cγ (PLCγ) causes hydrolysis of phosphatidylinositol 4,5-bisphosphate (PIP_2). The products of hydrolysis, diacylglycerol and inositol 1,4,5-triphosphate (IP3), induce a release of Ca^{2+} from endoplasmic reticulum (ER) stores and activate protein kinase C (PKC). Finally, these actions lead to degranulation of the mast cell, i.e., exocytosis of histamine.

6.1.4. The Glucocorticoid Receptor Complex

To relieve allergic symptoms, the release of chemicals by mast cells and, thus, the allergic reaction, is supressed by administration of glucocorticoids (GCs) to the patient suffering from allergy. On the cellular level, the glucocorticoid receptor (GR) complex located in the cytoplasm and the plasma membrane of mast cells is responsible for enabling and disabling certain downstream pathways. In the cytoplasm of a mast cell, the GR is bound to the heat shock protein 90 (HSP90) and is thus not active (**Fig. 6.3a**). A fluorescence

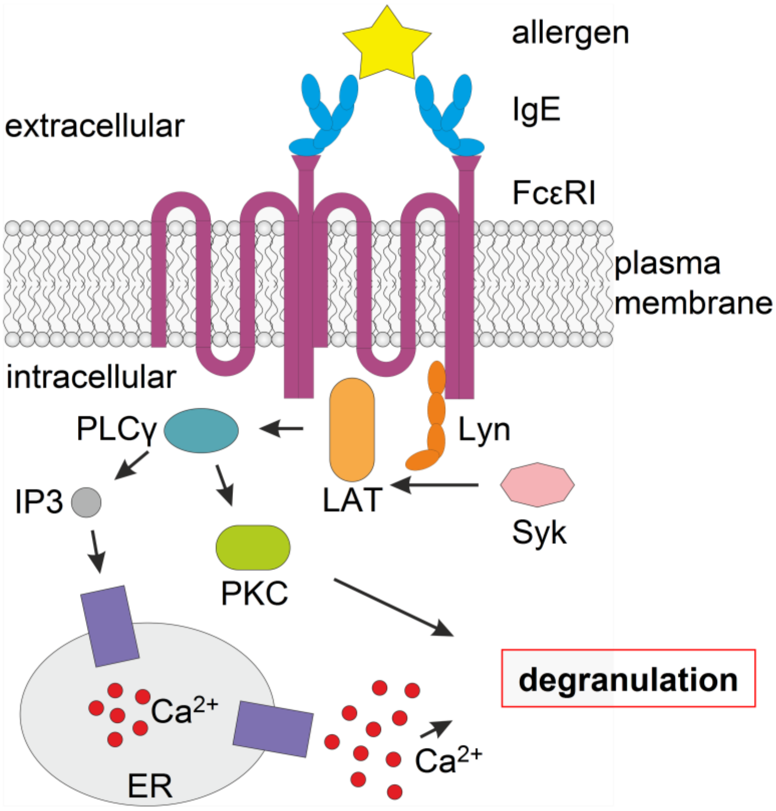
allergen
IgE
FcεRI
extracellular
plasma membrane
intracellular
PLCγ
Lyn
IP3
LAT
Syk
PKC
degranulation
Ca2+
ER
Ca2+

Figure 6.2.: Scheme of IgE-FcϵRI mediated signaling in mast cells as explained in the text. Adopted from Torres et al. [152].

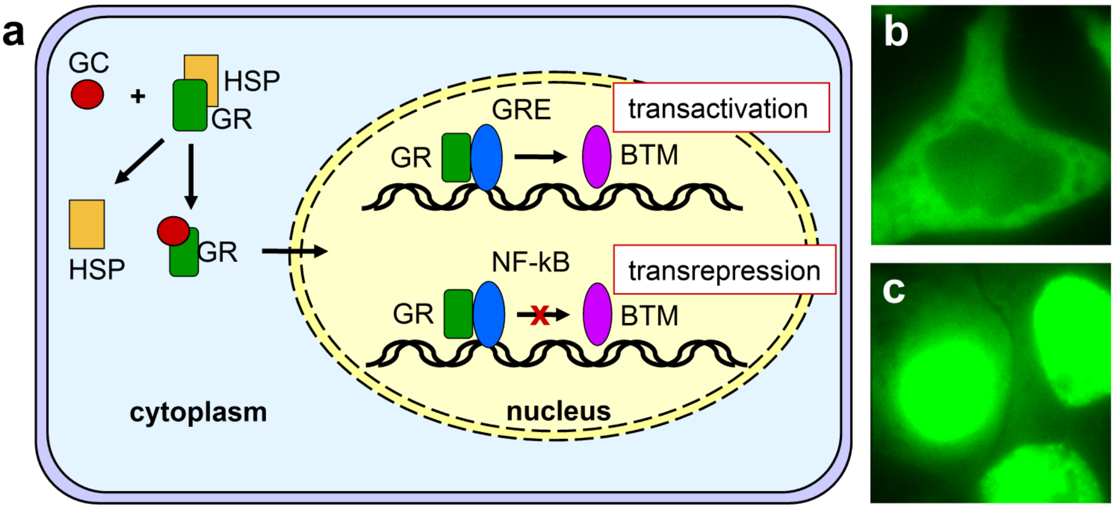
a
GC
+
HSP
GR
HSP
GR
GRE
transactivation
GR
BTM
NF-kB
transrepression
GR
BTM
cytoplasm
nucleus
b
c

Figure 6.3.: (**a**) Genomic actions of the GR as explained in the text. GR-GFP fluorescence in mast cells (**b**) before and (**c**) after treatment with GCs.

image of a mast cell expressing the fusion protein GR-GFP is shown in **Fig. 6.3b**. It can be seen that there is a fluorescence signal from the cytoplasm but not from the nucleus. However, administration of GCs such as dexamethasone (DEX) cause a release of HSP90 from the GR. As a consequence, the GR can translocate into the nucleus of the cell causing transactivation and transrepression of certain genes (**Fig. 6.3c**). Acting as a transcription factor, the GR binds to the glucocorticoid response element (GRE) [153–155]. Thus, the GRE functions as an inducible enhancer element resulting in elevated gene expression [156–158]. In other experiments it has been demonstrated that DEX downregulates the expression of secreted proteases such as collagenase [159–161]. As an example, GC hormone inhibits transcription of collagenase by interaction of the GR with AP-1, the most important enhancer of the collagenase promoter [162, 163]. Furthermore, uptake of the GR by the nucleus triggered by GCs causes inhibition of NF-κB activity [164]. NF-κB increases the expression of cytokine and chemokine genes in acute inflammation. These are the genomic actions of the GR. However, there are several hints for non-genomic actions of the GR. Rapid actions occur within seconds to minutes following GC administration. Those effects of GC vanish rapidly as well. Rapid actions do not involve protein synthesis and may be mediated by the classical cytoplasmic receptor responsible for the genomic actions, but it could also be an effect caused by proteins in the plasma cell membrane including the GR [165]. Therefore, the aim of this study was to further elucidate the rapid, non-genomic actions of the GR using the mast cell as a model.

6.1.5. Non-genomic Actions of the GR Studied by Spatial Regulation

An allergic reaction is triggered by antigens binding to IgE (see subsection 6.1.3). Because the allergens are multivalent ligands, the IgE-FcϵRI receptor complexes located in the plasma membrane of mast cells are cross-linked. Such clustering drives association with lipid rafts, activating all other downstream events. Yet, the role of the GR in this signaling cascade is not known. However, involvement of the GR in IgE-FcϵRI mediated signaling could explain the rapid actions of GCs. To study the effects of the GR at the plasma membrane, the DNA sequence encoding the GR was fused to the GFP sequence and stably expressed in rat basophil leukemia (RBL) mast cells, the model system of this study (**Fig. 6.4a**). Unfortunately, standard time-resolved fluorescence imaging of the GR-GFP at the plasma membrane is not feasible. Direct observation of a spatial redistribution of the GR-GFP in the cell membrane is limited by the heterogeneity of the cells and, more importantly, the stimuli.

However, advances in micro- and nanofabrication for surface patterning allow for structurally defined ligands. Such structures are used to stimulate cells in a defined, spatially well controlled manner. Consequently, the cellular response can be precisely related to the stimuli and quantified. For this study, a structured lipid bilayer containing the allergen to initiate IgE-FcϵRI-mediated signaling was written on a coverslip by dip-pen nanolithography (DPN). In DPN, the tip of an AFM is used as a pen that can be moved on a substrate with nanometer precision [166]. A solution of lipids can be used as ink.

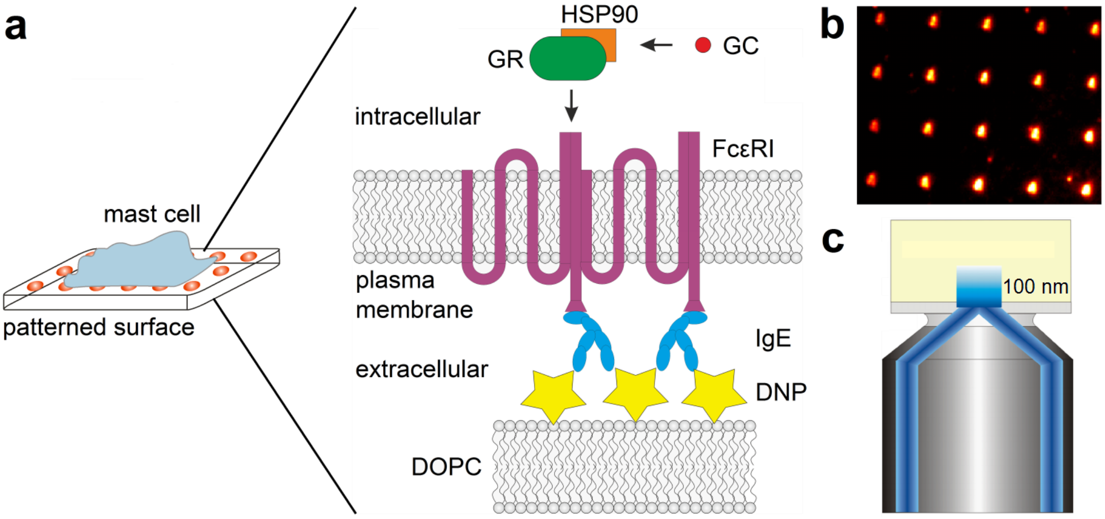

Figure 6.4.: (**a**) Model system to study the non-genomic actions of the GR. (**b**) Fluorescence image of a DNP pattern. (**c**) Objective-type TIRF microscopy.

Here, the ink was a mixture of DOPC loaded with the multivalent ligand dinitrophenole (DNP) and the fluorophore rhodamine to visualize the pattern. Dots of ∼ 1 µm diameter were placed at a distance of 5 µm on a glass slide. A fluorescence image of such a pattern is shown in **Fig. 6.4b**. By imaging such patterns, clustering of fluorescently labeled IgE-FcϵRI receptors on the surface of the plasma membrane have been visualized after settling of mast cells on the substrate [167]. In that experiment, the fluorescence of labeled IgE at the plasma membrane has been detected using standard confocal microscopy because there was no labeled IgE within the cells that would have caused background. However, cytoplasmic GR-GFP involved in the genomic actions adds a high fluorescence background, which obfuscates any signal from the membrane. Therefore, standard epifluorescence microscopy, in which the entire sample is illuminated in the axial direction, cannot be used. Confocal microscopy provides axial sectioning, yet, the thickness of each section is limited by diffraction to > 500 nm, which is still too much to distinguish membrane fluorescence from cytoplasmic background. TIRFM, however, excites only molecules within a ∼ 100-nm deep sheet illuminated by the evanescent wave. Therefore, we chose this technique to study the GR-GFP at the plasma membrane of mast cells (**Fig. 6.4c**).

6.2. Rapid Actions of the GR Visualized by TIRF Microscopy

6.2.1. Rapid Actions of the IgE Receptor

RBL mast cells were used as a model system to study the non-genomic actions of the GR. These cells were loaded with anti-DNP IgE attaching to FcϵRI receptors located at the plasma membrane. A fluorescently labeled, patterned lipid bilayer containing the allergen DNP was used to stimulate the cells. After settling of the cells on the surface, DNP could bind and cross-link the IgE-FcϵRI complexes, triggering the signaling cascade as described in subsection 6.1.3. The spatial regulation of this process due to the structure of the pattern allowed for a direct visualization of proteins involved in IgE-FcϵRI clustering over time. As a first experiment, anti-DNP IgE was fluorescently labeled with Alexa488 to show cross-linking via DNP. The results are presented in **Fig. 6.5**. After transferring the cell solution to the glass surface, TIRFM images were acquired in two color channels monitoring the fluorescence of the DNP-patterned surface (**Fig. 6.5a-d**) as well as the fluorescence of Alexa488-IgE (**Fig. 6.5e-h**) at time intervals of 15 s. First signs of IgE-FcϵRI clustering were observed 2 min after the beginning of the experiment (**Fig. 6.5f**). After 6 min, a pattern had emerged in the green channel that clearly matched the structure of the DNP-patterned surface, which is in good agreement with results from similar experiments [168]. This accumulation of fluorescence at the dots of the patterned lipid bilayer is strong evidence of cross-linking of IgE-FcϵRI receptors by DNP.

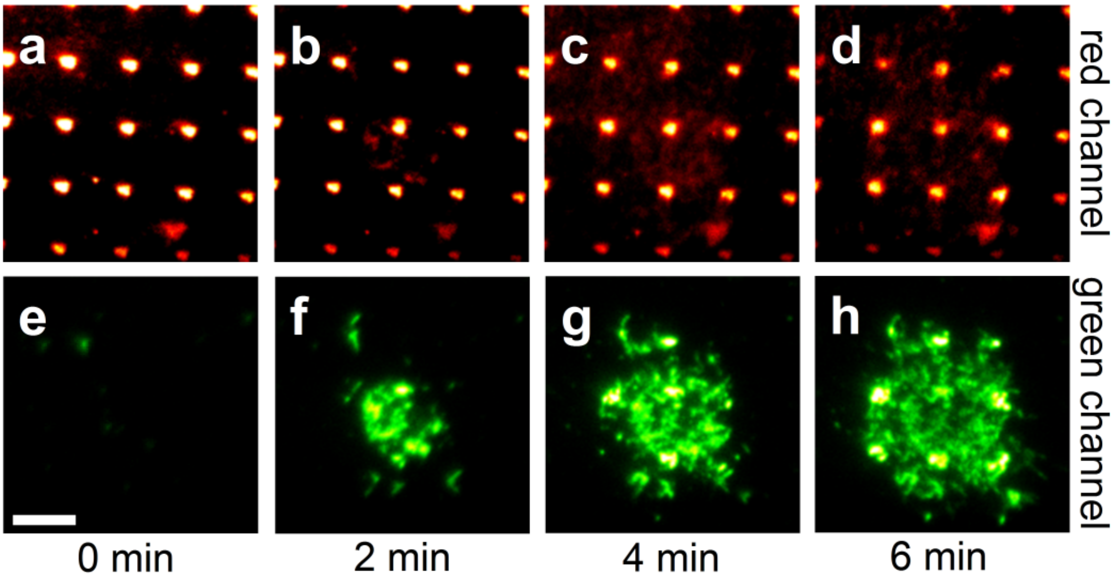

Figure 6.5.: Clustering of IgE-FcϵRI. (**a-d**) TIRFM images of rhodamine fluorescence from the DNP-patterned glass surface. (**e-h**) TIRFM images of anti-DNP Alexa488-IgE in mast cells. Scale bar, 5 µm.

Materials and Methods

Cell preparation: For studying IgE-FcϵRI-mediated signaling, RBL-2H3 mast cells, cultured in DMEM supplemented with 15% fetal bovine serum (FBS) at 37°C, 5% CO_2 and 95% humidity, were incubated with Alexa488-IgE (15 µM) for 90 min. The cells were then harvested, washed twice with calcium free PBS (137 mM NaCl, 2.7 mM KCl, 6.4 mM Na_2HPO_4, 1.5 mM KH_2PO_4) and resuspended in Tyrode's buffer (137 mM NaCl, 2.7 mM KCl, 1 mM $MgCl_2$, 1.8 mM $CaCl_2$, 0.2 mM Na_2HPO_4, 12 mM $NaHCO_3$, 5.5 mM D-glucose) with 0.1% BSA. The cell suspension was transferred to a DNP-patterned glass surface. Mast cells were prepared by Emmanuel Oppong.

TIRF microscopy: For TIRFM, the setup described in subsection 4.2.2 was used. Green fluorescence of Alexa488 was excited by 473-nm light at a power density of 10 W/cm^2, reflected off a 555LP dichroic mirror, filtered by a 525/50 nm bandpass filter and detected on one half of the EMCCD camera chip. Red fluorescence of rhodamine was excited by 561-nm light at a power density of $0 - 5$ W/cm^2 and filtered by a 610/75 nm bandpass filter after having passed through the 555LP dichroic mirror before detected on the other half of the EMCCD camera chip. During the experiment, the sample chamber as well as the objective lens were heated to 37°C by the incubation system.

DNP pattern: DOPC lipids (Avanti Polar Lipids) were mixed with 5% DNP (Sigma-Aldrich) and rendered fluorescent by addition of rhodamine B (18:1 Liss Rhod PE, Avanti Polar Lipids). With the tip of an AFM, dots of 1 µm diameter were placed at 5 µm spacing onto coverslips (No. 1, Menzel). DNP-patterned glass surfaces were prepared by Sylwia Sekula-Neuner using DPN.

6.2.2. Rapid Actions of the GR-GFP

The ability of our model system to study rapid actions at the plasma membrane of mast cells has been demonstrated in the previous subsection on the basis of fluorescently labeled IgE. Yet, this study was focused on the role of GR at the plasma membrane during activation of IgE-FcϵRI-mediated signaling. Therefore, mast cells stably expressing GR-GFP were loaded with anti-DNP IgE and transferred onto patterned lipid bilayers containing the allergen DNP. Subsequently, TIRFM images were acquired at time intervals of 15 s (**Fig. 6.6**). After 5 min, first signs of GR-GFP recruitment were observed (**Fig. 6.6f**). As for Alexa488-IgE, GR-GFP fluorescence accumulated at the dots of the DNP-patterned surface, resulting in a colocalization with the pattern approximately 15 min after the cells were transferred onto the glass surface (**Fig. 6.6h**). At the same time, kinase Lyn gathers at such patterned regions as previously shown by Wu et al. [168]. This is strong evidence that the GR is directly involved in IgE-FcϵRI-mediated signaling.

Extensive screening of the sample after 15 min showed that colocalization of GR-GFP with the DNP-patterned surface was different for each cell (**Fig. 6.7**). While for

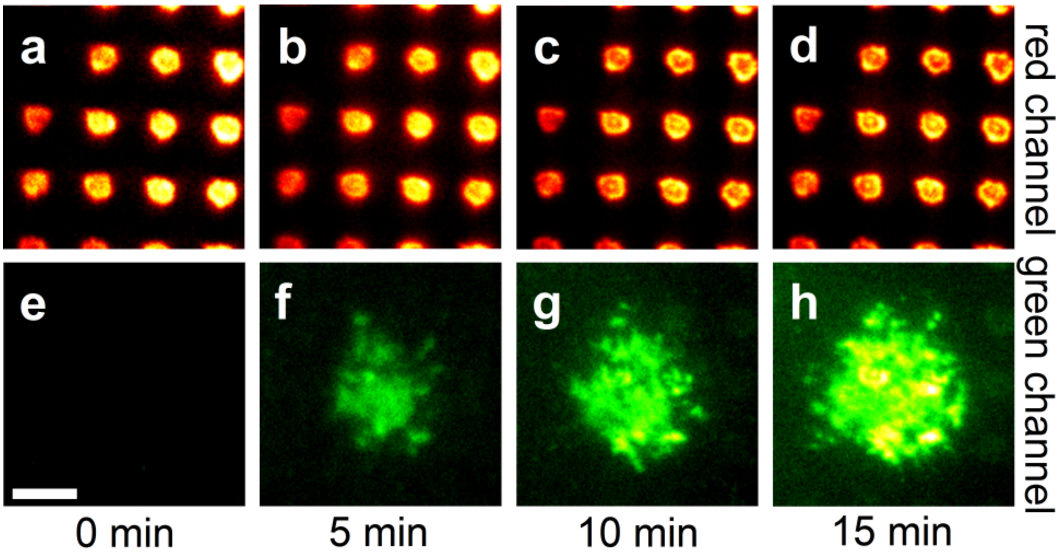
a
b
c
d
red channel
e
f
g
h
green channel
0 min
5 min
10 min
15 min

Figure 6.6.: TIRFM images of the recruitment of GR-GFP to the plasma membrane. (**a-d**) Rhodamine fluorescence from the DNP-patterned surface, (**e-h**) Images of GR-GFP in mast cells. Scale bar, 5 µm.

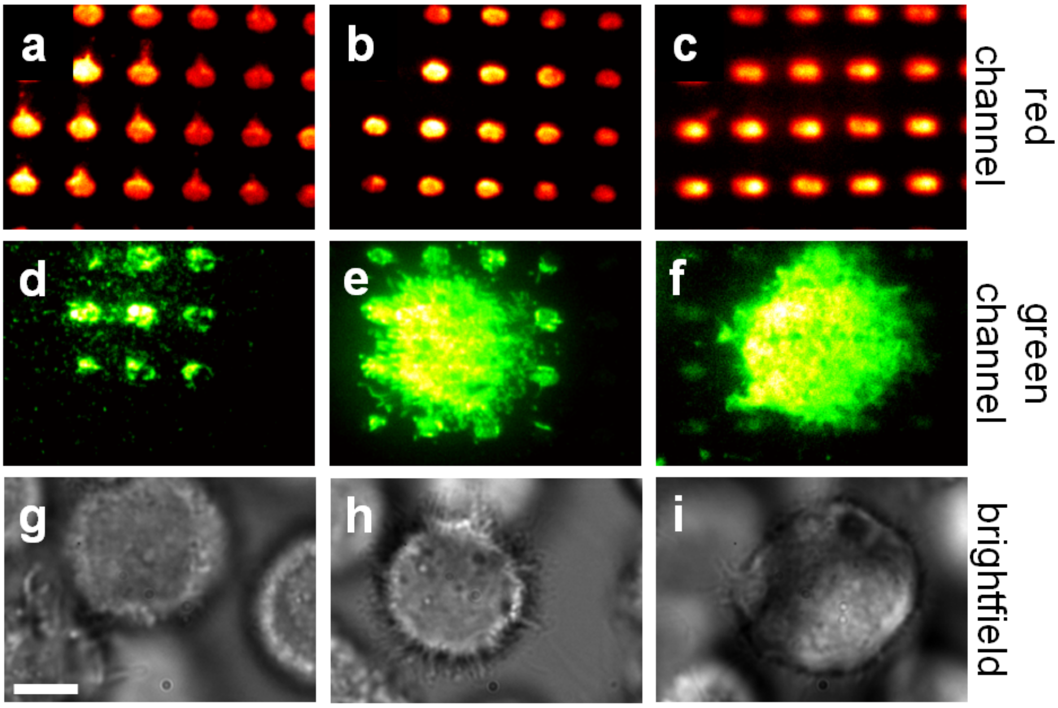
a
b
c
red channel
d
e
f
green channel
g
h
i
brightfield

Figure 6.7.: Accumulation of GR-GFP at the DNP-patterned surface. (**a-c**) TIRFM images of rhodamine fluorescence from the DNP-patterned surface. (**d-f**) TIRFM images of GR-GFP fluorescence in mast cells. (**g-i**) Brightfield images. Scale bar, 5 µm.

some cells, almost all fluorescence signal originated from the positions of the DNP islands (**Fig. 6.7d**), other cells such as the one presented in **Fig. 6.6** exhibited only partial colocalization (**Fig. 6.7e**). There were even cells that displayed no spots of accumulated fluorescence at all (**Fig. 6.7f**). This heterogeneous response is an interesting result and demands further studies. Therefore, the redistribution dynamics of GR-GFP was probed by means of FRAP experiments.

To exclude any effects related to the presence of the fusion partner GFP, mast cells stably expressing GFP were subjected to the same procedure as the cells expressing GR-GFP. As a consequence of adhesion to the glass surface, an increase of GFP fluorescence was observed by TIRF microscopy (**Fig. 6.8**). Yet, no accumulation of fluorescence at the DNP pattern or any other clustering was observed.

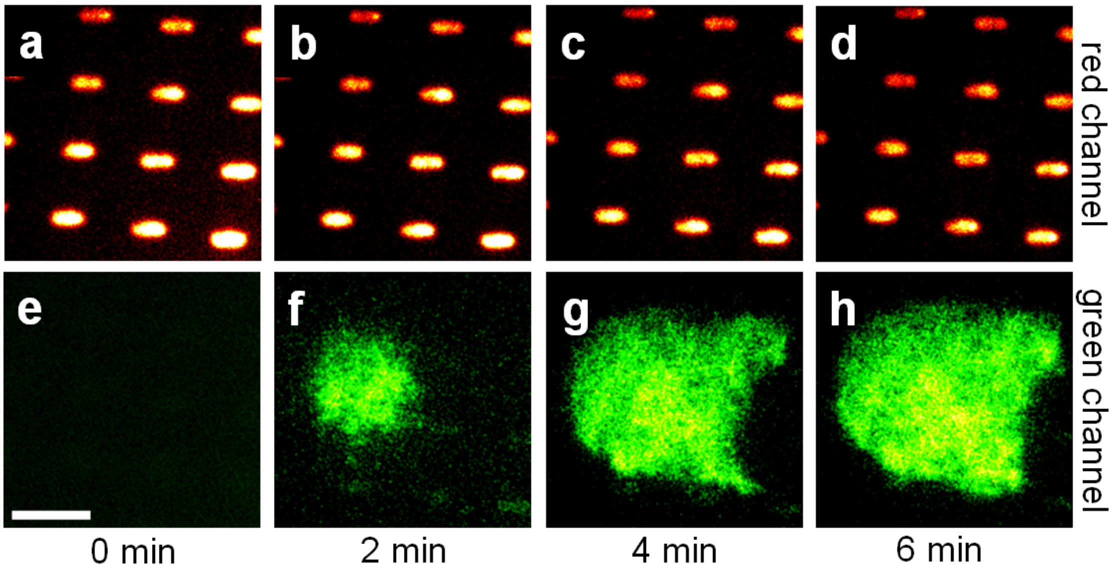

Figure 6.8.: Images of mast cells expressing GFP. (**a-d**) TIRFM images of rhodamine fluorescence from the DNP-patterned glass surface. (**e-h**) TIRFM images of GFP in mast cells. Scale bar, 5 µm.

Materials and Methods

Cell preparation: For studying rapid actions of the GR at the plasma membrane, RBL-2H3 mast cells stably expressing GR-GFP were cultured, incubated with anti-DNP IgE (15 µM), harvested and transferred to a DNP-patterned glass surface as described in subsection 6.2.1. Mast cells were prepared by Emmanuel Oppong.

TIRF microscopy: TIRFM images were acquired with the same excitation wavelengths, intensities and fluorescence filters as described in subsection 6.2.1. The temperature of the sample chamber and the objective lens were maintained at 37°C.

6.2.3. Redistribution Dynamics of the GR Studied by FRAP

In a FRAP experiment, the mobility of a fluorescently labeled species can be measured. In this subsection, two questions are adressed by FRAP. First, is there any difference in the kinetics of the GR at the dots of the DNP-patterned surface compared to other locations within the plasma membrane, indicating linkage to FcϵRI receptors? Second, if not at a dot, does GR-GFP diffuse freely in the membrane or is it bound to other proteins? To answer these questions, the fluorescence recovery was measured within the membrane of GR-GFP expressing mast cells and, as a reference, within the membrane of mast cells expressing only GFP. Representative recovery curves are shown in **Fig. 6.9**. In the case of GR-GFP, a recovery time of $\sim 5\,$s was obtained for non-DNP areas by fitting a single exponential to the data (**Fig. 6.9a**). For GFP expressing cells, however, the recovery due to free diffusion was so fast that it exceeded the temporal resolution of the image acquisition process (50 ms per frame) (**Fig. 6.9c**). Such a big difference cannot be explained by the discrepancy in molecular mass of GFP ($\sim 30\,$kDa) and GR-GFP ($\sim 120\,$kDa), which would result in a factor of only 1.6 for the respective diffusion coefficients. As a consequence, GR-GFP must be bound to other proteins restricting its mobility. In order to obtain further insight, fluorescence recovery was also probed at the membrane of GR-GFP expressing mast cells activated by a DNP-patterned surface. Fluorescence recovery at spots of accumulated GR-GFP fluorescence coinciding with dots of the DNP pattern were compared to the results from non-colocalizing areas. The recovery times at non-coinciding areas did not differ from the kinetics obtained for cells not activated by DNP (**Fig. 6.9a**). However, the dynamics was significantly slower at spots of accumulated GR-GFP fluorescence coinciding with the DNP pattern (**Fig. 6.9b**). These results stongly suggest that GR-GFP binds to intracellular domains of FcϵRI. IgE-FcϵRI is a large, membrane-bound receptor complex ($\sim 300\,$kDa including only IgE [169, 170]) associated with multiple other proteins, which explains why the dynamics was much slower than expected from free diffusion of the GR. Furthermore,

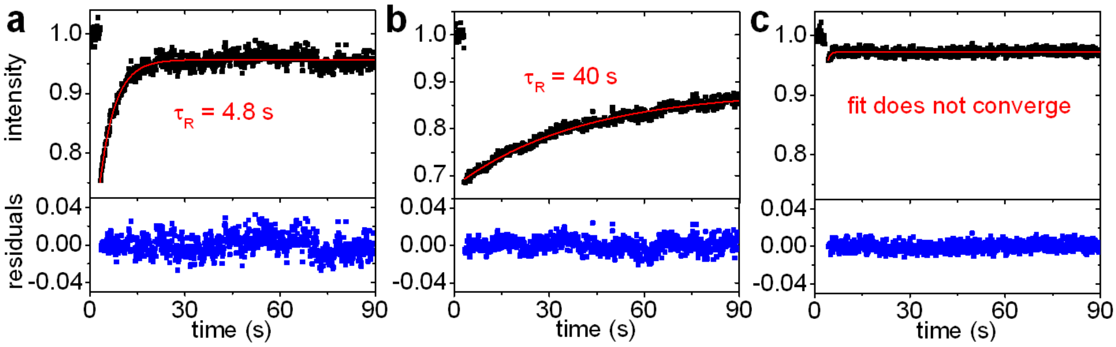

Figure 6.9.: FRAP experiments at the plasma membrane of mast cells. Fluorescence recovery of GR-GFP at areas that (**a**) did not and (**b**) did coincide with the DNP pattern. (**c**) Fluorescence recovery of GFP. The fluorescence recovery (squares) was fitted with a single exponential (red line).

FcϵRI is trapped at the dots of the DNP-patterned surface due to cross-linking via DNP, explaining the further reduced mobility of GR-GFP at those spots.

6.2.4. Quantification of the Redistribution Dynamics of the GR

Free diffusion of unbound GR-GFP should be similar to diffusion of GFP, yet the dynamics of both proteins were different in our measurements. Thus, for GR-GFP, the fluorescence recovery measured was determined by binding to other proteins. Consequently, diffusion was neglected in GR-GFP data analysis. A simple, single exponential binding model (equation 3.23 without diffusion term) was used to fit the FRAP data. The resulting lifetimes of the bound state, τ_R, of GR-GFP at areas of the plasma membrane not coinciding with the DNP pattern were combined in a histogram (**Fig. 6.10b**). The recovery times measured in different cells were very consistent and their distribution was fitted with a Gaussian, resulting in an average lifetime of the bound state of $\tau_\mathrm{R} = (5.4 \pm 2.0)\,\mathrm{s}$. Yet, the kinetics of the recovery of GR-GFP fluorescence at areas of the plasma membrane coinciding with the DNP pattern was heterogeneously distributed (**Fig. 6.10d**). This result coincides with the unequally distributed colocalization of GR-GFP with the DNP pattern as presented in subsection 6.2.2. Not only did the recovery times vary from cell to cell but also within the same cell. Even the peak at non-DNP areas was present within the broadened distribution, indicating that, in a subpopulation of cells, the GR was not recruited to DNP areas at all. In this experiment, the applica-

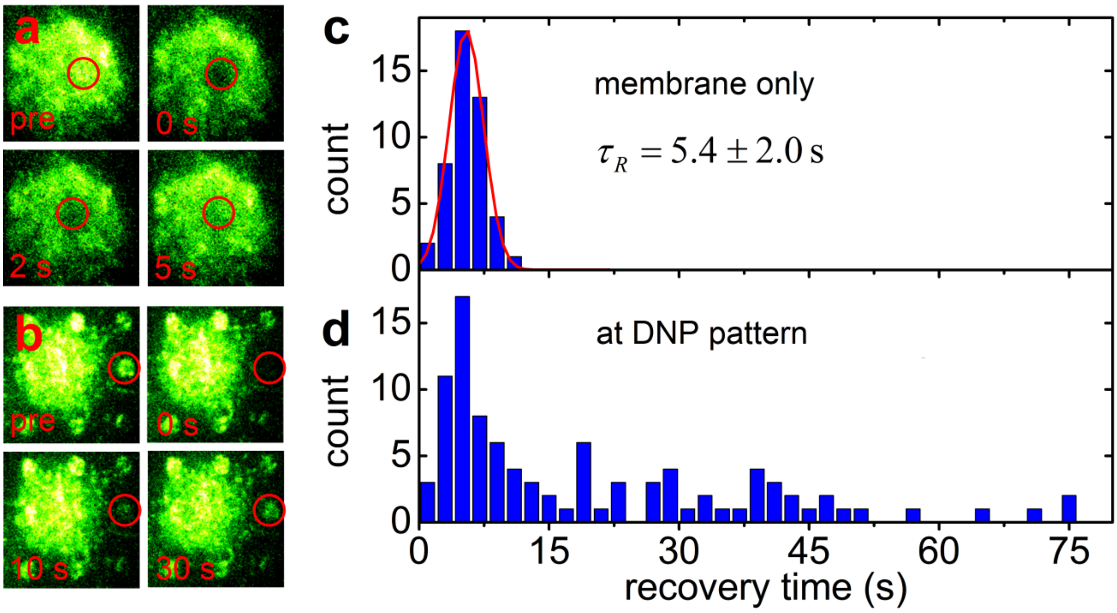

Figure 6.10.: Recovery times of GR-GFP fluorescence. (**a,b**) Exemplary images of GR-GFP fluorescence recovery at areas that did not/did coincide with the DNP pattern. (**c,d**) Histogram of the fluorescence recovery times at areas that did not/did coincide with the DNP pattern.

tion of the stimulant was well controlled by patterning. However, other parameters that determine the response of a cell cannot be controlled at all. For example, each individual cell may express different amounts of IgE-FcϵRI receptors, kinase Lyn or any other proteins involved in the signaling cascade. Even within the same cell, local concentrations can vary. In the end, these factors strongly influence the local response of each cell.

Materials and Methods

FRAP experiments: GFP was bleached by focusing the excitation beam to a spot of 1 µm diameter at the sample. This spot was irradiated with 473-nm light at a power density of $\sim 200\,\mathrm{kW/cm^2}$ for 1 s. Pre-bleaching fluorescence and fluorescence recovery were measured using the same imaging conditions as in subsection 6.2.1. The sample and the objective lens temperature were maintained at 37°C.

FRAP data analysis: Fluorescence recovery of the bleached areas was divided by the average fluorescence emanating from the rest of the cell to correct for bleaching. The resulting fluorescence intensity trace was normalized to the average of the initial fluorescence at the target area. Subsequently, the fluorescence intensity data, $F_R(t)$, were fitted with equation 3.23 neglecting the diffusion term,

$$F_R(t) = F_R(\infty) - (F_R(\infty) - F_R(0))e^{-\frac{t}{\tau_{\mathrm{R}}}}.$$

6.2.5. Influence of Hormone Administration on the Non-genomic Actions of the GR

The final part of the puzzle is the influence of the GC hormone on the non-genomic actions of the GR. For the genomic actions, it is known that GCs bind to GRs inducing translocation of GRs to the nucleus. Therefore, we loaded mast cells expressing GR-GFP with anti-DNP IgE and transferred them to a DNP-patterned glass surface as in the previous experiments. After 15 min to allow for accumulation of GR-GFP at the DNP dots, DEX was administered to the cells. However, no influence on the colocalization of GR-GFP with the DNP pattern was observed (**Fig. 6.11d-f**). Similarly, FRAP experiments did not reveal any changes in the redistribution dynamics of GR-GFP compared to the dynamics in cells not treated with hormone (**Fig. 6.11g**). There was no indication of an effect of GC administration to GRs that had been recruited to cross-linked IgE-FcϵRI receptors. But what about triggering of the reaction in the first place? In another experiment, mast cells expressing GR-GFP were treated with hormone before transferring them to the patterned surface. Subsequently, TIRFM images were acquired at intervals of 15 s for 15 min. The temporal evolution of the recruitment of GR-GFP to the plasma membrane at the DNP pattern was compared for cells treated and not treated with hormone. The average intensity over time, obtained from different cells at locations of DNP, is shown in **Fig. 6.12a**. In cells treated with GCs prior to their transfer to the DNP-patterned surface, GR-GFP was recruited more rapidly to the locations of DNP. This observation raised the question if there are any consequences in

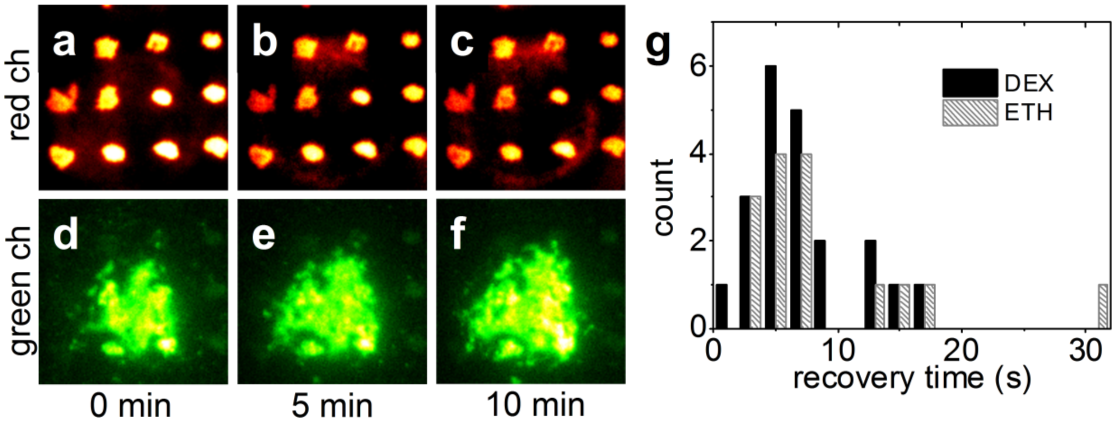

Figure 6.11.: Colocalization pattern after hormone administration. (**a-c**) TIRFM images of rhodamine fluorescence from the DNP-patterned surface. (**d-f**) GR-GFP fluorescence immediately, 5 min and 10 min after hormone administration. (**g**) Fluorescence recovery times at spots of accumulated GR-GFP fluorescence coinciding with the DNP-pattern after administration of hormone (DEX) and only the solvent ethanol (ETH).

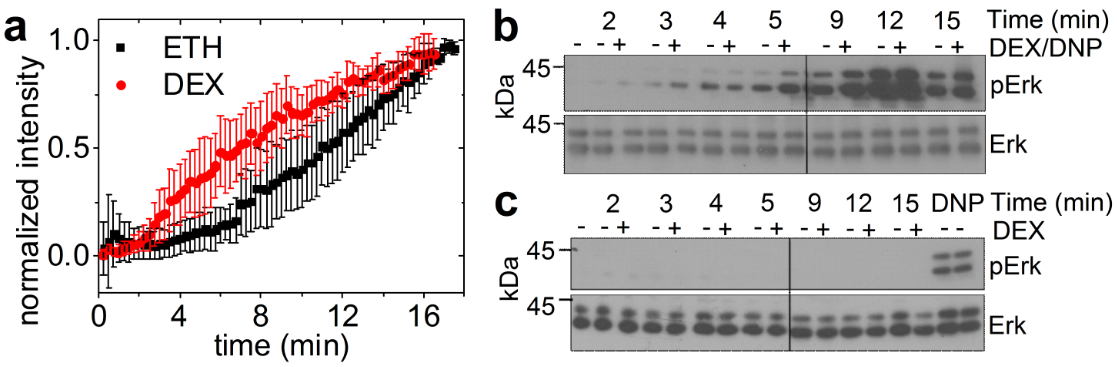

Figure 6.12.: Effects of hormone administration. (**a**) Average GR-GFP fluorescence during mast cell activation by a DNP-patterned surface measured at the pattern with (DEX) and without (ETH) prior hormone administration. (**b,c**) Mast cell lysates were subjected to immunoblot analysis using phosphospecific Erk1/2 and Erk1/2 antibodies. Cells were either sensitized with anti-DNP IgE (panel b) or left unsensitized (panel c) and then treated with medium containing dinitrophenyl-HSA and DEX or dinitrophenyl-HSA and ethanol for $2 - 15$ min. Immunoblot analysis was performed by Emmanuel Oppong.

downstream signaling due to GC administration initiated at the plasma membrane in activated mast cells. To this end, extracellular signal-regulated kinase (Erk)1/2 phosphorylation was analyzed in immunoblotting experiments. A rapidly enhanced Erk1/2 phosphorylation was observed as a consequence of GC administration to activated mast cells (**Fig. 6.12b**), whereas Erk1/2 phosphorylation was entirely absent in unsensitized cells (**Fig. 6.12c**).

Materials and Methods

Hormone administration: DEX was dissolved in ethanol and 10 µl of that solution were added to 100 µl of cell suspension, yielding a final DEX concentration of 100 nM for both, the post- and pre-DNP-activation experiments. Hormone was applied by Emmanuel Oppong.

6.3. Summary and Outlook

6.3.1. Model for the Actions of the GR Including GC Administration

GCs produced in the adrenal cortex are steroid hormones involved in a variety of physiological processes including metabolic, cardiovascular and immunological action [171,172]. In medicine, synthetic analogues of GCs such as prednisone and dexamethasone are used as a treatment of inflammatory disorders and in immunosuppressive therapy. The effects of GCs are mediated by binding to the GR. In the cytoplasm, other proteins such as HSP90 are bound to the GR forming a multi-protein complex [173]. Upon binding of GCs, GRs translocate into the nucleus where they cause transactivation of immunosuppressive genes [174] and transrepression of inflammatory genes [175]. Furthermore, it has been shown that inflammatory transcription factors are modulated by direct interaction with the GR, significantly reducing target gene expression [176]. Because the genomic actions of the GR involve protein synthesis and/or degradation, these effects occur hours to days after GC administration. However, rapid, non-genomic effects of GCs occurring within minutes and mediated by receptors located in the plasma membrane have been reported [177]. Among these, G-protein-coupled receptors have been found to convey non-genomic effects of GCs [178]. Furthermore, there is increasing evidence for non-genomic actions of membrane-bound GRs involved in transmembrane signaling within, e.g., immune cells [179]. Still, the specific functional role of membrane-associated GRs has not yet been determined.

This study focused on unraveling the involvement of the GR in IgE-FcϵRI-mediated signaling in mast cells. Mast cells sensitized with anti-DNP IgE were activated by microfabricated DNP-patterned glass surfaces in a spatially controlled manner. By stable expression of a GR-GFP fusion protein and the application of TIRF microscopy, the redistribution of membrane-associated GRs was followed over time. We showed that the GR accumulates in areas of the plasma membrane coinciding with the DNP pattern. This accumulation occurred approximately 15 min after transfer of the cells to the DNP-patterned surface, and 10 min after activation of the cells by cross-linking IgE-FcϵRI receptors via DNP, respectively. At a similar time, kinase Lyn has been reported to get recruited to DNP induced IgE-FcϵRI clusters [168]. In addition, FRAP was applied to probe the redistribution dynamics of GR-GFP. These experiments revealed significantly slower fluorescence recovery of GR-GFP at the DNP sites compared to the fluorescence recovery of GR-GFP within the rest of the membrane. Both, accumulation and slow recovery of GR-GFP fluorescence at the DNP pattern indicate binding of GRs to FcϵRI receptors.

Furthermore, a comparison of the recovery times of GR-GFP and GFP fluorescence support the presence of membrane-bound GRs in addition to the cytosolic form of the GR. And, unlike cytoplasmic GRs, membrane-bound GRs were not observed to translocate into the nucleus after hormone administration. Instead, hormone treatment of the mast cells caused a more rapid recruitment of GRs to sites of IgE-FcϵRI receptors cross-linked by DNP.

Finally, approximately 5 min after hormone administration, the GR was observed to cause phosphorylation of Erk as a consequence of IgE-FcϵRI-mediated signaling. In mast cells, Erk controls the release of allergic mediators as well as the expression of pro-inflammatory cytokine genes. In other experiments, it has been shown that Erk phosphorylation was inhibited 16 h after hormone administration implicated by the genomic actions of the GR [180]. In a nutshell, membrane-associated GRs in activated mast cells massively enhance Erk phosphorylation within the first few minutes after GC hormone treatment, whereas Erk phosphorylation is downregulated at later times when the slower, genomic actions of cytoplasmic GRs spring into action (**Fig. 6.13**, plot of Erk activity).

Overview of the Rapid, Non-genomic Actions of the GR

- In mast cells, besides cytoplasmic GRs, there is a membrane-associated form of the GR that binds to IgE-FcϵRI receptors.

- Unlike cytoplasmic GRs, membrane-associated GRs do not translocate into the nucleus after treating the cells with GC hormone.

- GC hormone treatment of mast cells causes a more rapid accumulation of GRs at sites of IgE-FcϵRI receptors cross-linked by DNP.

- The GR causes phosphorylation of Erk as a consequence of IgE-FcϵRI-mediated signaling and GC hormone treatment.

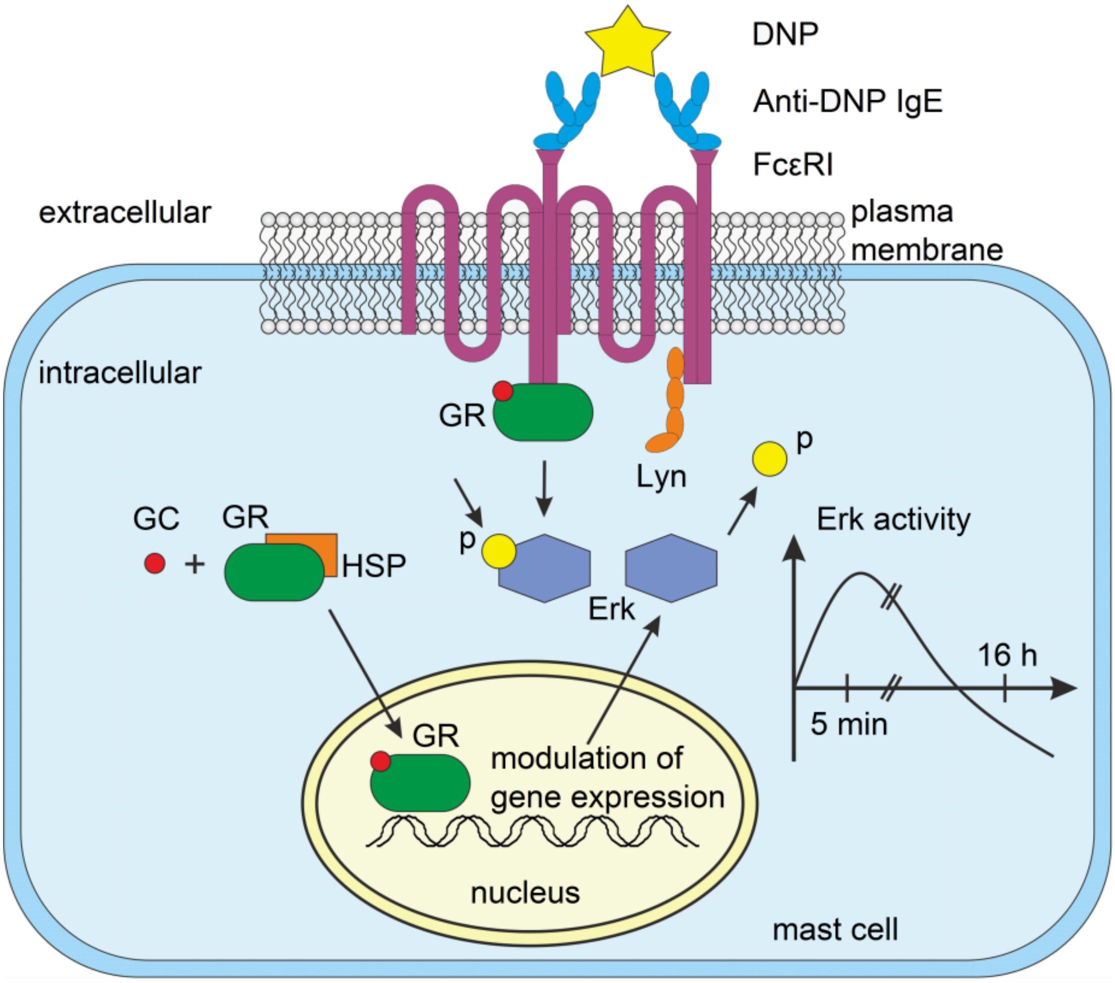
DNP
Anti-DNP IgE
FcεRI
extracellular
plasma membrane
intracellular
GR
Lyn
p
GC
GR
HSP
p
Erk
Erk activity
16 h
5 min
GR
modulation of gene expression
nucleus
mast cell

Figure 6.13.: Model for the actions of GCs including rapid actions of the GR at the plasma membrane of activated mast cells as explained in the text.

6.3.2. Future Plans Studying the GR

The data obtained in this study strongly support the existence of membrane-associated GRs. In other studies it has been suggested that the membrane-bound GR is a modified form of the GR [181]. As yet, there is no evidence for the existence of two distinct types of GRs. Therefore, the current view is that the function of the GR is determined by the binding of accessory proteins such as HSP90. However, it remains elusive if there is an exchange between membrane-associated and cytosolic GRs. Future studies including pulse-chase experiments by using photoconvertible fluorescent proteins may provide further insight into a potential link between GRs of different function. This could help to develop drugs that specifically target membrane-bound GRs to only modify the non-genomic actions. This strategy may help to reduce side effects caused by a treatment with conventional GCs.

7. Organization of Filament Assembly in Live Cells Visualized by PALM

7.1. Organization of Perinuclear Actin in Live Tobacco Cells

7.1.1. The Role of Actin as Part of the Cytoskeleton

As part of the cytoskeleton, actin performs a great variety of different tasks within cells. Importantly, actin is essential for intracellular transport of various cargoes such as organelles including peroxisomes [182], mitochondria [183] or golgi vesicles [184]. In plant cells, which is the system of interest for this study, actin is also indispensable for chloroplast movement [185, 186]. Mostly myosins, a class of mechano-chemical enzymes, are responsible for actin-based motility [187, 188]. In addition to these dynamic tasks, the actin cytoskeleton is also responsible for supporting the integrity of the plasma membrane [189] as well as anchoring organelles at appropriate intracellular positions [190]. Furthermore, the vacuolar and transvacuolar cytoplasmic strands in plant cells are structured by actin filaments (AFs) [191,192]. This means that depending on the context, the structure of the actin cytoskeleton must be able to change from a network of heavily bundled to fine cross-linked filamentous structures or *vice versa*. During interphase, static AFs are required to maintain cell shape, whereas highly dynamic filaments are needed in cortical regions of a cell to allow for a reaction to changing requirements concerning vesicle transport or external stimulations such as pathogens [193]. Actin is extremely conserved, 83-88% amino acid sequence identity is shared with actins of plants, green algae, most protists, fungi, and animals. Within one of these kingdoms of organisms, the amino acid sequence identity can even reach up to 95% [194]. Thus, the diverse functionality of actin is not covered by different isoforms. Instead, the variety of tasks is mastered by association with additional binding partners. For example, the assembly, maintenance and disassembly of monomeric actin into filamentous actin (F-actin) is regulated by a vast number of actin-binding proteins (ABPs) [195]. This specific decoration of AFs with different sets of ABPs allows for the formation of numerous subpopulations providing the functional diversity in order to perform different tasks as mentioned above.

7.1.2. Localization of Lifeact-psRFP in BY-2 Cells

During the course of this study, two different fluorescent proteins, the tetrameric photoswitchable red fluorescent protein (psRFP) [196] and the monomeric IrisFP (mIrisFP) [86], were C-terminally fused to the actin-binding probe Lifeact [197]. These fusions proteins were then stably expressed in tobacco *Nicotiana tabacum* L. cv. Bright Yellow 2 (BY-2) cells, in order to follow the organization of the actin cytoskeleton. In tobacco BY-2 cells stably transfected with the fusion construct Lifeact-psRFP, fluorescence was observed exclusively from around the nucleus. No fluorescence emanated from structures in the cell cortex or from the transvacuolar strands. Only a tight filamentous, basket-like structure around the nucleus was labeled (**Fig. 7.1a,b**). To reveal other actin subpopulations beyond those of the nuclear basket that were not marked via Lifeact-psRFP expression, actin was also labeled with an Alexa488-phalloidin stain (**Fig. 7.1e**). For the nuclear basket, the images of green Alexa488-phalloidin and red Lifeact-psRFP clearly colocalized. However, in the cell cortex, only the green fluorescence of Alexa488-phalloidin was observed, whereas red fluorescence of Lifeact-psRFP was completely absent, suggesting that there is a clear structural difference between these actin subpopulations.

In addition to the stably transformed Lifeact-psRFP ox BY-2 cell line, a biolistic, transient transformation was performed. Numerous cells expressed Lifeact-psRFP 24 h after transient transformation (**Fig. 7.1e**). Interestingly, the intracellular pattern showed fully labeled actin similar to the Alexa488-phalloidin stain. Furthermore, a nearly identical, fully labeled actin pattern was observed for a Lifeact-mIrisFP fusion construct in stably (**Fig. 7.1f**) as well as transiently (**Fig. 7.1g**) transformed BY-2 cells. The Lifeact-mIrisFP construct contained the identical vector backbone and Lifeact sequence as the Lifeact-psRFP construct. During stable transfection, a small subpopulation of

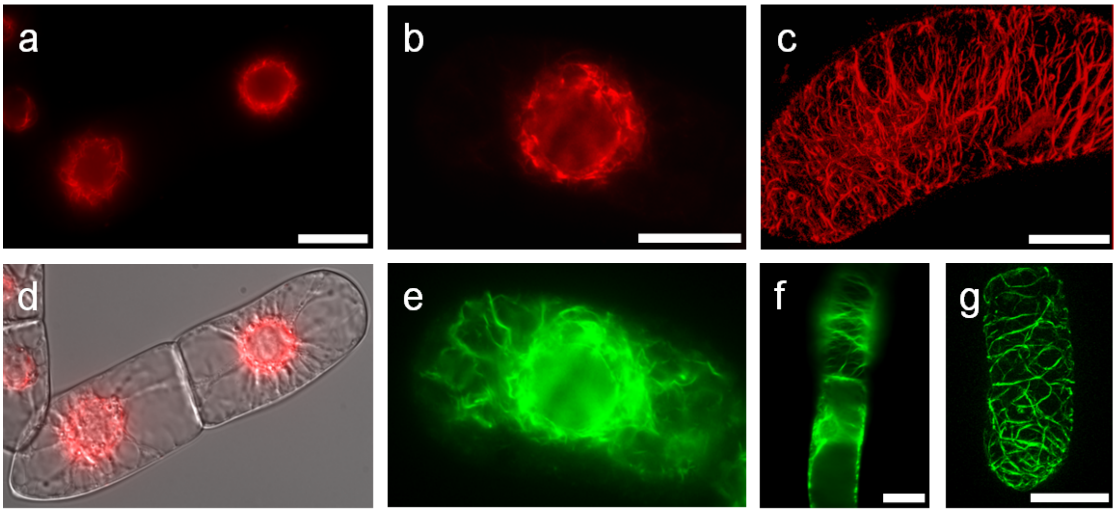

Figure 7.1.: Visualization of actin filaments in ox BY-2 cells. (**a,b**) Stable and (**c**) transient expression of Lifeact-psRFP. (**d**) Overlay of red psRFP fluorescence with DIC image. (**e**) Alexa488-phalloidin fluorescence. (**f**) Stable and (**g**) transient expression of Lifeact-mIrisFP. Actin in BY-2 cells was imaged by Steffen Durst. Scale bars, 20 µm.

Lifeact-psRFP overexpressing cells displayed a fully decorated actin cytoskeleton comprising both central and cortical arrays (data not shown). However, these cells underwent cell death, as indicated by an almost complete cessation of cytoplasmic streaming, membrane detachment and deformation in cell shape. After this natural selection, only those cells with the Lifeact-psRFP fluorescence limited to the nuclear basket remained.

Materials and Methods

Cloning procedure: Plasmids for stable and transient transformation of BY-2 wild type (wt) cells were constructed using the Gateway cloning technology (Invitrogen). The sequences encoding Lifeact-psRFP and Lifeact-mIrisFP were amplified by polymerase chain reaction (PCR) using oligonucleotide primers with Gateway-specific flanks. As template, pcDNA3 vectors (Invitrogen) containing the sequences of Lifeact-psRFP and Lifeact-mIrisFP were used. The sizes of the amplicons were verified by electrophoresis and purified via NucleoSpin Extract II (Macherey-Nagel, Düren, Germany) according to the manufacturer's instructions. The resulting gene regions were inserted into the binary vector pH7WG2 [198] following the manufacturer's protocol (Invitrogen). To confirm the accuracy of the sequences, both fusion constructs were verified by restriction digest and sequencing (GATC, Konstanz, Germany). Plasmids were constructed by Steffen Durst.

Biolistic, transient expression: For biolistic transformation, gold particles (1.5 – 3.0 µm, Sigma-Aldrich) were coated with the constructs encoding Lifeact-psRFP or Lifeact-mIrisFP according to the system manual (PDS-1000/He Particle Delivery System manual, Bio-Rad, Hercules, USA) with the following modifications: Gold particles coated with 1 µg plasmid-DNA and placed on macrocarriers (Bio-Rad) were used for each transformation. Non-transformed BY-2 wt cells (750 µL), collected 2 d after subcultivation, were placed on petrislides (Millipore) containing 2 mL of solid medium. These loaded slides were transferred to a particle gun, custom-made according to Finer et al. [199], and bombarded by three shots with a pressure of 1.5 bar in a vacuum chamber of 0.2 bar. Following bombardment, the cells were incubated for 4 – 24 h in the dark at 26°C and subsequently studied using fluorescence microscopy. BY-2 cells were transiently transformed by Steffen Durst.

Agrobacterium-mediated, stable expression: Non-transformed BY-2 wt cells were stably transformed with the binary vector constructs pH7WG2-Lifeact-psRFP and pH7-WG2-Lifeact-mIrisFP according to a protocol of Buschmann et al. [200] with minor modifications. Both constructs were transformed into *Agrobacterium tumefaciens* (strain LBA 4404, Invitrogen) via heat shock treatment (5 min, 37°C). After three days of cultivation on selective medium, a single colony was raised in a 3-mL over-night culture. The preparation of the BY-2 cells started with subcultivation of 3 mL of a 7 d old non-transformed tobacco BY-2 cell culture in 60 mL Murashige & Skoog (MS) media in a sterile 200 mL flask for three days at standard conditions. Thereafter, the cells were washed twice with 200 mL sterile Paul's medium (4.3 g L-1 MS salts without vitamins (Duchefa Biochemie, Haarlem, The Netherlands), 10 g L-1 sucrose, pH 5.8) and resuspended in 10 mL of Paul's medium leading to a five-fold increase in cell density. 1 mL of this concentrated cell suspension was added to *A. tumefaciens* bacteria transformed as described above and processed as follows. The optical density at 600 nm (OD600) of the bacterial over-night culture was determined and 5 mL of fresh lysogeny broth (LB)-media (plus corresponding antibiotics) were inoculated with these bacteria to an OD600 of 0.15. After several hours of growth, 1 mL of the transformed *A. tumefaciens* bacteria was harvested at an OD600 of 0.8 by centrifugation at 10,000 g (Heraeus Pico 17 Centrifuge, Thermo Scientific) for 1 min in a 1.5 mL reaction tube. The supernatant was removed and the pellet resuspended in 30 µL of Paul's medium. After adding the concentrated BY-2 cells to the resuspended bacteria, the reaction tube was agitated for 5 min at 100 rpm for better mixing of the cells. In the next step, this mixture was dropped in 100 µL aliquots on plates with Paul's agar (Paul's medium solidified with 0.5% (w/v) Phytagel (Sigma-Aldrich), without antibiotics). After 4 d of incubation at 26°C in the dark, the grown cell plaques were transferred and cultivated on new plates containing MS agar and 100 mg L-1 cefotaxime and 50 mg L-1 hygromycin driving selection pressure. BY-2 cells were stably transformed by Steffen Durst.

7.1.3. PALM with Optical Sectioning of Lifeact-psRFP in BY-2 Cells

In standard widefield epifluorescence and confocal images of stably transformed Lifeact-psRFP ox BY-2 cells, only perinuclear actin was labeled. However, from standard microcopy images, it was not entirely clear if the actin arrangement around the nucleus was still composed of filamentous structures and how these were arranged. To study the organization of perinuclear actin in detail, super-resolution PALM images were acquired by using the photoswitching mechanism of Lifeact-psRFP. **Fig. 7.2** shows an exemplary standard widefield image compared to the PALM image of stably transformed Lifeact-psRFP ox cells focusing 2 µm deep into the sample. Additionally, PALM images at multiple layers

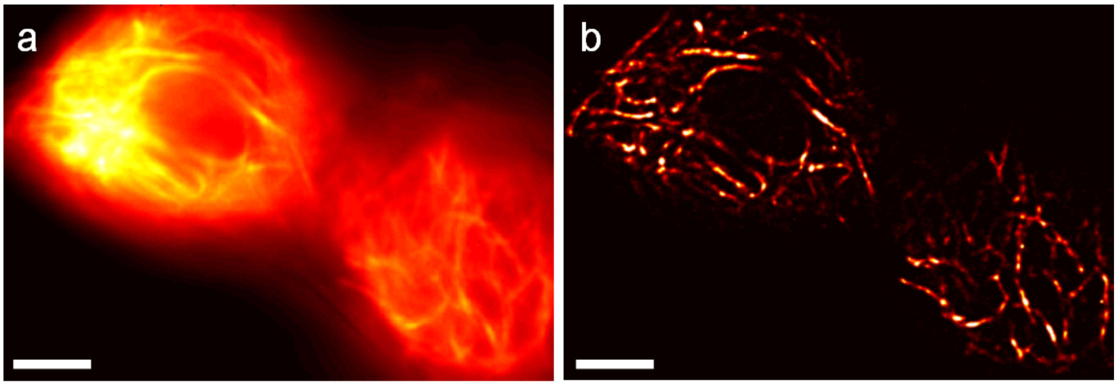

Figure 7.2.: Fluorescence images of Lifeact-psRFP in ox BY-2 cells. (**a**) Standard epifluorescence image of the nuclear actin basket of two adjacent cells. (**b**) PALM image reconstructed from single molecule localization within 10,000 image frames. Fine actin filaments were exclusively wrapped around the nucleus. Scale bars, 5 µm.

were acquired to yield a 3D stack of the entire nuclear basket with high lateral resolution ((35±18) nm localization precision). **Fig. 7.3** displays the full projection of the widefield acquisition, the reconstructed PALM image projection as well as the PALM images of the individual sections. As with conventional fluorescence microscopy, only actin around the nucleus was visible via single-molecule localization of Lifeact-psRFP fusion proteins. Furthermore, the super-resolution data clearly showed a network of AFs enclosing the nucleus in a lamellar fashion. In another example, the gradient indicating the direction of nuclear migration was visualized (**Fig. 7.4**). Throughout all sections of the 3D stack, perinuclear actin labeled by Lifeact-psRFP was oriented toward one particular side of the nucleus. As indicated by the inset in **Fig. 7.4e**, the width of a single filament was measured as 54 nm. Considering the intrinsic width of an actin filament of > 35 nm, this confirms the excellent lateral resolution.

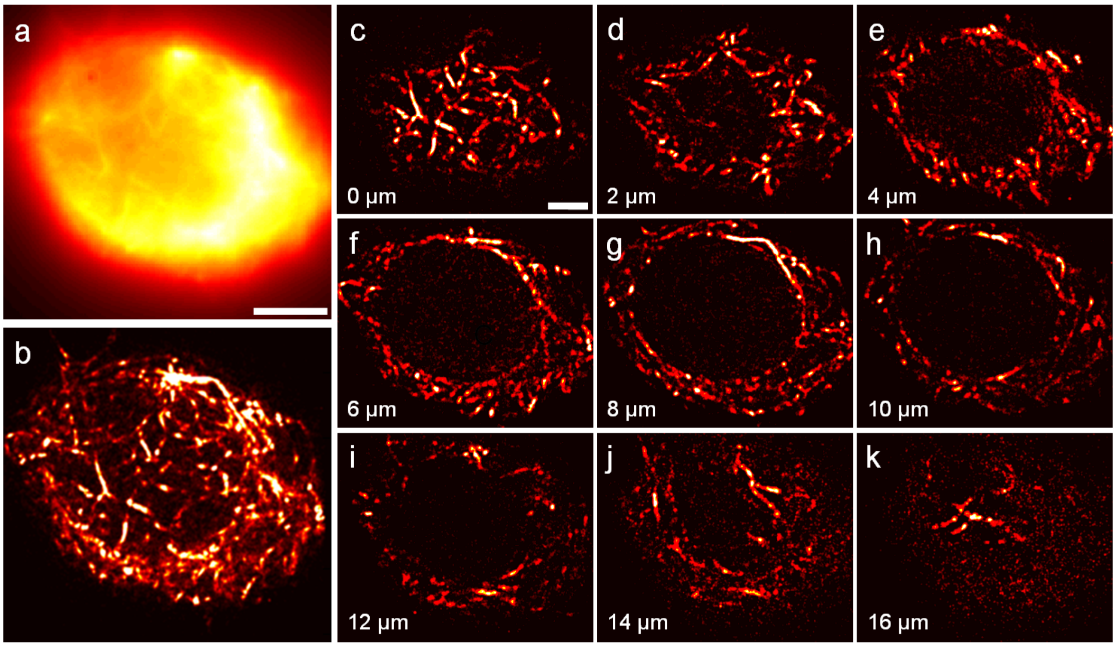

Figure 7.3.: PALM analysis of Lifeact-psRFP in ox BY-2 cells. (**a**) Standard epifluorescence image of a nuclear actin basket representing the sum of 27,000 single images from nine sections (3,000 frames each) acquired with 2 µm spacings. Scale bar, 5 µm. (**b**) PALM image projection reconstructed from the locations of the individual fluorophores; fine actin filaments were exclusively observed around the nucleus. (**c-k**) PALM images of each of the nine sections, z-axis positions are indicated in the lower left. Scale bars, 3 µm.

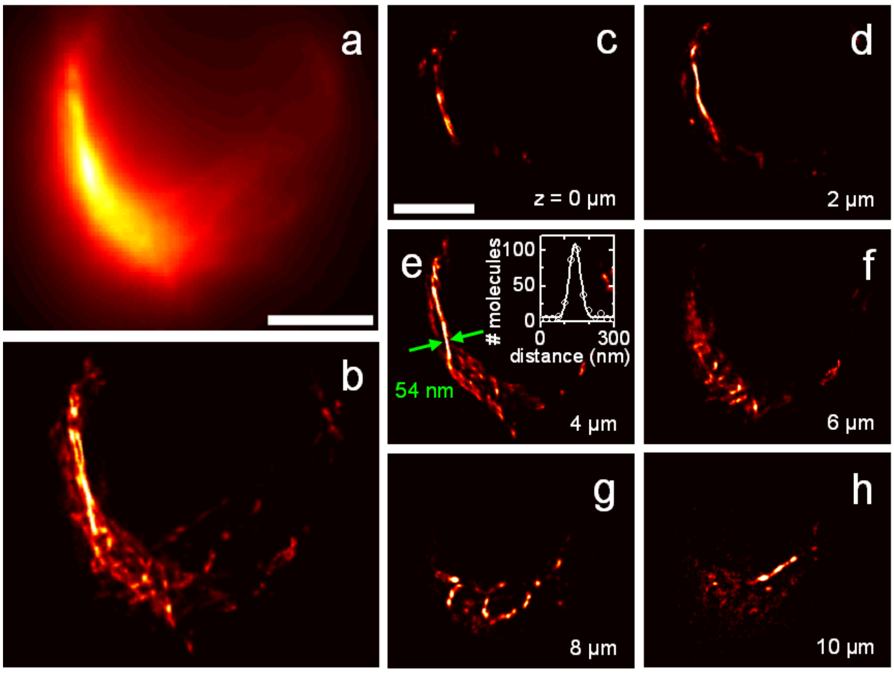

Figure 7.4.: Nuclear migration in BY-2 cells. (**a**) Standard epifluorescence image of a nuclear actin basket. (**b**) Projection of the marker positions in 18,000 images from six sections (3,000 frames each) with a z-axis distance of 2 µm; fine actin filaments are found only near the nucleus with a clear orientation toward the direction of nuclear migration. (**c-h**) Individual sections; the inset in panel (**e**) shows a cross section through an actin filament at the location indicated by the arrows with a FWHM of 54 nm. Scale bars, 5 µm.

Materials and Methods

PALM with optical sectioning: For PALM of Lifeact-psRFP in ox BY-2 cells, 0.5 mL of cell solution 4 d after subcultivation were transferred from their cultivation flasks into chamber slides (Thermo Scientific) and imaged using the setup described in subsection 4.2.2. After acquisition of 3,000 frames per layer, the objective lens was moved in z-direction (2 µm steps) with the stepper motor of the objective drive. A total of $6-9$ layers ($18,000-27,000$ frames) were imaged per stack. For psRFP, the photoactivation and excitation wavelength is the same (positive switcher). Red fluorescence of Lifeact-psRFP was excited with 561-nm light at $50-200\,\mathrm{W/cm^2}$. Especially in the beginning of the imaging procedure, the density of activated markers was sometimes too high. Therefore, off-switching was induced using 473-nm light at $< 10\,\mathrm{W/cm^2}$. Fluorescence light was filtered by a 610/75 nm bandpass (Chroma HQ610/75, Chroma) and detected with a camera exposure time of $30-50$ ms. PALM images were analyzed by fitting a 2D Gaussian distribution to the single molecule signals detected, using a homemade algorithm written in Matlab (MathWorks) [79].

7.1.4. Summary and Discussion

PALM with Optical Sectioning of Lifeact-psRFP in BY-2 Cells

In animal cells, the structure and function of the cytoskeleton was extensively studied by super-resolution microscopy over the last few years. Plant cells are difficult to image even by means of conventional fluorescence microscopy. High background due to autofluorescent compounds such as chlorophyll or secondary plant metabolites can render fluorescence imaging impossible. Also, compared to flat, adhering animal cells, the pronounced three-dimensional structure of plant cells enclosed by a rigid cell wall is problematic. This aspect, for example, prohibits application of TIRFM, since the range of the evanescent wave is below the thickness of the cell wall. Consequently, TIRFM is only feasible after enzymatic digestion of the cell wall [189]. Still, by application of an improved protocol for plant cell transformation, localization-based super-resolution microscopy images using paFPs were acquired in living plant cells with intact cell walls for the first time (**Fig. 7.2**). Furthermore, apart from PALM imaging of a single plane only, this work showed how several super-resolved planes can be acquired resulting in a three-dimensional stack with a high lateral resolution (**Fig. 7.3,7.4**). In PALM, epi-illumination of the sample results in photoactivation followed by photobleaching of fluorophores below and above the focal plane. Thus, PALM imaging is often resricted to a single layer. In other publications, only those fluorophores within the focal plane were photoactivated by a two-photon process [201, 202]. Yet, despite the ingenuity of this approach, the high spatio-temporal photon densities required for this procedure complicate microscope design and application. Here, the excellent photostability of psRFP (**Fig. 7.5**) in combination with a more subtle mechanism of chromophore maturation [196] and the relatively slow dynamics of perinuclear actin allowed for extensive PALM imaging at multiple z-positions. The live plant cell super-resolution PALM images presented here resolved the lamellar arrangement of AFs wrapped around the nucleus for the Lifeact-psRFP fusion.

Localization of Lifeact-psRFP in BY-2 Cells

For Lifeact-mIrisFP expressing cells, filamentous structures were labeled throughout the entire cell. However, for the Lifeact-psRFP expressing cells, fluorescence was only detected from a basket-like structure around the nucleus. Co-staining with Alexa488-phalloidin revealed that the structures marked by both Lifeact fusions were still filamentous actin. Yet, this control also showed that the regular arrangements of filamentous actin were still present in Lifeact-psRFP expressing cells, but not labeled by the fusion probe. The stability and dynamics of filamentous actin are controlled by ABPs and their complexes, since actin isoforms are highly conserved (see subsection 7.1.1). Therefore, it is obvious to suggest that the formation of functionally different subpopulations of actin is caused by decoration with different ABPs. Here, the subpopulation enclosing the nuclear basket may be accessible for the Lifeact-psRFP fusion protein due to a scarcer decoration with ABPs. In contrast, binding of the tetrameric probe to the cortical filaments is inhibited by dense ABP coverage (**Fig. 7.6**). Thus, we suggest that

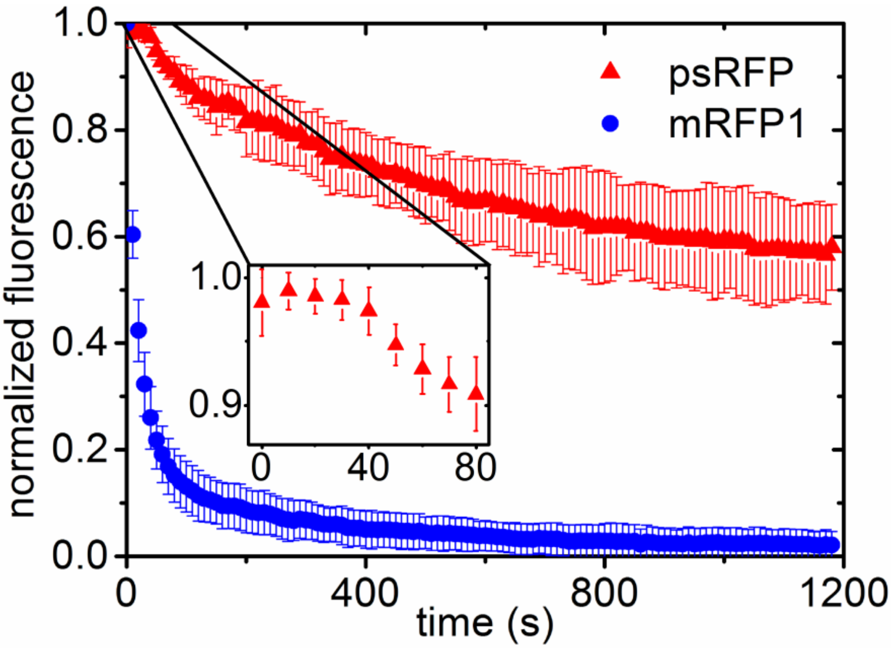

Figure 7.5.: Normalized fluorescence of Lifeact-psRFP (triangles) and Lifeact-mRFP1 (dots) expressed in BY-2 cells recorded during continuous irradiation with 561-nm light (35 W/cm^2). The average and standard deviation of the fluorescence of five (psRFP) and six (mRFP1) cells were computed. In the beginning of the experiment, the on-switching of psRFP due to 561-nm light irradiation can be observed (inset).

different subpopulations of actin within a cell can be specifically visualized by the sole difference of the nature of the FP label (tetramer vs. monomer). In a similar fashion, Leduc et al. [203] showed that it is possible to generate traffic jams on microtubules by molecular crowding of kinesin-8-motor proteins. More support for this model of steric hindrance comes from the observation that cortical AFs were labeled by Lifeact-psRFP in dying cells. Probably, these cells had stopped to control their ABP decoration leading to free accessibility of the Lifeact-psRFP binding motif. By the same token, the complete decoration of AFs in transiently transformed BY-2 cells expressing Lifeact-psRFP can also be explained. In transient transformation, only those cells with the highest level of expression are bright fluorescent and subsequently imaged by fluorescence microscopy. However, those cells are not viable over longer periods of time. They are extremely stressed by the functional disruption of the cytoskeleton as a consequence of Lifeact-psRFP overexpression. By natural selection, only cells in which the expression level of the probe does not impair cellular functions will survive. By stable transformation, physiological levels of the probe can be expected. Using localization microscopy, a specific functional actin subpopulation was selectively visualized in 3D at a high lateral resolution by means of the tetrameric Lifeact-psRFP probe in tobacco BY-2 cells. In

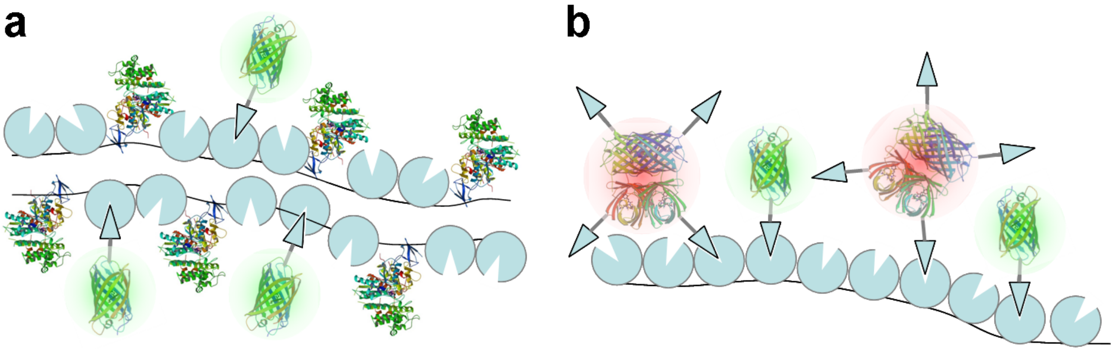

Figure 7.6.: Lifeact-psRFP model. (**a**) Only small, monomeric fluorescent probes can bind to cortical actin filaments via Lifeact due to dense coverage with ABPs. (**b**) Perinuclear actin is decorated less with ABPs and, thus, can also be labeled by large, tetrameric fluorescent probes.

animal cells, intermediate filaments are known to preserve the nuclear structure. Despite considerable research efforts, intermediate filaments including the nuclear lamina could not be detected in plant cells. The subpopulation of actin filaments revealed by localization of Lifeact-psRFP might represent the functional plant analogue of the nuclear lamina. The sterically different AF population discovered in this nuclear basket further refines existing models of nuclear migration, even though the whole mechanism is still far from being completely understood. In the future, psRFP fused to Lifeact (or other proteins of interest) might be used as a probe to address the problem of functional compartmentalization, i.e., the coexistence of functionally distinct subsets of organelles or protein complexes without separation by a membrane.

7.2. Desmin Filament Assembly Visualized by Dual Color PALM

7.2.1. The Desmin Protein and ARVC

Muscle cells contain several intermediate filament (IF) proteins such as desmin, vimentin, nestin, synemin, syncoilin, lamins, and cytokeratins [204]. Desmin is the major muscle-specific IF protein found in cardiac, skeletal and smooth muscle cells. It forms a three-dimensional scaffold around the myofibrillar Z-disk and connects the entire contractile apparatus to the subsarcolemmal cytoskeleton, the nuclei and membrane localized, multi-protein complexes like desmosomes and costamers [205, 206]. Therefore, it is essential for maintaining muscle cytoarchitecture. Desmin also forms longitudinal connections between the peripheries of successive Z-disks and along the plasma membranes of striated muscle cells. It is particularly abundant at the myotendinous junctions and at the neuromuscular junctions of skeletal muscle, and also in the intercalated disks, the attachment sites between cardiomyocytes in cardiac muscle. Desmin is encoded by a single gene present in all species studied to date. Like other IF proteins, desmin consists of a central, helical rod-domain built from 303 amino acids flanked by a globular N-terminal head and a C-terminal tail domain (**Fig. 7.7**). The central rod domain is constructed from four helical subdomains called 1A, 1B, 2A and 2B, which are separated by three non-helical linker regions L1, L12 and L2. Desmin filament assembly can be dissected into three major steps [207]. The elementary building block of desmin filaments

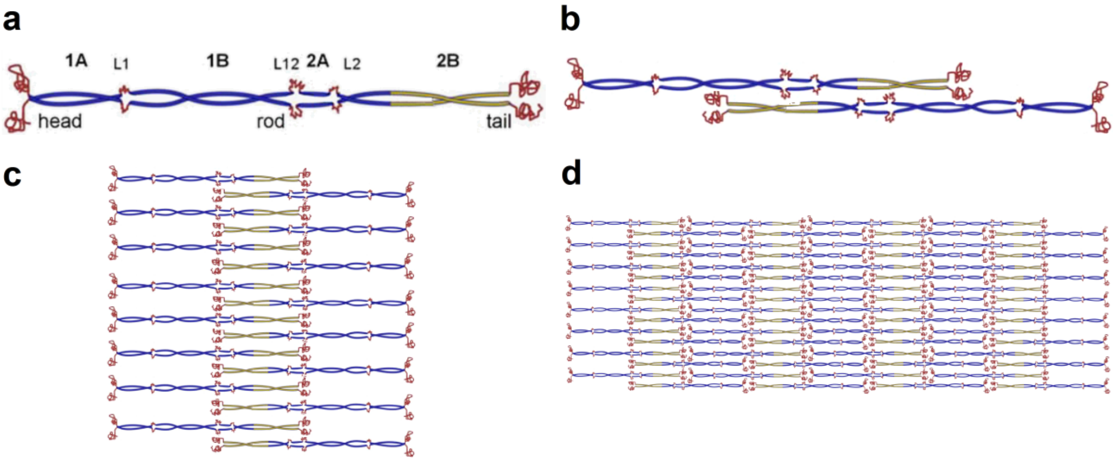

Figure 7.7.: IF assembly. (**a**) Single dimer consisting of a head, tail and a central rod domain, which is divided into four helical subdomains (1A, 1B, 2A, 2B) connected by linker regions (L1, L12, L2). (**b**) Two anti-parallel dimers assemble into tetramers. (**c**) Eight tetramers associate into ULFs. (**d**) ULFs longitudinally associate into full filaments. Scheme adopted from Ackbarow et al. [208].

are tetramers, which are built in an anti-parallel alignment of two desmin coiled-coil dimers. In the first step of desmin assembly, ULFs are built by lateral association of eight tetramers. In the second step, short filaments arise by longitudinal annealing of ULFs. In the third and final assembly step, these filaments are extended into longer filaments with a diameter of approximately $10 - 15\,\mathrm{nm}$.

Mice with an inactive desmin gene (desmin knockout mice) develop normally and are fertile. The absence of desmin does not affect the early stages of muscle development or the subsequent maturation of muscle fibers. However, after birth, mice lacking desmin suffer from cardiomyopathy, skeletal myopathy, and smooth muscle dysfunction, reducing the life span of the desmin knockout mice. The hearts of desmin knockout mice are most severely defective [209,210]. A heart without desmin develops cardiomyocyte hypertrophy and desmin-related myopathy (DRM), characterized by extensive cardiomyocyte death, calcification and multiple ultrastructural alteration. DRMs have been linked to skeletal and cardiac myopathies in which the desmin filament network is lost and abnormal aggregates of desmin are formed in muscle fibers [211]. The clinical effects are heterogeneous, including one or more characteristic symptoms, such as skeletal myopathy, different forms of cardiomyopathy, respiratory deficiency, neuropathy, and smooth muscle disorders. Some of these hereditary or sporadic disorders are attributable to missense mutations and deletions in the desmin gene [212–214]. Arrhythmogenic right ventricular cardiomyopathy (ARVC) is such an inherited heart muscle disease, frequently accompanied by terminal heart failure [215].

ARVC is characterized by predominant dilation of the right ventricle and arrhythmia. Presumably, loss of cardiomyocytes by apoptosis and replacement of heart muscle tissue by fatty and fibrous tissue lead to heart failure and sudden death under physical stress. It is well accepted that mutations in the five cardiac desmosomal proteins DSG2, DSC2, DSP, PKP2, and JUP cause ARVC. In addition to adherent and gap junctions, desmosomes are one of the three adhesive elements which are localized at intercalated discs in cardiac tissue. In contrast to adherens junctions, which are connected to actin filaments, desmosomes are linked to IFs by desmoplakin. Therefore, it is believed that ARVC is a disease of altered adhesion among cardiomyocytes, resulting in an inhibited force transmission and decreased cohesion between cardiomyocytes.

Recently, several groups identified heterozygous mutations in different domains of the desmin gene of ARVC patients. Yet, it is not known how desmin mutations contribute to the arrhythmogenic phenotype of ARVC. Some of these mutations cause desmin to conglomerate into abnormal aggregates. Since all ARVC-related desmin mutations known so far are heterozygous, it is essential to analyze the composition of desmin filaments and aggregates to understand the pathomechanisms. It is unknown if wild type (wt) and mutant desmin coexist in the same protein complexes, i.e., filaments and aggregates, or if, e.g., aggregates are exclusively composed of mutant desmin. Therefore, we studied how coexpression of mutant and wt desmin affects filament assembly using super-resolution dual color PALM.

7.2.2. Cells Used to Study the Effects of Desmin Mutations

In the experiments presented here, the influence of five different ARVC-related desmin mutations on filament assembly was studied. The mutants were coexpressed with wt desmin and imaged using super-resolution dual color PALM [85,105]. The human adrenal carcinoma cell line SW-13 (ATCC, CLL-105) used in numerous other investigations of intermediate filament proteins was chosen for this study. SW-13 cells do not endogenously express cytoplasmatic intermediate filament proteins like desmin or vimentin that could have altered the results. Another advantage of this cell line is the high transfection efficiency. First, we tested our system by transient tranfection of wt desmin fused to mEosFP*thermo* [86]. mEosFP*thermo* is a green fluorescent protein that can be converted to a red emitting form by inducing a backbone cleavage with 400-nm light (see subsection 2.5.7). It is a variant of monomeric EosFP [95] where the alanine at position 69 has been replaced by a valine. This single point mutation improves the expression of functional proteins at 37°C. The resulting fluorescence images yielded the typical filamentous structures known for the desmin protein (**Fig. 7.8**). In the PALM images, filament arrangement was revealed in a much greater detail. A quantitative evaluation

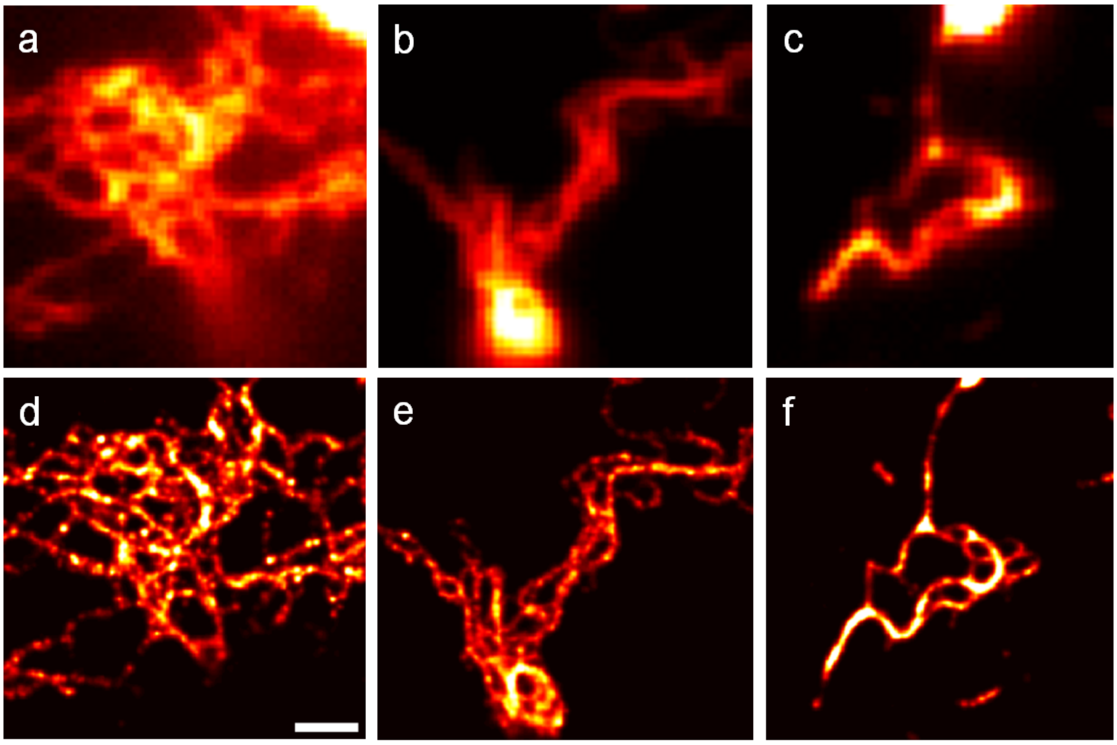

Figure 7.8.: Fluorescence images of desmin-mEosFP*thermo* in live SW-13 cells. (**a-c**) Epifluorescence images. (**d-f**) PALM images reconstructed from 20,000 frames acquired at 3 ms camera exposure time. Scale bar, 1 µm.

of the localization precision (see subsection 7.2.4) yielded a $5-6$ fold increase in image resolution by PALM. From the images, it can also be seen that individual desmin filaments tended to cluster into larger superstructures when expressed in SW-13 cells.

Materials and Methods

Cloning and mutagenesis: The desmin constructs were created by cloning the full-length cDNA of human desmin in frame into pEYFP-N1 or pECFP-N1 plasmids (Clontech, Mountain View, USA). The single point mutations S13F, E114del, N116S, N342D and R454W were introduced by site-directed mutagenesis (QuikChange Lightning, Stratagene, Santa Clara, USA). Plasmids used for PALM experiments were generated by replacing EYFP with mEosFP*thermo* and mIrisGFP. The accuracy of each plasmid was controlled by sequencing on an ABI-310 genetic analyser (Applied Biosystems, Foster City, USA) using the Big Dye Terminator v3.1 cycle sequencing kit (Applied Biosystems). Desmin was cloned and mutated by Andreas Brodehl.

Cell culture and transfection: SW-13 cells were grown in culture dish assemblies on glass coverslips in DMEM without phenol red, supplemented with 10% FBS and penicillin/streptomycin (Gibco, Invitrogen). Cells were transfected using Lipofectamine 2000 (Invitrogen) according to the manufacturer's protocol. 800 ng of plasmid was used for single transfections, whereas 400 ng of each plasmid were used for double transfections. Cells were analyzed 24 h after transfection. SW-13 cells were cultured and transfected by Andreas Brodehl.

7.2.3. Dual Color PALM

A major issue in dual color PALM experiments is the choice of paFPs. In addition to the excitation wavelength, paFPs need to be irratiated with light of another, blue-shifted wavelength to induce photoconversion or photoswitching. Usually, to maximize localization precision in PALM imaging, fluorescence is excited at power densities of up to several $\mathrm{kW/cm^2}$ to gain as many photons per fluorophore as possible in a single image frame. On the other hand, the number of fluorescence emitters in the field of view should be low enough to ensure their spatial separation. Thus, the molecules are only sparsely photoactivated using comparatively low power densities. Consequently, for simultaneous imaging of two color channels, the excitation and activation wavelengths of the two fluorophores employed must not overlap. Furthermore, the photoactivation yield is different for each paFP, especially amongst photoconvertible and photoswitchable proteins. Therefore, the activation wavelengths of both markers should also be different to ensure an optimal number of fluorescing molecules by an independent control of photoconversion in both simultaneously acquired color channels. **Tab. 7.1** gives an overview of the current monomeric paFPs showing that, unfortunately, there is always a conflict in wavelengths. Thus, until now, dual color PALM imaging is usually performed in a sequential manner.

Table 7.1.: Overview of excitation/emission and photoactivation wavelengths of monomeric paFPs used in PALM imaging.

Fluorescent protein	Form	Excitation/ emission (nm)	Activation (nm)	Activation mode	Switching mode
PA-GFP [69]		504/517	405	irreversible	-
PAmCherry1 [216]		564/595	405	irreversible	-
PS-CFP2 [104]	cyan	402/468	-	-	-
	green	490/511	405	irreversible	-
Dronpa [101]		503/518	405	reversible	negative
Padron [105]		503/522	405	reversible	positive
rsFastLime [217]		496/518	405	reversible	negative
mIrisFP [86]	green	486/516	405	reversible/	negative
	red	546/578	473	irreversible	negative
mEos2 [218]	green	506/519	-	-	-
	red	573/584	405	irreversible	-
Dendra2 [219]	green	490/507	-	-	-
	red	553/573	405	irreversible	-
rsCherry [220]		572/610	450	reversible	positive
rsCherryRev [220]		572/608	450	reversible	negative

We decided to use the combination of mEosFP*thermo* (red channel) and mIrisGFP (green channel). As a green-to-red converter, mEosFP*thermo* provides a contrast and brightness superior to any red fluorescent on-off-switcher currently in use. The disadvantage for dual color imaging is the green fluorescence of mEosFP*thermo* before photoconversion, as it interferes with the emission spectrum of the green emitting mIrisGFP. Therefore, the red channel has to be imaged first. During imaging of red fluorescence, the photoconversion of all mEosFP*thermo* molecules guarantees the absence of any green fluorescent mEosFP*thermo* molecules before data acquisition is continued in the green channel. mIrisGFP is a variant of mIrisFP lacking the green-to-red photoconversion mode but staying photoswitchable in the green [91]. As a negative photoswitcher, off-switching is induced by the same wavelength as the one used for excitation (473 nm), whereas on-switching can be induced by illumination with 400-nm light. The high off-switching rate of mIrisGFP induced by strong 473-nm irradiation for excitation requires fast imaging with camera exposure times of just a few milliseconds. Yet, this circumstance is not of any disadvantage. In live-cell imaging, temporal resolution is an important point since movements of cellular structures during data acquisition lead to image blurring. This becomes an even more severe issue in a colocalization experiment, where both channels are recorded in a sequential manner. Here, movement not just blurs each of the two images, but also causes an artificial displacement between the labeled structures after overlay of both images – a severe problem in a colocalization study. We employed a camera exposure time of 3 ms only, so that an entire PALM image set of 20,000 individual frames was recorded within one minute. Another advantage of short acquisition times was the negligible mechanical drift of the microscopy setup ($< 7\,\mathrm{nm}$), thereby avoiding drift corrections.

Materials and Methods

PALM imaging: After transfection of SW-13 cells, red PALM images were acquired at room temperature (24°C) on the setup described in subsection 4.2.2 set to epifluorescence mode. Before and after PALM imaging, we acquired a DIC image of each cell to monitor cell morphology. PALM images of single transfected cells expressing a mEosFP*thermo* fusion protein were acquired using an EMCCD camera (Ixon DV897ECS-BV, Andor) with 512×512 pixels and a field of view of $55 \times 55\,\mu\mathrm{m}^2$. A total of $10,000 - 20,000$ frames with a camera exposure time of 50 ms were acquired for each high resolution image. Fluorescence of the red form of mEosFP*thermo* was excited with 561-nm laser light at $0.3 - 0.5\,\mathrm{kW/cm^2}$ and green-to-red photoconversion was induced by 405-nm laser light at $0 - 0.02\,\mathrm{kW/cm^2}$. Fluorescence light was filtered by a 610/75 nm bandpass (HQ 610/75, Chroma) after passing the excitation dichroic (z 405/473/561, AHF). PALM images of double transfected cells expressing mEosFP*thermo* as well as mIrisGFP fusion proteins were acquired using a second, faster EMCCD camera (Ixon EM+ DU-860, Andor). Dual color PALM images were acquired with an exposure time of 3 ms per frame (128×128 pixels, $14 \times 14\,\mu\mathrm{m}^2$ field of view). For each color channel, $5,000 - 20,000$ frames were recorded depending on the protein expression of the individual cells. Fluorescence of the red form of mEosFP*thermo* was excited with 561-nm laser light at $2.5 - 4.5\,\mathrm{kW/cm^2}$ and green-to-red photoconversion was induced by 405-nm laser light at $0 - 0.2\,\mathrm{kW/cm^2}$. For excitation and off-switching of mIrisGFP, 473-nm light at $2.8 - 3.6\,\mathrm{kW/cm^2}$ was used, whereas on-switching was induced by 405-nm light at $0 - 0.2\,\mathrm{kW/cm^2}$. Fluorescence light was separated by the excitation dichroic mirror and filtered by a 610/75 nm bandpass (HQ 610/75, Chroma) for detection of red fluorescence and by a 535/70 nm bandpass (HQ 535/70, Chroma) for detection of green fluorescence. PALM images were analyzed by fitting a 2D Gaussian distribution to the single molecule signals detected, using a homemade algorithm written in Matlab (MathWorks) [79].

7.2.4. Control Experiments

Full photoconversion of mEosFPthermo

As the criterion for finishing data acquisition in the red channel and starting data acquisition in the green channel, we chose the point when no new molecules appeared in the red channel despite strong illumination with 405-nm light, assuming that all molecules had been converted and subsequently bleached. Thus, it was necessary to show that there were no green mEosFP*thermo* molecules left that had escaped photoconversion. Due to the nearly identical spectra of the green emission of mEosFP*thermo* and mIrisGFP, it was not possible to prove that point within the dual color coexpression experiments. In a control experiment, we imaged cells expressing only desmin-mEosFP*thermo* by PALM using the same illumination and image acquisition protocol as for the coexpression experiments. **Fig. 7.9** shows that no molecules were detected by the reconstruction algorithm in the green channel after photoconversion.

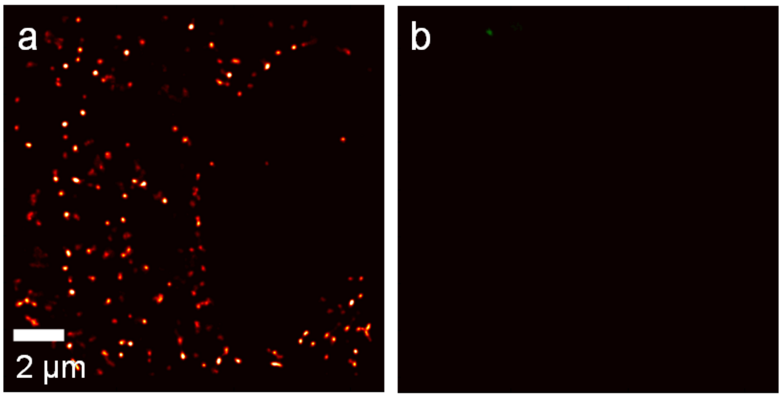

Figure 7.9.: PALM images of live SW-13 cells expressing N116S-mEosFP*thermo*. (**a**) Red channel and (**b**) green channel after photoconversion of mEosFP*thermo*.

Absence of Photoconversion of mIrisGFP

To exclude crosstalk, it was necessary to prove that mIrisGFP did not convert to a red emitting form at the power level of 405-nm irradiation used in the experiments. For this purpose, cells expressing only desmin-mIrisGFP were prepared and subjected to PALM. The images shown in **Fig. 7.10** were reconstructed after application of the same illumination and image acquisition protocol as used for the coexpression experiments. It is evident that no molecules were detectable in the red channel.

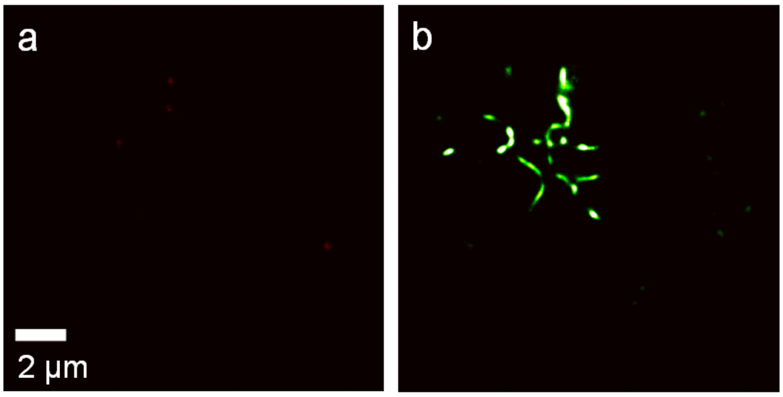

Figure 7.10.: PALM images of live SW13 cells expressing wt-mIrisGFP. (**a**) Red channel and (**b**) green channel after attempted photoconversion of mIrisGFP.

Spatial Drift of the Imaging System

We imaged 20 nm red fluorescent beads (Invitrogen) dried in on a glass surface in order to monitor the spatial drift of the microscope setup. **Fig. 7.11** displays the drift that occurred within 130 s, which was the maximum acquisition time for our experiments (two times 60 s for red and green image plus 10 s for filter change). The drift did not exceed 7 nm. The width of the distribution of the emitter locations within the scatter plot reflects the localization precision obtained for the fluorescent beads, which was 3 nm.

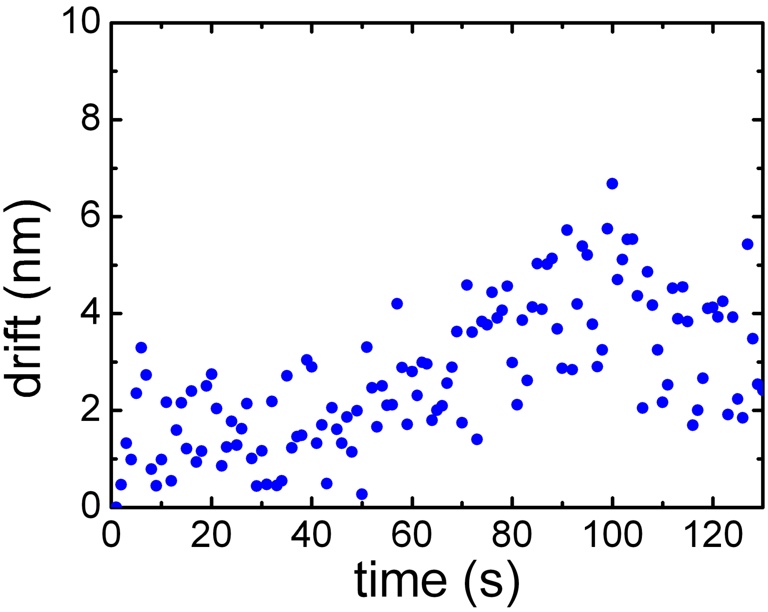

Figure 7.11.: Drift of the microscope setup within 130 s monitored by tracking 20 nm red fluorescent beads (Invitrogen). One frame was acquired every second.

Cell Morphology

As with any other fluorescence microscopy technique, photodamage induced by high intensity light irradiation can be an issue in PALM. Therefore, we acquired DIC images before and after each PALM measurement to monitor changes in cell morphology indicating severe damage to the cell. **Fig. 7.12** shows an example of such pre- and post-PALM images, no adverse effects of illumination with the employed protocol were detected.

Localization Precision

The resolution of a PALM image depends on the localization precision of the individual fluorophores (subsection 2.5.6, equation 2.107) and on the density of labels. **Fig. 7.13**

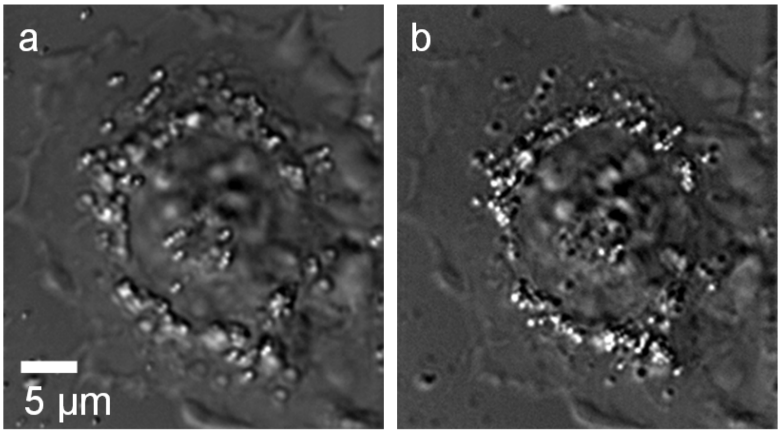

Figure 7.12.: (**a**) Pre- and (**b**) post-PALM DIC picture of a double transfected SW-13 cell. The illumination protocol applied between the acquisition of both images is described in subsection 7.2.3.

shows the distribution of signal photons, background photons and 2D position errors representative for the PALM images presented in subsection 7.2.5. The number of signal photons detected for mEosFP*thermo* was higher and, at the same time, background was lower than for mIrisGFP. Thus, the mean localization precision in the red channel was $\sim$ 10 nm higher than in the green channel. Still, the resolution of the green widefield image (226 nm, calculated from an emission wavelength of 516 nm and a NA of 1.46) was substantially surpassed. With 50 ms of integration time per frame, the average number of photons detected per burst increased from 204 to 316 photons. Interestingly, the localization precision was the same, since the background also increased with the camera exposure time. These results are consistent with the numbers for mEos2, a paFP with similar properties as mEosFP*thermo*. At a camera exposure time of 100 ms, an average of 360 photons were detected per burst for mEos2 resulting in a 1D position error of 11 nm [218]. It has to be noted that the photon numbers heavily depend on the threshold setting of the data evaluation because, thereby, a cut-off at the lower end is set. Therefore, the results from different groups using different algorithms and settings are not directly comparable.

7.2.5. Observed Effects of Desmin Mutants

Overview of Desmin Mutants

All examples shown for the double transfected cells represent typical results of $10 - 20$ cells imaged. The examples shown for the single transfected cells represent typical results of $\sim$ 5 PALM images. In the coexpression experiments, mIrisGFP was fused to the wt and mEosFP*thermo* was fused to the mutated form of desmin, unless indicated otherwise. **Fig. 7.14** displays an overview in single transfected cells of all desmin variants studied, namely wt, R454W, S13F, N342D, N116S and E114del fused to mEosFP*thermo*. The

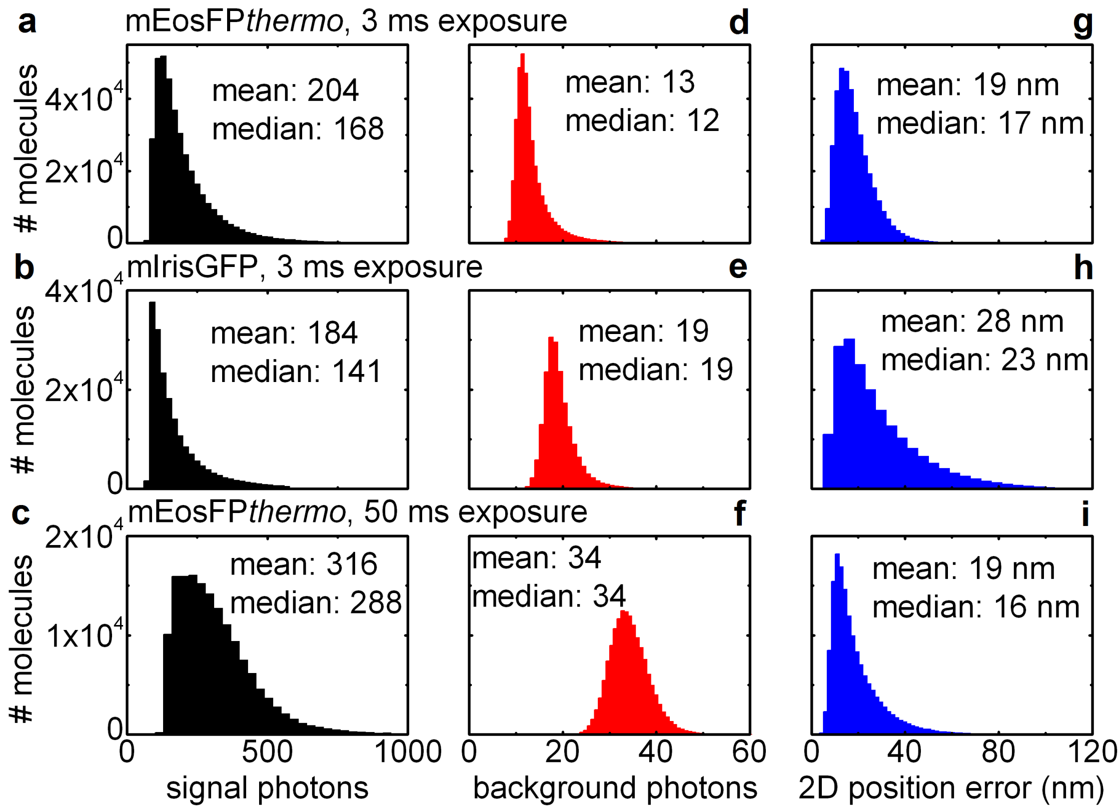

Figure 7.13.: Single molecule statistics representative of the PALM measurements with the paFPs mEosFP*thermo* and mIrisGFP. (**a-c**) Number of signal photons detected per burst, (**d-f**) number of background photons detected per molecule per pixel and (**g-i**) 2D localization error.

standard epifluorescence images already revealed different effects of the various mutations on filament assembly, if only the mutant was expressed. The structures formed by R454W and S13F resembled those of wt desmin, whereas the mutants N342D, N116S and E114del formed abnormal aggregates.

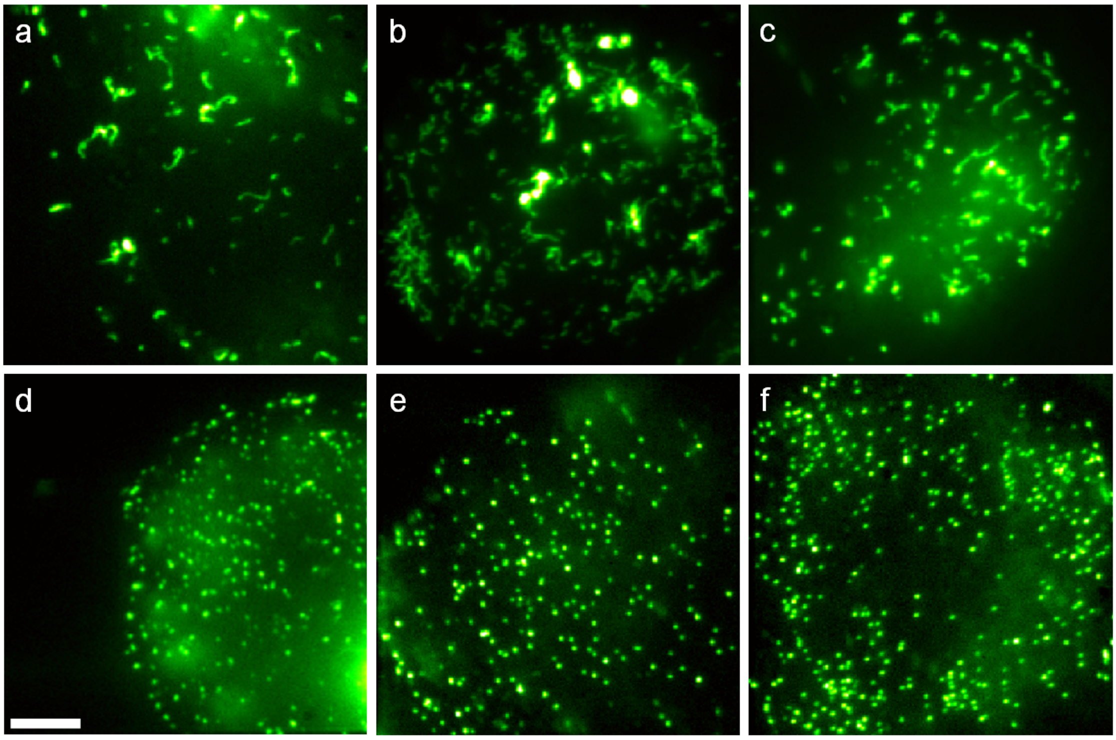

Figure 7.14.: Standard epifluorescence images of live SW-13 cells expressing desmin-mEosFP*thermo* fusion constructs. (**a**) wt, (**b**) R454W, (**c**) S13F, (**d**) N342D, (**e**) N116S and (**f**) E114del. Scale bar, 5 µm.

Desmin Wild Type

Transfected SW-13 cells expressing wt-mEosFP*thermo* displayed filamentous structures as expected for the desmin protein (**Fig. 7.15**). The substantial resolution enhancement of the PALM image compared to the standard epifluorescence image is clearly visible. When expressed in SW-13 cells, individual desmin filaments tended to cluster into larger superstructures. Double transfected cells expressing wt-mIrisGFP as well as wt-mEosFP*thermo* were imaged in order to assess the data quality that is to be expected from the following coexpression experiments. Typical desmin filaments can be seen in **Fig. 7.15c-k**. In all examples shown, colocalization of the structures in the green and red channel are clearly visible. Yet, there are some slight variations that need further explanation. Slight movement of the structures might had occurred during acquisition of the high resolution PALM images, taking one minute per color channel. We minimized

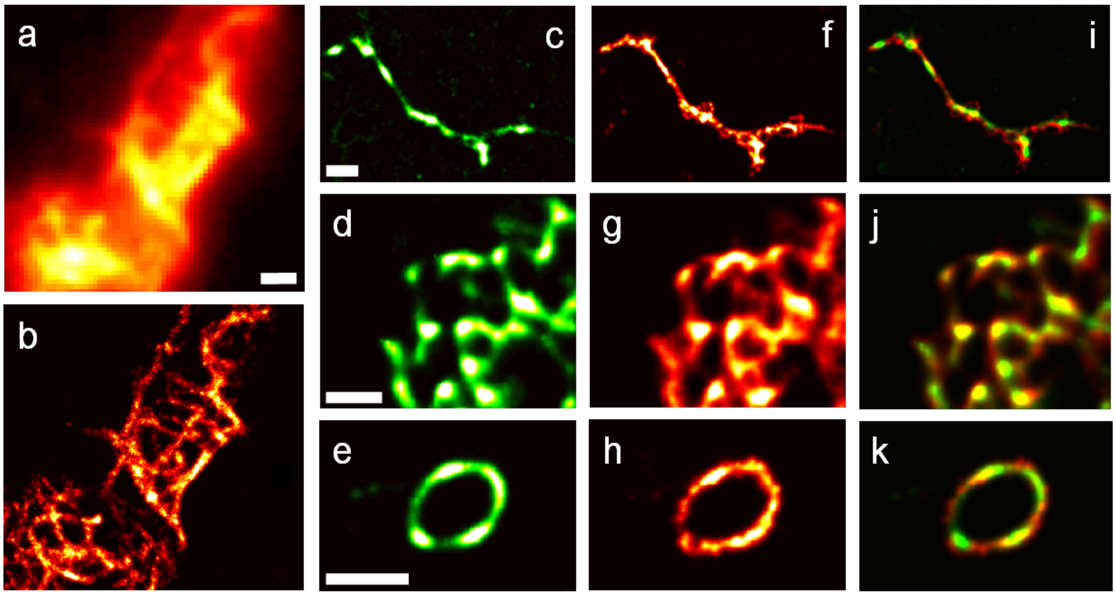

Figure 7.15.: (**a,b**) Fluorescence images of live single transfected SW-13 cells expressing wt-mEosFP*thermo*. (**a**) Epifluorescence image depicting a close-up of a cluster of desmin filaments. (**b**) PALM image of the same area revealing much greater structural detail. (**c-k**) PALM images of live SW-13 cells expressing wt-mEosFP*thermo* and wt-mIrisGFP. (**c-e**) Green PALM images, (**f-h**) red PALM images and (**i-k**) overlay of both color channels. Scale bars, 1 µm.

cell movement by measuring at room temperature (24°C) instead of 37°C. Still, cellular dynamics was not completely inhibited. If the shift occurred in the lateral direction, it could be monitored and, typically, it was less than 100 nm. A more severe problem was a shift in the axial direction. In this case, the structure moved out of focus. Thus, the diffuse images of the single emitters could no longer be evaluated by the localization algorithm and were discarded. Although the optical elements in the microscope setup were fully color corrected, chromatic aberration can occur at larger imaging depths since the fluorescence light has to penetrate cell material. Another issue were the different photophysical properties of the employed fluorophores such as quantum yield, brightness and photoactivation characteristics. In localization analysis, all events below a certain photon threshold are not detected and/or evaluated. Weak single molecule fluorescence, e.g., from slightly defocused areas, is considered as background and discarded. Consequently, such structures are not represented in the final PALM image. This cut-off was different for the green and red image due to the differences in brightness and contrast of the employed fluorophores.

Desmin R454W

Single transfected cells expressing R454W-mEosFP*thermo* (**Fig. 7.16a,b**) displayed filamentous structures comparable to those of wt desmin, barely showing any sign of aggregate formation. Double transfected cells expressing wt-mIrisGFP as well as R454W-mEosFP*thermo* fusions (**Fig. 7.16c-k**) showed no sign of aggregate formation. Also, both forms colocalized within the same filaments, indicating that the mutant R454W has only a minor influence on filament assembly.

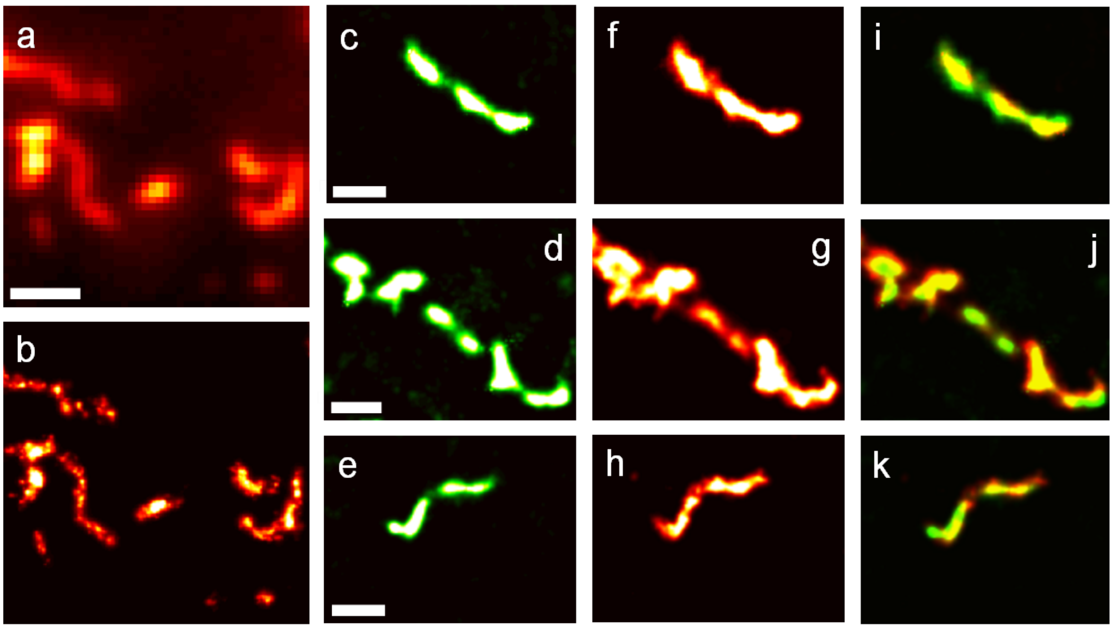

Figure 7.16.: (**a**) Epifluorescence and (**b**) PALM image of R454W-mEosFP*thermo* expressed in live SW13 cells. (**c-k**) PALM images of wt-mIrisGFP coexpressed with R454W-mEosFP*thermo* in live SW-13 cells. (**c-e**) Green PALM images, (**f-h**) red PALM images and (**i-k**) overlay of both color channels. Scale bars, 1 µm.

Desmin S13F

Similar to the mutant R454W, single transfected cells expressing S13F-mEosFP*thermo* (**Fig. 7.17a,b**) displayed filamentous structures comparable to those of wt desmin, only little aggregate formation occurred. Double transfected cells expressing wt-mIrisGFP as well as S13F-mEosFP*thermo* (**Fig. 7.17c-k**), showed very little sign of aggregate formation. Again, the mutant was incorporated into the filaments and, thus, it affected filament assembly minimally – if at all.

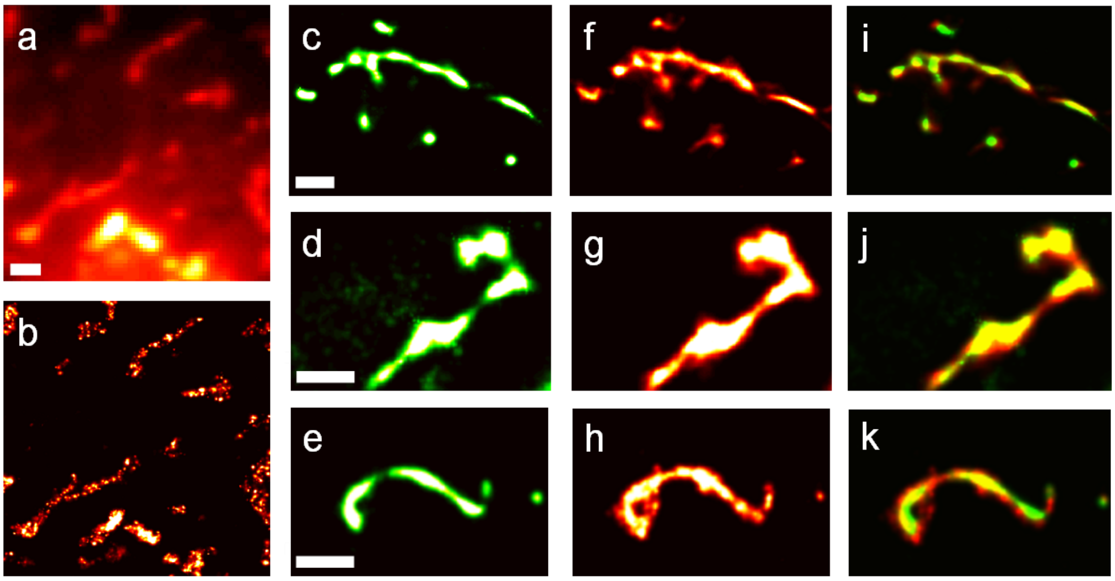

Figure 7.17.: (**a**) Epifluorescence and (**b**) PALM image of S13F-mEosFP*thermo* expressed in live SW13 cells. (**c-k**) PALM images of wt-mIrisGFP coexpressed with S13F-mEosFP*thermo* in live SW-13 cells. (**c-e**) Green PALM images, (**f-h**) red PALM images and (**i-k**) overlay of both color channels. Scale bars, 1 µm.

Desmin N342D

In single transfected cells expressing N342D-mEosFP2A69V (**Fig. 7.18a,b**), filament assembly was disrupted as only aggregates were visible. When coexpressed with wt desmin, filament assembly was recovered. Yet, both forms colocalized within the same structures (**Fig. 7.18c-k**). This indicates that this mutation has only minor influence on filament assembly when coexpressed with the wt in contrast to the heavy aggregate formation in cells expressing the mutant only.

Desmin N116S

In single transfected cells expressing N116S-mEosFP*thermo*, filament assembly was completely inhibited (**Fig. 7.19a,b**), only aggregates were visible. When coexpressed with wt desmin, filaments as well as aggresomes appeared (**Fig. 7.19c-k**) and, thus, filament assembly was partially recovered. Again both forms colocalized within both structures. Yet, the mutant N116S clearly disrupts filament assembly.

Desmin E114del

Single transfected cells expressing E114del-mEosFP*thermo* showed similar behavior to N116S-mEosFP*thermo* expressing cells. Filament assembly was completely inhibited

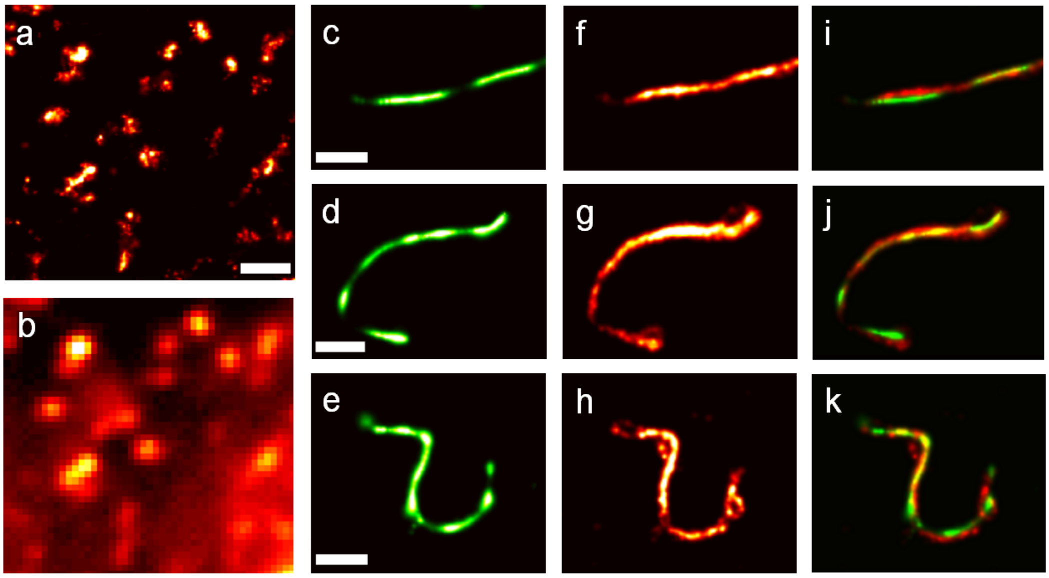

Figure 7.18.: (**a**) Epifluorescence and (**b**) PALM image of N342D-mEosFP*thermo* expressed in live SW13 cells. (**c-k**) PALM images of wt-mIrisGFP coexpressed with N342D-mEosFP*thermo* in live SW-13 cells. (**c-e**) Green PALM images, (**f-h**) red PALM images and (**i-k**) overlay of both color channels. Scale bars, 1 µm.

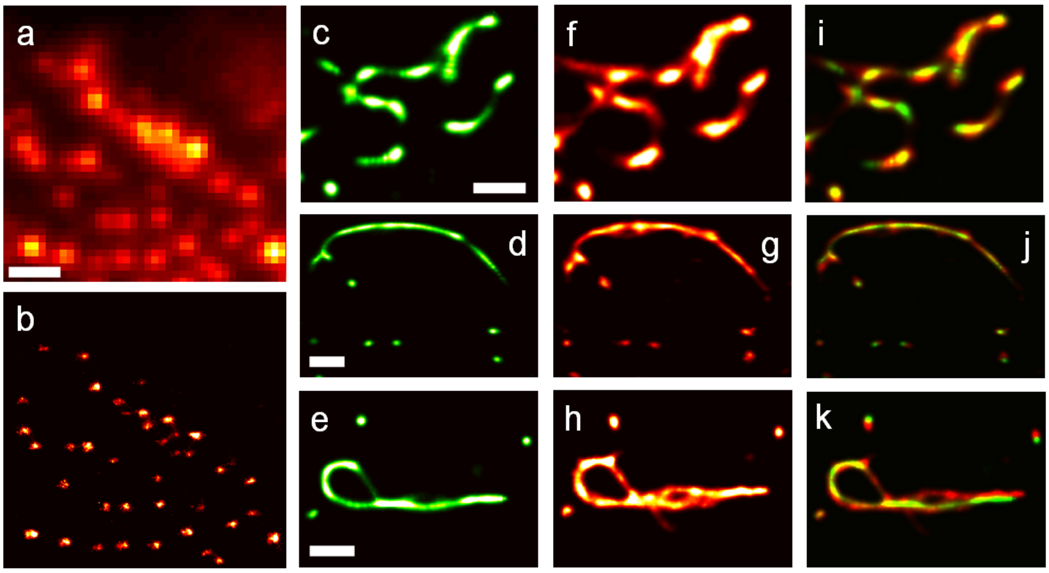

Figure 7.19.: (**a**) Epifluorescence and (**b**) PALM image of N116S-mEosFP*thermo* expressed in live SW13 cells. (**c-k**) PALM images of wt-mIrisGFP coexpressed with N116S-mEosFP*thermo* in live SW-13 cells. (**c-e**) Green PALM images, (**f-h**) red PALM images and (**i-k**) overlay of both color channels. Scale bars, 1 µm.

(**Fig. 7.20a,b**), only aggresomes were visible. When the mutant E114del was coexpressed with wt desmin, only aggresomes appeared (**Fig. 7.20c-k**). Yet again, both forms colocalized within those structures, although filament assembly was completely inhibited.

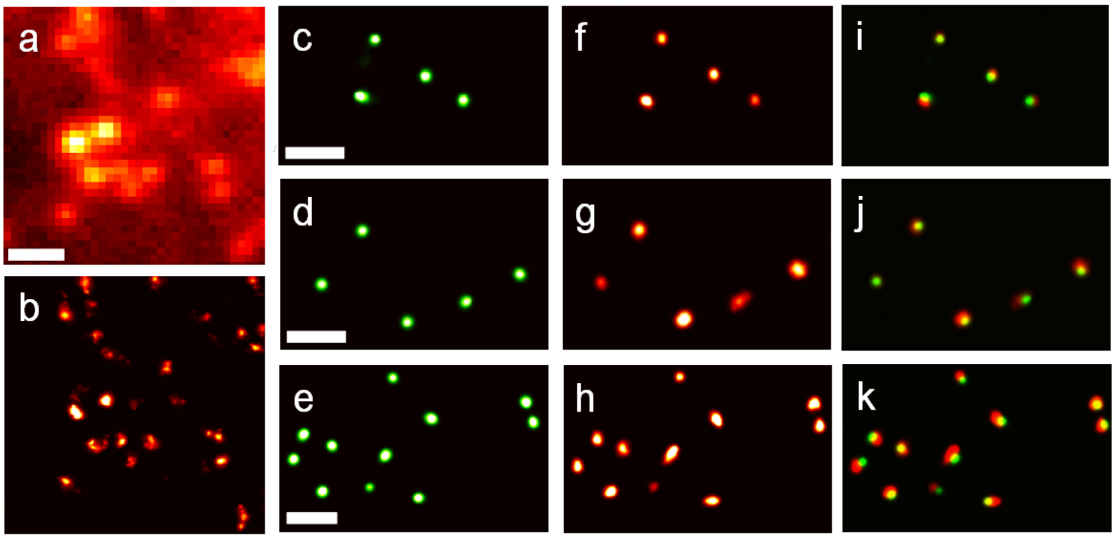

Figure 7.20.: (**a**) Epifluorescence and (**b**) PALM image of E114del-mEosFP*thermo* expressed in live SW13 cells. (**c-k**) PALM images of wt-mIrisGFP coexpressed with E114del-mEosFP*thermo* in live SW-13 cells. (**c-e**) Green PALM images, (**f-h**) red PALM images and (**i-k**) overlay of both color channels. Scale bars, 1 µm.

7.2.6. Summary

Since all ARVC-associated desmin mutations presently known are heterozygous, we analyzed filament or aggregate formation in mutant and wt co-transfected SW-13 cells. This cell line lacks endogenous cytoplasmic IF proteins, and was subsequently used to characterize filament formation in a controlled, heterozygous constellation. Using super-resolution dual color PALM, we compared for the first time the influence of different ARVC-related desmin mutations on filament assembly in living cells. The ARVC-related desmin mutations R454W, S13F, N342D, N116S and E114del differ in their effects on desmin filament assembly in SW-13 cells. An overview of the consequences of these five different mutations is displayed in **Fig. 7.21**. While the mutants R454W and S13F formed filamentous networks similar to wt desmin, the mutants N342D, N116S and E114del induced the formation of abnormal aggregates, when they were homozygously expressed. Coexpression of E114del in combination with wt desmin blocked the filament assembly process completely. In contrast, coexpression of the mutant N116S and wt desmin inhibited filament assembly to a lesser extent because, in co-transfected SW-13-cells, filaments as well as aggregates were visible. Coexpression of the mutant N342D

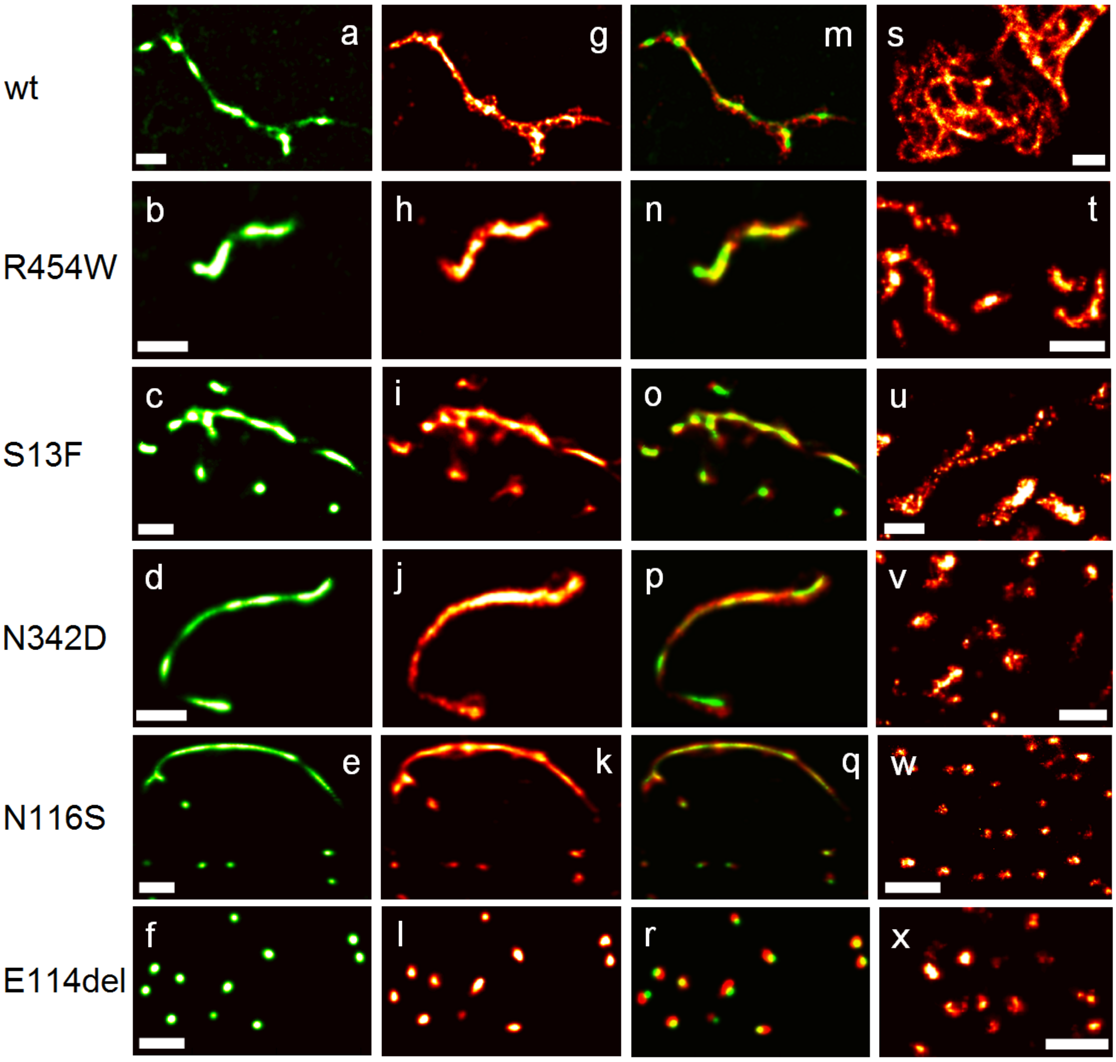
wt
R454W
S13F
N342D
N116S
E114del
a
b
c
d
e
f
g
h
i
j
k
l
m
n
o
p
q
r
s
t
u
v
w
x

Figure 7.21.: Typical structures of wt desmin and the ARVC-related mutations R454W, S13F, N342D, N116S and E114del (top to bottom) when (**a-r**) coexpressed with wt desmin as well as (**s-x**) in single transfected cells. (**a-f**) Green PALM images, (**g-l, s-x**) red PALM images and (**m-r**) overlay of both color channels. Scale bars, 1 µm.

and wt desmin led to incorporation of mutated molecules into IFs, indicating that this mutation has a minor effect on filament assembly *in vivo*. The coexpression of the other two mutants S13F and R454W seemed not to differ in phenotype of wt transfected cells.

By FRET imaging, we further confirmed the results of the PALM experiments. In FRET experiments, the energy transfer is measured due to dipole-dipole interactions between two fluorophores, the donor and the acceptor. This energy transfer strongly decreases with increasing distance between donor and acceptor. The distance for a significant energy transfer is typically limited to values $< 10\,\mathrm{nm}$. Thus, FRET can be used as a ruler to resolve intramolecular distances. For a review on FRET imaging, see Jares-Erijman et al. [221]. We imaged cells transfected with ECFP- and EYFP-tagged desmins [222]. A high FRET efficiency is expected if the two proteins are in close proximity. Thus, FRET imaging provided information on the molecular assembly of desmin filaments and aggregates (**Fig. 7.22**). As a control, wt desmin fused to both fluorescence tags was expressed in SW-13 cells. We detected FRET in all filaments, indicating that this approach was suitable for our study. For the mutants S13F, N342D and R454W,

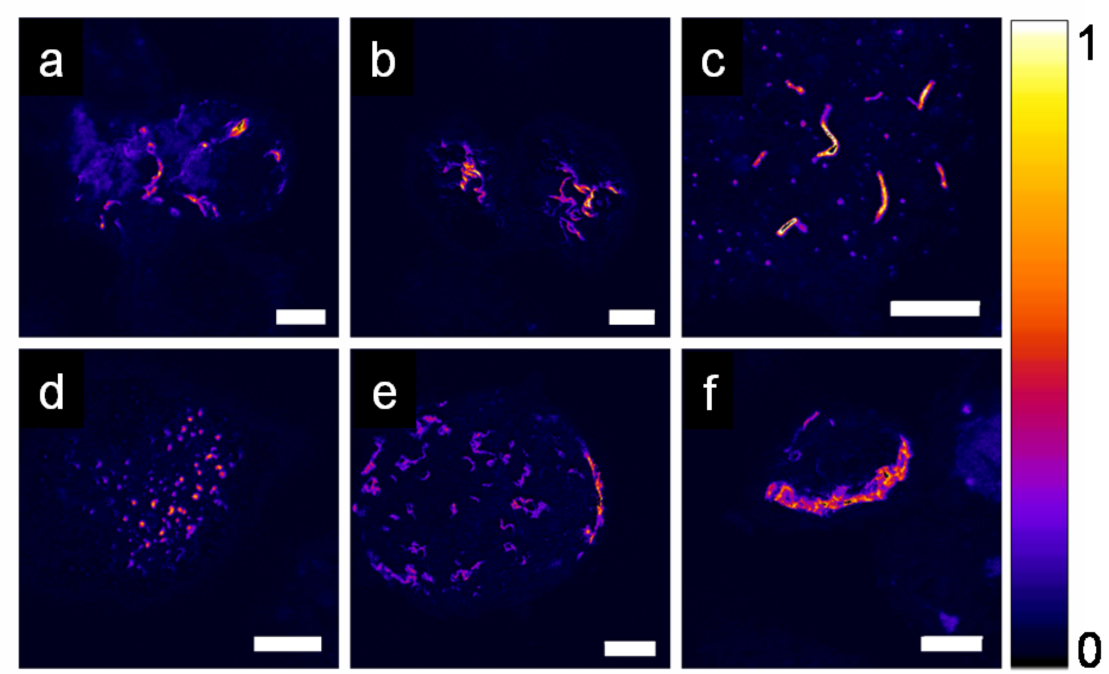

Figure 7.22.: Representative fluorescence images of SW-13 cells coexpressing wt and mutant desmin, color-coded for normalized FRET efficiency. Wt desmin was labeled with EYFP as acceptor, the indicated desmin mutants were labeled with ECFP as donor. (**a**) wt, (**b**) S13F, (**c**) N116S, (**d**) E114del, (**e**) N342D and (**f**) R454W. FRET images were acquired and analyzed by Andreas Brodehl. Scale bars, 5 µm.

mutant desmin was incorporated into the same filaments as wt desmin and, for these, no aggregates were detected. However, in cells coexpressing N116S mutant and wt desmin, small filaments as well as aggregates were visible and FRET was detected from both. For the mutant E114del coexpressed with the wt desmin, only cytoplasmic aggregates were visible. Again, strong FRET indicated coexistence of mutant and wt desmin. From the FRET experiments, it can be concluded that mutant and wt desmin always coassembles and that mutant desmin partially (N116S) or completely (E114del) prevents formation of functional filaments by wt desmin. These findings agree well with the results obtained from dual color PALM.

7.2.7. Discussion

Until now, more than fifty disease-causing desmin mutations distributed over the entire amino acid sequence have been identified [223]. The phenotypes of these diseases are clinically heterogeneous ranging from isolated myopathy, dilated cardiomyopathy with or without skeletal muscle disorder, hypertrophic, restrictive or arrhythmogenic right ventricular cardiomyopathy, respectively [224]. In this study, the effects of five recently identified ARVC-associated desmin mutations on filament formation were systematically compared to obtain further molecular insights into the assembly defects of this subgroup of mutants. Moreover, the desmin mutations analyzed in this study were found in patients as a heterozygous genotype. For each mutant, four scenarious are possible when coexpressed with wt desmin (**Fig. 7.23**):

(A) Only filaments are formed. Mutant and wt molecules are incorporated into the same filaments.

(B) Only aggregates are formed, composed of a mixture of wt and mutant molecules.

(C) Aggregates and filaments are found within the same cell, composed of a mixture of wt and mutant molecules.

(D) Aggregates and filaments are found within the same cell. Wt desmin is found exclusively in filaments, whereas only the mutant forms aggregates.

In order to identify which of these types might be found in desminopathies, we analyzed ARVC-related mutations in cell culture. Sharma et al. [225] and Pica et al. [226] found equivocal results on the desmin mutant S13F, since it formed small filaments and aggregates after homozygous transfection in different cell lines. In our experiments, the homozygous transfection of S13F revealed exclusively filaments in the majority of cells, whereas the heterozygously transfected cells displayed mixed filaments of mutant and wt. Thus, S13F forms filaments according to types (A) and (C). The amino acid serine 13 is localized within the conserved nonapeptide in the head domain, which is essential for filament assembly [227]. The heterogeneous *in vitro* effects found for the mutant S13F might depend on the degree of phosphorylation at serine 13 [228]. The mutant E114del revealed a severe aggregate formation defect, which is consistent with previous

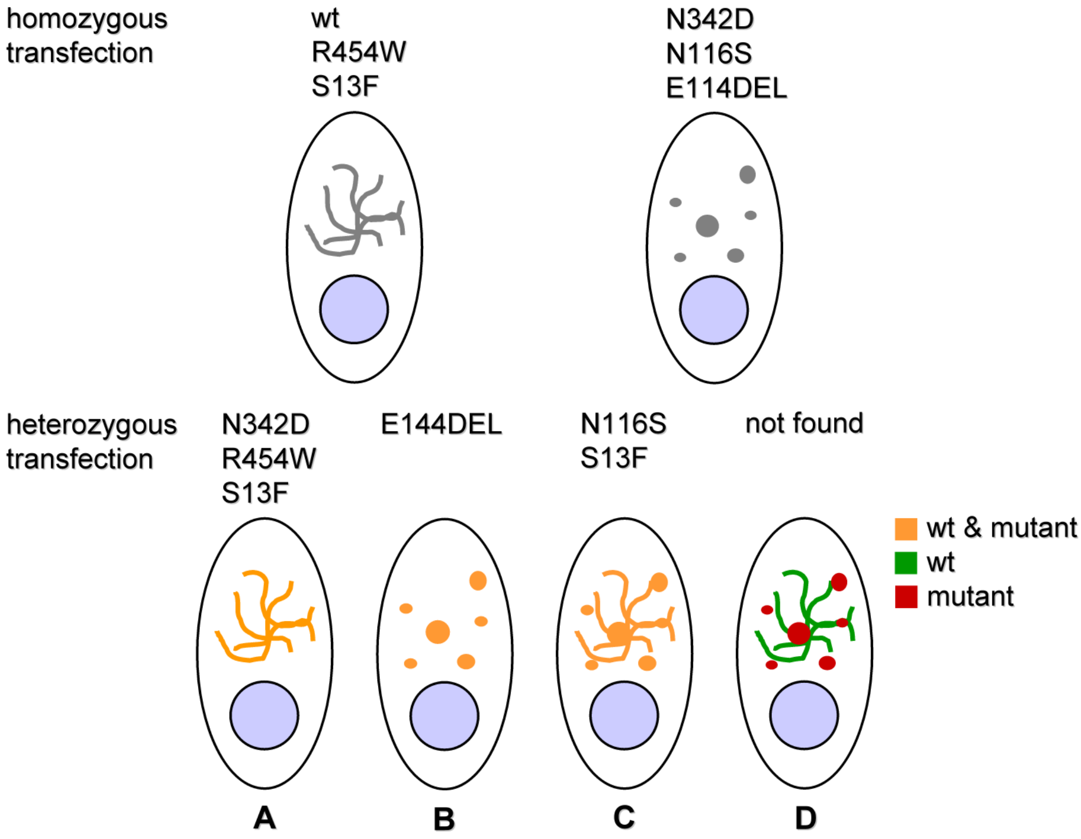

Figure 7.23.: Model depicting filament and/or aggregate formation in cells coexpressing wt and mutant desmin.

studies on homozygously transfected SW-13, 3T3 and C2C12 cells [229]. In the heterozygously transfected cells, the mutant E114del showed a dominant effect, even on wt desmin and led to aggregates, which incorporated wt desmin according to type (B). This deletion mutant has also been reported to impair protein interactions with the IF-protein synemin, resulting in a complete coaggregation of both proteins [230]. E114del presumably induces a twist of the hydrophobic seam, which is essential for the formation of the coiled-coil dimer [229]. It can be concluded that this mutant provides a dominant loss of the ability of wt desmin molecules to form filaments. Previously, the mutant N116S was reported to induce aggregate formation when homozygously expressed in SW-13 cells. However, in cardiac tissue of the patient, both filaments and aggregates of desmin were found [215]. In the heterozygous cell culture experiments, the mutant N116S formed filaments as well as aggregates within the same cell, composed of both desmin forms according to type (C). Homozygous expression of N342D-desmin led to a phenotype comparable to the one previously described [231]. However, in heterozygous coexpression experiments, a dominant inhibiting effect on filament assembly could be excluded. Mutant and wt desmin molecules were incorporated into the same filamentous structures without aggregate formation, according to type (A). Different groups have investigated the homozygous expression of R454W desmin in different cell lines, leading to conflicting results concerning the degree of aggregate formation [232, 233]. In this study, homozygously transfected R454W-desmin formed filamentous networks. Furthermore, heterozygously expressed R454W desmin formed mixed filaments in transfected cells according to type (A). Coexpression experiments with similar results have been reported by Bär et al. [234]. However, in that study, colocalization of wt and mutant desmin could not be analyzed for technical reasons. The amount of dimers, tetramers and oligomers of R454W in transfected cells has previously been determined by single particle fluorescence spectroscopy, demonstrating that R454W differs only marginally in comparison to the wt [232]. Consequently, the pathogenic role of this variant is not clear. Further studies might clarify the clinical effects of this sequence variant.

The data obtained by PALM as well as FRET clearly revealed that all mutants form mixed filaments or aggregates, according to types (A-C). Interestingly, in none of the mutations analyzed in this study, we found a separation of mutant and wt desmin into filaments and aggregates within the same cell, as suggested by type (D). Despite this systematic absence of segregation, it should be noted that slight variations in the local concentration of mutant and wt desmin were observed in the PALM images as well as in the FRET data. Also, it cannot be excluded that some other desmin mutants might lead to a type (D) filament formation defect.

The existence of filaments composed of wt and mutant desmin raises the question if the nanomechanical properties in mixed filaments are impaired by incorporation of the mutant forms. The methodological approach of this study included two complementary techniques for the analysis of desmin filament formation in living cells. Whereas the dual color PALM experiments provided insight into the structural composition of mutant and wt desmin, the FRET data indicated close proximity of these IF-forms within a spatial range below 10 nm. From the dual color PALM experiments of the investigated mutants, the hypothetical type (D) filament formation defect could be excluded. In summary, the methological approach using high resolution dual color PALM and FRET measurements has substantially improved our understanding of the structures and molecular assembly of heterozygously expressed desmin mutants in living cells. The experiments led to a more sophisticated scheme of filament formation defects caused by mutated desmin proteins.

8. Summary - Super-resolution Techniques for Cellular Studies

8.1. Technical Considerations and Limitations

In this work, different fluorescence microscopy techniques were utilized according to their ability to unravel the structure and dynamics of specific biological systems. In general, the performance of a microscope can be judged by the field of view, spatial and temporal resolution. However, those three parameters are difficult to optimize in a single experiment.

According to the sampling criterion, the pixel size must be less than half the desired spatial resolution. In a scanning setup, the field of view and the number of image pixels can be varied separately. Thus, it is possible to image a large area while maintaining high spatial resolution. However, in such a configuration, the scanning process will take quite long due to the strongly increased number of pixels, resulting in a poor temporal resolution. In super-resolution STED microscopy, a confocal raster-scanning technique, the loss of field of view and/or temporal resolution is a direct consequence of the reduced pixel size needed for increased optical resolution. Fast, video-rate imaging is still possible, but limited to micron-sized regions of interest. A distinctive feature of raster-scanning is the time structure contained within each image, determined by the pixel dwell time, which is in the range of a few microseconds. This additional information can be harnessed by correlation analysis. In this work, fast STED microscopy was utilized in RICS to simultaneously quantify translation dynamics of proteins and lipids in multiple sub-micron sized cellular moieties. Mapping of a large area by sequential imaging of several regions was also possible, provided that the molecule dynamics persisted within the total acquisition time of a few minutes.

In a widefield microscope, the number of pixels is determined by the camera chip. Thus, by varying the objective magnification, one can either monitor a large area at limited spatial resolution, or accept a smaller field of view if high spatial resolution is desired. Independent of the observation area, current widefield detectors allow for fast, video-rate imaging. In this work, a particular kind of widefield microscope was implemented by using total reflection. In TIRFM, the excitation depth of the sample is limited to $\sim 100\,\mathrm{nm}$ by illumination with an evanescent wave. For membrane-based studies, TIRF is an excellent way to limit cytoplasmic background fluorescence. In combination with FRAP to probe redistribution dynamics, TIRFM was ideally suited to study the rapid actions of a steroid receptor (GR) at the plasma membrane of live immune cells.

In super-resolution localization microscopy, the pixel size does not need to be decreased in the image acquisition process. Only after localization of the individual fluorophores, their positions are drawn on a finer grid; therefore, the field of view is not compromised. On the other hand, it usually takes several thousand individual frames until enough marker signals are captured to fulfil the sampling criterion. Thus, the temporal resolution in localization microscopy is poor and, in contrast to STED microscopy, can hardly be recovered by limiting the field of view. Nevertheless, if structures of rather slow dynamics are under study, super-resolution localization microscopy is a preeminent tool for live cell imaging. In this work, the tetrameric probe psRFP fused to Lifeact was observed to exclusively label perinuclear actin when stably expressed in plant cells. The optical switching mechanism of psRFP was used to acquire super-resolution images including z-stacking by means of PALM. In this way, the lamellar arrangement of perinuclear actin around the nucleus was resolved in great detail. Finally, dual color PALM revealed the effects on desmin filament assembly caused by several mutations in the gene encoding for the desmin protein, which is essential for heart muscle function.

8.2. Fluorescent Markers and Labeling

Besides hardware limitations, another aspect is of great importance in super-resolution microscopy. The diffraction barrier is not broken by optical elements but by an intrinisic, non-linear response of the employed markers. STED or RESOLFT microscopy rely on the depletion of the bright state of the markers within most of the illumination volume resulting in thousands of switching cycles during image acquisition. Thus, the fluorophores must feature a high resistance to switching fatigue. In localization microscopy, each marker needs to appear in the bright state only once; consequently, only a single switching cycle is required. In contrast, the number of photons emitted from each molecule directly affects the localization precision and, thus, the spatial resolution. In STED or RESOLFT microscopy, a single detected photon can be sufficient. In addition, all super-resolution techniques rely on dense labeling conditioned by the sampling criterion. But, super-resolution is a consequence of being able to isolate a tiny, sub-diffractional population of markers within a large, diffraction-limited volume. This requires a high contrast between dark and bright marker states. In a nutshell, application of super-resolution microscopy is limited by the fluorophores.

Organic dyes such as Atto647N exhibit excellent photostability and are preferred in STED microscopy. As an example, by labeling of the IgE antibody with Atto647N, the spatial distribution and dynamics of FcϵRI receptors at the plasma membrane of live mast cells was studied by STED-RICS. In contrast, up to now, labeling of the intracellular glucocorticoid receptor was only feasible by fusing it to the genetically encoded GFP. Compared to high-end dyes, fluorescent proteins display inferior photostability. Also, the spectral properties of GFP are not ideal for STED. The high power density required for efficient depletion is likely to cause photodamage due to application of short depletion wavelengths compatible with the spectrum of a green-emitting fluorophore. In future experiments, new labeling systems could allow the application of STED-RICS to simultaneously probe the dynamics of intracellular proteins at multiple regions of interest to better accommodate heterogeneities of the cellular environment.

TIRFM, on the other hand, is compatible with any fluorophore. Yet, with this technique, a fusion of the GR to a photoconvertible FP such as mEosFP*thermo* could provide further insight in the study of the immune response of mast cells. The setup implemented in this work allows for a quick change between TIRF and epi-illumination of the sample. In a so-called pulse-chase experiment, green fluorescent, membrane-associated GR-mEosFP*thermo* could be photoconverted to the red fluorescent form in TIRF mode, followed by imaging of the cytoplasm using epi-illumination to unravel any potential exchange between membrane-bound and cytoplasmic GRs.

Just as in a pulse-chase experiment, particular marker properties can be exploited to design new biological assays. When tetrameric Lifeact-psRFP was stably expressed in plant cells, it was observed to exclusively label perinuclear actin. Presumably, sparse accessory protein decoration of perinuclear actin allowed for binding of the rather large, tetrameric fusion probe, whereas a more dense decoration prevented labeling of other subpopulations of actin. This steric-hindrance approach to label certain subpopulations of proteins and protein structures could be refined by designing markers of specific sizes and, thus, might constitute a helpful tool for other studies.

Finally, an improved spatial resolution, as provided by dual color PALM, is highly demanded for live cell colocalization studies. Camera exposure times as short as 3 ms allowed for data acquisition in both color channels in ~ 2 min. To further enhance dual color PALM, new paFPs with different excitation/emission and photoconversion properties are required. Parallel imaging of both color channels could further reduce the acquisition time and help to establish dual color PALM as a standard imaging technique in cell biology.

Over the last years, super-resolution techniques have emerged and proven to be powerful tools to answer fundamental biological questions. However, to fully exploit their capabilities, advanced markers and labeling systems need to be developed. For labeling, new methods such as SNAP- and CLIP-tagging aim for a more universal, intracellular application of organic dyes and nanocrystals in living cells. In terms of marker development, there is great effort to improve the photophysics of current fluorescent proteins to catch up with their non-genetically encoded siblings. Thus, versatile visible light microscopy providing molecular resolution feels within the grasp of the next decades.

Zusammenfassung - Hochauflösungstechniken für Studien in lebenden Zellen

Technische Betrachtungen und Einschränkungen

In dieser Arbeit wurden mit Hilfe verschiedener Methoden der Fluoreszenzmikroskopie diverse biologische Fragestellungen behandelt. Im Allgemeinen kann die Leistung eines Mikroskops durch die Größe des Beobachtungsfeldes, die räumliche und die zeitliche Auflösung bewertet werden. Allerdings ist es schwierig, diese drei Parameter gleichzeitig zu optimieren.

Das Abtasttheorem besagt, dass die Größe der Bildelemente weniger als die Hälfte der erwarteten Auflösung betragen muss. Erfolgt die Bildgebung durch ein Abrastern der Probe, so kann gleichzeitig sowohl das Beobachtungsfeld als auch die Größe der Bildelemente verändert werden. Daher ist es möglich, eine hohe räumliche Auflösung auch bei der Abbildung eines großen Bereichs zu erzielen. Aufgrund der hohen Anzahl an Bildelementen wird der Aufnahmeprozess jedoch sehr lange dauern. Daher ist in der hochauflösenden STED Mikroskopie die Reduzierung des Beobachtungsfeldes und/oder der zeitlichen Auflösung eine direkte Konsequenz der reduzierten Größe der Bildelemente. Diese ist jedoch nötig für eine höhere räumliche Auflösung. Schnelle Aufnahmen auf Zeitskalen unterhalb einer Sekunde pro Bild sind auf Areale im Mikrometerbereich beschränkt. Ein wesentliches Merkmal mittels Rasterung aufgenommener Bilder ist deren implizit enthaltene Zeitstruktur, bestimmt durch die Integrationszeit pro Bildelement, welche im Bereich einiger Mikrosekunden liegt. Diese zusätzliche Information kann mit Hilfe von Korrelationsanalyse genutzt werden. Im Rahmen dieser Arbeit wurde ein schnell abrasterndes STED Mikroskop aufgebaut und mit Raster-Bild-Korrelations-Spektroskopie (RICS) kombiniert, um die Translationsdynamik von Proteinen und Lipiden gleichzeitig in mehreren Zellregionen kleiner einem Mikrometer zu untersuchen. Dabei konnte durch eine sequentielle Aufnahme von mehreren Regionen ein großer Bereich abgedeckt werden. Dieses Verfahren setzt voraus, dass sich die Dynamik der Moleküle während der Messung von einigen Minuten Dauer nicht ändert.

Bei einem Weitfeldmikroskop ist die Anzahl der Bildelemente durch den Kamerachip festgelegt. Folglich kann durch eine Veränderung der Vergrößerung des Objektivs entweder ein großer Bereich mit eingeschränkter räumlicher Auflösung, oder ein kleiner Bereich mit hoher Auflösung abgebildet werden. Unabhängig von der Größe des beobachteten Areals können mit aktuellen Flächendetektoren Bilder mit Videorate aufgenommen werden. In dieser Arbeit wurde unter Ausnutzung von Totalreflexion ein bestimmter Typ von Weitfeldmikroskop aufgebaut. Bei der Totalreflexionsmikroskopie (TIRFM) ist die Eindringtiefe der evaneszenten Welle für die Anregung der Probe auf etwa 100 nm beschränkt. Bei Studien an der Zellmembran ist dies ein hervorragender Ansatz um zytoplasmatische Hintergrundfluoreszenz zu unterdrücken. In Kombination mit der Methode der Fluoreszenzerholung nach Photobleichen (FRAP) konnte damit die schnelle Dynamik eines Steroidrezeptors (GR) an der Membran von lebenden Immunzellen untersucht werden.

Bei der hochauflösenden Lokalisationsmikroskopie muss die Größe der Bildelemente nicht verringert werden. Die Bestimmung der genauen Positionen der einzelnen Farbstoffe erfolgt erst nach der Aufnahme. Daher ist das Beobachtungsfeld bei der Lokalisationsmikroskopie nicht eingeschränkt. Auf der anderen Seite braucht es üblicherweise mehrere tausend Einzelbilder, um den Großteil der Marker einzufangen. Daher ist die zeitliche Auflösung bei der Lokalisationsmikroskopie schlecht, und kann auch nur schwerlich durch eine Einschränkung des Beobachtungsfeldes verbessert werden. Falls die zu untersuchenden Strukturen jedoch nur eine relativ langsame Dynamik aufweisen, ist die hochauflösende Lokalisationsmikroskopie eine überragende Methode für die Bildgebung in lebenden Zellen. Mit Hilfe des optischen Schaltmechanismus von psRFP konnten hochauflösende PALM Bilder der lamellenartigen Anordnung von Aktin um den Zellkern aufgenommen werden. Weiterhin konnte mit PALM in zwei Farbkanälen der Einfluss verschiedener Mutationen des Desmin-Gens auf die Ausbildung von Desmin-Filamenten untersucht werden, welche sehr wichtig für die Funktion des Herzmuskels sind.

Fluorophore und Fluoreszenzmarkierungen

In der Hochauflösungsmikroskopie kommt einem weiteren Aspekt eine große Bedeutung zu. Die Beugungsgrenze wird nicht mit Hilfe optischer Elemente, sondern durch eine nichtlineare Antwort der Marker selbst erreicht. Die STED oder RESOLFT Mikroskopie beruht auf der Entvölkerung des fluoreszenten Zustands der Marker in einem Großteil des Anregungsvolumens, was sich in tausenden von Schaltzyklen der einzelnen Marker niederschlägt. Daher müssen die Farbstoffe über ein hohes Maß an Resistenz gegen Ermüdung durch Schalten verfügen. Bei der Lokalisationsmikroskopie müssen die Marker nur ein einziges Mal in einem fluoreszenten Zustand sein. Daher ist nur ein einziger Schaltprozess nötig. Allerdings hat hier die Zahl der emittierten Fluoreszenzphotonen einen direkten Einfluss auf die Lokalisationsgenauigkeit und damit auf die Auflösung. Bei der STED Mikroskopie hingegen genügt prinzipiell die Detektion eines einzigen Fluoreszenzphotons. Des Weiteren ist bei der Hochauflösungsmikroskopie ein hoher Kontrast zwischen Dunkel- und Hellzustand vonnöten, um einzelne Marker innerhalb eines großen beugungsbegrenzten Volumens isolieren zu können. Diese Kriterien schränken die Auswahl der möglichen Marker für die Anwendung dieser Methoden ein.

Organische Farbstoffe wie z.B. Atto647N sind extrem photostabil und werden daher bei der STED Mikroskopie bevorzugt eingesetzt. Zum Beispiel konnte durch eine Anfärbung von IgE Antikörpern mit Atto647N die räumliche Verteilung und Dynamik des FcϵRI Rezeptors in der Membran von lebenden Mastzellen mit Hilfe von STED-RICS bestimmt werden. Dagegen konnte der intrazelluläre Glucocorticoid Rezeptor bis jetzt nur durch eine Fusion an GFP markiert werden. Verglichen mit den besten Farbstoffen, weisen fluoreszente Proteine (FPs) nur eine geringe Photostabiliät auf. Auch sind die spektralen Eigenschaften von GFP nicht ideal für die STED Mikroskopie. Die hohen Intensitäten des STED Strahls kurzer Wellenlänge, welche für eine effiziente Entvölkerung des angeregten Zustands eines grün fluoreszierenden Markers nötig sind, können die biologische Probe schädigen. In zukünftigen Experimenten könnten mit Hilfe von z.B. SNAP-tags die Dynamik von GR oder anderen Proteinen gleichzeitig in mehreren Regionen durch STED-RICS untersucht werden.

Dagegen funktioniert TIRFM mit jedem beliebigen Fluorophor. Für die Untersuchung mit Totalreflexionsmikroskopie wäre eine Fusion von GR mit einem photokonvertierbaren FP wie mEosFP eine große Hilfe. Die Möglichkeit schnell zwischen TIRF und Epi-Beleuchtung umzuschalten ermöglicht *pulse-chase* Experimente, um einen eventuell möglichen Austausch zwischen membrangebundenem und zytoplasmatischem GR aufzudecken.

Bestimmte Eigenschaften von Markern können auch für biologische Studien ausgenutzt werden. Stabil exprimiert bindet der tetramere Marker psRFP nach einer Fusion an Lifeact nur an solches Aktin, welches den Zellkern umlagert. Mit Hilfe des optischen Schaltmechanismus von psRFP konnten hochauflösende PALM Bilder der lamellenartigen Anordnung von Aktin um den Zellkern aufgenommen werden. Diese Methode der spezifischen Markierung von Subpopulationen bestimmter Proteine über sterische Behinderung könnte durch eine Entwicklung von Markern verschiedener Größen weiter verfeinert werden.

Schließlich konnte mit PALM in zwei Farbkanälen der Einfluss verschiedener Mutationen des Desmin-Gens auf die Ausbildung von Desmin-Filamenten untersucht werden, welche sehr wichtig für die Funktion des Herzmuskels sind. Durch Kamera-Belichtungszeiten von lediglich 3 ms konnten PALM Bilder in weniger als einer Minute aufgenommen werden. Um diese Methode weiter zu optimieren, sind neue paFP mit anderen Anregungs-/Emissionsspektren nötig. Denn durch eine parallele Aufnahme von beiden Farbkanälen könnte die Aufnahmegeschwindigkeit weiter gesteigert werden und Zwei-Farben-PALM zu einer Standardmethode in der Untersuchung von Zellproben zu machen.

Die in den letzten Jahren aufgekommene hochauflösende Fluoreszenzmikroskopie hat schon jetzt viel dazu beigetragen fundamentale biologische Fragestellungen zu beantworten. Um die Möglichkeiten dieser Methoden vollständig nutzen zu können, müssen allerdings noch neue Marker und Methoden der Markierung entwickelt werden. So erlauben z.B. SNAP- und CLIP-tags bereits den Einsatz von organischen Farbstoffen und Nanopartikeln innerhalb lebender Zellen. Auch werden große Anstrengungen unternommen, um fluoreszente Proteine in Hinblick auf ihre photophysikalischen Eigenschaften zu optimieren, so dass diese ähnlich hell und photostabil wie organische Farbstoffe sind. Damit scheint die Entwicklung von Fluoreszenzmikroskopie mit annähernd molekularer Auflösung innerhalb der Reichweite der nächsten Jahrzehnte.

Acronyms

ABP	actin-binding protein.
AF	actin filament.
AFM	atomic force microscopy.
AOTF	acousto optic tunable filter.
APD	avalanche photodiode.
ARVC	arrhythmogenic right ventricular cardiomyopathy.
ATP	adenosine triphosphate.
BSA	bovine serum albumin.
BY-2	*Nicotiana tabacum* L. cv. Bright Yellow 2.
CCD	charge coupled device.
CW	continuous wave.
DAC	digital-to-analog converter.
DEX	dexamethasone.
DIC	differential interference contrast.
DMEM	Dulbecco's modified Eagle's medium.
DMSO	dimethyl sulfoxide.
DNP	dinitrophenole.
DOPC	1,2-dioleoyl-sn-glycero-phosphocholine.
DPN	dip-pen nanolithography.
DPPE	dipalmitoylphosphatidylethanolamine.
DRM	desmin-related myopathy.
EM	electron microscopy.
EMCCD	electron multiplying charge coupled device.
ER	endoplasmic reticulum.
Erk	extracellular signal-regulated kinase.
F-actin	filamentous actin.
FBS	fetal bovine serum.
FCS	fluorescence correlation spectroscopy.
FLIM	fluorescence lifetime imaging.
FP	fluorescent protein.
FPALM	fluorescence photoactivation localization microscopy.

FRAP	fluorescence recovery after photobleaching.
FRET	Foerster resonance energy transfer.
FWHM	full width at half maximum.
GC	glucocorticoid.
GFP	green fluorescent protein.
Glu	glutamic acid.
GR	glucocorticoid receptor.
GRE	glucocorticoid response element.
GUV	giant unilamellar vesicle.
HDMEM	HEPES-buffered Dulbecco's modified Eagle's medium.
HEPES	4-(2-hydroxyethyl)-1-piperazineethanesulfonic acid.
His	histidine.
HSA	human serum albumin.
HSP90	heat shock protein 90.
IF	intermediate filament.
IgE	immunoglobulin E.
IP3	inositol 1,4,5-triphosphate.
IR	infrared.
LAT	linker for activation of T cells.
LB	lysogeny broth.
LP	longpass.
MMF	multi mode fiber.
MRI	magnetic resonance imaging.
MS	Murashige & Skoog.
NA	numerical aperture.
NSOM	near-field scanning optical microscopy.
OCT	optical coherence tomography.
OD600	optical density at 600 nm.
paFP	photoactivatable fluorescent protein.
PALM	photoactivated localization microscopy.
PBS	phosphate buffered saline.
PCR	polymerase chain reaction.
PET	positron-emission tomography.
Phe	phenylalanine.
PKC	protein kinase C.

PMT	photomultiplier.
PP	phase plate.
PSD	position sensing photodiode.
PSF	point spread function.
psRFP	photoswitchable red fluorescent protein.
QD	quantum dot.
RBL	rat basophil leukemia.
RESOLFT	reversible saturable optical fluorescence transitions.
RICS	raster image correlation spectroscopy.
SMF	single-mode fiber.
SOFI	superresolution optical fluctuation imaging.
SP	shortpass.
SPIM	selective plane illumination microscopy.
STED	stimulated emission depletion.
STORM	stochastic optical reconstruction microscopy.
TCSPC	time-correlated single photon counting.
Ti:Sa	sapphire doped with titanium.
TIRF	total internal reflection.
TIRFM	total internal reflection microscopy.
ULF	unit-length filament.
UV	ultra violet.
wt	wild type.
XTC	*Xenopus* tissue culture.

List of Companies

AA Opto Electronic

AA Opto Electronic, 18 rue Nicolas Appert, 91898 Orsay Cedex, France.

AHF

AHF Analysentechnik AG, Kohlplattenweg 18, 72074 Tübingen, Germany.

Andor

Andor Technology plc., 7 Millennium Way, Springvale Business Park, Belfast, BT12 7AL, UK.

Applied Biosystems

Applied Biosystems, 850 Lincoln Centre Drive, Foster City, CA 94404, USA.

Atto-Tec

ATTO-TEC GmbH, Am Eichenhang 50, 57076 Siegen, Germany.

Avanti Polar Lipids

Avanti Polar Lipids Inc., 700 Industrial Park Drive, Alabaster, Alabama 35007-9105, USA.

BBI

BBInternational, Alchemy House, Tom Mc Donald Avenue, Medipark, Dundee, DD2 1NH, United Kingdom.

Becker & Hickl

Becker & Hickl GmbH, Nahmitzer Damm 30, 12277 Berlin, Germany.

BFI Optilas

BFI Optilas GmbH, Oppelner Strasse 5, 82194 Gröbenzell, Germany.

Bio-Rad

Bio-Rad Laboratories Inc., 1000 Alfred Nobel Drive, Hercules, CA 94547, USA.

Blue Sky

Blue Sky Research, 1537 Centre Pointe Drive, Milpitas, CA 95035, USA.

Chroma

Chroma Technology Corporation, 10 Imtec Lane, Bellows Falls, VT 05101, USA.

Clontech

Clontech Laboratories Inc., 1290 Terra Bella Ave., Mountain View, CA 94043, USA.

CrystaLaser

CrystaLaser, 4750 Longley Lane, Reno, NV 89502, USA.

Duchefa Biochemie

Duchefa Biochemie B.V., A. Hofmanweg 71, 2031 BH, Haarlem, The Netherlands.

Fianium

Fianium Ltd, 20 Compass Point, Ensign Way, Southampton SO31 4RA, United Kingdom.

GATC

GATC Biotech AG, European Genome and Diagnostics Centre, Jakob-Stadler-Platz 7, 78467 Konstanz, Germany.

Hybridoma Bank

Developmental Studies Hybridoma Bank, University of Iowa, Department of Biology, 028 Biology Building East, Iowa City, Iowa 52242-1324, USA.

Imaging Source

The Imaging Source Europe GmbH, Sommerstrasse 36, 28215 Bremen, Germany.

Invitrogen

Life Technologies, 3175 Staley Road, Grand Island, NY 14072, USA.

Laser 2000

Laser 2000 GmbH, Argelsrieder Feld 14, 82234 Wessling, Germany.

Laserlight

Laserlight Showdesign, Grunowstr. 3, 13187 Berlin, Germany.

Leica

Leica Microsystems GmbH, Ernst-Leitz-Strasse 17-37, 35578 Wetzlar, Germany.

Macherey-Nagel

Macherey-Nagel GmbH & Co. KG, Neumann Neander Str. 6-8, 52355 Düren, Germany.

MathWorks

MathWorks, Adalperostraße 45, 85737 Ismaning, Germany.

Max-Planck-Innovation

Max-Planck-Innovation GmbH, Amalienstr. 33, 80799 München, Germany.

Menzel

Gerhard Menzel GmbH, Thermo Fisher Scientific, Saarbrückener Strasse 248, 38116 Braunschweig, Germany.

Millipore

Merck Millipore, 290 Concord Road, Billerica, MA 01821, USA.

MW Dental

M+W Dental, Müller & Weygandt GmbH, Industriestrasse 25, 63654 Büdingen, Germany.

National Instruments

National Instruments Germany GmbH, Ganghoferstr. 70 b, 80339 München, Germany.

OZ Optics

OZ Optics Limited, 219 Westbrook Rd, Ottawa, Ontario, K0A 1L0, Canada.

Pecon

PeCon GmbH, Ziegeleistrasse 50, 89155 Erbach, Germany.

Physik Instrumente

Physik Instrumente GmbH & Co. KG, Auf der Römerstrasse 1, 76228 Karlsruhe/Palmbach, Germany.

PicoQuant

PicoQuant GmbH, Rudower Chaussee 29, 12489 Berlin, Germany.

RPC Photonics

RPC Photonics Inc., 330 Clay Road, Rochester, NY 14623, USA.

Schäfter und Kirchhoff

Schaefter + Kirchhoff GmbH, Kieler Str. 212, 22525 Hamburg, Germany.

Semrock

Semrock, Inc., 3625 Buffalo Road, Suite 6, Rochester, NY 14624, USA.

Sigma-Aldrich

Sigma-Aldrich, 3050 Spruce Street, St. Louis, MO 63103, USA.

Spectra-Physics

Newport Spectra-Physics GmbH, Guerickeweg 7, 64291 Darmstadt, Germany.

Stratagene

Agilent Technologies Inc., Life Sciences and Chemical Analysis Group, 5301 Stevens Creek Boulevard, Santa Clara, CA 95051, USA.

Thermo Scientific

Thermo Scientific, Robert-Bosch-Strasse 1, 63505 Langenselbold, Germany.

Thorlabs

Thorlabs GmbH, Hans-Boeckler-Str. 6, 85221 Dachau/München, Germany.

Till Photonics

TILL Photonics GmbH, Lochhamer Schlag 21, 82166 Gräfelfing, Germany.

Weicon

WEICON GmbH & Co. KG, Königsberger Strasse 255, 48157 Münster, Germany.

Zeiss

Carl Zeiss Microscopy GmbH, Carl-Zeiss-Promenade 10, 07745 Jena, Germany.

Bibliography

[1] Knoll, M., Ruska, E.: Das Elektronenmikroskop. *Z. Physik* **78** (1932), 318–339

[2] Koster, A. J., Klumperman, J.: Electron microscopy in cell biology: integrating structure and function. *Nat. Rev. Mol. Cell Biol.* **4** (2003), SS6–S10

[3] Ter-Pogossian, M. M., Phelps, M. E., Hoffman, E. J., Mullani, N. A.: A positron-emission transaxial tomograph for nuclear imaging (PETT). *Radiology* **114** (1975), 89–98

[4] Lauterbur, P. C.: Image Formation by Induced Local Interactions: Examples Employing Nuclear Magnetic Resonance. *Nature* **242** (1973), 190–191

[5] Mansfield, P., Grannell, P.: NMR 'diffraction' in solids. *J. Phys. C: Solid State Phys.* **6** (1973), 422–426

[6] Huang, D., Swanson, E. A., Lin, C. P., Schuman, J. S., Stinson, W. G., Chang, W., Hee, M. R., Flotte, T., Gregory, K., Puliafito, C. A.: Optical coherence tomography. *Science* **254** (1991), 1178–1181

[7] Voie, A. H., Burns, D. H., Spelman, F. A.: Orthogonal-plane fluorescence optical sectioning: three-dimensional imaging of macroscopic biological specimens. *J. Microsc.* **170** (1993), 229–236

[8] Huisken, J., Swoger, J., Del Bene, F., Wittbrodt, J., Stelzer, E. H. K.: Optical sectioning deep inside live embryos by selective plane illumination microscopy. *Science* **305** (2004), 1007–1009

[9] Denk, W., Strickler, J. H., Webb, W. W.: Two-photon laser scanning fluorescence microscopy. *Science* **248** (1990), 73–76

[10] Palero, J., Santos, S. I. C. O., Artigas, D., Loza-Alvarez, P.: A simple scanless two-photon fluorescence microscope using selective plane illumination. *Opt. Express* **18** (2010), 8491–8498

[11] Planchon, T. A., Gao, L., Milkie, D. E., Davidson, M. W., Galbraith, J. A., Galbraith, C. G., Betzig, E.: Rapid three-dimensional isotropic imaging of living cells using Bessel beam plane illumination. *Nat. Methods* **8** (2011), 417–423

[12] Duerig, U., Pohl, D., Rohner, F.: Near-field optical-scanning microscopy. *J. Appl. Phys.* **59** (1986), 3318–3327

[13] Binnig, G., Quate, C. F., Gerber, C.: Atomic force microscope. *Phys. Rev. Lett.* **56** (1986), 930–933

[14] Hell, S. W., Wichmann, J.: Breaking the diffraction resolution limit by stimulated emission: stimulated-emission-depletion fluorescence microscopy. *Opt. Lett.* **19** (1994), 780–782

[15] Betzig, E., Patterson, G. H., Sougrat, R., Lindwasser, O. W., Olenych, S., Bonifacino, J. S., Davidson, M. W., Lippincott-Schwartz, J., Hess, H. F.: Imaging intracellular fluorescent proteins at nanometer resolution. *Science* **313** (2006), 1642–1645

[16] Hess, S. T., Girirajan, T. P. K., Mason, M. D.: Ultra-high resolution imaging by fluorescence photoactivation localization microscopy. *Biophys. J.* **91** (2006), 4258–4272

[17] Rust, M. J., Bates, M., Zhuang, X.: Sub-diffraction-limit imaging by stochastic optical reconstruction microscopy (STORM). *Nat. Methods* **3** (2006), 793–795

[18] Rittweger, E., Han, K. Y., Irvine, S. E., Eggeling, C., Hell, S. W.: STED microscopy reveals crystal colour centres with nanometric resolution. *Nat. Photonics* **3** (2009), 144–147

[19] Fernández-Suárez, M., Ting, A. Y.: Fluorescent probes for super-resolution imaging in living cells. *Nat. Rev. Mol. Cell Biol.* **9** (2008), 929–943

[20] Shaanan, B.: Structure of human oxyhaemoglobin at 2.1 A resolution. *J. Mol. Biol.* **171** (1983), 31–59

[21] Science Photo Library: *Scanning electron microscopy image of a herpes virus. C007/4753.* http://www.sciencephoto.com/, called on the 09.03.2013

[22] Swaminathan, B., Hayes, P.: *Listeria monocytogenes Sequencing Project, Broad Institute of Harvard and MIT.* http://www.broadinstitute.org/, called on the 09.03.2013

[23] Cavanagh, A.: *Human embryonic stem cell.* http://wellcomeimages.org/, called on the 09.03.2013

[24] Leptin, M.: *Zebrafish embryo at the somitogenesis stage.* http://www.genetik.uni-koeln.de/groups/Leptin/, called on the 09.03.2013

[25] Cramer, M. L.: *House Mouse.* http://peppysdevelopments.wordpress.com/, called on the 09.03.2013

[26] Digman, M. A., Brown, C. M., Sengupta, P., Wiseman, P. W., Horwitz, A. R., Gratton, E.: Measuring fast dynamics in solutions and cells with a laser scanning microscope. *Biophys. J.* **89** (2005), 1317–1327

[27] Axelrod, D.: Cell-substrate contacts illuminated by total internal reflection fluorescence. *J. Cell Biol.* **89** (1981), 141–145

[28] Axelrod, D., Koppel, D. E., Schlessinger, J., Elson, E., Webb, W. W.: Mobility measurement by analysis of fluorescence photobleaching recovery kinetics. *Biophys. J.* **16** (1976), 1055–1069

[29] Zernike, F.: Phase contrast, a new method for the microscopic observation of transparent objects. *Physica* **9** (1942), 686–698

[30] Bugiel, I., Koenig, K., Wabnitz, H.: Investigations of cells by fluorescence laser scanning microscopy with subnanosecond time resolution. *Lasers Life Sci.* **3** (1989), 47–53

[31] Foerster, T.: Intermolecular energy migration and fluorescence. *Ann. Phys.* **2** (1948), 55–75

[32] Soret, J.-L.: Analyse spectrale: Sur le spectre d'absorption du sang dans la partie violette et ultra-violette. *Comptes rendus* **97** (1883), 1269–1270

[33] Franck, J., Dymond, E.: Elementary processes of photochemical reactions. *Trans. Faraday Soc.* **21** (1926), 536–542

[34] Condon, E.: A Theory of Intensity Distribution in Band Systems. *Phys. Rev.* **28** (1926), 1182–1201

[35] Jablonski, A.: Ueber den Mechanismus der Photolumineszenz von Farbstoffphosphoren. *Z. Physik* **94** (1935), 38–46

[36] Kasha, M.: Characterization of electronic transitions in complex molecules. *Disc. Farad. Soc.* **9** (1950), 14–19

[37] Gayda, S., Hedde, P. N., Nienhaus, K., Nienhaus, G. U.: *Probes for Nanoscopy: Fluorescent Proteins.* Springer Berlin Heidelberg, 2011. – 1–48 S.

[38] Klar, T. A., Jakobs, S., Dyba, M., Egner, A., Hell, S. W.: Fluorescence microscopy with diffraction resolution barrier broken by stimulated emission. *Proc. Natl. Acad. Sci. USA* **97** (2000), 8206–8210

[39] Shimomura, O., Johnson, F. H., Saiga, Y.: Extraction, purification and properties of aequorin, a bioluminescent protein from the luminous hydromedusan, Aequorea. *J. Cell Comp. Physiol.* **59** (1962), 223–239

[40] Shimomura, O.: Structure of the chromophore of Aequorea green fluorescent protein. *FEBS Letters* **104** (1979), 220–222

[41] Prasher, D. C., Eckenrode, V. K., Ward, W. W., Prendergast, F. G., Cormier, M. J.: Primary structure of the Aequorea victoria green-fluorescent protein. *Gene* **111** (1992), 229–233

[42] Chalfie, M., Tu, Y., Euskirchen, G., Ward, W. W., Prasher, D. C.: Green fluorescent protein as a marker for gene expression. *Science* **263** (1994), 802–805

[43] Matz, M. V., Fradkov, A. F., Labas, Y. A., Savitsky, A. P., Zaraisky, A. G., Markelov, M. L., Lukyanov, S. A.: Fluorescent proteins from nonbioluminescent Anthozoa species. *Nat. Biotechnol.* **17** (1999), 969–973

[44] Wiedenmann, J., Vallone, B., Renzi, F., Nienhaus, K., Ivanchenko, S., Röcker, C., Nienhaus, G. U.: Red fluorescent protein eqFP611 and its genetically engineered dimeric variants. *J. Biomed. Opt.* **10** (2005), 14003

[45] Campbell, R. E., Tour, O., Palmer, A. E., Steinbach, P. A., Baird, G. S., Zacharias, D. A., Tsien, R. Y.: A monomeric red fluorescent protein. *Proc. Natl. Acad. Sci. USA* **99** (2002), 7877–7882

[46] Lukyanov, K. A., Chudakov, D. M., Lukyanov, S., Verkhusha, V. V.: Innovation: Photoactivatable fluorescent proteins. *Nat. Rev. Mol. Cell Biol.* **6** (2005), 885–891

[47] Lippincott-Schwartz, J., Patterson, G. H.: Fluorescent proteins for photoactivation experiments. *Methods Cell Biol.* **85** (2008), 45–61

[48] Lippincott-Schwartz, J., Patterson, G. H.: Photoactivatable fluorescent proteins for diffraction-limited and super-resolution imaging. *Trends Cell Biol.* **19** (2009), 555–565

[49] Hofmann, M., Eggeling, C., Jakobs, S., Hell, S. W.: Breaking the diffraction barrier in fluorescence microscopy at low light intensities by using reversibly photoswitchable proteins. *Proc. Natl. Acad. Sci. USA* **102** (2005), 17565–17569

[50] Michalet, X., Pinaud, F. F., Bentolila, L. A., Tsay, J. M., Doose, S., Li, J. J., Sundaresan, G., Wu, A. M., Gambhir, S. S., Weiss, S.: Quantum dots for live cells, in vivo imaging, and diagnostics. *Science* **307** (2005), 538–544

[51] Fu, C. C., Lee, H. Y., Chen, K., Lim, T. S., Wu, H. Y., Lin, P. K., Wei, P. K., Tsao, P. H., Chang, H. C., Fann, W.: Characterization and application of single fluorescent nanodiamonds as cellular biomarkers. *Proc. Natl. Acad. Sci. USA* **104** (2007), 727–732

[52] Zheng, J., Nicovich, P. R., Dickson, R. M.: Highly fluorescent noble-metal quantum dots. *Annu. Rev. Phys. Chem.* **58** (2007), 409–431

[53] Yu, S.-J., Kang, M.-W., Chang, H.-C., Chen, K.-M., Yu, Y.-C.: Bright fluorescent nanodiamonds: no photobleaching and low cytotoxicity. *J. Am. Chem. Soc.* **127** (2005), 17604–17605

[54] Han, K. Y., Willig, K. I., Rittweger, E., Jelezko, F., Eggeling, C., Hell, S. W.: Three-dimensional stimulated emission depletion microscopy of nitrogen-vacancy centers in diamond using continuous-wave light. *Nano Lett.* **9** (2009), 3323–3329

[55] Chen, N., He, Y., Su, Y., Li, X., Huang, Q., Wang, H., Zhang, X., Tai, R., Fan, C.: The cytotoxicity of cadmium-based quantum dots. *Biomaterials* **33** (2012), 1238–1244

[56] Dertinger, T., Colyer, R., Iyer, G., Weiss, S., Enderlein, J.: Fast, background-free, 3D super-resolution optical fluctuation imaging (SOFI). *Proc. Natl. Acad. Sci. USA* **106** (2009), 22287–22292

[57] Stößel, S.: *Fourier-Optik.* Springer, Berlin, Heidelberg, 1993

[58] Lauterborn, W.: *Kohärente Optik.* Springer, Berlin, 1993

[59] Lipson, A., Lipson, S. G., Lipson, H.: *Optical Physics.* Cambridge University Press, 2010

[60] Born, M., Wolf, E.: *Principles of Optics.* Cambridge University Press, 1999

[61] Burnett, J. H., Kaplan, S. G., Shirley, E. L., Horowitz, D., Clauss, W., Grenville, A., Van Peski, C.: High-index optical materials for 193nm immersion lithography. *Proc. SPIE Optical Microlithography XIX* **6154** (2006), 445–456

[62] Heisenberg, W.: Über den anschaulichen Inhalt der quantentheoretischen Kinematik und Mechanik. *Z. Physik* **43** (1927), 172–198

[63] De Broglie, L.: A tentative theory of light quanta. *Phil. Mag.* **47** (1924), 446–458

[64] Heisenberg, W.: *The Physical Principles of the Quantum Theory.* Dover Pubns, 1930

[65] Hecht, E.: *Optik.* 3. Oldenbourg, 2001

[66] Nyquist, H.: Certain topics in telegraph transmission theory. *Trans. AIEE* **47** (1928), 617–644

[67] Shannon, C. E.: Communication in the presence of noise. *Proceedings of the IRE* **37** (1949), 10–21

[68] Cremer, C., Cremer, T.: Considerations on a laser-scanning-microscope with high resolution and depth of field. *Microsc. Acta.* **81** (1978), 31–44

[69] Patterson, G. H., Lippincott-Schwartz, J.: A photoactivatable GFP for selective photolabeling of proteins and cells. *Science* **297** (2002), 1873–1877

[70] Vicidomini, G., Moneron, G., Han, K. Y., Westphal, V., Ta, H., Reuss, M., Engelhardt, J., Eggeling, C., Hell, S. W.: Sharper low-power STED nanoscopy by time gating. *Nat. Methods* **8** (2011), 571–573

[71] Willig, K. I., Harke, B., Medda, R., Hell, S. W.: STED microscopy with continuous wave beams. *Nat. Methods* **4** (2007), 915–918

[72] Harke, B.: *3D STED Microscopy with Pulsed and Continuous Wave Lasers.*, Georg-August-Universität zu Göttingen, PhD thesis, 2008

[73] Rittweger, E., Rankin, B., Westphal, V., Hell, S.: Fluorescence depletion mechanisms in super-resolving STED microscopy. *Chem. Phys. Letters* **442** (2007), 483–487

[74] Hell, S., Kroug, M.: Ground-state-depletion fluorscence microscopy: A concept for breaking the diffraction resolution limit. *Applied Physics B.* **60** (1995), 495–497

[75] Bretschneider, S., Eggeling, C., Hell, S. W.: Breaking the diffraction barrier in fluorescence microscopy by optical shelving. *Phys. Rev. Lett.* **98** (2007), 218103

[76] Hell, S. W.: Toward fluorescence nanoscopy. *Nat. Biotechnol.* **21** (2003), 1347–1355

[77] Dedecker, P., Hotta, J., Flors, C., Sliwa, M., Uji-i, H., Roeffaers, M. B. J., Ando, R., Mizuno, H., Miyawaki, A., Hofkens, J.: Subdiffraction imaging through the selective donut-mode depletion of thermally stable photoswitchable fluorophores: numerical analysis and application to the fluorescent protein Dronpa. *J. Am. Chem. Soc.* **129** (2007), 16132–16141

[78] Thoene, S.: *Herstellung einer Phasenplatte für die STED-Mikroskopie.*, Karlsruhe Inst. f. Tech. (KIT), Bachelor thesis, 2012

[79] Hedde, P. N., Fuchs, J., Oswald, F., Wiedenmann, J., Nienhaus, G. U.: Online image analysis software for photoactivation localization microscopy. *Nat. Methods* **6** (2009), 689–690

[80] Thompson, R. E., Larson, D. R., Webb, W. W.: Precise nanometer localization analysis for individual fluorescent probes. *Biophys. J.* **82** (2002), 2775–2783

[81] van de Linde, S., Sauer, M., Heilemann, M.: Subdiffraction-resolution fluorescence imaging of proteins in the mitochondrial inner membrane with photoswitchable fluorophores. *J. Struct. Biol.* **164** (2008), 250–254

[82] Wombacher, R., Heidbreder, M., van de Linde, S., Sheetz, M. P., Heilemann, M., Cornish, V. W., Sauer, M.: Live-cell super-resolution imaging with trimethoprim conjugates. *Nat. Methods* **7** (2010), 717–719

[83] Bates, M., Blosser, T. R., Zhuang, X.: Short-range spectroscopic ruler based on a single-molecule optical switch. *Phys. Rev. Lett.* **94** (2005), 108101

[84] Bates, M., Huang, B., Dempsey, G. T., Zhuang, X.: Multicolor super-resolution imaging with photo-switchable fluorescent probes. *Science* **317** (2007), 1749–1753

[85] Shroff, H., Galbraith, C. G., Galbraith, J. A., White, H., Gillette, J., Olenych, S., Davidson, M. W., Betzig, E.: Dual-color superresolution imaging of genetically

expressed probes within individual adhesion complexes. *Proc. Natl. Acad. Sci. USA* **104** (2007), 20308–20313

[86] Fuchs, J., Böhme, S., Oswald, F., Hedde, P. N., Krause, M., Wiedenmann, J., Nienhaus, G. U.: A photoactivatable marker protein for pulse-chase imaging with superresolution. *Nat. Methods* **7** (2010), 627–630

[87] Hess, S. T., Gould, T. J., Gudheti, M. V., Maas, S. A., Mills, K. D., Zimmerberg, J.: Dynamic clustered distribution of hemagglutinin resolved at 40 nm in living cell membranes discriminates between raft theories. *Proc. Natl. Acad. Sci. USA* **104** (2007), 17370–17375

[88] Shroff, H., Galbraith, C. G., Galbraith, J. A., Betzig, E.: Live-cell photoactivated localization microscopy of nanoscale adhesion dynamics. *Nat. Methods* **5** (2008), 417–423

[89] Heilemann, M., Margeat, E., Kasper, R., Sauer, M., Tinnefeld, P.: Carbocyanine dyes as efficient reversible single-molecule optical switch. *J. Am. Chem. Soc.* **127** (2005), 3801–3806

[90] Adam, V., Lelimousin, M., Boehme, S., Desfonds, G., Nienhaus, K., Field, M. J., Wiedenmann, J., McSweeney, S., Nienhaus, G. U., Bourgeois, D.: Structural characterization of IrisFP, an optical highlighter undergoing multiple photo-induced transformations. *Proc. Natl. Acad. Sci. USA* **105** (2008), 18343–18348

[91] Gayda, S.: *Development and characterization of a unique photoactivatable label.*, Karlsruhe Inst. f. Tech. (KIT), PhD thesis, 2011

[92] Verkhusha, V. V., Sorkin, A.: Conversion of the monomeric red fluorescent protein into a photoactivatable probe. *Chem. Biol.* **12** (2005), 279–285

[93] Ando, R., Hama, H., Yamamoto-Hino, M., Mizuno, H., Miyawaki, A.: An optical marker based on the UV-induced green-to-red photoconversion of a fluorescent protein. *Proc. Natl. Acad. Sci. USA* **99** (2002), 12651–12656

[94] Tsutsui, H., Karasawa, S., Shimizu, H., Nukina, N., Miyawaki, A.: Semi-rational engineering of a coral fluorescent protein into an efficient highlighter. *EMBO Rep.* **6** (2005), 233–238

[95] Wiedenmann, J., Ivanchenko, S., Oswald, F., Schmitt, F., Röcker, C., Salih, A., Spindler, K.-D., Nienhaus, G. U.: EosFP, a fluorescent marker protein with UV-inducible green-to-red fluorescence conversion. *Proc. Natl. Acad. Sci. USA* **101** (2004), 15905–15910

[96] Nienhaus, K., Nienhaus, G. U., Wiedenmann, J., Nar, H.: Structural basis for photo-induced protein cleavage and green-to-red conversion of fluorescent protein EosFP. *Proc. Natl. Acad. Sci. USA* **102** (2005), 9156–9159

[97] Wiedenmann, J., Nienhaus, G. U.: Live-cell imaging with EosFP and other photoactivatable marker proteins of the GFP family. *Exp. Rev. Proteomics* **3** (2006), 361–374

[98] Mizuno, H., Mal, T. K., Tong, K. I., Ando, R., Furuta, T., Ikura, M., Miyawaki, A.: Photo-induced peptide cleavage in the green-to-red conversion of a fluorescent protein. *Mol. Cell* **12** (2003), 1051–1058

[99] Dickson, R. M., Cubitt, A. B., Tsien, R. Y., Moerner, W. E.: On/off blinking and switching behaviour of single molecules of green fluorescent protein. *Nature* **388** (1997), 355–358

[100] Lukyanov, K. A., Fradkov, A. F., Gurskaya, N. G., Matz, M. V., Labas, Y. A., Savitsky, A. P., Markelov, M. L., Zaraisky, A. G., Zhao, X., Fang, Y., Tan, W., Lukyanov, S. A.: Natural animal coloration can be determined by a nonfluorescent green fluorescent protein homolog. *J. Biol. Chem.* **275** (2000), 25879–25882

[101] Ando, R., Mizuno, H., Miyawaki, A.: Regulated fast nucleocytoplasmic shuttling observed by reversible protein highlighting. *Science* **306** (2004), 1370–1373

[102] Mizuno, H., Mal, T. K., Wälchli, M., Kikuchi, A., Fukano, T., Ando, R., Jeyakanthan, J., Taka, J., Shiro, Y., Ikura, M., Miyawaki, A.: Light-dependent regulation of structural flexibility in a photochromic fluorescent protein. *Proc. Natl. Acad. Sci. USA* **105** (2008), 9227–9232

[103] Mizuno, H., Mal, T. K., Wälchli, M., Fukano, T., Ikura, M., Miyawaki, A.: Molecular basis of photochromism of a fluorescent protein revealed by direct 13C detection under laser illumination. *J. Biomol. NMR* **48** (2010), 237–246

[104] Chudakov, D. M., Verkhusha, V. V., Staroverov, D. B., Souslova, E. A., Lukyanov, S., Lukyanov, K. A.: Photoswitchable cyan fluorescent protein for protein tracking. *Nat. Biotechnol.* **22** (2004), 1435–1439

[105] Andresen, M., Stiel, A. C., Fölling, J., Wenzel, D., Schönle, A., Egner, A., Eggeling, C., Hell, S. W., Jakobs, S.: Photoswitchable fluorescent proteins enable monochromatic multilabel imaging and dual color fluorescence nanoscopy. *Nat. Biotechnol.* **26** (2008), 1035–1040

[106] Betzig, E., Hess, H. F., Shroff, H., Patterson, G. H., Lippincott-Schwartz, J., Davidson, M. W.: *Introduction to Photoactivated Localization Microscopy.* http://zeiss-campus.magnet.fsu.edu/, called on the 24.03.2013

[107] Yguerabide, J., Schmidt, J. A., Yguerabide, E. E.: Lateral mobility in membranes as detected by fluorescence recovery after photobleaching. *Biophys. J.* **40** (1982), 69–75

[108] Schwille, P., Haustein, E.: *Fluorescence correlation spectroscopy. An introduction to its concepts and applications.* Biophysics Textbook Online, 2001

[109] Magde, D., Elson, E. L.: Fluorescence Correlation Spectroscopy. I. Conceptual Basis and Theory. *Biopolymers* **13** (1974), 1–27

[110] Magde, D., Elson, E. L., Webb, W. W.: Fluorescence correlation spectroscopy. II. An experimental realization. *Biopolymers* **13** (1974), 29–61

[111] Einstein, A.: Über die von der molekularkinetischen Theorie der Wärme geforderte Bewegung von in ruhenden Flüssigkeiten suspendierten Teilchen. *Annalen d. Phys.* **322** (1905), 549–560

[112] Smoluchowski, M.: Zur kinetischen Theorie der Brownschen Molekularbewegung und der Suspensionen. *Annalen d. Phys.* **326** (1906), 756–780

[113] Röcker, C., Pötzl, M., Zhang, F., Parak, W. J., Nienhaus, G. U.: A quantitative fluorescence study of protein monolayer formation on colloidal nanoparticles. *Nat. Nanotechnol.* **4** (2009), 577–580

[114] Widengren, J., Rigler, R.: Fluorescence correlation spectroscopy as a tool to investigate chemical reactions in solutions and on cell surfaces. *Cell Mol. Biol.* **44** (1998), 857–879

[115] Schwille, P., Kummer, S., Heikal, A. A., Moerner, W. E., Webb, W. W.: Fluorescence correlation spectroscopy reveals fast optical excitation-driven intramolecular dynamics of yellow fluorescent proteins. *Proc. Natl. Acad. Sci. USA* **97** (2000), 151–156

[116] Digman, M. A., Sengupta, P., Wiseman, P. W., Brown, C. M., Horwitz, A. R., Gratton, E.: Fluctuation correlation spectroscopy with a laser-scanning microscope: exploiting the hidden time structure. *Biophys. J.* **88** (2005), L33–L36

[117] Magde, D., Webb, W. W., Elson, E. L.: Fluorescence Correlation Spectroscopy. III. Uniform Translation and Laminar Flow. *Biopolymers* **17** (1978), 361–376

[118] Dertinger, T., Pacheco, V., von der Hocht, I., Hartmann, R., Gregor, I., Enderlein, J.: Two-focus fluorescence correlation spectroscopy: a new tool for accurate and absolute diffusion measurements. *Chemphyschem* **8** (2007), 433–443

[119] Harke, B., Keller, J., Ullal, C. K., Westphal, V., Schönle, A., Hell, S. W.: Resolution scaling in STED microscopy. *Opt. Express* **16** (2008), 4154–4162

[120] Wildanger, D., Bückers, J., Westphal, V., Hell, S. W., Kastrup, L.: A STED microscope aligned by design. *Opt. Express* **17** (2009), 16100–16110

[121] Reuss, M., Engelhardt, J., Hell, S. W.: Birefringent device converts a standard scanning microscope into a STED microscope that also maps molecular orientation. *Opt. Express* **18** (2010), 1049–1058

[122] Wildanger, D., Rittweger, E., Kastrup, L., Hell, S. W.: STED microscopy with a supercontinuum laser source. *Opt. Express* **16** (2008), 9614–9621

[123] Hao, X., Kuang, C., Wang, T., Liu, X.: Effects of polarization on the de-excitation dark focal spot in STED microscopy. *Journal of Optics* **12** (2010), 115707

[124] Prunsche, B.: *Aufbau und Ansteuerung einer Optik für FRAP Experimente an einem Fluoreszenzmikroskop.*, Karlsruhe Inst. f. Tech. (KIT), Bachelor thesis, 2011

[125] Meyer, L., Wildanger, D., Medda, R., Punge, A., Rizzoli, S. O., Donnert, G., Hell, S. W.: Dual-color STED microscopy at 30-nm focal-plane resolution. *Small* **4** (2008), 1095–1100

[126] Donnert, G., Keller, J., Wurm, C. A., Rizzoli, S. O., Westphal, V., Schönle, A., Jahn, R., Jakobs, S., Eggeling, C., Hell, S. W.: Two-color far-field fluorescence nanoscopy. *Biophys. J.* **92** (2007), L67–L69

[127] Westphal, V., Rizzoli, S. O., Lauterbach, M. A., Kamin, D., Jahn, R., Hell, S. W.: Video-rate far-field optical nanoscopy dissects synaptic vesicle movement. *Science* **320** (2008), 246–249

[128] Mueller, V., Ringemann, C., Honigmann, A., Schwarzmann, G., Medda, R., Leutenegger, M., Polyakova, S., Belov, V. N., Hell, S. W., Eggeling, C.: STED nanoscopy reveals molecular details of cholesterol- and cytoskeleton-modulated lipid interactions in living cells. *Biophys. J.* **101** (2011), 1651–1660

[129] Leutenegger, M., Ringemann, C., Lasser, T., Hell, S. W., Eggeling, C.: Fluorescence correlation spectroscopy with a total internal reflection fluorescence STED microscope (TIRF-STED-FCS). *Opt. Express* **20** (2012), 5243–5263

[130] Hedde, P. N., Nienhaus, G. U.: Optical imaging of nanoscale cellular structures. *Biophys. Rev.* **2** (2010), 147–158

[131] Yildiz, A., Tomishige, M., Vale, R. D., Selvin, P. R.: Kinesin walks hand-over-hand. *Science* **303** (2004), 676–678

[132] Reck-Peterson, S. L., Yildiz, A., Carter, A. P., Gennerich, A., Zhang, N., Vale, R. D.: Single-molecule analysis of dynein processivity and stepping behavior. *Cell* **126** (2006), 335–348

[133] Cyrklaff, M., Kudryashev, M., Leis, A., Leonard, K., Baumeister, W., Menard, R., Meissner, M., Frischknecht, F.: Cryoelectron tomography reveals periodic material at the inner side of subpellicular microtubules in apicomplexan parasites. *J. Exp. Med.* **204** (2007), 1281–1287

[134] Reisler, E., Egelman, E. H.: Actin Structure and Function: What We Still Do Not Understand. *J. Biol. Chem.* **282** (2007), 36133–36137

[135] Pollard, T. D., Cooper, J. A.: Actin, a central player in cell shape and movement. *Science* **326** (2009), 1208–1212

[136] Sjöblom, B., Salmazo, A., Djinovic-Carugo, K.: Alpha-actinin structure and regulation. *Cell Mol. Life Sci.* **65** (2008), 2688–2701

[137] Eggeling, C., Ringemann, C., Medda, R., Schwarzmann, G., Sandhoff, K., Polyakova, S., Belov, V. N., Hein, B., Middendorff, C. von, Schönle, A., Hell, S. W.: Direct observation of the nanoscale dynamics of membrane lipids in a living cell. *Nature* **457** (2009), 1159–1162

[138] Digman, M. A., Wiseman, P. W., Horwitz, A. R., Gratton, E.: Detecting protein complexes in living cells from laser scanning confocal image sequences by the cross correlation raster image spectroscopy method. *Biophys. J.* **96** (2009), 707–716

[139] Vendelin, M., Birkedal, R.: Anisotropic diffusion of fluorescently labeled ATP in rat cardiomyocytes determined by raster image correlation spectroscopy. *Am. J. Physiol. Cell Physiol.* **295** (2008), C1302–C1315

[140] Weissman, M., Schindler, H., Feher, G.: Determination of molecular weights by fluctuation spectroscopy: application to DNA. *Proc. Natl. Acad. Sci. USA* **73** (1976), 2776–2780

[141] Petersen, N. O., Johnson, D. C., Schlesinger, M. J.: Scanning fluorescence correlation spectroscopy. II. Application to virus glycoprotein aggregation. *Biophys. J.* **49** (1986), 817–820

[142] Ries, J., Chiantia, S., Schwille, P.: Accurate determination of membrane dynamics with line-scan FCS. *Biophys. J.* **96** (2009), 1999–2008

[143] Ruan, Q., Cheng, M. A., Levi, M., Gratton, E., Mantulin, W. W.: Spatial-temporal studies of membrane dynamics: scanning fluorescence correlation spectroscopy (SFCS). *Biophys. J.* **87** (2004), 1260–1267

[144] Digman, M. A., Gratton, E.: Analysis of diffusion and binding in cells using the RICS approach. *Microsc. Res. Tech.* **72** (2009), 323–332

[145] Ries, J., Schwille, P.: Studying slow membrane dynamics with continuous wave scanning fluorescence correlation spectroscopy. *Biophys. J.* **91** (2006), 1915–1924

[146] Rossow, M. J., Sasaki, J. M., Digman, M. A., Gratton, E.: Raster image correlation spectroscopy in live cells. *Nat. Protoc.* **5** (2010), 1761–1774

[147] Keppler, A., Pick, H., Arrivoli, C., Vogel, H., Johnsson, K.: Labeling of fusion proteins with synthetic fluorophores in live cells. *Proc. Natl. Acad. Sci. USA* **101** (2004), 9955–9959

[148] Gautier, A., Juillerat, A., Heinis, C., Corrêa, I. R. Jr, Kindermann, M., Beaufils, F., Johnsson, K.: An engineered protein tag for multiprotein labeling in living cells. *Chem. Biol.* **15** (2008), 128–136

[149] Kask, P., Piksarv, P., Mets, ., Pooga, M., Lippma, E.: Fluorescence correlation spectroscopy in the nanosecond time range: rotational diffusion of bovine carbonic anhydrase B. *Eur. Biophys. J.* **14** (1987), 257–261

[150] Blomley, R. M.: *Aufbau und Anwendung eines Titan:Saphir-Lasersystems fuer STED-Mikroskopie.*, Karlsruhe Inst. f. Tech. (KIT), Dimploma thesis, 2013

[151] National Institute of Allergy and Infectious Diseases: Understanding the Immune System How It Works. *NIH Publication* **7** (2007), 5423

[152] Torres, A. J., Wu, M., Holowka, D., Baird, B.: Nanobiotechnology and cell biology: micro- and nanofabricated surfaces to investigate receptor-mediated signaling. *Annu. Rev. Biophys.* **37** (2008), 265–288

[153] Geisse, S., Scheidereit, C., Westphal, H. M., Hynes, N. E., Groner, B., Beato, M.: Glucocorticoid receptors recognize DNA sequences in and around murine mammary tumour virus DNA. *EMBO J.* **1** (1982), 1613–1619

[154] Pfahl, M.: Specific binding of the glucocorticoid-receptor complex to the mouse mammary tumor proviral promoter region. *Cell* **31** (1982), 475–482

[155] Scheidereit, C., Geisse, S., Westphal, H. M., Beato, M.: The glucocorticoid receptor binds to defined nucleotide sequences near the promoter of mouse mammary tumour virus. *Nature* **304** (1983), 749–752

[156] Chandler, V. L., Maler, B. A., Yamamoto, K. R.: DNA sequences bound specifically by glucocorticoid receptor in vitro render a heterologous promoter hormone responsive in vivo. *Cell* **33** (1983), 489–499

[157] Majors, J., Varmus, H. E.: A small region of the mouse mammary tumor virus long terminal repeat confers glucocorticoid hormone regulation on a linked heterologous gene. *Proc. Natl. Acad. Sci. USA* **80** (1983), 5866–5870

[158] Hynes, N., van Ooyen, A. J., Kennedy, N., Herrlich, P., Ponta, H., Groner, B.: Subfragments of the large terminal repeat cause glucocorticoid-responsive expression of mouse mammary tumor virus and of an adjacent gene. *Proc. Natl. Acad. Sci. USA* **80** (1983), 3637–3641

[159] Vassalli, J. D., Hamilton, J., Reich, E.: Macrophage plasminogen activator: modulation of enzyme production by anti-inflammatory steroids, mitotic inhibitors, and cyclic nucleotides. *Cell* **8** (1976), 271–281

[160] Werb, Z., Foley, R., Munck, A.: Glucocorticoid receptors and glucocorticoid-sensitive secretion of neutral proteinases in a macrophage line. *J. Immunol.* **121** (1978), 115–121

[161] Frisch, S. M., Ruley, H. E.: Transcription from the stromelysin promoter is induced by interleukin-1 and repressed by dexamethasone. *J. Biol. Chem.* **262** (1987), 16300–16304

[162] Jonat, C., Rahmsdorf, H. J., Park, K. K., Cato, A. C., Gebel, S., Ponta, H., Herrlich, P.: Antitumor promotion and antiinflammation: down-modulation of AP-1 (Fos/Jun) activity by glucocorticoid hormone. *Cell* **62** (1990), 1189–1204

[163] Heck, S., Kullmann, M., Gast, A., Ponta, H., Rahmsdorf, H. J., Herrlich, P., Cato, A. C.: A distinct modulating domain in glucocorticoid receptor monomers in the repression of activity of the transcription factor AP-1. *EMBO J.* **13** (1994), 4087–4095

[164] Heck, S., Bender, K., Kullmann, M., Göttlicher, M., Herrlich, P., Cato, A. C.: I kappaB alpha-independent downregulation of NF-kappaB activity by glucocorticoid receptor. *EMBO J.* **16** (1997), 4698–4707

[165] Löwenberg, M., Verhaar, A. P., van den Brink, G. R., Hommes, D. W.: Glucocorticoid signaling: a nongenomic mechanism for T-cell immunosuppression. *Trends Mol. Med.* **13** (2007), 158–163

[166] Piner, R. D., Zhu, J., Xu, F., Hong, S., Mirkin, C. A.: "Dip-Pen" nanolithography. *Science* **283** (1999), 661–663

[167] Orth, R. N., Wu, M., Holowka, D. A., Craighead, H. G., Baird, B. A.: Mast Cell Activation on Patterned Lipid Bilayers of Subcellular Dimensions. *Langmuir* **19** (2003), 1599–1605

[168] Wu, M., Holowka, D., Craighead, H. G., Baird, B.: Visualization of plasma membrane compartmentalization with patterned lipid bilayers. *Proc. Natl. Acad. Sci. USA* **101** (2004), 13798–13803

[169] Kinet, J. P.: The high-affinity IgE receptor (Fc epsilon RI): from physiology to pathology. *Annu. Rev. Immunol.* **17** (1999), 931–972

[170] Vangelista, L., Cesco-Gaspere, M., Lorenzi, R., Burrone, O.: A minimal receptor-Ig chimera of human FcepsilonRI alpha-chain efficiently binds secretory and membrane IgE. *Protein Eng.* **15** (2002), 51–57

[171] Franchimont, D.: Overview of the actions of glucocorticoids on the immune response: a good model to characterize new pathways of immunosuppression for new treatment strategies. *Ann. N. Y. Acad. Sci.* **1024** (2004), 124–137

[172] Newton, R.: Molecular mechanisms of glucocorticoid action: what is important? *Thorax* **55** (2000), 603–613

[173] Pratt, W. B., Galigniana, M. D., Morishima, Y., Murphy, P. J. M.: Role of molecular chaperones in steroid receptor action. *Essays Biochem.* **40** (2004), 41–58

[174] Auphan, N., DiDonato, J. A., Rosette, C., Helmberg, A., Karin, M.: Immunosuppression by glucocorticoids: inhibition of NF-kappa B activity through induction of I kappa B synthesis. *Science* **270** (1995), 286–290

[175] Dostert, A., Heinzel, T.: Negative glucocorticoid receptor response elements and their role in glucocorticoid action. *Curr. Pharm. Des.* **10** (2004), 2807–2816

[176] Adcock, I. M., Caramori, G.: Cross-talk between pro-inflammatory transcription factors and glucocorticoids. *Immunol. Cell Biol.* **79** (2001), 376–384

[177] Tasker, J. G., Di, S., Malcher-Lopes, R.: Minireview: rapid glucocorticoid signaling via membrane-associated receptors. *Endocrinology* **147** (2006), 5549–5556

[178] Maier, C., Rünzler, D., Schindelar, J., Grabner, G., Waldhäusl, W., Köhler, G., Luger, A.: G-protein-coupled glucocorticoid receptors on the pituitary cell membrane. *J. Cell Sci.* **118** (2005), 3353–3361

[179] Bartholome, B., Spies, C. M., Gaber, T., Schuchmann, S., Berki, T., Kunkel, D., Bienert, M., Radbruch, A., Burmester, G. R., Lauster, R., Scheffold, A., Buttgereit, F.: Membrane glucocorticoid receptors (mGCR) are expressed in normal human peripheral blood mononuclear cells and up-regulated after in vitro stimulation and in patients with rheumatoid arthritis. *FASEB J.* **18** (2004), 70–80

[180] Kassel, O., Sancono, A., Krätzschmar, J., Kreft, B., Stassen, M., Cato, A. C.: Glucocorticoids inhibit MAP kinase via increased expression and decreased degradation of MKP-1. *EMBO J.* **20** (2001), 7108–7116

[181] Falkenstein, E., Tillmann, H. C., Christ, M., Feuring, M., Wehling, M.: Multiple actions of steroid hormones–a focus on rapid, nongenomic effects. *Pharmacol. Rev.* **52** (2000), 513–556

[182] Mathur, J., Mathur, N., Hülskamp, M.: Simultaneous visualization of peroxisomes and cytoskeletal elements reveals actin and not microtubule-based peroxisome motility in plants. *Plant Physiol.* **128** (2002), 1031–1045

[183] Van Gestel, K., Köhler, R. H., Verbelen, J.-P.: Plant mitochondria move on F-actin, but their positioning in the cortical cytoplasm depends on both F-actin and microtubules. *J. Exp. Bot.* **53** (2002), 659–667

[184] Boevink, P., Oparka, K., Santa Cruz, S., Martin, B., Betteridge, A., Hawes, C.: Stacks on tracks: the plant Golgi apparatus traffics on an actin/ER network. *Plant J.* **15** (1998), 441–447

[185] Kadota, A., Yamada, N., Suetsugu, N., Hirose, M., Saito, C., Shoda, K., Ichikawa, S., Kagawa, T., Nakano, A., Wada, M.: Short actin-based mechanism for light-directed chloroplast movement in Arabidopsis. *Proc. Natl. Acad. Sci. USA* **106** (2009), 13106–13111

[186] Yamashita, H., Sato, Y., Kanegae, T., Kagawa, T., Wada, M., Kadota, A.: Chloroplast actin filaments organize meshwork on the photorelocated chloroplasts in the moss Physcomitrella patens. *Planta* **233** (2011), 357–368

[187] Shimmen, T., Yokota, E.: Cytoplasmic streaming in plants. *Curr. Opin. Cell Biol.* **16** (2004), 68–72

[188] Ueda, H., Yokota, E., Kutsuna, N., Shimada, T., Tamura, K., Shimmen, T., Hasezawa, S., Dolja, V. V., Hara-Nishimura, I.: Myosin-dependent endoplasmic reticulum motility and F-actin organization in plant cells. *Proc. Natl. Acad. Sci. USA* **107** (2010), 6894–6899

[189] Hohenberger, P., Eing, C., Straessner, R., Durst, S., Frey, W., Nick, P.: Plant actin controls membrane permeability. *Biochim. Biophys. Acta.* **1808** (2011), 2304–2312

[190] Frey, N., Klotz, J., Nick, P.: A kinesin with calponin-homology domain is involved in premitotic nuclear migration. *J. Exp. Bot.* **61** (2010), 3423–3437

[191] Staiger, C. J., Yuan, M., Valenta, R., Shaw, P. J., Warn, R. M., Lloyd, C. W.: Microinjected profilin affects cytoplasmic streaming in plant cells by rapidly depolymerizing actin microfilaments. *Curr. Biol.* **4** (1994), 215–219

[192] Sheahan, M. B., Rose, R. J., McCurdy, D. W.: Actin-filament-dependent remodeling of the vacuole in cultured mesophyll protoplasts. *Protoplasma* **230** (2007), 141–152

[193] Qiao, F., Chang, X.-L., Nick, P.: The cytoskeleton enhances gene expression in the response to the Harpin elicitor in grapevine. *J. Exp. Bot.* **61** (2010), 4021–4031

[194] Meagher, R. B., McKinney, E. C., Kandasamy, M. K.: Isovariant dynamics expand and buffer the responses of complex systems: the diverse plant actin gene family. *Plant Cell* **11** (1999), 995–1006

[195] Hussey, P. J., Allwood, E. G., Smertenko, A. P.: Actin-binding proteins in the Arabidopsis genome database: properties of functionally distinct plant actin-depolymerizing factors/cofilins. *Philos. Trans. R. Soc. Lond. B. Biol. Sci.* **357** (2002), 791–798

[196] Fuchs, J.: *Characterization and Application of Photoswitchable Fluorescent Proteins for Nanoscopy.*, Karlsruhe Inst. f. Tech. (KIT), PhD thesis, 2011

[197] Riedl, J., Crevenna, A. H., Kessenbrock, K., Yu, J. H., Neukirchen, D., Bista, M., Bradke, F., Jenne, D., Holak, T. A., Werb, Z., Sixt, M., Wedlich-Soldner, R.: Lifeact: a versatile marker to visualize F-actin. *Nat. Methods* **5** (2008), 605–607

[198] Karimi, M., Inzé, D., Depicker, A.: GATEWAY vectors for Agrobacterium-mediated plant transformation. *Trends Plant Sci.* **7** (2002), 193–195

[199] Finer, J., Vain, P., Jones, M., McMullen, M.: Development of the particle inflow gun for DNA delivery to plant cells. *Plant Cell Rep.* **11** (1992), 323–328

[200] Buschmann, H., Green, P., Sambade, A., Doonan, J. H., Lloyd, C. W.: Cytoskeletal dynamics in interphase, mitosis and cytokinesis analysed through Agrobacterium-mediated transient transformation of tobacco BY-2 cells. *New Phytologist* **190** (2011), 258–267

[201] Fölling, J., Belov, V., Kunetsky, R., Medda, R., Schönle, A., Egner, A., Eggeling, C., Bossi, M., Hell, S. W.: Photochromic rhodamines provide nanoscopy with optical sectioning. *Angew. Chem. Int. Ed. Engl.* **46** (2007), 6266–6270

[202] Vaziri, A., Tang, J., Shroff, H., Shank, C. V.: Multilayer three-dimensional super resolution imaging of thick biological samples. *Proc. Natl. Acad. Sci. USA* **105** (2008), 20221–20226

[203] Leduc, C., Padberg-Gehle, K., Varga, V., Helbing, D., Diez, S., Howard, J.: Molecular crowding creates traffic jams of kinesin motors on microtubules. *Proc. Natl. Acad. Sci. USA* **109** (2012), 6100–6105

[204] Carlsson, L., Thornell, L. E.: Desmin-related myopathies in mice and man. *Acta Physiol. Scand.* **171** (2001), 341–348

[205] Fuchs, E., Weber, K.: Intermediate filaments: structure, dynamics, function, and disease. *Annu. Rev. Biochem.* **63** (1994), 345–382

[206] Small, J. V., Gimona, M.: The cytoskeleton of the vertebrate smooth muscle cell. *Acta Physiol. Scand.* **164** (1998), 341–348

[207] Herrmann, H., Strelkov, S. V., Burkhard, P., Aebi, U.: Intermediate filaments: primary determinants of cell architecture and plasticity. *J. Clin. Invest.* **119** (2009), 1772–1783

[208] Ackbarow, T., Buehler, M. J.: Superelasticity, energy dissipation and strain hardening of vimentin coiled-coil intermediate filaments: atomistic and continuum studies. *J. Mat. Science* **42** (2007), 8771–8787

[209] Milner, D. J., Weitzer, G., Tran, D., Bradley, A., Capetanaki, Y.: Disruption of muscle architecture and myocardial degeneration in mice lacking desmin. *J. Cell. Biol.* **134** (1996), 1255–1270

[210] Thornell, L., Carlsson, L., Li, Z., Mericskay, M., Paulin, D.: Null mutation in the desmin gene gives rise to a cardiomyopathy. *J. Mol. Cell Cardiol.* **29** (1997), 2107–2124

[211] Paulin, D., Huet, A., Khanamyrian, L., Xue, Z.: Desminopathies in muscle disease. *J. Pathol.* **204** (2004), 418–427

[212] Goldfarb, L. G., Park, K. Y., Cervenáková, L., Gorokhova, S., Lee, H. S., Vasconcelos, O., Nagle, J. W., Semino-Mora, C., Sivakumar, K., Dalakas, M. C.: Missense mutations in desmin associated with familial cardiac and skeletal myopathy. *Nat. Genet.* **19** (1998), 402–403

[213] Muñoz-Mármol, A. M., Strasser, G., Isamat, M., Coulombe, P. A., Yang, Y., Roca, X., Vela, E., Mate, J. L., Coll, J., Fernández-Figueras, M. T., Navas-Palacios, J. J., Ariza, A., Fuchs, E.: A dysfunctional desmin mutation in a patient with severe generalized myopathy. *Proc. Natl. Acad. Sci. USA* **95** (1998), 11312–11317

[214] Schröder, R., Goudeau, B., Simon, M. C., Fischer, D., Eggermann, T., Clemen, C. S., Li, Z., Reimann, J., Xue, Z., Rudnik-Schöneborn, S., Zerres, K., van der Ven, P. F. M., Fürst, D. O., Kunz, W. S., Vicart, P.: On noxious desmin: functional effects of a novel heterozygous desmin insertion mutation on the extrasarcomeric desmin cytoskeleton and mitochondria. *Hum. Mol. Genet.* **12** (2003), 657–669

[215] Klauke, B., Kossmann, S., Gaertner, A., Brand, K., Stork, I., Brodehl, A., Dieding, M., Walhorn, V., Anselmetti, D., Gerdes, D., Bohms, B., Schulz, U., Zu Knyphausen, E., Vorgerd, M., Gummert, J., Milting, H.: De novo desmin-mutation N116S is associated with arrhythmogenic right ventricular cardiomyopathy. *Hum. Mol. Genet.* **19** (2010), 4595–4607

[216] Subach, F. V., Patterson, G. H., Manley, S., Gillette, J. M., Lippincott-Schwartz, J., Verkhusha, V. V.: Photoactivatable mCherry for high-resolution two-color fluorescence microscopy. *Nat. Methods* **6** (2009), 153–159

[217] Stiel, A. C., Trowitzsch, S., Weber, G., Andresen, M., Eggeling, C., Hell, S. W., Jakobs, S., Wahl, M. C.: 1.8 A bright-state structure of the reversibly switchable fluorescent protein Dronpa guides the generation of fast switching variants. *Biochem. J.* **402** (2007), 35–42

[218] McKinney, S. A., Murphy, C. S., Hazelwood, K. L., Davidson, M. W., Looger, L. L.: A bright and photostable photoconvertible fluorescent protein. *Nat. Methods* **6** (2009), 131–133

[219] Gurskaya, N. G., Verkhusha, V. V., Shcheglov, A. S., Staroverov, D. B., Chepurnykh, T. V., Fradkov, A. F., Lukyanov, S., Lukyanov, K. A.: Engineering of a monomeric green-to-red photoactivatable fluorescent protein induced by blue light. *Nat. Biotechnol.* **24** (2006), 461–465

[220] Stiel, A. C., Andresen, M., Bock, H., Hilbert, M., Schilde, J., Schönle, A., Eggeling, C., Egner, A., Hell, S. W., Jakobs, S.: Generation of monomeric reversibly switchable red fluorescent proteins for far-field fluorescence nanoscopy. *Biophys. J.* **95** (2008), 2989–2997

[221] Jares-Erijman, E. A., Jovin, T. M.: FRET imaging. *Nat. Biotechnol.* **21** (2003), 1387–1395

[222] Brodehl, A., Hedde, P. N., Dieding, M., Fatima, A., Walhorn, V., Gayda, S., Šaric, T., Klauke, B., Gummert, J., Anselmetti, D., Heilemann, M., Nienhaus, G. U., Milting, H.: Dual color photoactivation localization microscopy of cardiomyopathy-associated desmin mutants. *J. Biol. Chem.* **287** (2012), 16047–16057

[223] Hong, D., Wang, Z., Zhang, W., Xi, J., Lu, J., Luan, X., Yuan, Y.: A series of Chinese patients with desminopathy associated with six novel and one reported mutations in the desmin gene. *Neuropathol. Appl. Neurobiol.* **37** (2011), 257–270

[224] van Spaendonck-Zwarts, K., van Hessem, L., Jongbloed, J. D. H., Walle, H. E. K., Capetanaki, Y., van der Kooi, A. J., van Langen, I. M., van den Berg, M. P., van Tintelen, J. P.: Desmin-related myopathy: a review and meta-analysis. *Clin. Genet.* **80** (2010), 354–366

[225] Sharma, S., Mücke, N., Katus, H. A., Herrmann, H., Bär, H.: Disease mutations in the "head" domain of the extra-sarcomeric protein desmin distinctly alter its assembly and network-forming properties. *J. Mol. Med.* **87** (2009), 1207–1219

[226] Pica, E. C., Kathirvel, P., Pramono, Z. A. D., Lai, P.-S., Yee, W.-C.: Characterization of a novel S13F desmin mutation associated with desmin myopathy and heart block in a Chinese family. *Neuromuscul. Disord.* **18** (2008), 178–182

[227] Raats, J. M., Pieper, F. R., Vree Egberts, W. T., Verrijp, K. N., Ramaekers, F. C., Bloemendal, H.: Assembly of amino-terminally deleted desmin in vimentin-free cells. *J. Cell. Biol.* **111** (1990), 1971–1985

[228] Kitamura, S., Ando, S., Shibata, M., Tanabe, K., Sato, C., Inagaki, M.: Protein kinase C phosphorylation of desmin at four serine residues within the non-alpha-helical head domain. *J. Biol. Chem.* **264** (1989), 5674–5678

[229] Vernengo, L., Chourbagi, O., Panuncio, A., Lilienbaum, A., Batonnet-Pichon, S., Bruston, F., Rodrigues-Lima, F., Mesa, R., Pizzarossa, C., Demay, L., Richard, P., Vicart, P., Rodriguez, M.-M.: Desmin myopathy with severe cardiomyopathy in a Uruguayan family due to a codon deletion in a new location within the desmin 1A rod domain. *Neuromuscul. Disord.* **20** (2010), 178–187

[230] Chourbagi, O., Bruston, F., Carinci, M., Xue, Z., Vicart, P., Paulin, D., Agbulut, O.: Desmin mutations in the terminal consensus motif prevent synemin-desmin heteropolymer filament assembly. *Exp. Cell Res.* **317** (2011), 886–897

[231] Dalakas, M. C., Dagvadorj, A., Goudeau, B., Park, K. Y., Takeda, K., Simon-Casteras, M., Vasconcelos, O., Sambuughin, N., Shatunov, A., Nagle, J. W., Sivakumar, K., Vicart, P., Goldfarb, L. G.: Progressive skeletal myopathy, a phenotypic variant of desmin myopathy associated with desmin mutations. *Neuromuscul. Disord.* **13** (2003), 252–258

[232] Levin, J., Bulst, S., Thirion, C., Schmidt, F., Bötzel, K., Krause, S., Pertl, C., Kretzschmar, H., Walter, M. C., Giese, A., Lochmüller, H.: Divergent molecular effects of desmin mutations on protein assembly in myofibrillar myopathy. *J. Neuropathol. Exp. Neurol.* **69** (2010), 415–424

[233] Bär, H., Goudeau, B., Wälde, S., Casteras-Simon, M., Mücke, N., Shatunov, A., Goldberg, Y. P., Clarke, C., Holton, J. L., Eymard, B., Katus, H. A., Fardeau, M., Goldfarb, L., Vicart, P., Herrmann, H.: Conspicuous involvement of desmin tail mutations in diverse cardiac and skeletal myopathies. *Hum. Mutat.* **28** (2007), 374–386

[234] Bär, H., Schopferer, M., Sharma, S., Hochstein, B., Mücke, N., Herrmann, H., Willenbacher, N.: Mutations in desmin's carboxy-terminal "tail" domain severely modify filament and network mechanics. *J. Mol. Biol.* **397** (2010), 1188–1198

A. List of Publications

Hedde, P. N., Fuchs, J., Oswald, F., Wiedenmann, J., & Nienhaus, G. U.: **Online Image Analysis for Photoactivation Localization Microscopy.** *Nature Methods* **6** (2009) 689-690.

Quan, Q., Li, P., Long, F., Zeng, S., Luo, Q., Hedde, P. N., Nienhaus, G. U., & Huang, Z.-L.: **Ultra-fast, High-precision Image Analysis for Localization-based Superresolution Microscopy.** *Optics Express* **18** (2010) 11867-11876.

Hedde, P. N., & Nienhaus, G. U.: **Optical Imaging of Nanoscale Cellular Structures.** *Biophysical Reviews* **2** (2010) 147-158.

Fuchs, J.*, Böhme, S.*, Oswald, F.*, Hedde, P. N., Krause, M., Wiedenmann, J., & Nienhaus, G. U.: **A Photoactivatable Marker Protein for Pulse-chase Imaging with Superresolution.** *Nature Methods* **7** (2010) 627-630.

Brodehl, A., Hedde, P. N., Dieding, M., Fatima, A., Walhorn, V., Gayda, S., Saric, T., Klauke, B., Gummert, J., Anselmetti, D., Heilemann, M., Nienhaus, G. U., & Milting, H.: **Molecular Insights into Filament Assembly Defects of ARVC-related Desmin Mutations.** *The Journal of Biological Chemistry* **287** (2012) 16047-16057.

Hedde, P. N. & Nienhaus, G. U.: **Sub-wavelength Optical Fluorescence Microscopy for Biological Applications.** in Springer Series: *NATO Science for Peace and Security Series B: Physics and Biophysics, Nano-Optics for Enhancing Light-Matter Interactions on a Molecular Scale: Plasmonics, Photonic Crystals, Metamaterials and Sub-Wavelength Resolution*, eds.: B. di Bartolo, J. Collins, Springer Science + Business Media B.V., Dordrecht (2013), pp. 47-71.

Gayda, S., Hedde, P. N., Nienhaus K., & Nienhaus, G. U.: **Probes for Nanoscopy: Fluorescent Proteins.** in Springer Series on Fluorescence: *Far-Field Optical Nanoscopy*, eds.: P. Tinnefeld, C. Eggeling and S. W. Hell, Springer Verlag, Berlin (2013)

Durst, S., Hedde, P. N., Brochhausen, L., Nick, P., Nienhaus, G. U., & Maisch, J.: **Organization of Perinuclear Actin in Live Tobacco Cells Observed by PALM with Optical Sectioning.** submitted.

Li, Y., Ishitsuka, Y., Hedde, P. N., & Nienhaus, G. U.: **Fast and Robust Molecule Detection in Localization-based Super-resolution Microscopy.** *ACS Nano* **7** (2013) 5207-5214.

Hedde, P. N., Dörlich, R. M., Blomley, R., Gradl, D., Oppong, E., Cato, A. C. B., & Nienhaus, G. U.: **Stimulated Emission Depletion-based Raster Image Correlation Spectroscopy Reveals Biomolecular Dynamics in Live Cells.** *Nature Communications* **4** (2013) 2093.

Oppong, E.*, Hedde, P. N.*, Sekula-Neuner, S., Brinkmann, F., Ambili, M., Dörlich, R. M., Hirtz, M., Fuchs, H., Nienhaus, G. U., & Cato, A. C. B.: **Localisation and Dynamics of Glucocorticoid Receptor at the Plasma Membrane of Mast Cells.** submitted.

*These authors contributed equally.

B. List of Presentations

2008 *annual Deutsche Gesellschaft für Biophysik (DGfB) meeting in Berlin, Germany.* Hedde, P. N., Fuchs, J., & Nienhaus, G. U.: **Realization and application of high resolution microscopy.** Poster presentation.

2009 *sectional Deutsche Gesellschaft für Biophysik (DGfB) meeting in Hühnfeld, Germany.* Fuchs, J., Hedde, P. N., Gundel, S., Wiedenmann, J., & Nienhaus, G. U.: **A new red fluorescent protein for high resolution microscopy.** Poster presentation.

2010 *annual Deutsche Gesellschaft für Biophysik (DGfB) meeting in Bochum, Germany.* Hedde, P. N., Dörlich, R. M., Fuchs, J., Gayda, S., Oswald, F., & Nienhaus, G. U.: **High resolution microscopy in live-cell imaging.** Poster presentation.

2011 *Focus on Microscopy (FOM) conference in Konstanz, Germany.* Li, Y., Hedde, P. N., & Nienhaus, G. U.: **Online photoactivation localization microscopy (PALM) imaging.** Poster presentation.

2011 *sectional Deutsche Gesellschaft für Biophysik (DGfB) meeting in Hühnfeld, Germany.* Hedde, P. N., Oppong, E., Sekula-Neuner, S., Cato, A. C. B., & Nienhaus, G. U.: **Studying non-genomic actions of glucocorticoids in mast cells using TIRF microscopy.** Poster presentation.

2012 *annual Deutsche Gesellschaft für Biophysik (DGfB) meeting in Göttingen, Germany.* Dörlich, R. M., Hedde, P. N., & Nienhaus, G. U.: **Fluorescence correlation spectroscopy techniques to determine molecular interactions.** Poster presentation.

2012 *annual Biophysical Society meeting in San Diego, USA.* Hedde, P. N., Gayda, S., Brodehl, A., Gummert, J., Milting, H., & Nienhaus, G. U.: **Colocalization analysis of mutant and wildtype desmin using dual color super-resolution microscopy.** Poster presentation.

C. Curriculum Vitae

About my Person

Per Niklas Hedde
Blumenstraße 19
76133 Karlsruhe, Germany
Born on March 7th, 1983 in Ulm, Germany

Education and Research Experience

1993 – 2002	Attendance of the Kepler Gymnasium Ulm, concluded with the general qualification for university entrance on June 21st, 2002.
2002 – 2003	Community service at the Rehabilitationskrankenhaus Ulm (RKU), 01-Aug-2002–31-May-2003.
2003 – 2009	Student at the University of Ulm, study of physics. Intermediate diploma on March 13th, 2006. Diploma thesis: PALM in living cells, 01-July-2008–01-July-2009.
2009 – 2013	Research assistant at the Karlsruhe Institute of Technology (KIT). PhD project: Light microscopy beyond the diffraction barrier, 01-Oct-2009–01-Mar-2013. Laser safety representative at the Institute of Applied Physics (APH), 01-Nov-2009–01-Nov-2012. Grant of the Applied Life Sciences (ALS) start-up-funds 2011 (KIT, Forschungsförderung - FOR).

D. Acknowledgement

At this point I would like to take the opportunity to express my sincere gratitude to all the people that have contributed, supported and helped me with this thesis. Among these, I would specifically like to mention

- Ulrich Nienhaus for giving me the opportunity to work on this PhD project in his lab. I very much appreciated his careful supervision of my work while at the same time giving me free rein in a lot of concerns. He taught me a lot about biophysics and scientific research in general.
- Thomas Schimmel for making himself available as second referee and for his interest in this work.
- Dagmar Gerthsen for making herself available as mentor during the course of this work.
- Jochen Fuchs for indispensible discussion and support. Especially during the start-up period, he more than once pointed me in the right direction.
- Susan Gayda for her help with all issues related to fluorescent proteins. Without her expertise, many experiments would not have been possible.
- René Dörlich for his support of this work. Discussion with him helped me a lot to understand the subtleties of correlation spectroscopy.
- Andreas Brodehl, Emmanuel Oppong, Steffen Durst, Dietmar Gradl and Claudia Winter for their essential work regarding cell culture and cell biology. Without their support, this thesis would not contain so many biological applications and, of course, colorful pictures.
- Alexander Hepting, Michael Hippe, Mario Nusche, Frank Landhäußer and Werner Wagner for many custom-built optomechanical and electronic parts very important for microscope construction.
- Karin Nienhaus for proofreading numerous abstracts and her help with bureaucracy while purchasing new equipment.
- Benjamin Harke for his hospitality in Göttingen and valuable advice on STED microscopy.
- Jonas Conradt for his help for this thesis to comply with all the formalities relevant for submission.

- Andrei Kobitski, Robert Rieger, Stefan Brandholt, Anika Hense, Naghmeh Azadfar, Pauline Maffre, Florian Stockmar and David Evans for diverse support and their excellent cooperation.
- My parents for their unconditioned support of all my projects.
- My grandparents for their inspiration and intercession of endurance.